

New Methods and Theory for Increasing Transmission of Light through Highly-Scattering Random Media

by

Curtis Jin

A dissertation submitted in partial fulfillment
of the requirements for the degree of
Doctor of Philosophy
(Electrical Engineering: Systems)
in The University of Michigan
2014

Doctoral Committee:

Professor Rajesh Rao Nadakuditi, Chair
Professor Jeffrey Fessler
Professor Eric Michielssen
Professor Stephen C. Rand
Professor John C. Schotland

For the light

ACKNOWLEDGEMENTS

My thesis work all started from a curiosity on a very fascinating but obscure phenomenon of light, perfect transmission of light. My Ph.D. has been a journey to convince myself that this phenomenon is true, and to get a better understanding on this. I am so glad that I have learned so many things throughout this wonderful journey, and gained a better insight and understanding on the phenomenon.

Because this work lies at the interface of computational electromagnetics, optics, statistical signal processing and applied math, I have had many helps and advices from faculty members from different fields. I could not have accomplished all the work without my committee members. I am especially indebted to my adviser professor Raj, who gave me an opportunity to join this exciting scientific expedition, who always had patience, and who encouraged me to overcome all the challenging problems. I am grateful to professor Michielssen for introducing me to computation electromagnetics, which is a very beautiful area that bridges the gap between theory and practice with mathematical rigor, and to professor Rand for all the valuable advices on the experimental side of the work. I also thank professor Fessler for the advices on the iterative methods that I have developed.

I hope my work leads to a greater scientific discovery.

TABLE OF CONTENTS

DEDICATION	ii
ACKNOWLEDGEMENTS	iii
LIST OF FIGURES	vii
LIST OF TABLES	xiii
LIST OF ALGORITHMS	xiv
LIST OF APPENDICES	xv
ABSTRACT	xvi
CHAPTER	
I. Introduction	1
1.1 Numerical Verification	3
1.2 Algorithms Development	5
1.3 Derivation of the Transmission Coefficient Distribution	7
II. Scattering Matrix	8
2.1 Modes	9
2.2 Scattering Matrix & Transfer Matrix	10
2.3 Number of modes to use in the matrix	13
2.4 Properties of the scattering matrix	15
2.4.1 Power Conservation	15
2.4.2 Time-reversal Symmetry	16
2.4.3 Reciprocity	19
2.5 Useful Formulas	23
2.5.1 Cascading Formula	24
2.5.2 Intermediate Waves	27
2.6 Construction of Scattering Matrix	29
2.6.1 Assumptions on the scatterers and modes	30

2.6.2	Scattering Matrix Generating Algorithm	33
2.6.3	Maxwell's equations solver - aperiodic case	34
2.6.4	Maxwell's equations solver - periodic case	42
2.6.5	Cylinder waves to Planewaves conversion	44
2.6.6	Computational Issue - Speed	53
2.6.7	Computational Issue - Accuracy	59
III. Transmission Maximization and Focusing of Light		61
3.1	Setup	62
3.2	Problem formulation	63
3.2.1	Transmission maximization	63
3.2.2	Focusing	64
3.3	Recognizing physically realizable matrix-vector operations . .	66
3.4	Iterative, physically realizable algorithms for transmission maximization	68
3.4.1	Steepest descent method	68
3.4.2	Conjugate gradient method	72
3.5	An iterative, physically realizable focusing algorithm	75
3.6	Numerical simulations and validation of the existence of highly transmitting eigen-wavefronts	77
IV. Phase-only Algorithms for Transmission Maximization		88
4.1	Setup	89
4.2	Problem formulation	90
4.3	Non-iterative, phase-only modulating algorithms for transmission maximization	91
4.4	Theoretical limit of phase-only modulated light transmission .	94
4.5	Iterative, phase-only modulated algorithms for transmission maximization	97
4.5.1	Steepest Descent Method	97
4.5.2	Gradient Method	99
4.6	Numerical simulations	101
V. Theory of Perfect Transmission		110
5.1	Setup	110
5.2	Problem Formulation	112
5.3	Basics	113
5.3.1	Relationship between τ and λ	113
5.3.2	Free Probability	116
5.4	Proposed Random Matrix Model : Random Point-Symmetric Matrix	117
5.4.1	Observations	118

5.4.2	Construction of Random Point-Symmetric Matrix . . .	120
5.4.3	Singular Values of the Random Point-Symmetric Trans- fer Matrix	122
5.4.4	<i>S</i> -Transform of the Distribution	122
5.5	Results	125
5.5.1	Distribution Comparison	125
5.5.2	Moments	127
VI. Conclusion		130
APPENDICES		132
INDEX		157
BIBLIOGRAPHY		158

LIST OF FIGURES

<u>Figure</u>		
1.1	Theoretical transmission coefficient distribution in (3.7) for $L/l = 3$.	1
1.2	The breakthrough experiments of Vellekoop and Mosk, which exemplifies the existence of highly transmitting eigen-wavefronts.	2
1.3	Empirical transmission coefficients distribution.	3
1.4	Wavefield plot of the incident-plus-backscatter wave corresponding to one of the perfectly transmitting inputs. The pink box is the scattering system considered, and the blue circles are the cylindrical scatterers. The perfectly transmitting input is shined from the left to the right, and the color represents the height of the wave corresponding to the colorbar.	4
1.5	Schematic for the experimental setup. (Figure from Steve C. Rand)	6
2.1	Propagating Mode and Evanescent Mode	10
2.2	Four major waves related to the scattering system, φ_1^+ , φ_1^- , φ_2^+ and φ_2^- . φ_1^+ and φ_1^- 's reference coordinate is O_1 and φ_2^+ and φ_2^- 's reference coordinate is O_2	11
2.3	Partitions of scattering matrix and their meanings	13
2.4	If the mode carries significant amount of power in the region of interest, we can not discard it. (a)Propagating mode; since the propagating mode never decays, we must always include it in the scattering matrix. (b)Strong evanescent mode; if the evanescent mode is still strong at the boundary, we must include it in the matrix. (c)Weak evanescent mode; if the evanescent mode is weak at the boundary, it will diminish in the region, thus can be neglected.	14
2.5	Original solution and the Time-reversed solution to the system. . .	17

2.6	Cascading two scattering matrices.	24
2.7	Cascading two transfer matrices	25
2.8	When scattering systems are cascaded, we have to make sure we are including all the modes that are still significant to the neighboring system.	26
2.9	N-cascaded scattering systems. We are interested in the intermediate waves.	27
2.10	To obtain the intermediate wave, E_n^+ and E_n^- , we deal with two cascaded scattering matrices S_1 and S_2	28
2.11	Currents in between the cascaded scattering system are plotted when the system is excited with the optimal input yielding 0.99 transmitted power at the end. Notice that there is a huge forward current in the middle, and correspondingly huge backward current to make the net current remain nearly constant.	29
2.12	Geometrical Situation. The scatterer is a cylinder infinitely long in z direction, and wave propagates on the xy -plane.	30
2.13	Geometrical situation on the xy -plane gives a simpler point of view.	31
2.14	Incident planewave should be expressed as J_n since it is finite everywhere. Because of the symmetric shape of the cylinder, if a n -th order cylinder wave is incident on a cylinder, two n -th order cylinder waves will be produced. One is an outgoing cylinder wave, $H_n^{(2)}$, and the other is a standing wave inside the cylinder, J_n . The scattering coefficient z_n can be obtained by solving boundary value problem.	35
2.15	Scattering Situation with multiple cylinders. It is important to consider the scattered waves from the other cylinders as an input to each cylinder.	37
2.16	Planewave with incident angle ϕ^{inc} is shined on a cylinder positioned at $(clocx, clocy)$. We have to describe planewave whose coordinate system is O in cylinder waves whose coordinate systems is the cylinder coordinate o'	38
2.17	Absolute value of the scattering coefficient versus the order of the mode; Result from a PEC cylinder with radius of 0.5 when the wavelength is 0.93. Notice that the scattering coefficient becomes nearly zero after a certain order of mode.	39

2.18	<p>T Matrix transforms the cylinder wave coming from the source cylinder into a cylinder wave going into the object cylinder. This involves a coordinate transformation from the source cylinder's coordinate system O' to the object cylinder's coordinate system O.</p>	40
2.19	<p>Intensity plot of 6 PEC cylinders, depicted as black circles , when plane wave of $\phi^{inc} = 90^\circ$ was shined. (a) There is a strong scattered wave on the upper region, but it is canceled out in plot (b) because of the incident wave, thus forming a shade region on the upper region.</p>	42
2.20	<p>Periodic system. We denote the original system as the '0-th system', and we repeat it with a period in the x direction.</p>	42
2.21	<p>We have to consider the scattered wave from the repeated systems in periodic case.</p>	43
2.22	<p>When the incident light is perpendicular to the periodic system, the scattering patters in all the repeated systems will be the same.</p>	43
2.23	<p>If we shine a tilted light to a periodic system, the repeated systems will have phase delayed inputs depending how far they are from the 0^{th} system. As a result, the phase delayed input will cause a phased delayed output from each repeated system.</p>	44
2.24	<p>Obtaining the modal coefficients of the scattered wave for S_{11} partition.</p>	46
2.25	<p>To extract the modal coefficients, we have to use the fact that S_{11} partition only considers the waves going down.</p>	46
2.26	<p>Obtaining the modal coefficients of the scattered wave for S_{21} partition. The scattered wave going upwards are based on the coordinate system $O_2(x_2, y_2)$. So we have to be careful since the coordinate system is changing from $O_1(x_1, y_1)$ to $O_2(x_2, y_2)$.</p>	48
2.27	<p>To extract the modal coefficients, we have to use the fact that S_{21} partition only considers the waves going up, and we also have to take into account that the coordinate system changes from $O_1(x_1, y_1)$ to $O_2(x_2, y_2)$ where the distance between them are D in the y direction.</p>	49

2.28	Obtaining the modal coefficient of the scattered wave for S_{12} partition. The scattered wave going downwards are based on the coordinate system $O_2(x_2, y_2)$. So we have to be careful since the coordinate system is changing from $O_1(x_1, y_1)$ to $O_2(x_2, y_2)$ which are separated by D in y direction. Note that the cylinders are positioned below the first quadrant of $O_1(x_1, y_1)$. So we have to shift the y positions of all the cylinders by $-D$	50
2.29	To extract the modal coefficients, we have to use the fact that S_{12} partition only considers the waves going down, and we also have to take into account that the coordinate system changes from $O_1(x_1, y_1)$ to $O_2(x_2, y_2)$ where the distance between them are D	51
2.30	Obtaining the modal coefficients of for S_{22} partition. Note that all the cylinders are positioned below the first quadrant.	52
2.31	To extract the modal amplitude, we have to use the fact that S_{22} partition only considers the waves going up.	52
2.32	Optimal parameter setting for Shanks transformation.	57
2.33	The geometrical relationships between the cylinders makes the T matrix have a quasi-symmetric structure.	58
2.34	When cascading, including enough amount of modes or buffer is important to increase the accuracy of the result. All the modes that have significant activity at the first scatterer they encounter in the neighboring system must be included.	59
3.1	Geometry of the scattering system considered.	62
3.2	Theoretical distribution in (3.7) for $L/l = 3$	65
3.3	The relationship between wavefronts in a medium that exhibits reciprocity	67
3.4	Empirical transmission coefficients distribution.	78
3.5	Wavefield plot.	79
3.6	The modal coefficients of the optimal wavefront.	80
3.7	The transmitted power versus the number of iterations.	81
3.8	Stepsize sensitivity of the algorithm.	82

3.9	Gain versus the number of control modes.	83
3.10	Intensity plot around the target.	84
3.11	Spectrum of the optimal focusing wavefront.	85
3.12	Intensity at target as a function of the number of bases vectors.	86
3.13	Gain plot in a lossy setting.	87
4.1	Schematic for the experimental setup considered. (Figure from Steve C. Rand)	89
4.2	Geometry of the scattering system considered.	89
4.3	Plot of the transmitted power by SVD and SDP.	102
4.4	The transmitted power versus the number of iterations.	104
4.5	Maximum transmitted power.	105
4.6	Heatmap of stepsize sensitivity of steepest descent method versus the number of iterations.	106
4.7	Heatmap of stepsize sensitivity of steepest descent method versus the thickness of the scattering medium.	107
4.8	Heatmap of stepsize sensitivity of gradient descent method versus the thickness of the scattering medium.	108
4.9	Number of iterations to get 95% of the respective maximum transmitted power.	109
5.1	Setup.	110
5.2	Histogram of the reflection matrix of a point layer.	118
5.3	Field plot of a point layer.	119
5.4	α , the largest singular value of the reflection matrix of a point layer, is plotted versus the index of refraction.	120
5.5	Distribution comparison for fixed index of refraction.	125

5.6	Distribution comparison for randomly distributed index of refraction. (Atomic case)	126
5.7	Distribution comparison for randomly distributed index of refraction. (Uniform case)	127
6.1	Distribution comparison for atomic distributed index of refraction. .	130
B.1	T Matrix transforms the cylinder wave coming from the source cylinder into a cylinder wave going into the object cylinder. This involves a coordinate transformation from the source cylinder's coordinate system O' to the object cylinder's coordinate system O	136
B.2	Geometric figure for Graf's additional theorem.	137
B.3	Detailed geometric figure for Graf's additional theorem combined to our situation.	138
C.1	Planewave with incident angle ϕ^{inc} is shined on a cylinder positioned at $(clocx, clocy)$. We have to convert planewave, whose coordinate system is O into cylinder waves, whose coordinate systems is the cylinder coordinate o'	140
D.1	$J_n(k_{out}\rho)e^{jn\phi}$ is incident on the scatterer, and scattered waves are produced inside and outside of the scatterer. We find the scattering coefficients, a_n s and b_n s, by matching the boundary conditions. . . .	144
D.2	For arbitrary-shaped homogeneous scatterer we have to choose finite n points at the boundary, and obtain n equations with finite amount of unknown scattering coefficients.	149
E.1	Cascading two scattering matrices	150

LIST OF TABLES

Table

2.1	Matrix-vector representation of time-reversal operation. $F = \text{flipud}(I)$ where I is an identity matrix and flipud is an operator that flips a vector or a matrix upside-down.	17
2.2	The scattering coefficients for cylinder-shaped scatterers.	36
3.1	Steepest descent algorithm for transmission maximization.	71
3.2	Conjugate gradient algorithm for transmission maximization.	75
3.3	The Lanczos algorithm and its physical counterpart.	77
4.1	Steepest descent algorithm for refining a highly transmitting phase-only modulated wavefront	99
4.2	Gradient descent algorithm for transmission maximization.	101

LIST OF ALGORITHMS

Algorithm

1	Scattering Matrix generating algorithm (Simple Version)	12
2	Scattering Matrix generating algorithm	33
3	Steepest descent algorithm for finding the optimal wavefront	68
4	Distribution computation algorithm from S-transform	117
5	Transmission Coefficient Distribution Computation Algorithm	124

LIST OF APPENDICES

Appendix

A.	Orthogonality of the periodic modes	133
B.	Additional Theorem	136
C.	Planewave and Cylinder wave conversion formula	140
D.	Boundary Value Problem	144
E.	Cascading Formula	150
F.	Scattering Matrix and Transfer Matrix conversion formula	152
G.	Derivation of Eq. (4.45)	155

ABSTRACT

New Methods and Theory for Increasing Transmission of Light through
Highly-Scattering Random Media

by
Curtis Jin

Chair: Rajesh Rao Nadakuditi

Scattering hinders the passage of light through random media and consequently limits the usefulness of optical techniques for sensing and imaging. Thus, methods for increasing the transmission of light through such random media are of interest. Against this backdrop, recent theoretical and experimental advances have suggested the existence of a few highly transmitting eigen-wavefronts with transmission coefficients close to one in strongly backscattering random media.

Here, we numerically analyze this phenomenon in 2-D with fully spectrally accurate simulators and provide the first rigorous numerical evidence confirming the existence of these highly transmitting eigen-wavefronts in random media with periodic boundary conditions that is composed of hundreds of thousands of non-absorbing scatterers.

We then develop physically realizable algorithms for increasing the transmission and the focusing intensity through such random media using backscatter analysis. Also, we develop physically realizable iterative algorithms using phase-only modulated wavefronts and non-iterative algorithms for increasing the transmission through such random media using backscatter analysis. We theoretically show that, despite the phase-only modulation constraint, the non-iterative algorithms will achieve at least about $25\pi\% \approx 78.5\%$. We show via numerical simulations that the algorithms converge rapidly, yielding a near-optimum wavefront in just a few iterations.

Finally, we theoretically analyze this phenomenon of perfect transmission and provide the first mathematically, justified random matrix model for such scattering media that can accurately predict the transmission coefficient distribution so that the existence [1] of an eigen-wavefront with transmission coefficient approaching one for random media can be rigorously analyzed.

CHAPTER I

Introduction

Media such as glass and air are transparent because light propagates through them without being scattered or absorbed. In contrast, materials such as turbid water, white paint, and egg shells are opaque because the randomly arranged particles cause light to scatter in random directions, thereby hindering its passage. As the thickness of a slab of highly scattering random medium increases, this effect becomes more pronounced, and less and less of a normally incident light is transmitted through [2].

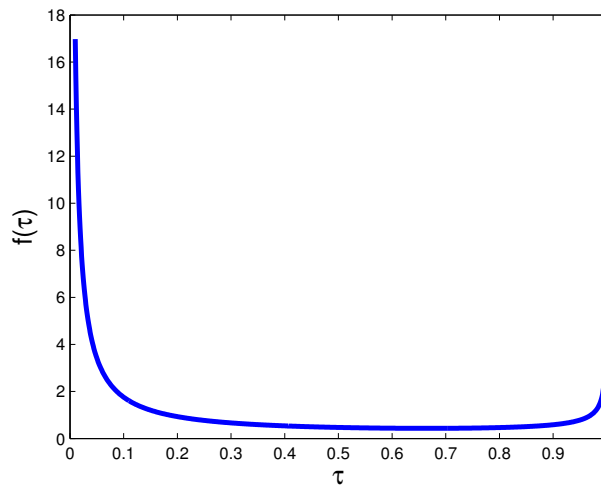


Figure 1.1: Theoretical transmission coefficient distribution in (3.7) for $L/l = 3$.

In this context, the theoretical work of Dorokhov [3], Pendry [4, 5], and others [6, 7] provides unexpected insight into how, and the extent to which, the limitations imposed by random scattering may be overcome. Specifically, these authors predict that in highly scattering random media composed of non-absorbing scatterers at random locations, the eigen-wavefronts associated with the right singular vectors of the S_{21} or transmission matrix will have transmission coefficients whose distribution has a bimodal shape as in Fig. 1.1. Consequently, while many eigen-wavefronts have a small transmission coefficient, a small number of eigen-wavefronts exist that have a

transmission coefficient close to one, i.e., they propagate with almost no scattering loss.

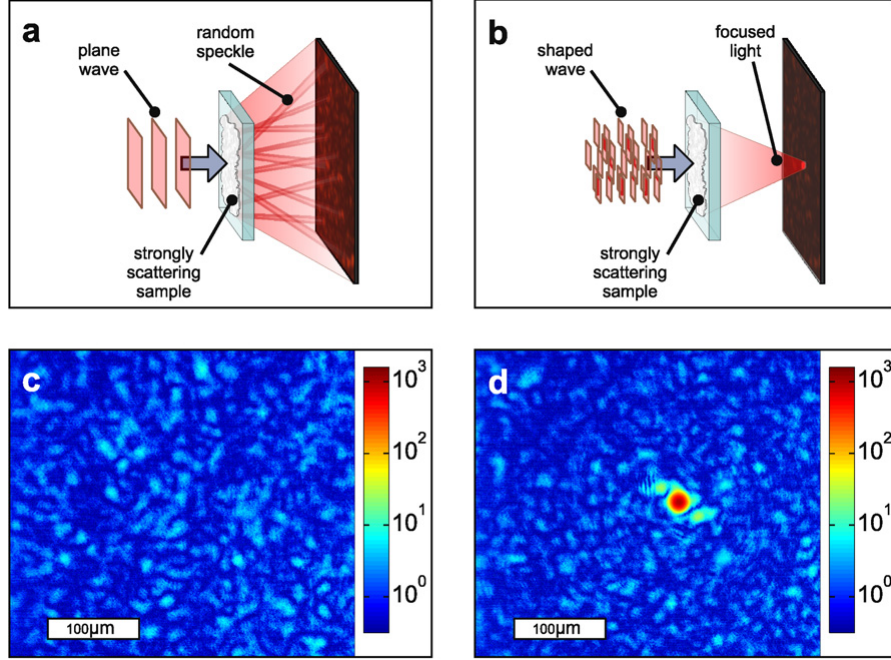


Figure 1.2: (a) Shining an unshaped wave through a $10 \mu\text{m}$ thick layer of TiO_2 pigment. (b) Shining a shaped wave through a $10 \mu\text{m}$ thick layer of TiO_2 pigment. (c) Intensity plot on the transmission side when wave is unshaped corresponding to **a**. (d) Intensity plot on the transmission side when wave is shaped corresponding to **b**. (Figure taken from the paper by I. M. Vellekoop and Allard P. Mosk [8])

The breakthrough experiments of Vellekoop and Mosk [8, 1] provide evidence of the existence of these highly transmitting eigen-wavefronts in random media. Vellekoop and Mosk showed [8] that intensity measurements on the transmission side of a scattering medium could be used to construct a wavefront that produced about $1000\times$ intensity enhancement at a target point over that due to a normally incident wavefront (Fig. 1.2). Their work set off a flurry of research on methods for measuring the transmission matrix and comparing the transmission coefficient distribution with the theoretical prediction [9, 10, 11, 12], faster experimental methods for focusing [13, 14, 15, 16, 17], and numerical work on the properties of the eigen-wavefronts [18].

Our research is inspired by these three lines of inquiry, and my thesis work can be summarized as follows,

1. Numerical verification of the perfectly transmitting eigen-wavefronts,
2. Development of physically realizable algorithms to utilize these eigen-wavefronts,

3. Theoretical derivation of the transmission coefficient distribution.

I will briefly describe about these as follows.

1.1 Numerical Verification

First, we numerically analyze the phenomenon using a spectrally accurate simulator for 2D scattering systems with periodic boundary conditions and provide the first numerically rigorous confirmation of the shape of the transmission coefficient distribution and the existence [1] of an eigen-wavefront with transmission coefficient approaching one for random media with a large number of scatterers (Fig. 1.3).

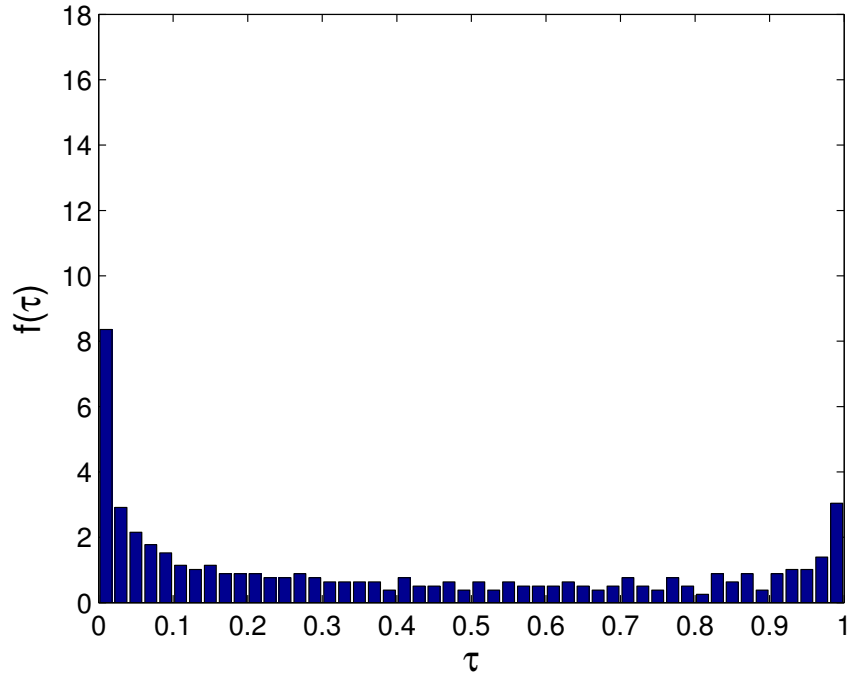


Figure 1.3: Empirical transmission coefficients distribution from our numerical simulator.

Also, we were the first to provide a physical insight on how the perfectly transmitting input should look like. Not surprisingly, the perfectly transmitting input is formed in a way that it avoids where the scatterers are located effectively, and Fig. 1.4 shows the response of the scattering system to one of the perfectly transmitting inputs yielding nearly 100% transmission.

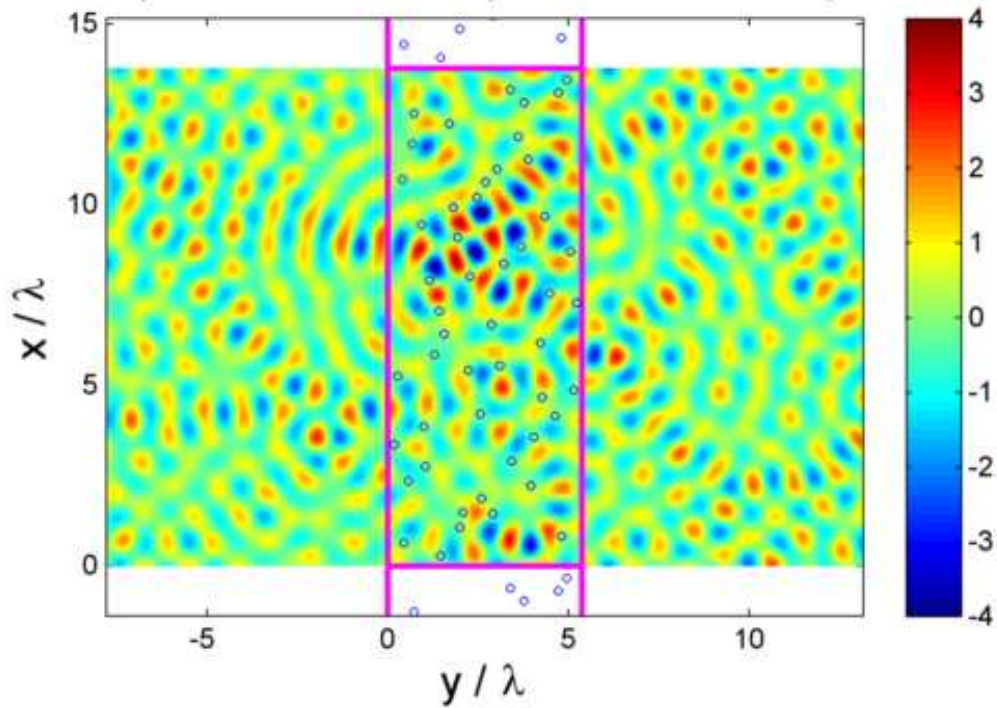


Figure 1.4: Wavefield plot of the incident-plus-backscatter wave corresponding to one of the perfectly transmitting inputs. The pink box is the scattering system considered, and the blue circles are the cylindrical scatterers. The perfectly transmitting input is shined from the left to the right, and the color represents the height of the wave corresponding to the colorbar.

1.2 Algorithms Development

Second, we develop iterative, physically realizable algorithms for transmission maximization that utilize backscatter analysis to produce a highly transmitting wavefront in just a few iterations. These algorithms build on the initial work presented in [19].

These algorithms which utilize the information in the backscatter field can be useful in applications, such as in bio-imaging, where it might not be possible to measure the transmitted fields. Our algorithms yield a highly-transmitting wavefront using significantly fewer measurements than required to measure the whole reflection or S_{11} matrix and then generate the wavefront (associated with the smallest right singular vector of the S_{11} matrix) that produces the smallest backscatter (and hence the highest transmission in a lossless medium).

Since our methods maximize transmission by minimizing backscatter, it is important for most of the backscatter field to be captured to fully realize these advantages. Otherwise, given a limited viewing aperture, the principle of backscatter minimization cannot guarantee increased forward transmission and might even produce ‘transmission’ into the unobserved portion of the backscatter field.

Furthermore, we develop an iterative, physically realizable algorithm for focusing that utilizes intensity measurements at the desired point and backscatter analysis to produce a near-optimal focusing wavefront with significantly fewer measurements than other approaches. In effect, we are increasing the rate of convergence to the optimal focusing wavefront. Changing the focusing point or the number of foci do not affect the convergence behavior. We show that we retain this property even when we control fewer than the total number of propagating modes.

A crucial feature of the algorithms we have developed is that it allows the number of modes being controlled via a spatial light modular (SLM) in experiments to be increased without increasing the number of measurements that have to be made.

An additional advantage conferred by these rapidly converging algorithms is that they might facilitate their use in applications where the duration in which the S_{21} or S_{11} matrix can be assumed to be quasi-static is relatively small compared to the time it would take to make all measurements needed to estimate the S_{21} or S_{11} matrix or in settings where a near-optimal solution obtained fast is preferable to the optimal solution that takes many more measurements to compute.

The task of amplitude and phase modulating an optical wavefront is not, however, trivial. Calibration and alignment issues prevent its use of two independent spatial light modulators in series that separately modulate the signal amplitude and phase. A viable option is to use the innovative method developed by van Putten et al. in [20] for full spatial phase and amplitude control using a twisted nematic LCD combined with a spatial filter.

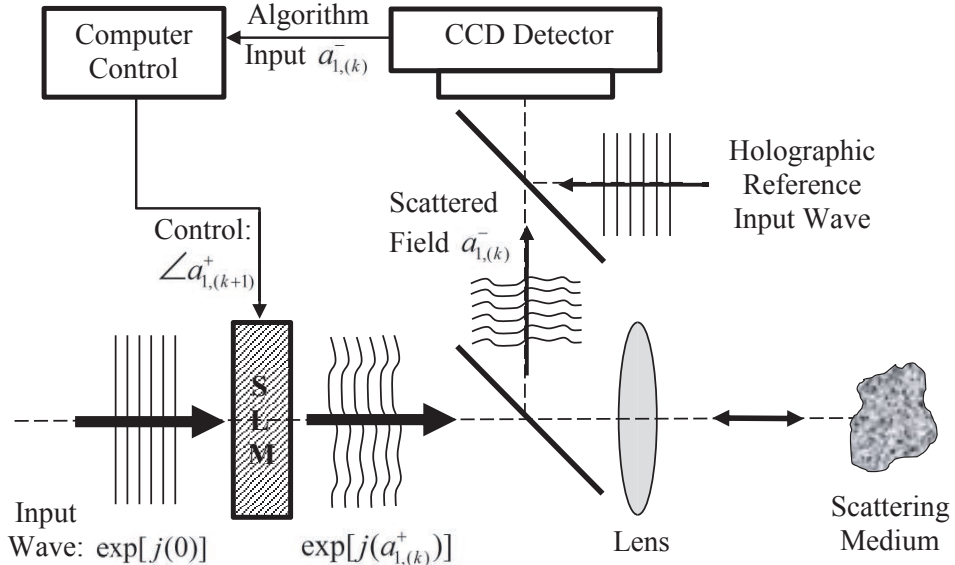


Figure 1.5: Schematic for the experimental setup. (Figure from Steve C. Rand)

We place ourselves in the setting where we seek to increase transmission via backscatter analysis but are restricted to phase-only modulation. The phase-only modulation constraint was initially motivated by the simplicity of the resulting experimental setup (see Fig. 1.5) and the commercial availability of finely calibrated phase-only spatial light modulators (SLMs) (e.g. the PLUTO series from Holoeye). As we shall shortly see there is another engineering advantage conferred by these methods. We do not, however, expect to achieve perfect transmission using phase-only modulation as is achievable by amplitude and phase modulation. However, we theoretically show that we can expect to get at least (about) $25\pi\% \approx 78.5\%$ provided that 1) the system modal reflection (or transmission) matrix is known, 2) its right singular vectors obey a maximum entropy principle by being isotropically random, and 3) full amplitude and phase modulation permits at least one perfectly transmitting wavefront. We also develop iterative, physically realizable algorithms for transmission maximization that utilize backscatter analysis to produce a highly transmitting phase-only modulated wavefront in just a few iterations. These rapidly converging algorithms build on the ideas developed in [19, 21] by incorporating the phase-only constraint. An additional advantage conferred by these rapidly converging algorithms is that they might facilitate their use in applications where the duration in which the modal transmission or reflection matrix can be assumed to be constant is relatively small compared to the time it would take to make all measurements needed to estimate the modal transition or reflection matrix or in settings where a near-optimal solution obtained fast is preferable to the optimal solution that takes many more measurements to compute. As in [21], the iterative algorithms we have developed retain the feature that they allow the number of modes being controlled via an SLM

in experiments to be increased without increasing the number of measurements that have to be made.

We numerically analyze the limits of phase-only modulated transmission in 2-D with fully spectrally accurate simulators and provide rigorous numerical evidence confirming our theoretical prediction in random media with periodic boundary conditions that is composed of hundreds of thousands of non-absorbing scatterers. Specifically, we show that the best performing iterative algorithm yields $\approx 70\%$ transmission using just 15 – 20 measurements in the regime where the non-iterative algorithms yield $\approx 78.5\%$ transmission.

This theoretical prediction brings into sharp focus an engineering advantage to phase-only modulation relative to amplitude and phase modulation that we did not anticipate when we started on this line of inquiry. The clever idea in van Putten et al’s work was to use spatial filtering to combine four neighboring pixels into one superpixel and then independently modulate the phase and the amplitude of light at each superpixel. This implies that an SLM with M pixels can control at most $M/4$ spatial modes. For the given aperture, we can expect the undersampling of the S_{21} to reduce transmission. Undersampling the spatial modes by 75% will reduce the amount of transmission by between 65 – 75%. In contrast, controlling all M spatial modes using phase-only modulation will reduce transmission by only 30%. Thus, we can achieve higher transmission with phase-only modulation using all pixels in an SLM than by (integer-valued) undersampling of the pixels to implement amplitude and phase modulation!

1.3 Derivation of the Transmission Coefficient Distribution

Finally, we theoretically analyze the perfect transmission phenomenon and provide the first mathematically, justified random matrix model for such scattering media that can accurately predict the transmission coefficient distribution so that the existence [1] of an eigen-wavefront with transmission coefficient approaching one for random media can be rigorously analyzed. The biggest contribution of our work is that we provide the transmission coefficient distribution in a closed form, which is parameterized by practical parameters such as the number of scatterers, the number of control modes or the index of refraction distribution of the scatterers, and we can compare our theoretical results to the results from our accurate scattering simulator, thus proving the sanity of our results perfectly.

The thesis is organized as follows. We describe the numerical scattering solver we developed in Chapter II. We develop the physically realizable transmission maximization and focusing algorithms in Chapter III. To assist the development of the physically realizable algorithms in the current technology such as spatial light modulator, we developed phase-only modulating algorithms in Chapter IV. We highlight the derivation on the transmission coefficient distribution in Chapter V, and summarize our findings in Chapter VI.

CHAPTER II

Scattering Matrix

In this chapter, we are going to discuss about our main approach towards dealing with scattering problem: matrix methods. Two types of matrix have been used to describe the behavior of a scattering system, *Scattering Matrix* and *Transfer Matrix*. Both matrices describe the same phenomenon of scattering but use different notations and this made differences between them. The advantage of using transfer matrix is that the cascading formula for it is extremely simple. Because of this strong feature, transfer matrix has been used by Dorokhov, Mellow and Beenakker [3, 22, 5, 23, 24] who wanted to investigate the behavior of large scattering system by cascading. However, the transfer matrix lacks of numerical stability when used in numerical simulations. On the other hand, although the cascading formula for scattering matrix is more complicated, it is much more numerically stable [25]. Since our main focus is to investigate the scattering phenomenon in an accurate manner, our main focus will be on the scattering matrix.

Matrix methods bring scattering problem into the linear algebra realm, and this enables us to model the whole scattering system as a black box, thus making the problem easier to analyze. Notation becomes easy and we can also extract physical quantities such as transmitted power, reflected power or transmission coefficients easily. In order to use matrix methods, we need to establish a countable basis. This leads us to the concept of *mode* which forms the basis of waves in the scattering system and we will discuss about the mode in section 2.1. With the modes, we define the scattering matrix and transfer matrix in section 2.2. Then, the next natural question to ask is how many modes are enough to include in the matrix. It is always better to include as many modes as possible when formulating a matrix. But in the real world it is impossible to include all the modes and it is meaningless since some modes do not affect the final results at a certain accuracy level. We will discuss about how many modes to include in the matrix in the context of accuracy in section 2.3.

Since the scattering matrix describes a physical phenomenon, *scattering*, it follows the conventional laws of physics such as Power Conservation, Time-reversal Symmetry and Reciprocity. We will show how these laws appear in the scattering matrix perspective in section 2.4. We can use these laws to check whether the matrix we generated is correct or not.

In section 2.6, we will describe how to generate a scattering matrix numerically.

We will define the modes to be periodic plane waves in order to establish a countable basis. Then, we describe how to solve Maxwell's equations for periodic scattering system.

2.1 Modes

The first step to formulate a matrix is to find a countable basis to describe the wave in the scattering system. In electromagnetic scattering, we can have finite or countably infinite wave solutions to Maxwell's equations by confining the geometrical structure (*waveguide*) or making a periodic structure. We call such solutions *modes*.

For example, a well-known solution to the Maxwell's equations in a freespace is a n -th mode planewave,

$$\varphi_n^\pm(\underline{\rho}, t) = e^{j(\omega t - \underline{k}_n^\pm \cdot \underline{\rho})}, \quad (2.1)$$

where $\underline{\rho}$ is the position vector, t is time, ω is angular frequency, \underline{k}_n^\pm is the n -th wavevector and \pm in the superscript denotes the propagating direction of the wave, $+$ for the forward direction and $-$ for the backward direction. In general, an arbitrary wave $\varphi(\underline{\rho}, t)$ can be decomposed in terms of its forward direction and backward direction waves such as $\varphi(\underline{\rho}, t) = \varphi^+(\underline{\rho}, t) + \varphi^-(\underline{\rho}, t)$ where

$$\varphi^\pm(\underline{\rho}, t) = \sum_{n=-N}^N h_n a_n^\pm \varphi_n^\pm(\underline{\rho}, t) = \sum_{n=-N}^N h_n a_n^\pm e^{j(\omega t - \underline{k}_n^\pm \cdot \underline{\rho})}, \quad (2.2)$$

where $h_n a_n^\pm$, h_n and a_n^\pm are the n -th modal coefficient, the n -th normalizing coefficient and the n -th normalized modal coefficient of $\varphi^\pm(\underline{\rho}, t)$, respectively. We will discuss about the normalizing issue at the end of this section.

If we are dealing with time-harmonics, i.e. monochromatic light, we can drop the $e^{j\omega t}$ term and Eq. (2.2) reduces to

$$\varphi^\pm(\underline{\rho}) = \sum_{n=-N}^N h_n a_n^\pm e^{-j\underline{k}_n^\pm \cdot \underline{\rho}}. \quad (2.3)$$

We call Eq. (2.3) as the *modal expansion* of wave $\varphi^\pm(\underline{\rho})$.

There are two types of modes, evanescent modes and propagating modes. Evanescent mode is the mode whose wavevector \underline{k}_n contains an imaginary part, so that it will decay and diminish. On the other hand, if the wavevector of the mode does not have an imaginary part, it will not diminish and propagate, and is called *propagating mode*. (See Fig. 2.1)

Note that since evanescent mode dies in the forward direction, it does not carry power. So when we consider power conservation or flux conservation, evanescent modes should be excluded. However, this does not mean that evanescent modes are meaningless. These modes are the modes that describe the near-field effect at the

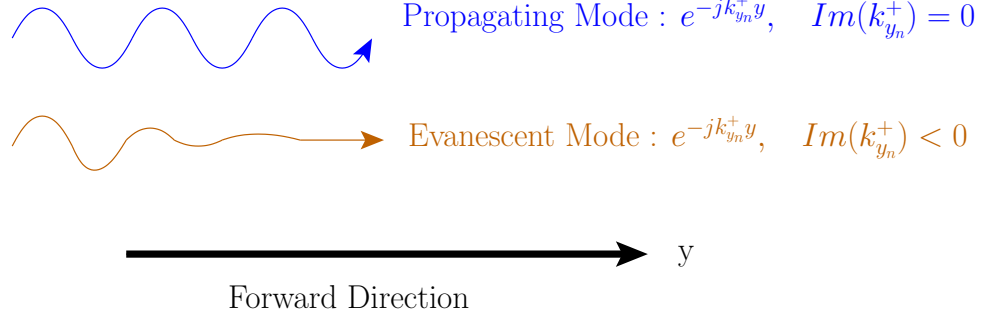


Figure 2.1: Propagating Mode and Evanescent Mode

boundary of the scatterers or at the boundary of the system.

Now let us bring this concept into the linear algebra domain. By Eq. (2.3), we will express a wave $\varphi^\pm(\rho)$ as a $(2N+1)$ by 1 modal coefficient vector by stacking a_n^\pm s from $-N$ to N and denote it as \underline{a}_n^\pm , i.e. $\underline{a}_n^\pm = [a_{-N}^\pm \ \dots \ a_0^\pm \ \dots \ a_N^\pm]^T$, where T denotes transposition. Moreover, a_n^\pm s are the normalized coefficients in the sense that,

$$\|\underline{a}_n^\pm\|_2^2 = (\underline{a}_n^\pm)^H \cdot \underline{a}_n^\pm = \begin{cases} \text{Power flowing in the forward direction for } + \\ \text{Power flowing in the backward direction for } - \end{cases},$$

where H denotes complex conjugate transpose. There is one important hidden assumption made in this equation: we assume that the modes are orthogonal to each other. The proof of the orthogonality of the modes and the normalizing coefficients h_n s are discussed in appendix VI.

In summary, we describe a wave as a linear combination of modes of the scattering system. To use this in a matrix vector equation, we stack the normalized modal coefficients in a column vector, and the norm squared of this column vector will represent the power flow.

2.2 Scattering Matrix & Transfer Matrix

We denote the four major waves related to a scattering system as φ_1^+ , φ_1^- , φ_2^+ and φ_2^- as in Fig. 2.2, where the $+$ and $-$ in the superscript denote forward and backward direction waves, while the 1 and 2 in the subscripts denote waves on the left and right of the scattering medium. We do a modal expansion on φ_1^+ and φ_1^- with respect to coordinate O_1 and denote as \underline{a}_1^+ and \underline{a}_1^- , respectively. Similarly, we do a modal expansion on φ_2^+ and φ_2^- with respect to coordinate O_2 and denote as \underline{a}_2^+ and \underline{a}_2^- , respectively.

Using these four modal coefficient vectors, scattering matrix and transfer matrix

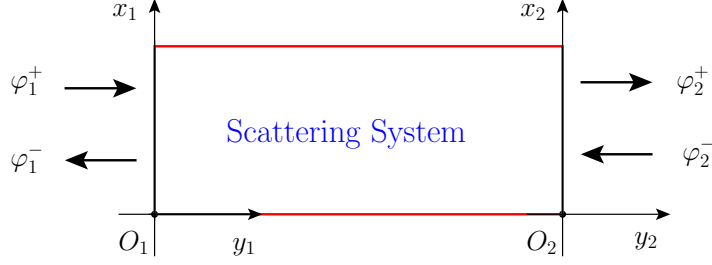


Figure 2.2: Four major waves related to the scattering system, φ_1^+ , φ_1^- , φ_2^+ and φ_2^- . φ_1^+ and φ_1^- 's reference coordinate is O_1 and φ_2^+ and φ_2^- 's reference coordinate is O_2 .

will be defined as below

$$\begin{bmatrix} \underline{a}_1^- \\ \underline{a}_2^+ \end{bmatrix} = S \cdot \begin{bmatrix} \underline{a}_1^+ \\ \underline{a}_2^- \end{bmatrix}, \quad \text{where } S \text{ is the scattering matrix} \quad (2.4)$$

$$\begin{bmatrix} \underline{a}_2^+ \\ \underline{a}_2^- \end{bmatrix} = T \cdot \begin{bmatrix} \underline{a}_1^+ \\ \underline{a}_1^- \end{bmatrix}, \quad \text{where } T \text{ is the transfer matrix.} \quad (2.5)$$

Transfer matrix relates the waves on the left side of the media to the right side of the media. Because of this feature, it can be considered as a matrix that relates the current on the left side to the current on the right side. As a result, cascade of the scattering systems will be simply a product of each transfer matrix in the order of propagating direction. This is why theories considering large scattering system uses transfer matrix approach.

Scattering matrix describes the physical causal relationship of the scattering system, the inputs to the scattering system \underline{a}_1^+ and \underline{a}_2^- produce the scattered waves \underline{a}_1^- and \underline{a}_2^+ . We use this *action and reaction* property of the scattering matrix to generate the scattering matrix. If we look at Eq. (2.4), to get the m^{th} column of the scattering matrix, we simply multiply the scattering matrix by a column vector whose entries are all zero except the m^{th} element. Physically, this corresponds to exciting the scattering system by the m^{th} mode with proper normalization, and doing a modal expansion on the scattered waves as in Eq. (2.3), and normalizing it. Then we stack the normalized coefficients in the m^{th} column of the scattering matrix. We repeat this procedure for all the modes. The algorithm description is written in Algorithm 1. Note that this is a brief description on the generation of the scattering matrix and detailed description will be done in section 2.6.

The scattering matrix has the following structure,

$$S = \begin{bmatrix} S_{11} & S_{12} \\ S_{21} & S_{22} \end{bmatrix}. \quad (2.6)$$

Algorithm 1 Scattering Matrix generating algorithm (Simple Version)

- 1: % Excite the system by φ_1^+
 - 2: **for** $m = -N$ to N **do**
 - 3: Excite the scattering system with the m^{th} mode of φ_1^+
 with the amplitude that makes the power going in y direction be 1
 - 4: Obtain the scattered wave going to the left side φ_1^-
 and the scattered wave going to the right side φ_2^+
 - 5: Do modal expansion on φ_1^- and φ_2^+ in modal expansion,
 i.e. $\varphi_1^-(\rho) = \sum_{n=-N}^N h_n b_n e^{-jk_n \cdot \rho}$ and $\varphi_2^+(\rho) = \sum_{n=-N}^N h_n d_n e^{-jk_n \cdot \rho}$
 - 6: Include the incident mode, i.e. $d_m \leftarrow d_m + 1$
 - 7: Stack b_n s and d_n s in one column vector as $\begin{bmatrix} \underline{b} \\ \underline{d} \end{bmatrix}$
 fill this into the $(m + N + 1)^{th}$ column of the scattering matrix
 - 8: **end for**
 - 9: % Excite the system by φ_2^-
 - 10: **for** $m = -N$ to N **do**
 - 11: Excite the scattering system with the m^{th} mode of φ_2^-
 with the amplitude that makes the power going in y direction be 1
 - 12: Obtain the scattered wave going to the left side φ_1^-
 and the scattered wave going to the right side φ_2^+
 - 13: Do modal expansion on φ_1^- and φ_2^+ in modal expansion,
 i.e. $\varphi_1^-(\rho) = \sum_{n=-N}^N h_n b_n e^{-jk_n \cdot \rho}$ and $\varphi_2^+(\rho) = \sum_{n=-N}^N h_n d_n e^{-jk_n \cdot \rho}$
 - 14: Include the incident mode, i.e. $b_m \leftarrow b_m + 1$
 - 15: Stack b_n s and d_n s in one column vector as $\begin{bmatrix} \underline{b} \\ \underline{d} \end{bmatrix}$
 fill this into the $(m + 3N + 2)^{th}$ column of the scattering matrix
 - 16: **end for**
-

Combining Eq. (2.4) and Eq. (2.6), we get two equation like below,

$$\underline{a}_1^- = S_{11} \cdot \underline{a}_1^+ + S_{12} \cdot \underline{a}_2^- \quad (2.7)$$

$$\underline{a}_1^+ = S_{21} \cdot \underline{a}_1^+ + S_{22} \cdot \underline{a}_2^- \quad (2.8)$$

Assuming that we only control the forward incident light, then no light is coming in the reverse direction, i.e. we can set $\underline{a}_2^- = 0$. Plugging this into Eq. (2.8), we get $\underline{a}_2^+ = S_{21} \cdot \underline{a}_1^+$. Since we defined the norm squared of the modal coefficient vector to be the propagating power,

$$\text{Transmitted Power} = \|\underline{a}_2^+\|_2^2 = (\underline{a}_1^+)^H \cdot S_{21}^H \cdot S_{21} \cdot \underline{a}_1^+ \quad (2.9)$$

Furthermore, we can extend this to extract transmission coefficient distribution from S_{21} . Let us denote the singular value decomposition(SVD) of S_{21} as $S_{21} = U \cdot \Sigma \cdot V^H$, where $U = [\underline{u}_1, \dots, \underline{u}_{2N+1}]$, $\Sigma = \text{Diag}(\{\sigma_n\}_{n=1}^{2N+1})$ and $V = [\underline{v}_1, \dots, \underline{v}_{2N+1}]$. Plugging this into Eq. (2.9), we can see that the singular value square represents the transmission coefficient, normalized transmitted power, when the corresponding right singular vector is sent into the system and the scattered wave will be the corresponding left singular vector. For this reason, we call the distribution of the singular value square as the transmission coefficient distribution, the right singular vectors as the eigen-channels, and S_{21} as the transmission matrix of the scattering system with respect to the forward incident wave.

The same argument will hold for S_{11} , S_{12} , and S_{22} . The results will be summarized as below.

	Reflection Matrix	Transmission Matrix
Foward Incident	S_{11}	S_{21}
Backward Incident	S_{22}	S_{12}

Figure 2.3: Partitions of scattering matrix and their meanings

2.3 Number of modes to use in the matrix

How many modes do we have to include in the scattering matrix? The answer is as many modes as possible. But in practice, including all the modes is impossible, because there might be infinite number of modes or the computation speed might be slow. So we must choose proper number of modes to use. Proper number of modes depends on how far the region of interest is from the scattering system. No matter

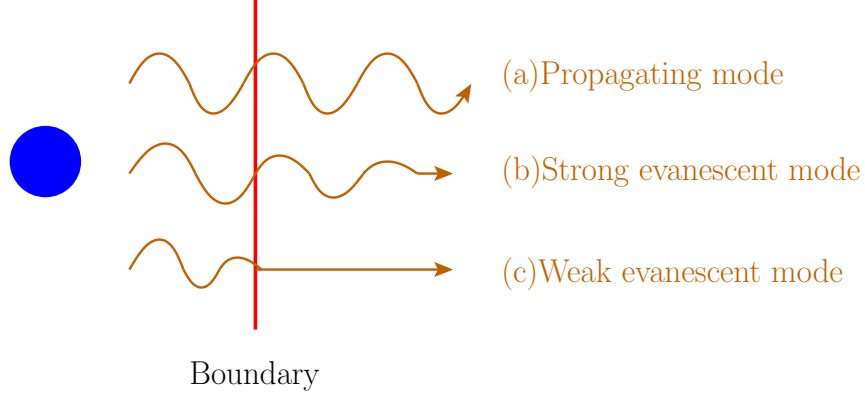


Figure 2.4: If the mode carries significant amount of power in the region of interest, we can not discard it. (a) Propagating mode; since the propagating mode never decays, we must always include it in the scattering matrix. (b) Strong evanescent mode; if the evanescent mode is still strong at the boundary, we must include it in the matrix. (c) Weak evanescent mode; if the evanescent mode is weak at the boundary, it will diminish in the region, thus can be neglected.

how far it is, we must always include the propagating modes since it exists all over the space. However, evanescent modes will only exist near to the scattering system. So if we are interested in the far field, including propagating modes will be sufficient since excluding the evanescent modes will not drop the accuracy.

On the other hand if we are interested in near field, it is better to include as many evanescent modes as possible. We can chop off the higher order modes depending on how much accurate results you want because higher order modes tend to decay faster than the lower ones. To determine whether the order is high or low, we consider the distance between the boundary of the scattering system and the closest scatterer to the boundary.

As you can see in Fig. 2.4, we should include all the evanescent modes that has considerably large amplitude at the boundary. Based on this we can write a criterion to determine the modes to include,

$$\{n \mid \max_{\underline{\rho}} \varphi_n(\underline{\rho}) > \text{Accuracy level}, \underline{\rho} \in (R^c \cup \partial R)\}, \quad (2.10)$$

where φ_n is the n^{th} mode wave
and R is the region of the scattering system

In summary, the proper number of modes depends on the highest order evanescent mode that can effect the result and highest order is determined by both the distance between the scattering system and the region you are interested in and the desirable accuracy level.

2.4 Properties of the scattering matrix

Because scattering matrix describes a physical phenomenon, it follows the laws of physics: power conservation, time-reversible symmetry and reciprocity. These laws will appear in a form of matrix vector equation. Later on, these equations will be the link that connects scattering to numerical linear algebra. Moreover, they provide us sanity checking routines for the scattering matrix we generate.

2.4.1 Power Conservation

In any kind of physical situation, power must conserve. This also holds for the scattering matrix unavoidably. We assume the scatterers are non-absorbing, thereby the power going into the system must be equal to the power going out from the system. One more thing we have to be careful about is that only the propagating modes should be included in the scattering matrix. This is because the propagating modes carry power throughout the scattering system and evanescent modes does not, they diminishes inside the scattering system.

Theorem 1. For lossless random media, scattering matrix with propagating modes must be unitary due to power conservation.

Proof. Let S be a scattering matrix that only includes all the propagating modes. For an arbitrary input \underline{a} with its output \underline{b} , we know

$$\underline{b} = S \cdot \underline{a}, \quad \text{where } \underline{a} = \begin{bmatrix} \underline{a}_1^+ \\ \underline{a}_2^- \end{bmatrix}, \underline{b} = \begin{bmatrix} \underline{b}_1^- \\ \underline{b}_2^+ \end{bmatrix}.$$

Power conservation gives us a condition like below,

$$\begin{aligned} \text{Incoming Power} &= \text{Outgoing Power} \\ (\underline{a}_1^+)^H \cdot \underline{a}_1^+ + (\underline{a}_2^-)^H \cdot \underline{a}_2^- &= (\underline{b}_1^-)^H \cdot \underline{b}_1^- + (\underline{b}_2^+)^H \cdot \underline{b}_2^+ \\ \underline{a}^H \cdot \underline{a} &= \underline{b}^H \cdot \underline{b} \\ &= (S \cdot \underline{a})^H \cdot (S \cdot \underline{a}) \\ 0 &= \underline{a}^H \cdot (S^H \cdot S - I) \cdot \underline{a}. \end{aligned}$$

Since this holds for any \underline{a} , we conclude

$$S^H \cdot S = I.$$

□

2.4.2 Time-reversal Symmetry

$$\nabla \cdot \mathbf{D} = \rho \quad (2.11)$$

$$\nabla \times \mathbf{E} = -\frac{d\mathbf{B}}{dt} \quad (2.12)$$

$$\nabla \cdot \mathbf{B} = 0 \quad (2.13)$$

$$\nabla \times \mathbf{H} = \mathbf{J} + \frac{d\mathbf{D}}{dt} \quad (2.14)$$

Maxwell's equations remain unchanged under replacements of t by $-t$ and \mathbf{H} by $-\mathbf{H}$ in the absence of source $\mathbf{J} = 0$. This tells us that given one solution to a electromagnetic problem, we can also have an alternative solution that can happen in a time-reversed way with negated magnetic field. This property is called *time-reversal symmetry*.

$$\nabla \cdot D = \rho \quad (2.15)$$

$$\nabla \times E = -j\omega\mu H \quad (2.16)$$

$$\nabla \cdot B = 0 \quad (2.17)$$

$$\nabla \times H = J + j\omega\epsilon E \quad (2.18)$$

Similarly to the previous case, time-harmonic Maxwell's equations tell us that we can always find an alternative solution by setting the alternative solution E' and H' as $E' = E^*$ and $H' = -H^*$ provided that the frequency ω is real and the medium is isotropic, i.e. $D = \epsilon E$ and $B = \mu H$, and lossless, i.e. $\epsilon(\omega)^* = \epsilon(\omega)$ and $\mu(\omega)^* = \mu(\omega)$.

To gain more insight, suppose the n^{th} mode solution is $\varphi(\underline{\rho}) = h_n a_n e^{-j\mathbf{k}_n \underline{\rho}}$, then the time-reversed solution will be $\varphi(\underline{\rho})' = h_n^* a_n^* e^{j\mathbf{k}_n \underline{\rho}}$.

Original Solution	Time-reversed Solution		(2.19)
$\varphi(\underline{\rho}) = h_n a_n e^{-j\mathbf{k}_n \underline{\rho}}$	\longrightarrow	$\varphi(\underline{\rho})' = h_n^* a_n^* e^{j\mathbf{k}_n \underline{\rho}}$	

Note that the wave direction has been reversed, \underline{k}_n became $-\underline{k}_n$, and this will reverse the input and output of the system. So the geometrical situation changes like the following diagram.

One tricky thing is the flip-upside-down operator involved in the Fig. 2.5. In order to explain this, we need to briefly explain about the wave vector notation used in section 2.6.1. In order to form a countable basis for the scattering matrix, we will make a periodic two dimensional structure on the xy -plane, which leads to periodic modes. The n^{th} periodic mode wave vector will be $\underline{k}_n = (k_{x_n}, k_{y_n}, 0)$ and the components will be

$$k_{x_n} = \frac{2\pi n}{L}, \quad \text{where } L \text{ is the period}$$

$$k_{y_n} = \pm \sqrt{\left(\frac{2\pi}{\lambda}\right)^2 - \left(\frac{2\pi n}{L}\right)^2}, \quad \text{where } \lambda \text{ is the wavelength}$$

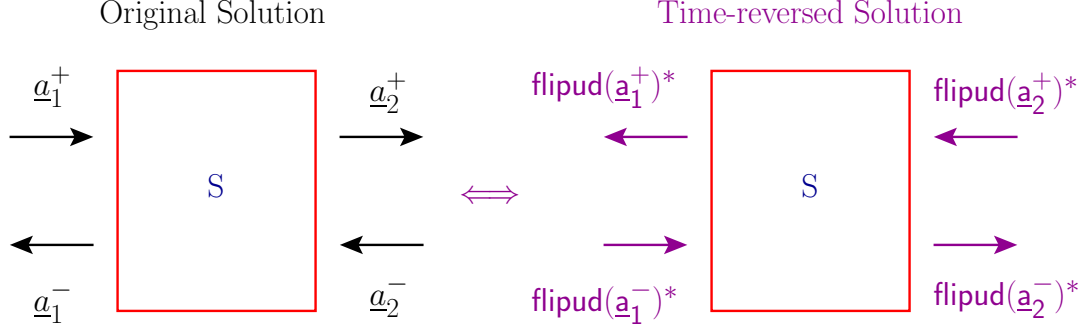


Figure 2.5: Original solution and the Time-reversed solution to the system.

The sign of k_{y_n} is plus if the wave is propagating in the forward direction and is negative if the wave is propagating in the reverse direction. Because of this notation,

$$\begin{aligned}
 -\underline{k}_n \text{ in forward direction} &= -\left(\frac{2\pi n}{L}, \sqrt{\left(\frac{2\pi}{\lambda}\right)^2 - \left(\frac{2\pi n}{L}\right)^2}, 0\right) \\
 &= \left(\frac{2\pi(-n)}{L}, -\sqrt{\left(\frac{2\pi}{\lambda}\right)^2 - \left(\frac{2\pi(-n)}{L}\right)^2}, 0\right) \\
 &= \underline{k}_{-n} \text{ in reverse direction}
 \end{aligned}$$

Thus, the coefficient of the n^{th} mode in the original solution will be related to the coefficient of the $(-n)^{\text{th}}$ mode in the time-reversed solution, making the modal coefficient vector flipped. Based on this result, we explicitly state that the time-reversed representation of the wave will be like below, where $F = \text{flipud}(I)$.

Vector Operation	Physical Operation
$\underline{a}_1^+ = F \cdot (\underline{a}_1^-)^*$	$\underline{a}_1^- \xrightarrow{\text{Time-reversal}} \underline{a}_1^+$

Table 2.1: Matrix-vector representation of time-reversal operation. $F = \text{flipud}(I)$ where I is an identity matrix and flipud is an operator that flips a vector or a matrix upside-down.

Theorem 2. For time-reversible random media, scattering matrix must satisfy the following equation,

$$\tilde{S}^* \cdot \tilde{S} = I, \text{ where } \tilde{S} = \begin{bmatrix} F & \underline{0} \\ \underline{0} & F \end{bmatrix} \cdot S, F = \text{flipud}(I)^1 \quad (2.20)$$

¹flipud is a matlab command that flips a vector or a matrix upside down

Proof. Let $\underline{a}_1^+, \underline{a}_2^-, \underline{a}_1^-$ and \underline{a}_2^+ be $(2N + 1) \times 1$ vectors that satisfies the scattering matrix,

$$\begin{bmatrix} \underline{a}_1^- \\ \underline{a}_2^+ \end{bmatrix} = S \cdot \begin{bmatrix} \underline{a}_1^+ \\ \underline{a}_2^- \end{bmatrix}$$

Using time-reversal symmetry, the time-reversed solution will satisfy the following equation

$$\begin{bmatrix} \text{flipud}(\underline{a}_1^+) \\ \text{flipud}(\underline{a}_2^-) \end{bmatrix}^* = S \cdot \begin{bmatrix} \text{flipud}(\underline{a}_1^-) \\ \text{flipud}(\underline{a}_2^+) \end{bmatrix}^*. \quad (2.21)$$

Denoting $\underline{a} = \begin{bmatrix} \underline{a}_1^+ \\ \underline{a}_2^- \end{bmatrix}$ and $\underline{b} = \begin{bmatrix} \underline{a}_1^- \\ \underline{a}_2^+ \end{bmatrix}$ and $\bar{F} = \begin{bmatrix} F & \underline{0} \\ \underline{0} & F \end{bmatrix}$, Eq. (2.21) can be written as

$$\begin{aligned} \bar{F} \cdot \underline{a}^* &= S \cdot \bar{F} \cdot \underline{b}^* \\ \bar{F} \cdot \underline{a} &= S^* \cdot \bar{F} \cdot \underline{b} \\ &= S^* \cdot \bar{F} \cdot S \cdot \underline{a} \\ \underline{a} &= \bar{F} \cdot S^* \cdot \bar{F} \cdot S \cdot \underline{a} \\ \therefore \bar{F} \cdot S^* \cdot \bar{F} \cdot S &= I \end{aligned} \quad (2.22)$$

Let

$$\tilde{S} = \bar{F} \cdot S$$

then Eq. (2.22) will be

$$\tilde{S}^* \cdot \tilde{S} = I.$$

□

Note that if a scattering systems is time-reversible, then the system is lossless. Assuming that the scattering matrix only includes the propagating modes, we can combine Theorem 1 and Theorem 2.

$$\begin{aligned} \tilde{S}^* &= \tilde{S}^{-1} = S^{-1} \cdot \bar{F} \\ &= S^H \cdot \bar{F}, \quad (\because \text{Theorem 1}) \\ &= (S^T)^* \cdot \bar{F} \\ \tilde{S} &= S^T \cdot \bar{F} \\ \therefore \tilde{S} &= (\tilde{S}^*)^T \end{aligned} \quad (2.23)$$

Plugging the submatrices S_{11}, S_{21}, S_{12} , and S_{22} into Eq. (2.23), we get

$$S_{11}^H = F \cdot S_{11}^* \cdot F \quad (2.24)$$

$$S_{22}^H = F \cdot S_{22}^* \cdot F \quad (2.25)$$

$$S_{12}^H = F \cdot S_{21}^* \cdot F. \quad (2.26)$$

These three equations describe the *reciprocity* of the scattering system in a matrix level. Using reciprocity directly, this result can be extended with evanescent modes .

2.4.3 Reciprocity

Suppose we have two sources (c) and (d) in an isotropic medium and the corresponding solutions are $\vec{E}^{(c)} \& \vec{H}^{(c)}$ and $\vec{E}^{(d)} \& \vec{H}^{(d)}$ respectively. From Maxwell's equations, we know that

$$\nabla \times \vec{E}^{(c)} = -j\omega\mu\vec{H}^{(c)} \quad (2.27)$$

$$\nabla \times \vec{H}^{(c)} = j\omega\epsilon\vec{E}^{(c)} \quad (2.28)$$

Dot multiplying $\vec{H}^{(d)}$ to Eq. (2.27) and $\vec{E}^{(d)}$ to Eq. (2.28) and adding them, we get

$$(\nabla \times \vec{E}^{(c)}) \cdot \vec{H}^{(d)} + (\nabla \times \vec{H}^{(c)}) \cdot \vec{E}^{(d)} = -j\omega(\mu\vec{H}^{(c)} \cdot \vec{H}^{(d)} - \epsilon\vec{E}^{(c)} \cdot \vec{E}^{(d)}) \quad (2.29)$$

We can get a similar result by interchanging (c) and (d) and get

$$(\nabla \times \vec{E}^{(d)}) \cdot \vec{H}^{(c)} + (\nabla \times \vec{H}^{(d)}) \cdot \vec{E}^{(c)} = -j\omega(\mu\vec{H}^{(d)} \cdot \vec{H}^{(c)} - \epsilon\vec{E}^{(d)} \cdot \vec{E}^{(c)}) \quad (2.30)$$

Subtracting Eq. (2.30) from Eq. (2.29),

$$\begin{aligned} (\nabla \times \vec{E}^{(c)}) \cdot \vec{H}^{(d)} - (\nabla \times \vec{H}^{(d)}) \cdot \vec{E}^{(c)} &= (\nabla \times \vec{E}^{(d)}) \cdot \vec{H}^{(c)} - (\nabla \times \vec{H}^{(c)}) \cdot \vec{E}^{(d)} \\ \nabla \cdot (\vec{E}^{(c)} \times \vec{H}^{(d)}) &= \nabla \cdot (\vec{E}^{(d)} \times \vec{H}^{(c)}) \end{aligned}$$

Integrating the last equation over a volume enclosed by a surface S , we get

$$\oint_S (\vec{E}^{(c)} \times \vec{H}^{(d)}) \cdot d\vec{S} = \oint_S (\vec{E}^{(d)} \times \vec{H}^{(c)}) \cdot d\vec{S} \quad (2.31)$$

This is the field-theoretical form of the reciprocity theorem. Note that reciprocity can hold even when the scattering system is lossy.

Theorem 3. For isotropic random media, scattering matrix must satisfy the following equation due to reciprocity,

$$(\tilde{S})^T = \tilde{S}, \text{ where } \tilde{S} = \begin{bmatrix} F & \underline{0} \\ \underline{0} & F \end{bmatrix} \cdot S, F = \text{flipud}(I)^1 \quad (2.32)$$

¹flipudis a matlab command that flips a vector or a matrix upside down

Proof. We will evaluate Eq. (2.31) by assuming we have TM waves whose electric field vectors are aligned in the z -direction, and we assume the structure of the medium has period L in the x -direction, and the surface S will be a rectangular box enclosing the scattering system. For detailed description about the assumptions, refer section 2.6.

1) S_{11} reciprocity.

Suppose we have two sources (c) and (d) on the left side of the medium, which emits waves represented by normalized modal coefficient vectors $\underline{c}_1^+ = [c_{1,-N}^+ \cdots c_{1,0}^+ \cdots c_{1,N}^+]^T$ and $\underline{d}_1^+ = [d_{1,-N}^+ \cdots d_{1,0}^+ \cdots d_{1,N}^+]^T$. Let us evaluate the integral on the LHS of Eq. (2.31). The fields on the left side are like below,

$$\begin{aligned} \bullet \vec{E}^{(c)} &= \sum_{n=-N}^N \{c_{1,n}^+ e^{-j(k_{x_n}x + k_{y_n}y)} \hat{z} + (S_{11} \cdot \underline{c}_1^+)_n e^{-j(k_{x_n}x - k_{y_n}y)} \hat{z}\} \\ \bullet \vec{H}^{(d)} &= \frac{1}{\eta} \sum_{n=-N}^N \{d_{1,n}^+ e^{-j(k_{x_n}x + k_{y_n}y)} \hat{h}_n + (S_{11} \cdot \underline{d}_1^+)_n e^{-j(k_{x_n}x - k_{y_n}y)} (-\hat{h}_{-n})\} \end{aligned}$$

where η is the impedance of the medium and $\hat{h}_n = \hat{k}_n \times \hat{z}$.

The fields on the right side are like below,

$$\begin{aligned} \bullet \vec{E}^{(c)} &= \sum_{n=-N}^N \{(S_{21} \cdot \underline{c}_1^+)_n e^{-j(k_{x_n}x + k_{y_n}y)} \hat{z}\} \\ \bullet \vec{H}^{(d)} &= \frac{1}{\eta} \sum_{n=-N}^N \{(S_{21} \cdot \underline{d}_1^+)_n e^{-j(k_{x_n}x + k_{y_n}y)} \hat{h}_n\} \end{aligned}$$

Plugging the fields into the LHS of (2.31),

$$\begin{aligned} \oint_S (\vec{E}^{(c)} \times \vec{H}^{(d)}) \cdot d\vec{S} &= \int_{S_{\text{left}}} (\vec{E}^{(c)} \times \vec{H}^{(d)}) \cdot d\vec{S} + \int_{S_{\text{right}}} (\vec{E}^{(c)} \times \vec{H}^{(d)}) \cdot d\vec{S} \\ &= \frac{L}{\eta} (\underline{c}_1^+)^T \cdot (-F - S_{11}^T \cdot F + F \cdot S_{11} + S_{11}^T \cdot F \cdot S_{11} + S_{21}^T \cdot F \cdot S_{21}) \cdot \underline{d}_1^+ \end{aligned} \quad (2.33)$$

Now let us evaluate the integral on the RHS of Eq. (2.31). The fields on the left side are like below,

$$\begin{aligned} \bullet \vec{E}^{(d)} &= \sum_{n=-N}^N \{d_{1,n}^+ e^{-j(k_{x_n}x + k_{y_n}y)} \hat{z} + (S_{11} \cdot \underline{d}_1^+)_n e^{-j(k_{x_n}x - k_{y_n}y)} \hat{z}\} \\ \bullet \vec{H}^{(c)} &= \frac{1}{\eta} \sum_{n=-N}^N \{c_{1,n}^+ e^{-j(k_{x_n}x + k_{y_n}y)} \hat{h}_n + (S_{11} \cdot \underline{c}_1^+)_n e^{-j(k_{x_n}x - k_{y_n}y)} (-\hat{h}_{-n})\} \end{aligned}$$

where η is the impedance of the medium and $\hat{h}_n = \hat{k}_n \times \hat{z}$.

The fields on the right side are like below,

$$\begin{aligned} \bullet \vec{E}^{(d)} &= \sum_{n=-N}^N \{(S_{21} \cdot \underline{d}_1^+) e^{-j(k_{x_n}x + k_{y_n}y)} \hat{z}\} \\ \bullet \vec{H}^{(c)} &= \frac{1}{\eta} \sum_{n=-N}^N \{(S_{21} \cdot \underline{c}_1^+) e^{-j(k_{x_n}x + k_{y_n}y)} \hat{h}_n\} \end{aligned}$$

Plugging the fields into the RHS of Eq. (2.31),

$$\begin{aligned} \oint_S (\vec{E}^{(d)} \times \vec{H}^{(c)}) \cdot d\vec{S} &= \int_{S_{\text{left}}} (\vec{E}^{(d)} \times \vec{H}^{(c)}) \cdot d\vec{S} + \int_{S_{\text{right}}} (\vec{E}^{(d)} \times \vec{H}^{(c)}) \cdot d\vec{S} \\ &= \frac{L}{\eta} (\underline{c}_1^+)^T \cdot (-F - F \cdot S_{11} + S_{11}^T \cdot F + S_{11}^T \cdot F \cdot S_{11} + S_{21}^T \cdot F \cdot S_{21}) \cdot \underline{d}_1^+ \end{aligned} \quad (2.34)$$

Plugging in Eq. (2.33) and Eq. (2.34) into (2.31),

$$S_{11}^T = F \cdot S_{11} \cdot F \quad (2.35)$$

2) S_{22} reciprocity.

Placing two sources (c) and (d) on the right side of the medium and using a similar argument as we did for S_{11} , we get

$$S_{22}^T = F \cdot S_{22} \cdot F \quad (2.36)$$

3) S_{21} reciprocity.

Suppose we place source (c) on the left side of the medium and (d) on the right side. And the waves produced from (c) and (d) are represented by normalized modal coefficient vectors $\underline{c}_1^+ = [c_{1,-N}^+ \cdots c_{1,0}^+ \cdots c_{1,N}^+]^T$ and $\underline{d}_2^- = [d_{1,-N}^- \cdots d_{1,0}^- \cdots d_{1,N}^-]^T$.

Let us evaluate the integral on the LHS of Eq. (2.31). The fields on the left side are like below,

$$\begin{aligned} \bullet \vec{E}^{(c)} &= \sum_{n=-N}^N \{c_{1,n}^+ e^{-j(k_{x_n}x + k_{y_n}y)} \hat{z} + (S_{11} \cdot \underline{c}_1^+) e^{-j(k_{x_n}x - k_{y_n}y)} \hat{z}\} \\ \bullet \vec{H}^{(d)} &= \frac{1}{\eta} \sum_{n=-N}^N \{(S_{12} \cdot \underline{d}_2^-) e^{-j(k_{x_n}x - k_{y_n}y)} (-\hat{h}_{-n})\} \end{aligned}$$

where η is the impedance of the medium and $\hat{h}_n = \hat{k}_n \times \hat{z}$.

The fields on the right side are like below,

$$\begin{aligned}\bullet \vec{E}^{(c)} &= \sum_{n=-N}^N \{(S_{21} \cdot \underline{c}_1^+) e^{-j(k_{x_n}x + k_{y_n}y)} \hat{z}\} \\ \bullet \vec{H}^{(d)} &= \frac{1}{\eta} \sum_{n=-N}^N \{d_{2,n}^- e^{-j(k_{x_n}x - k_{y_n}y)} (-\hat{h}_{-n}) + (S_{22} \cdot \underline{d}_2^-) e^{-j(k_{x_n}x + k_{y_n}y)} \hat{h}_n\}\end{aligned}$$

Plugging the fields into the LHS of Eq. (2.31),

$$\begin{aligned}\oint_S (\vec{E}^{(c)} \times \vec{H}^{(d)}) \cdot d\vec{S} &= \int_{S_{\text{left}}} (\vec{E}^{(c)} \times \vec{H}^{(d)}) \cdot d\vec{S} + \int_{S_{\text{right}}} (\vec{E}^{(c)} \times \vec{H}^{(d)}) \cdot d\vec{S} \\ &= \frac{L}{\eta} (\underline{c}_1^+)^T \cdot (F \cdot S_{12} + S_{11}^T \cdot F \cdot S_{12} - S_{21}^T \cdot F + S_{21}^T \cdot F \cdot S_{22}) \cdot \underline{d}_2^- \end{aligned} \quad (2.37)$$

Now let us evaluate the integral on the RHS of Eq. (2.31). The fields on the left side are like below,

$$\begin{aligned}\bullet \vec{E}^{(d)} &= \sum_{n=-N}^N \{(S_{12} \cdot \underline{d}_2^-) e^{-j(k_{x_n}x - k_{y_n}y)} \hat{z}\} \\ \bullet \vec{H}^{(c)} &= \frac{1}{\eta} \sum_{n=-N}^N \{c_{1,n}^+ e^{-j(k_{x_n}x + k_{y_n}y)} \hat{h}_n + (S_{11} \cdot \underline{c}_1^+) e^{-j(k_{x_n}x - k_{y_n}y)} (-\hat{h}_{-n})\}\end{aligned}$$

where η is the impedance of the medium and $\hat{h}_n = \hat{k}_n \times \hat{z}$.

The fields on the right side are like below,

$$\begin{aligned}\bullet \vec{E}^{(d)} &= \sum_{n=-N}^N \{d_{2,n}^- e^{-j(k_{x_n}x - k_{y_n}y)} \hat{z} + (S_{22} \cdot \underline{d}_2^-) e^{-j(k_{x_n}x + k_{y_n}y)} \hat{z}\} \\ \bullet \vec{H}^{(c)} &= \frac{1}{\eta} \sum_{n=-N}^N \{(S_{21} \cdot \underline{c}_1^+) e^{-j(k_{x_n}x + k_{y_n}y)} \hat{h}_n\}\end{aligned}$$

Plugging the fields into the RHS of Eq. (2.31),

$$\begin{aligned}\oint_S (\vec{E}^{(d)} \times \vec{H}^{(c)}) \cdot d\vec{S} &= \int_{S_{\text{left}}} (\vec{E}^{(d)} \times \vec{H}^{(c)}) \cdot d\vec{S} + \int_{S_{\text{right}}} (\vec{E}^{(d)} \times \vec{H}^{(c)}) \cdot d\vec{S} \\ &= \frac{L}{\eta} (\underline{c}_1^+)^T \cdot (-F \cdot S_{12} + S_{11}^T \cdot F \cdot S_{12} + S_{21}^T \cdot F + S_{21}^T \cdot F \cdot S_{22}) \cdot \underline{d}_1^+ \end{aligned} \quad (2.38)$$

Plugging in Eq. (2.37) and Eq. (2.38) into (2.31),

$$S_{21}^T = F \cdot S_{12} \cdot F \quad (2.39)$$

Combining Eq. (2.35), Eq. (2.36) and Eq. (2.39), we can write

$$\begin{aligned} & \begin{bmatrix} S_{11}^T \cdot F & S_{21}^T \cdot F \\ S_{12}^T \cdot F & S_{22}^T \cdot F \end{bmatrix} = \begin{bmatrix} F \cdot S_{11} & F \cdot S_{12} \\ F \cdot S_{21} & F \cdot S_{22} \end{bmatrix} \\ \left(\begin{bmatrix} F & 0 \\ 0 & F \end{bmatrix} \cdot \begin{bmatrix} S_{11} & S_{12} \\ S_{21} & S_{22} \end{bmatrix} \right)^T &= \begin{bmatrix} F & 0 \\ 0 & F \end{bmatrix} \cdot \begin{bmatrix} S_{11} & S_{12} \\ S_{21} & S_{22} \end{bmatrix} \\ (\tilde{S})^T &= \tilde{S} \end{aligned}$$

□

Note that reciprocity holds even when the scattering system is lossy.

At first glance it is hard to see why theorem 3 implies reciprocity. The following argument will give us intuitions on how this theorem is related to reciprocity.

Consider an input modal coefficient vector

$$\underline{a}_{\text{SparkA}}^+ = F \cdot C \cdot \underline{f}_A^* \quad (2.40)$$

where C is a diagonal matrix containing the normalizing coefficients for each mode and \underline{f}_A is a $(2N+1) \times 1$ *measurement vector* whose element is $\{f_A\}_{n+N+1} = e^{jk_n \cdot \underline{r}_A} = e^{j(k_{x_n} x_A \pm k_{y_n} y_A)}$, and \underline{r}_A is a position vector. Then, this input vector will represent a spark at point \underline{r}_A , because the maximum value of this wave will be obtained at \underline{r}_A . (If the spark is from the left side, the sign in the expression will be minus, vice versa.)

Then, the wave measured at point \underline{r}_B due to the spark from \underline{r}_A is like below,

$$\begin{aligned} \text{Wave measured at } \underline{r}_B \text{ due to } \underline{a}_{\text{SparkA}}^+ &= \underline{f}_B^H \cdot C \cdot S_{21} \cdot \underline{a}_{\text{SparkA}}^+ \\ &= \underline{f}_B^H \cdot C \cdot S_{21} \cdot F \cdot C \cdot \underline{f}_A^* \\ &= \underline{f}_A^H \cdot C^T \cdot F^T \cdot S_{21}^T \cdot C^T \cdot \underline{f}_B^*, \quad (\because \text{Transposing both sides}) \\ &= \underline{f}_A^H \cdot C \cdot S_{12} \cdot F \cdot C \cdot \underline{f}_B^*, \quad (\because \text{Theorem 3}) \\ &= \underline{f}_A^H \cdot C \cdot S_{12} \cdot \underline{a}_{\text{SparkB}}^+ \\ &= \text{Wave measured at } \underline{r}_A \text{ due to } \underline{a}_{\text{SparkB}}^+ \end{aligned}$$

Thus, theorem 3 represents reciprocity of the media, i.e. if I can see you, you can see me, too. For reference see [26, 27].

2.5 Useful Formulas

In this section, we will discuss about some useful formulas for investigating large scattering systems.

2.5.1 Cascading Formula

One of our main research interests is to see how light propagates in large scattering system. We can either directly obtain the matrix for the huge system or chop the scattering system into pieces and cascade them. Obtaining the scattering matrix directly can generate scatterers at random position. But it will require huge memory in order to deal with all the interactions between scatterers. We can reduce this computational overhead by using cascading formula because it reduces the number of scatterers in each slice. The only disadvantage of using cascading formula is that it will produce a scattering system where there's no scatterers near the boundary of each layers. But this can be negligible because the system is large.

There are two ways to cascade two scattering systems. One is via scattering matrix and the other is via transfer matrix.

2.5.1.1 Cascading formula for Scattering Matrix

For cascading two scattering matrices,

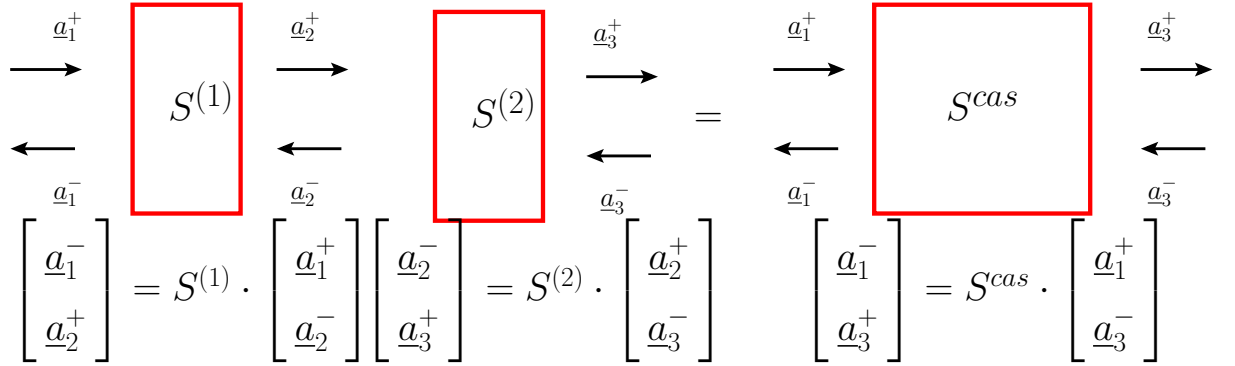


Figure 2.6: Cascading two scattering matrices.

$$\text{Let } S_1 = \begin{bmatrix} S_{11}^{(1)} & S_{12}^{(1)} \\ S_{21}^{(1)} & S_{22}^{(1)} \end{bmatrix} \text{ and } S_2 = \begin{bmatrix} S_{11}^{(2)} & S_{12}^{(2)} \\ S_{21}^{(2)} & S_{22}^{(2)} \end{bmatrix}$$

then S^{cas} will be like below,

$$S^{cas} = \begin{bmatrix} S_{11}^{(1)} + S_{12}^{(1)} \cdot (I - S_{11}^{(2)} \cdot S_{22}^{(1)})^{-1} \cdot S_{11}^{(2)} \cdot S_{21}^{(1)} & S_{12}^{(1)} \cdot (I - S_{11}^{(2)} \cdot S_{22}^{(1)})^{-1} \cdot S_{12}^{(2)} \\ S_{21}^{(2)} \cdot (I - S_{22}^{(1)} \cdot S_{11}^{(2)})^{-1} \cdot S_{21}^{(1)} & S_{22}^{(2)} + S_{21}^{(2)} \cdot (I - S_{22}^{(1)} \cdot S_{11}^{(2)})^{-1} \cdot S_{22}^{(1)} \cdot S_{12}^{(2)} \end{bmatrix}$$

Proof is in appendix VI.

2.5.1.2 Cascading formula for Transfer Matrix

Cascading formula for transfer matrix is extremely simple. It is merely a product of the transfer matrices in the order of cascades. A simple proof for the cascading

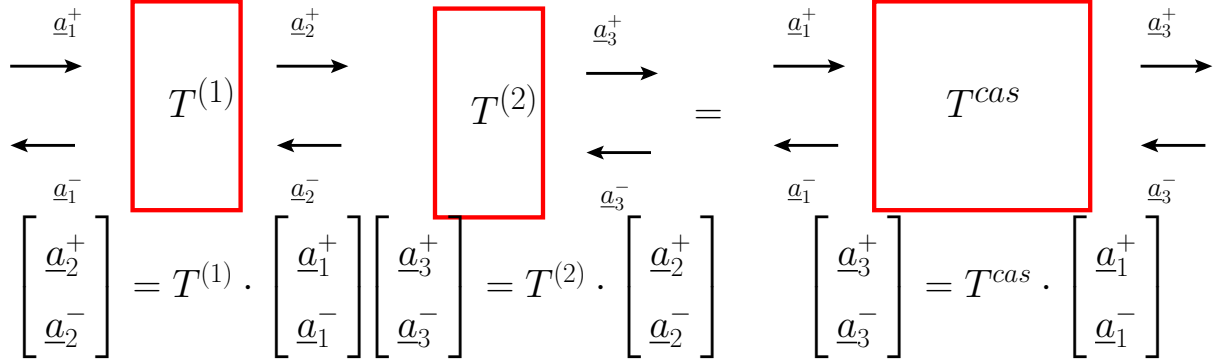


Figure 2.7: Cascading two transfer matrices

formula is like below,

$$\text{Let } \begin{bmatrix} a_2^+ \\ a_2^- \end{bmatrix} = T^{(1)} \cdot \begin{bmatrix} a_1^+ \\ a_1^- \end{bmatrix} \text{ and } \begin{bmatrix} a_3^+ \\ a_3^- \end{bmatrix} = T^{(2)} \cdot \begin{bmatrix} a_2^+ \\ a_2^- \end{bmatrix}$$

then,

$$\begin{aligned}
 \begin{bmatrix} a_3^+ \\ a_3^- \end{bmatrix} &= T^{(2)} \cdot \begin{bmatrix} a_2^+ \\ a_2^- \end{bmatrix} \\
 &= T^{(2)} \cdot T^{(1)} \cdot \begin{bmatrix} a_1^+ \\ a_1^- \end{bmatrix}
 \end{aligned}$$

$$\therefore T^{cas} = T^{(2)} \cdot T^{(1)} \quad (2.41)$$

In order to use the cascading formula for transfer matrix, all the scattering matrices will have to be converted to transfer matrices. The conversion formula is in appendix VI.

Although cascading formula for transfer matrix is simpler than that of scattering matrix, transfer matrix formula is not recommended because the conversion formula is not numerically stable. We will discuss about this in the next section.

2.5.1.3 Accuracy and Stability of the cascading formula

Let us define the *cascading error* like below,

$$\text{Cascading Error} = \|S^{cas} - S^{true}\|_F, \quad (2.42)$$

where S^{true} : the correct matrix generated without cascading
 S^{cas} : the cascaded matrix

One thing to be careful of is that even if the cascaded matrix S^{cas} satisfies the properties we have described in section 2.4, the cascading error can be huge. So, checking whether the cascaded matrix satisfies the properties will not be enough to check whether the cascaded result is correct or not.

The cascading error depends on the number of modes we use in the matrix. We need to include all effective modes in the scattering matrix in order to reduce the cascading error.

Since two systems are going to be merged next to each other, we have to take the

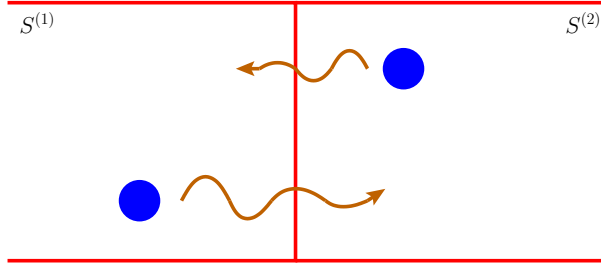


Figure 2.8: When scattering systems are cascaded, we have to make sure we are including all the modes that are still significant to the neighboring system.

near-field effect into account. If we are not including enough modes to describe the near-field of the scattering system, we will not get correct result. Again the logic to determine how many modes to include in the matrix is similar to the argument in section 2.3. We will have to include all the evanescent mode that has significant contribution at the boundary.

$$\{n | \max_{\underline{\rho}} \varphi_n(\underline{\rho}) > \text{Accuracy level}, \underline{\rho} \in R\}, \quad (2.43)$$

where φ_n is the n^{th} mode wave
and R is the boundary between two scattering systems

Now let us talk about the stability issue. Cascading by transfer matrices, we need to convert the scattering matrix into the transfer matrix by the conversion formula, which involves a matrix inversion of S_{12} partition. This part can cause cascading become unstable when we include evanescent modes in the matrix. The reason is because evanescent mode input does not give strong scattered output, thereby this will cause the scattering matrix to have nearly zero column corresponding to the evanescent mode. As a result the matrix will be nearly rank deficient numerically, so the inverse of the matrix becomes unstable. Since we need to include as many evanescent modes as possible to increase the accuracy of cascading, cascading by transfer matrices is not a good idea.

Cascading by scattering matrices is numerically stable even when we include

evanescent modes in the scattering matrix. It is because the matrix inversion in the cascading formula of scattering matrix in Eq. (2.41) is combined with identity matrix. This makes the cascading formula for scattering matrix stable. We recommend to use the scattering matrix approach when using cascading techniques.

2.5.2 Intermediate Waves

Suppose we have a N-cascaded scattering system like below, where we only have control on \underline{a}_1^+ and \underline{a}_{N+1}^-

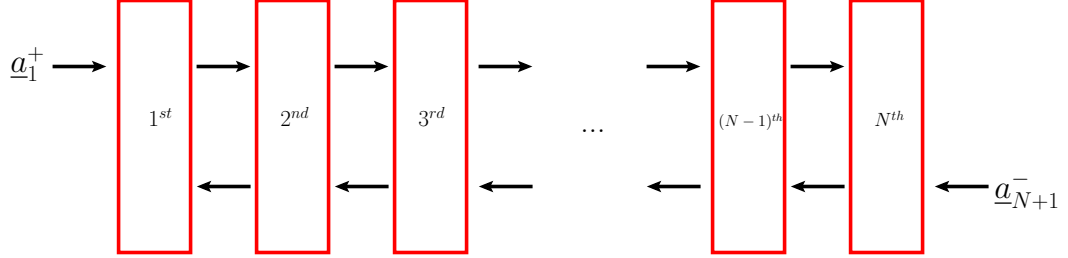


Figure 2.9: N-cascaded scattering systems. We are interested in the intermediate waves.

In this section, we are going to talk about how to extract the *intermediate waves*, which are the waves between the slices.

A simple idea to obtain these intermediate waves is like the following. First, find the \underline{a}_1^- by using the cascaded scattering matrix, and form a vector $\underline{a}_1^T = [(\underline{a}_1^+)^T \ (\underline{a}_1^-)^T]$. Convert each scattering matrix into transfer matrix and compute each intermediate wave step by step by multiplying it to the corresponding transfer matrix. This method will not work if we are including evanescent waves in the matrix because converting scattering matrix to transfer matrix is unstable. So this method is only valid when we are only dealing with propagating modes.

To obtain the intermediate wave stably, we have to stick to the scattering matrices. Suppose we want to find the intermediate waves between the n^{th} layer and $(n+1)^{th}$ layer. From the two cascaded matrix $S^{(1)}$ and $S^{(2)}$, we have the following two equations,

$$\underline{a}_{n+1}^+ = S_{21}^{(1)} \cdot \underline{a}_1^+ + S_{22}^{(1)} \cdot \underline{a}_{n+1}^- \quad (2.44)$$

$$\underline{a}_{n+1}^- = S_{11}^{(2)} \cdot \underline{a}_{n+1}^+ + S_{12}^{(2)} \cdot \underline{a}_{N+1}^- \quad (2.45)$$

Our goal is to express \underline{a}_{n+1}^+ and \underline{a}_{n+1}^- in terms of \underline{a}_1^+ and \underline{a}_{N+1}^- . Let us start with \underline{a}_{n+1}^+ .

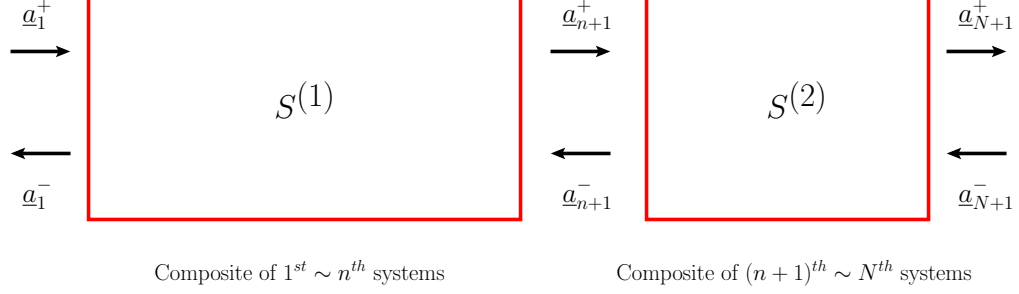


Figure 2.10: To obtain the intermediate wave, E_n^+ and E_n^- , we deal with two cascaded scattering matrices S_1 and S_2 .

$$\underline{a}_{n+1}^+ = S_{21}^{(1)} \cdot \underline{a}_1^+ + S_{22}^{(1)} \cdot \underline{a}_{n+1}^- \quad (2.46)$$

$$= S_{21}^{(1)} \cdot \underline{a}_1^+ + S_{22}^{(1)} \cdot (S_{11}^{(2)} \cdot \underline{a}_{n+1}^+ + S_{12}^{(2)} \cdot \underline{a}_{N+1}^-), \quad (\because \text{eq. (2.45)}) \quad (2.47)$$

$$(I - S_{22}^{(1)} \cdot S_{11}^{(2)}) \cdot \underline{a}_{n+1}^+ = S_{21}^{(1)} \cdot \underline{a}_1^+ + S_{22}^{(1)} \cdot S_{12}^{(2)} \cdot \underline{a}_{N+1}^- \quad (2.48)$$

$$\underline{a}_{n+1}^+ = (I - S_{22}^{(1)} \cdot S_{11}^{(2)})^{-1} \cdot (S_{21}^{(1)} \cdot \underline{a}_1^+ + S_{22}^{(1)} \cdot S_{12}^{(2)} \cdot \underline{a}_{N+1}^-) \quad (2.49)$$

Let us derive a similar result for \underline{a}_{n+1}^- .

$$\underline{a}_{n+1}^- = S_{11}^{(2)} \cdot \underline{a}_{n+1}^+ + S_{12}^{(2)} \cdot \underline{a}_{N+1}^- \quad (2.50)$$

$$= S_{11}^{(2)} \cdot (S_{21}^{(1)} \cdot \underline{a}_1^+ + S_{22}^{(1)} \cdot \underline{a}_{n+1}^-) + S_{12}^{(2)} \cdot \underline{a}_{N+1}^-, \quad (\because \text{eq. (2.44)}) \quad (2.51)$$

$$(I - S_{11}^{(2)} \cdot S_{22}^{(1)}) \cdot \underline{a}_{n+1}^- = S_{11}^{(2)} \cdot S_{21}^{(1)} \cdot \underline{a}_1^+ + S_{12}^{(2)} \cdot \underline{a}_{N+1}^- \quad (2.52)$$

$$\underline{a}_{n+1}^- = (I - S_{11}^{(2)} \cdot S_{22}^{(1)})^{-1} \cdot (S_{11}^{(2)} \cdot S_{21}^{(1)} \cdot \underline{a}_1^+ + S_{12}^{(2)} \cdot \underline{a}_{N+1}^-) \quad (2.53)$$

Our final formulas to get the intermediate wave are Eq. (2.49) and Eq. (2.53). Since the matrix inversion is done to a matrix added to an identity matrix, this method is stable. Paper related to stability of scattering matrix and transfer matrix can be found in [25].

We have simulated 300 cascaded system where each single system was generated from the setting in the following table.

Distribution	N_{cy}	λ	Width	Thickness	Period	Radius	IOR
Latin-Hyper cube	1440	0.93	183.31	1100	183.31	0.1	1.3

Very few open eigen-channels existed in the 300 cascaded system. We have excited the system with an open eigen-channel, and used Eq. (2.49) and Eq. (2.53) to

calculate the intermediate waves in the cascaded system. We defined *current* to be a power flowing in one direction, and depicted the forward current, backward current and the net current, which is the forward current minus the backward current.

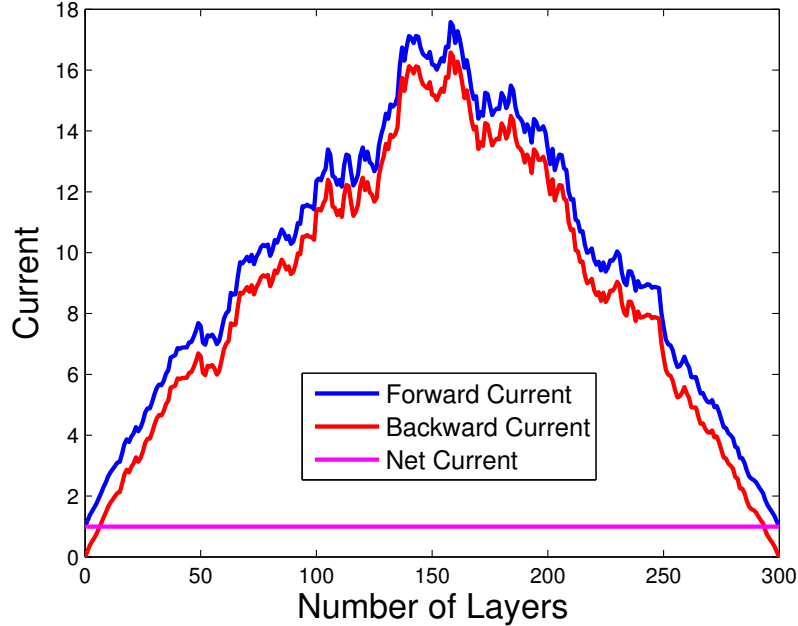


Figure 2.11: Currents in between the cascaded scattering system are plotted when the system is excited with the optimal input yielding 0.99 transmitted power at the end. Notice that there is a huge forward current in the middle, and correspondingly huge backward current to make the net current remain nearly constant.

We can see a huge amount of power flowing in the forward direction in the middle of the system. It is really hard to imagine that this is happening since what we only did to the system was shooting a light whose forward power was 1 from the left side of the system, and we are observing power higher than 1, almost reaching 18 in the forward direction. However, the *net current* remains nearly constant throughout the system because of correspondingly huge backward current, satisfying current conservation. This result gives us a clue about *localization of light* in random media.

2.6 Construction of Scattering Matrix

In this section, we are going to discuss about how to construct a highly-accurate scattering matrix.

2.6.1 Assumptions on the scatterers and modes

Our scattering situation is a two-dimensional periodic setting with cylindrical scatterers infinitely long in the z direction. Cylindrical shaped scatterer is chosen be-

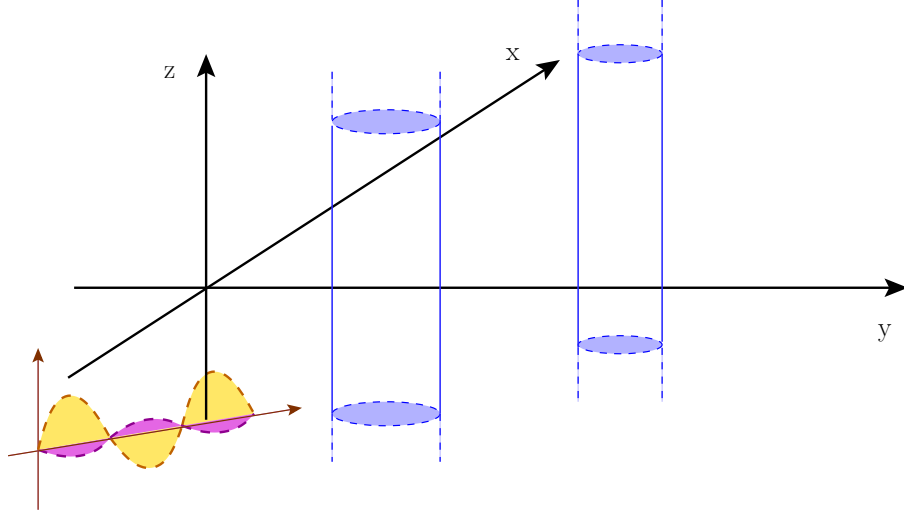


Figure 2.12: Geometrical Situation. The scatterer is a cylinder infinitely long in z direction, and wave propagates on the xy -plane.

cause the symmetric shape will let us have exact solutions from the boundary value problems, thereby eliminating any possible error source in our numerical simulation.

Recall that we need to form a set of countable modes in order to formulate a scattering matrix. We set our modes to be *periodic planewaves* by inducing periodicity in the x direction. Also, we assume the wave propagates on the xy -plane and its electric or magnetic field will oscillate in the z direction. Then, the n -th mode can be written as below,

$$\varphi_n(\rho) = e^{-j\mathbf{k}_n \cdot \rho} = e^{-j(k_{x_n}, k_{y_n}, 0) \cdot (x, y, z)} = e^{-j(k_{x_n}x + k_{y_n}y)}. \quad (2.54)$$

Because of the periodicity in the x direction,

$$k_{x_n} = \frac{2\pi}{L}n, \quad \text{where } L \text{ is period.} \quad (2.55)$$

Since the wavevector \underline{k}_n is restricted as $\|\underline{k}_n\|_2 = \frac{2\pi}{\lambda}$, where λ is the wavelength,

$$k_{y_n} = \pm \sqrt{\|\underline{k}_n\|_2^2 - k_{x_n}^2} = \pm \sqrt{\left(\frac{2\pi}{\lambda}\right)^2 - \left(\frac{2\pi}{L}n\right)^2}. \quad (2.56)$$

The sign depends on the propagating direction of the wave. Note that the mode is propagating mode when $n < \lfloor \frac{L}{\lambda} \rfloor$, and the mode is the evanescent mode when $n > \lfloor \frac{L}{\lambda} \rfloor$ because k_{y_n} becomes complex. When k_{y_n} is complex, we need to choose the sign of

k_{y_n} carefully, so that the wave could decay in the propagating direction in order to have a physical solution. The choice of sign is summarized as follows.

For forward direction waves (in +y direction),

$$k_{y_n} = k_{y_n}^+ = \begin{cases} \sqrt{\left(\frac{2\pi}{\lambda}\right)^2 - \left(\frac{2\pi}{L}n\right)^2} & , \text{ when } n < \lfloor \frac{L}{\lambda} \rfloor \\ -j\sqrt{\left(\frac{2\pi}{L}n\right)^2 - \left(\frac{2\pi}{\lambda}\right)^2} & , \text{ when } n > \lfloor \frac{L}{\lambda} \rfloor \end{cases} \quad (2.57)$$

For reverse direction waves (in -y direction),

$$k_{y_n} = k_{y_n}^- = \begin{cases} -\sqrt{\left(\frac{2\pi}{\lambda}\right)^2 - \left(\frac{2\pi}{L}n\right)^2} & , \text{ when } n < \lfloor \frac{L}{\lambda} \rfloor \\ +j\sqrt{\left(\frac{2\pi}{L}n\right)^2 - \left(\frac{2\pi}{\lambda}\right)^2} & , \text{ when } n > \lfloor \frac{L}{\lambda} \rfloor \end{cases} \quad (2.58)$$

The angle of the mode is defined as below,

$$\theta_n = \arcsin\left(\frac{k_{x_n}}{\|\underline{k}_n\|_2}\right) = \arcsin\left(\frac{\lambda}{L}n\right) \quad (2.59)$$

The whole geometric situation can be viewed in Fig. 2.13

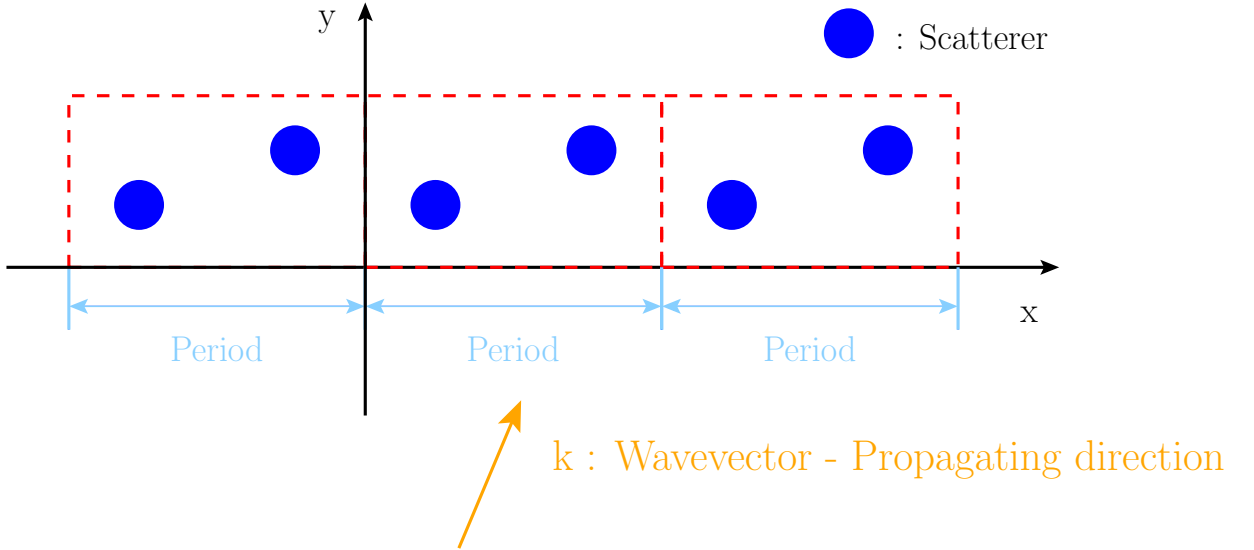


Figure 2.13: Geometrical situation on the xy -plane gives a simpler point of view.

With our periodic modes, the modal expansion of a periodic wave will look like below,

$$\varphi(\underline{\rho}) = \sum_{n=-N}^N h_n a_n e^{-j\underline{k}_n \cdot \underline{\rho}} = \sum_{n=-N}^N h_n a_n e^{-j(k_{x_n}x + k_{y_n}y)} \quad (2.60)$$

where h_n is the normalizing coefficient and a_n is the normalized modal coefficient. The y direction power carried by $\varphi(\underline{\rho})$ will be,

$$y \text{ direction power} = \sum_{n=-N}^N \cos(\theta_n) |h_n|^2 |a_n|^2 \quad (2.61)$$

$$= \sum_{n=-N}^N |a_n|^2, \quad (\text{By setting } h_n = \frac{1}{\sqrt{\cos(\theta_n)}}) \quad (2.62)$$

proof in appendix VI. Setting the normalizing coefficient as $h_n = \frac{1}{\sqrt{\cos(\theta_n)}}$ makes the normalized modal coefficient vector \underline{a}_n represent the power flow in the y direction.

2.6.2 Scattering Matrix Generating Algorithm

Using the periodic modes, we can write Algorithm 1 in a detailed manner. There

Algorithm 2 Scattering Matrix generating algorithm

- 1: % Excite the system by φ_1^+
 - 2: **for** $m = -N$ to N **do**
 - 3: Excite the system with $\frac{1}{\sqrt{\cos(\theta_n)}} e^{-j(k_{x_m}x + k_{y_m}^+y)}$, where $\theta_n = \arcsin(\frac{k_{x_n}}{k})$
 - 4: Solve Maxwell's equations and obtain φ_1^- and φ_2^+
 - 5: Express φ_1^- and φ_2^+ in modal expansion,
i.e. $\varphi_1^- = \sum_{n=-N}^N b_n e^{-j(k_{x_n}x + k_{y_n}^-y)}$ and $\varphi_2^+ = \sum_{n=-N}^N d_n e^{-j(k_{x_n}x + k_{y_n}^+y)}$
 - 6: Normalize $b_n s$ and $d_n s$,
i.e. $b_n \leftarrow \sqrt{\cos(\theta_n)} b_n$ and $d_n \leftarrow \sqrt{\cos(\theta_n)} d_n$
 - 7: Include the incident mode, i.e. $d_m \leftarrow d_m + 1 \cdot e^{-jk_{y_m}^+ D}$, where D is the thickness of the medium
 - 8: Stack $b_n s$ and $d_n s$ as $[\underline{b}^T, \underline{d}^T]^T$ and fill it into the $(m + N + 1)^{th}$ column
 - 9: **end for**
 - 10: % Excite the system by φ_2^-
 - 11: **for** $m = -N$ to N **do**
 - 12: Excite the system with the $\frac{1}{\sqrt{\cos(\theta_n)}} e^{-j(k_{x_m}x - k_{y_m}y)}$, where $\theta_n = \arcsin(\frac{k_{x_n}}{k})$
 - 13: Solve Maxwell's equations and obtain φ_1^- and φ_2^+
 - 14: Express φ_1^- and φ_2^+ in modal expansion,
i.e. $\varphi_1^- = \sum_{n=-N}^N b_n e^{-j(k_{x_n}x + k_{y_n}^-y)}$ and $\varphi_2^+ = \sum_{n=-N}^N d_n e^{-j(k_{x_n}x + k_{y_n}^+y)}$
 - 15: Normalize $b_n s$ and $d_n s$,
i.e. $b_n \leftarrow \sqrt{\cos(\theta_n)} b_n$ and $d_n \leftarrow \sqrt{\cos(\theta_n)} d_n$
 - 16: Include the incident mode, i.e. $b_m \leftarrow b_m + 1 \cdot e^{-jk_{y_m}^- (-D)}$, where D is the thickness of the medium
 - 17: Stack $b_n s$ and $d_n s$ as $[\underline{b}^T, \underline{d}^T]^T$ and fill it into the $(m + 3N + 2)^{th}$ column
 - 18: **end for**
-

are three important things to notice in Algorithm 2. The first thing is the normalization done in step 3, 6, 12 and 15. The normalization in step 3 and 12 are done for converting the normalized modal coefficients to modal coefficients, and the normalization in step 6 and 15 are done for converting the modal coefficients to normalized modal coefficients.

The second thing to notice is that the step 7 and 16. These step are done because the incident wave should be always included after calculating the scattered wave.

The last thing to mention is that step 4 and 13 are the core of the algorithm, which solves the Maxwell's equations, and the way of solving Maxwell's equations is not described precisely in the algorithm. We will explain how to solve the equations

and obtain the scattered waves step by step in the following sections. To deal with cylinder shaped scatterer, it is easy to solve the problem in cylindrical coordinate. So we convert the planewaves into cylinder waves. After that, the *key equation* will give us all the scattered waves from all the cylinders. At the end we convert the solution from the cylinder waves domain to planewaves domain.

Recall that we are dealing with periodic scattering system and solving Maxwell's equations for a periodic structure is a little bit more complicated than aperiodic structure. So we will first describe how to solve Maxwell's equations for an aperiodic structure in section 2.6.3. After that, we will discuss how to solve Maxwell's equations for a periodic structure in section 2.6.4.

2.6.3 Maxwell's equations solver - aperiodic case

2.6.3.1 Cylinder Waves and their vector representations

Solving Maxwell's equations involves three steps: (1) fix the coordinate system, (2) find the general solutions (linear combination of modes) for each region, (3) match the coefficients of the modes at the boundaries. We solve Maxwell's equations in a cylindrical coordinate. The general solutions to Maxwell's equations in cylindrical coordinate (ρ, ϕ, z) are like below,

$$\psi_n(\rho, \phi, z) = \mathcal{C}_n(k_\rho \rho) e^{jn\phi} e^{jk_z z} \quad (2.63)$$

where n is the mode index, k_ρ is the xy -plane component of the wavevector, k_z is the z -direction component of the wavevector and $\mathcal{C}_n(k_\rho \rho)$ is the Bessel function. Bessel function has four types,

1. $J_n(k_\rho \rho)$, Bessel function of the first kind, finite standing wave.
2. $Y_n(k_\rho \rho)$, Bessel function of the second kind, standing wave that blows up at the origin.
3. $H_n^{(1)}(k_\rho \rho)$, Hankel function of the first kind, inward traveling wave.
4. $H_n^{(2)}(k_\rho \rho)$, Hankel function of the second kind, outward traveling wave.

Since we assume that the electric field or the magnetic field oscillates in the z -direction (*TM Polarization* or *TE Polarization*), $k_z = 0$ in Eq. (2.63). We express the final solution as a linear combination of the modes defined above with the proper type of Bessel function. The type choice depends on type of the wave and the region of the wave exists. For example, if we have to describe a cylinder wave confined in a structure containing the origin we will have to use $\mathcal{C}_n(k\rho) = J_n(k\rho)$ because Bessel function of the first kind is the only solution that does not diverge at the origin. If we have to describe a wave, propagating outward from the cylinder, we choose $\mathcal{C}_n(k\rho) = H_n^{(2)}(k\rho)$.

Suppose that we had N_{cy} cylinders and we assign numbers to index them. Then,

the cylinder waves generated from the i -th cylinder will be expressed as

$$\psi^{(i)}(\rho, \phi) = \sum_{n=-\infty}^{\infty} c_n^{(i)} \psi_n(\rho, \phi) = \sum_{n=-\infty}^{\infty} c_n^{(i)} \mathcal{C}_n(k\rho) e^{jn\phi} \quad (2.64)$$

By assuming that we only consider the $-M$ th mode till the M th mode, we express the cylinder wave vector for the i -th cylinder as,

$$(\underline{c}^{(i)})^T = [c_{-M}^{(i)}, c_{-M+1}^{(i)}, \dots, c_M^{(i)}] \quad (2.65)$$

Furthermore, we denote the cylinder wave vector for the entire scatterers as,

$$\underline{c}^T = [(\underline{c}^{(1)})^T, (\underline{c}^{(2)})^T, \dots, (\underline{c}^{(N_{cy})})^T] \quad (2.66)$$

2.6.3.2 Scattering Coefficients

Scattering coefficients are coefficients of the scattered cylinder waves, which are produced when a unit cylinder wave is shined to a scatterer.

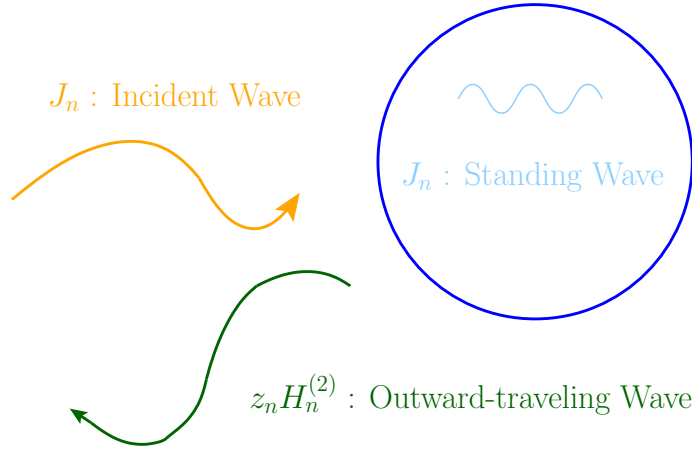


Figure 2.14: Incident planewave should be expressed as J_n since it is finite everywhere. Because of the symmetric shape of the cylinder, if a n -th order cylinder wave is incident on a cylinder, two n -th order cylinder waves will be produced. One is an outgoing cylinder wave, $H_n^{(2)}$, and the other is a standing wave inside the cylinder, J_n . The scattering coefficient z_n can be obtained by solving boundary value problem.

In general, when a single cylinder mode is shined on an arbitrary-shaped scatterer, it will produce different orders of modes inside and outside of the scatterer. In order to find the scattering coefficients for all the modes produced, we need to solve the boundary value problem corresponding to the situation.

For a cylinder-shaped scatterer, a single cylinder mode will only produce the same order of cylinder wave inside and outside of the cylinder-shaped scatterer, i.e. the

cylinder modes are decoupled for cylinder-shaped scatterers. Solving the boundary value problem becomes easier and more accurate than the arbitrary-shaped scatterer. The scattering coefficient obtained from solving the boundary value problem depends on the polarization of light, *TM* or *TE*, and the material property, *Perfect Electric Conductor (PEC)* or *Dielectric*. The table below summarizes the scattering coefficient for the n -th mode,

Polarization	PEC	Dielectric
TM	$-\frac{J_n(k_{out}a)}{H_n^{(2)}(k_{out}a)}$	$\frac{-\sqrt{\tilde{\epsilon}_{out}\tilde{\mu}_{cy}}J_n(k_{cy}a)J'_n(k_{out}a) + \sqrt{\tilde{\epsilon}_{cy}\tilde{\mu}_{out}}J_n(k_{out}a)J'_n(k_{cy}a)}{-\sqrt{\tilde{\epsilon}_{out}\tilde{\mu}_{cy}}J_n(k_{cy}a)H_n^{(2)}(k_{out}a) + \sqrt{\tilde{\epsilon}_{cy}\tilde{\mu}_{out}}J'_n(k_{cy}a)H_n^{(2)}(k_{out}a)}$
TE	$-\frac{J'_n(k_{out}a)}{H_n^{(2)}(k_{out}a)}$	$\frac{-\sqrt{\tilde{\epsilon}_{cy}\tilde{\mu}_{out}}J_n(k_{out}a)J'_n(k_{cy}a) + \sqrt{\tilde{\epsilon}_{out}\tilde{\mu}_{cy}}J_n(k_{cy}a)J'_n(k_{out}a)}{-\sqrt{\tilde{\epsilon}_{cy}\tilde{\mu}_{out}}J_n(k_{out}a)H_n^{(2)}(k_{cy}a) + \sqrt{\tilde{\epsilon}_{out}\tilde{\mu}_{cy}}J'_n(k_{out}a)H_n^{(2)}(k_{cy}a)}$

Table 2.2: The scattering coefficients for cylinder-shaped scatterers.

where $\tilde{\epsilon}_{out}$ and $\tilde{\epsilon}_{cy}$ denote the relative permittivity of the freespace and cylinder respectively, $\tilde{\mu}_{out}$ and $\tilde{\mu}_{cy}$ denote the relative permeability of the freespace and cylinder respectively, and $k_{out} = \frac{2\pi}{\lambda}\sqrt{\tilde{\epsilon}_{out}\tilde{\mu}_{out}}$ and $k_{cy} = \frac{2\pi}{\lambda}\sqrt{\tilde{\epsilon}_{cy}\tilde{\mu}_{cy}}$. Proof is in appendix VI.

To compute the derivatives of bessel functions in Table 2.2, we use the following property of bessel functions,

$$2\mathcal{C}'_n(z) = \mathcal{C}_{n-1}(z) - \mathcal{C}_{n+1}(z) \quad (2.67)$$

where \mathcal{C} denotes J, Y, H^1 , and H^2 or any linear combination of these functions [28].

Let us denote the scattering coefficient for the n -th mode as z_n and M as the highest order of the cylinder mode. We write the scattering coefficient vector for a single cylinder like below,

$$(\underline{z}^{(1)})^T = [z_{-M}^{(1)}, z_{-M+1}^{(1)}, \dots, z_M^{(1)}] \quad (2.68)$$

Using the cylinder wave vector we defined in the previous section, we can write an equation that describes a single scatterer situation,

$$\underline{c}^{out,(1)} = diag\{\underline{z}^{(1)}\} \cdot \underline{c}^{in,(1)} \quad (2.69)$$

where $\underline{c}^{in,(1)}$ is a cylinder wave vector describing the coefficients of the incident cylinder waves and $\underline{c}^{out,(1)}$ is a cylinder wave vector describing the coefficients of the scattered cylinder waves.

Furthermore, we denote the scattering coefficient vector and matrix for all the scatterers as,

$$\underline{z}^T = [(\underline{z}^{(1)})^T, (\underline{z}^{(2)})^T, \dots, (\underline{z}^{(N_{cy})})^T] \quad (2.70)$$

$$Z = diag\{\underline{z}\} \quad (2.71)$$

where N_{cy} is the number of scatterers. Note that the scattering coefficient matrix Z is a diagonal matrix because all the modes are decoupled.

For arbitrary shaped cylinders, the scattering coefficient matrix Z will not be diagonal anymore which means the incident n^{th} cylinder mode will produce other order cylinder modes as well. We have to use finite element method to find the coefficients of the modes that satisfy the boundary condition at finite points on the boundary of the arbitrary cylinder.

2.6.3.3 Key equation

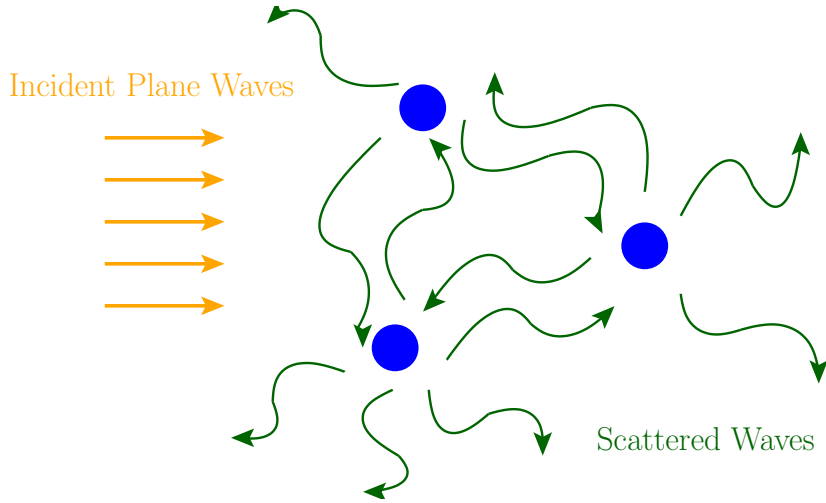


Figure 2.15: Scattering Situation with multiple cylinders. It is important to consider the scattered waves from the other cylinders as an input to each cylinder.

Let us formulate a matrix-vector equation that describes the scattering situation in Fig. (2.15). Important thing to notice from the figure is that the input to each cylinder is the incident planewave plus scattered cylinder waves coming from other cylinders. Thus this fact will make a difference from Eq. (2.69). The scattered cylinder wave vector \underline{c}^{out} will be the scattering coefficient matrix Z times the summation of both incident cylinder wave vector \underline{c}^{in} and scattered cylinder wave vector \underline{c}^{out} . This can be written in the following equation

$$\underline{c}^{out} = Z \cdot (\underline{c}^{in} + T \cdot \underline{c}^{out}) \quad (2.72)$$

where

- $(\underline{c}^{in})^T = [(\underline{c}^{in,(1)})^T, (\underline{c}^{in,(2)})^T, \dots, (\underline{c}^{in,(N_{cy})})^T]$
 \hookrightarrow Coefficients of bessel function of the first kind, J
- $(\underline{c}^{out})^T = [(\underline{c}^{out,(1)})^T, (\underline{c}^{out,(2)})^T, \dots, (\underline{c}^{out,(N_{cy})})^T]$
 \hookrightarrow Coefficients of bessel function of the third kind, $H^{(2)}$

- $Z = \text{diag}\{[(\underline{z}^{(1)})^T, (\underline{z}^{(2)})^T, \dots, (\underline{z}^{(N_{cy})})^T]\}$
 $\hookrightarrow Z$: coefficients of $J \mapsto$ coefficients of $H^{(2)}$
- T = Conversion matrix from \underline{c}^{in} format to \underline{c}^{out} format
 \hookrightarrow Do not be confused with the transfer matrix

Rearranging Eq. (2.72), we obtain the key equation Eq. (2.74)

$$(I - Z \cdot T) \cdot \underline{c}^{out} = Z \cdot \underline{c}^{in} \quad (2.73)$$

$$\underline{c}^{out} = (I - Z \cdot T)^{-1} \cdot Z \cdot \underline{c}^{in} \quad (2.74)$$

This key equation will give us the scattered solution for aperiodic scattering case. However, we still need to know \underline{c}^{in} , and T in order to compute \underline{c}^{out} . In the following sections, we will describe how to get \underline{c}^{in} and T .

2.6.3.4 Plane wave to Cylinder wave conversion : \underline{c}^{in}

\underline{c}^{in} is a vector which is the stack of cylinder waves going into each cylinder due to the incident planewave. So we need to find a way to convert an incident planewave into cylinder waves whose origin is centered at the center of the cylinder. Let us first consider a single cylinder case,

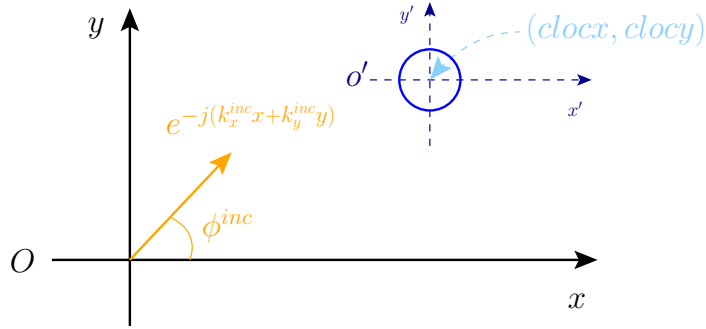


Figure 2.16: Planewave with incident angle ϕ^{inc} is shined on a cylinder positioned at $(clocx, clocy)$. We have to describe planewave whose coordinate system is O in cylinder waves whose coordinate systems is the cylinder coordinate o' .

Since the incident wave is a planewave, it has to be finite all over the space. Therefore, we choose bessel function of the first kind, $J_n(k\rho)$, to express the incident planewave.

$$e^{-j(k_x^{inc}x + k_y^{inc}y)} = \sum_{n=-\infty}^{\infty} a_n J_n(k\rho') e^{jn\phi'} \quad (2.75)$$

Using the integral representation of bessel functions, we get the following conversion formula.

$$a_n = e^{-j(k_x^{inc}clocx + k_y^{inc}clocy)} \cdot e^{-jn\phi^{inc}} \cdot e^{-j\frac{n\pi}{2}} \quad (2.76)$$

Proof is in the appendix VI.

Using eq. (2.76),

$$(\underline{c}^{in,(1)})^T = [a_{-M}, \dots, a_M] \quad (2.77)$$

where M is the highest order index of the cylinder modes.

For multiple cylinders, we repeat Eq. (2.77) for all the cylinders and form $(\underline{c}^{in})^T = [(\underline{c}^{in,(1)})^T, (\underline{c}^{in,(2)})^T, \dots, (\underline{c}^{in,(N_{cy})})^T]$.

2.6.3.5 Proper number of cylinder modes

Eq. (2.75) tells us that to express a planewave we need to use infinite number of cylinder waves. However, we can not take all the cylinder modes into account in practice. So how many modes are enough to take into account? The answer lies in the key equation Eq. (2.74).

From the key equation, we can see that \underline{c}^{in} is multiplied to the scattering coefficient matrix Z . Now, let us look at the scattering coefficient plot versus the mode index.

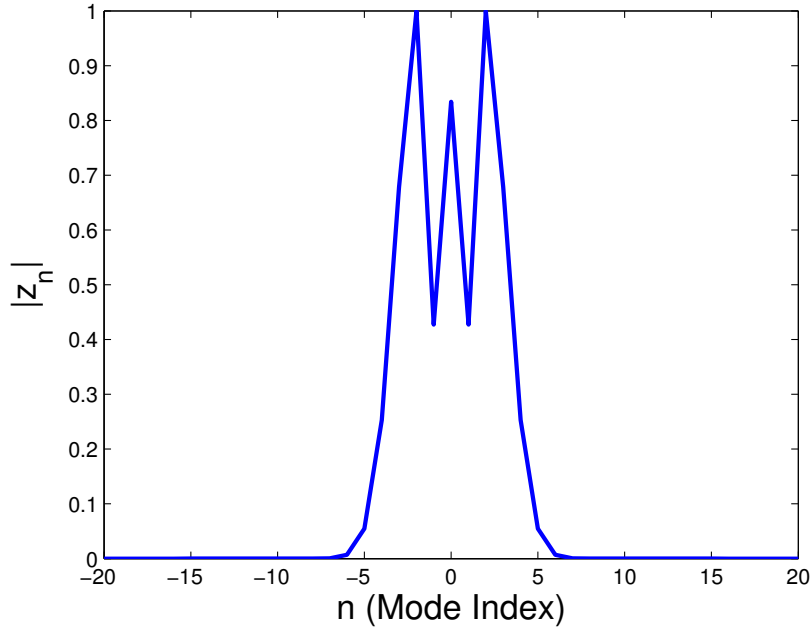


Figure 2.17: Absolute value of the scattering coefficient versus the order of the mode; Result from a PEC cylinder with radius of 0.5 when the wavelength is 0.93. Notice that the scattering coefficient becomes nearly zero after a certain order of mode.

The scattering coefficient suddenly drops close to zero after a certain order of mode. So we can chop off the cylinder modes with a certain tolerance level, tol ,

$$\text{Chop-off index} = \min\{n | \max_{k \geq n} |z_k| < tol\}. \quad (2.78)$$

From now on, let us denote M as the chop-off index of the cylinder modes.

2.6.3.6 T Matrix : Interaction matrix

Caution! This is not the transfer matrix

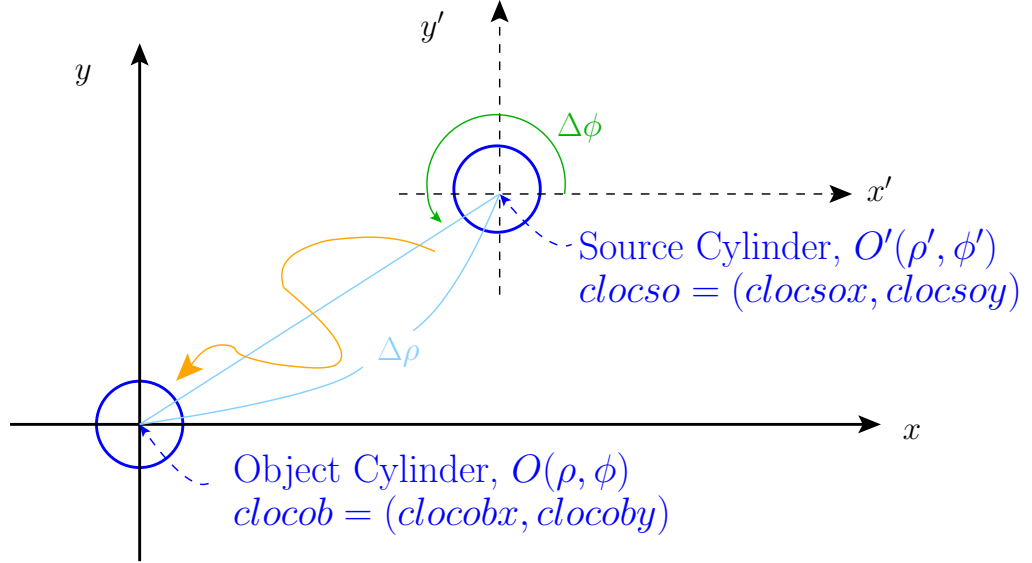


Figure 2.18: T Matrix transforms the cylinder wave coming from the source cylinder into a cylinder wave going into the object cylinder. This involves a coordinate transformation from the source cylinder's coordinate system O' to the object cylinder's coordinate system O .

The main role of the T matrix is to convert the cylinder waves originated at the source cylinder to the cylinder waves originated at the object cylinder. The tricky part is that cylinder waves depend on the origin of the coordinate system.

There are two things to keep in mind. The first is that the cylinder wave generated from the source cylinder is an outgoing traveling wave, $H_n^{(2)}(k\rho)e^{jn\phi}$. The second is that the converted cylinder waves at the destination cylinder should be expressed in terms of $J_n(k\rho)e^{jn\phi}$ since input vector to the scattering coefficient matrix is supposed to be the coefficients of Bessel function of the first kind, $J_n(k\rho)e^{jn\phi}$. So our problem boils down to find the coefficient $b_{cmob,cmso}$ such that

$$H_{cmso}^{(2)}(k\rho')e^{jcmso\phi'} = \sum_{cmob=-\infty}^{\infty} b_{cmob,cmso} J_{cmob}(k\rho)e^{jcmob\phi} \quad (2.79)$$

where $cmob$ is the mode index of the object cylinder and $cmso$ is the mode index of the source cylinder. Using Graf's Addition Theorem [28], we get

$$b_{cmob,cmso} = H_{cmso-cmob}^{(2)}(k\Delta\rho)e^{j(cmso-cmob)\Delta\phi} \quad (2.80)$$

where $\Delta\rho = \|\text{clocob} - \text{clocso}\|$ and $\Delta\phi = \arctan(\text{clocob} - \text{clocso})$. Detailed proof is in appendix VI. Eq. (2.80) tells us that the outgoing wave $H_{cmso}^{(2)}(k\rho)e^{jcmso\phi}$ has $b_{cmob,cmso}$ amount of component of $J_{cmob}(k\rho)e^{jcmob\phi}$ at coordinate O .

Now let us describe how to use Eq. (2.80) to fill in the T matrix. T matrix has a block structure like below,

$$T = \begin{bmatrix} 0 & T_{12} & T_{13} & \cdots & T_{1N_{cy}} \\ T_{21} & 0 & T_{23} & \cdots & T_{2N_{cy}} \\ \vdots & \vdots & \vdots & \ddots & \vdots \\ T_{N_{cy}1} & T_{N_{cy}2} & T_{N_{cy}3} & \cdots & 0 \end{bmatrix}$$

where N_{cy} is the number of cylinders, 0 is an $(2M + 1) \times (2M + 1)$ zero matrix.

It can be seen that $\underline{c}^{in,(a)}$, the scattered cylinder waves going into cylinder a by scattered wave \underline{c}^{out} , can be written as

$$\underline{c}^{in,(a)} = \sum_{b=1}^{N_{cy}} T_{ab} \cdot \underline{c}^{out,(b)}.$$

T_{ab} represents a $(2M + 1) \times (2M + 1)$ coordinate transform matrix from cylinder b to cylinder a , where $T_{ab} \cdot \underline{c}^{out,(b)}$ describes the incoming cylinder waves to cylinder a from cylinder b . So T_{ab} is constructed using Eq. (2.80) like below

$$[T_{ab}]_{mn} = H_{n-m}^{(2)}(k\Delta\rho_{ab})e^{j(n-m)\Delta\phi_{ab}} \quad (2.81)$$

where cloca and clocb are the position vector of cylinder a and b respectively, and $\Delta\rho_{ab} = \|\text{cloca} - \text{clocb}\|$ and $\Delta\phi_{ab} = \arctan(\text{cloca} - \text{clocb})$. In this manner, this matrix converts the scattered waves to incoming waves by adding up all the bessel wave contributed from each cylinder and cylinder mode.

There are two special things to notice in an aperiodic T matrix. One thing is that $T_{aa} = 0$ since the cylinder itself can not send any cylinder wave to itself. Second thing is that each T_{ab} block matrices are *Toeplitz Matrices*. This structure can be used to accelerate the multiplication of T matrix via FFT.

2.6.3.7 Aperiodic cylinder scattering - numerical result

Plugging \underline{c}^{in} , Z and T into the key equation Eq. (2.74), we obtain the scattered cylinder waves. The following plot shows the scattered intensity plot when 90° incident planewave is impinged at 6 PEC cylinders.

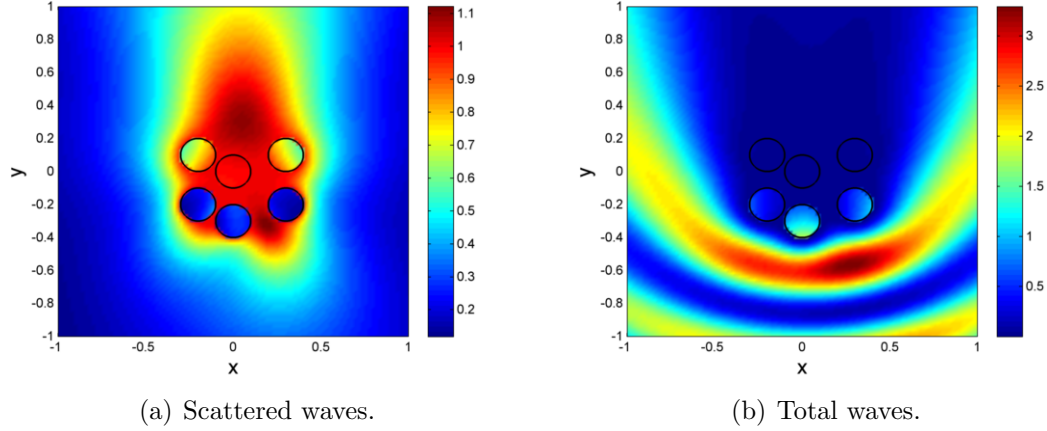


Figure 2.19: Intensity plot of 6 PEC cylinders, depicted as black circles, when plane wave of $\phi^{inc} = 90^\circ$ was shined. (a) There is a strong scattered wave on the upper region, but it is canceled out in plot (b) because of the incident wave, thus forming a shade region on the upper region.

2.6.4 Maxwell's equations solver - periodic case

Now let us deal with the periodic case. We denote the original system as '0-th system' and we repeat it with period L in the x direction (fig. 2.20).

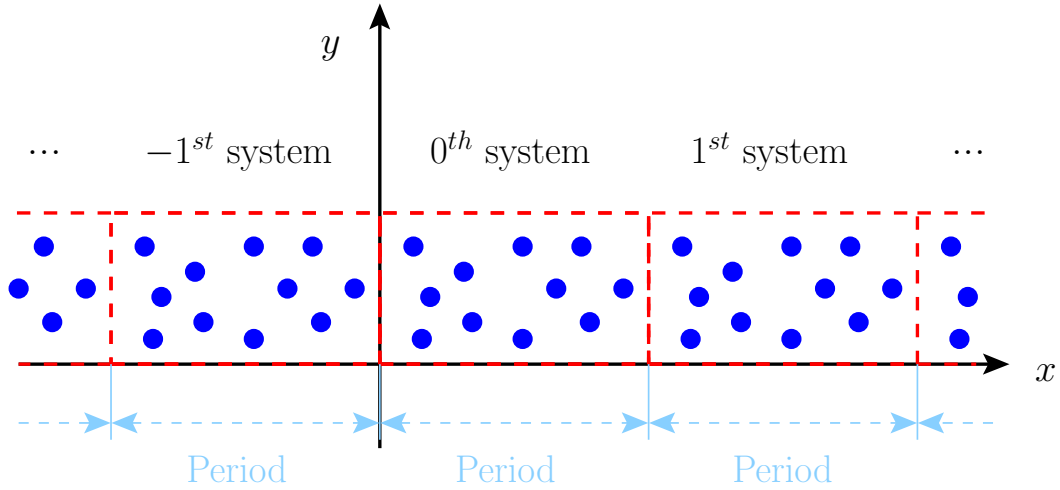


Figure 2.20: Periodic system. We denote the original system as the '0-th system', and we repeat it with a period in the x direction.

The significant difference from the aperiodic case is that we will have more scattered light going into the 0-th system from the other repeated systems. This can be handled by modifying the T matrix. As a result, the T_{aa} partitions in the T matrix are no longer zero matrices because the cylinder itself will have scattered wave from its repeated cylinders.

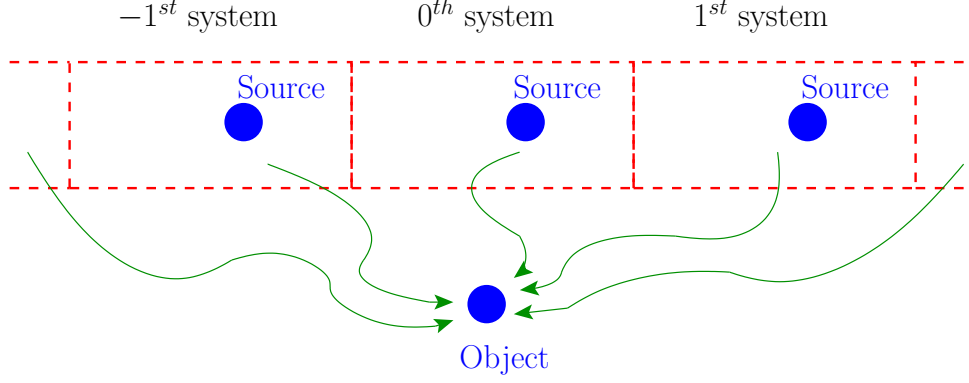


Figure 2.21: We have to consider the scattered wave from the repeated systems in periodic case.

To derive the modified formula for the T matrix, let us first look at the simple case where the incident beam is perpendicular to the system as in Figure 2.22. Since

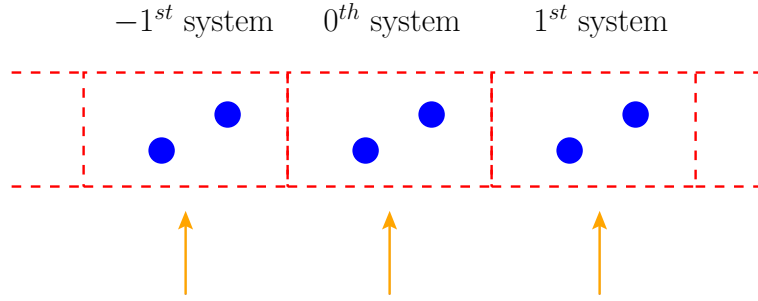


Figure 2.22: When the incident light is perpendicular to the periodic system, the scattering patterns in all the repeated systems will be the same.

the structure is periodic and the incident wave is shined on the system equivalently, the scattering pattern in the 0^{th} system will be the same as the scattering pattern in the repeated systems due to the periodic structure. When the source cylinder and the object cylinder are different as in figure 2.21, we modify the T_{ab} as below,

$$[\tilde{T}_{ab}]_{cmob,cmso} = \sum_{n=-\infty}^{\infty} H_{cmso-cmob}^{(2)}(k\Delta\rho_n) e^{j(cmso-cmob)\Delta\phi_n} \quad (2.82)$$

where L is the period, $\Delta\rho_n = \|clocob - (clocso + n(L, 0))\|$ and $\Delta\phi_n = \arctan(clocob - (clocso + n(L, 0)))$. We call this summation *Spatial sum*.

When the source cylinder and the object cylinder are identical, i.e. T_{aa} case, we have to be careful since it does not have the 0^{th} index in the summation because the cylinder in the 0^{th} system can not send a wave to itself. So the formula will be

$$[\tilde{T}_{aa}]_{cmob,cmso} = \sum_{n \neq 0} H_{cmso-cmob}^{(2)}(k\Delta\rho_n) e^{j(cmso-cmob)\Delta\phi_n} \quad (2.83)$$

We call this summation *Self sum*.

Now let us consider a more general case where the incident wave is not perpendicular to the system as below,

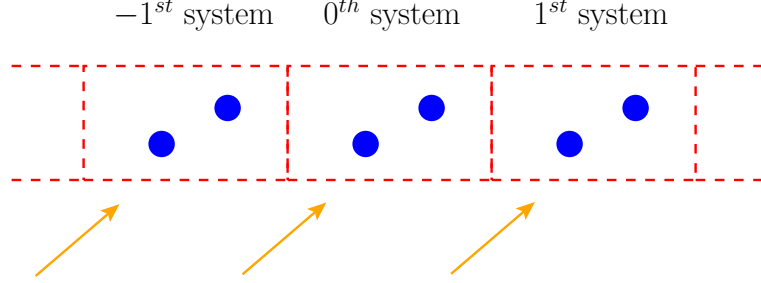


Figure 2.23: If we shine a tilted light to a periodic system, the repeated systems will have phase delayed inputs depending how far they are from the 0^{th} system. As a result, the phase delayed input will cause a phased delayed output from each repeated system.

Everything is the same except the fact that the incident light is entering each system with different phases. The n -th system has $e^{-jk_x^{inc}(n \cdot L)}$ phase delay input compared to the 0-th system. Since these systems are LTI system, we will have phased delayed output from each system. Thus the general T matrix formula for the periodic case should be modified like below,

$$\left\{ \begin{array}{l} \text{Spatial sum} : \sum_{n=-\infty}^{\infty} H_{cmso-cmob}^{(2)}(k\Delta\rho_n) e^{j(cmso-cmob)\Delta\phi_n} \cdot e^{-jk_x^{inc}n \cdot L} \\ \text{Self sum} : \sum_{n \neq 0} H_{cmso-cmob}^{(2)}(k\Delta\rho_n) e^{j(cmso-cmob)\Delta\phi_n} \cdot e^{-jk_x^{inc}n \cdot L} \end{array} \right. \quad (2.84)$$

where L is the period, $\Delta\rho_n = \|clocob - (clocso + n(L, 0))\|$ and $\Delta\phi_n = \arctan(clocob - (clocso + n(L, 0)))$.

In summary, the only difference of computing the scattered waves between aperiodic structure and periodic structure is the T matrix. We only have to compute the T matrix according to equation 2.84 and plug it into the key formula,

$$\underline{c}^{out} = (I - Z \cdot \tilde{T})^{-1} \cdot Z \cdot \underline{c}^{in} \quad (2.85)$$

where \underline{c}^{in} is the incident coefficient vector with respect to the Bessel function of the first kind, \underline{c}^{out} is the scattered coefficient vector with respect to the Bessel function of the third kind, Z is the scattering coefficient matrix and \tilde{T} is the periodic T matrix.

2.6.5 Cylinder waves to Planewaves conversion

After computing the scattered waves, we need to convert the scattered cylinder waves into planewaves, i.e. do a modal expansion on the scattered waves. For

each cylinder's cm -th mode, we add up all the waves of its counterparts from the 0-th system and the repeated systems with proper phase delay, and it becomes

$\sum_{n=-\infty}^{\infty} H_{cm}^{(2)}(k\Delta\rho_n)e^{j(cm)\Delta\phi_n} \cdot e^{-jk_x^{inc}n\cdot L}$. Using integral representation of bessel functions, we can write this summation as a summation of planewaves as below,

$$\begin{aligned} & \sum_{n=-\infty}^{\infty} H_{cm}^{(2)}(k\Delta\rho_n)e^{j(cm)\Delta\phi_n} \cdot e^{-jk_x^{inc}n\cdot L} \\ = & \sum_{n=-\infty}^{\infty} \text{sign}(\tilde{y})^{cm} \cdot e^{-jk_{x_n}\tilde{x}} \cdot e^{-jk_{y_n}|\tilde{y}|} \cdot e^{-jcm(\text{sign}(\tilde{y})\cdot\arcsin(\frac{k_{x_n}}{k})-\pi)} \cdot \frac{2}{k_{y_n} \cdot L} \end{aligned} \quad (2.86)$$

, where $cm =$ order of the cylinder mode,

$$\tilde{x} = \text{clocobx} - \text{clocsox} , \tilde{y} = \text{clocoby} - \text{clocsoy},$$

$$\Delta\rho_n = \|\text{clocob} - (\text{clocso} + n(L, 0))\|$$

$$\Delta\phi_n = \arctan(\text{clocob} - (\text{clocso} + n(L, 0)))$$

$$k_x^{inc} = k \cdot \cos(\phi^{inc}), x \text{ component of the incident wavevector}$$

$$k_{x_n} = k_x^{inc} + \frac{2\pi}{L}n, k_{y_n} = k_y(k_{x_n})$$

$$k_y(\beta) = \begin{cases} \sqrt{k^2 - \beta^2}, & |\beta| \leq k \\ -j\sqrt{\beta^2 - k^2}, & |\beta| > k \end{cases}$$

Proof is in appendix VI. Note that since the x component of the wave vector is $k_x^{inc} = \frac{2\pi}{L}n$, $e^{-jk_{x_n}\cdot L}$ term in the LHS of Eq. (2.86) will be 1.

One thing to observe is

$$\begin{cases} \text{if } \tilde{y} > 0, & e^{-jk_{y_n}|\tilde{y}|} = e^{-jk_{y_n}^+\tilde{y}} & : \text{Wave propagating in } +y \text{ direction} \\ \text{if } \tilde{y} < 0, & e^{-jk_{y_n}|\tilde{y}|} = e^{jk_{y_n}^-\tilde{y}} & : \text{Wave propagating in } -y \text{ direction} \end{cases} \quad (2.87)$$

We are going to convert each cm^{th} mode wave from a particular cylinder into planewaves and extract the modal amplitudes by Eq. (2.86). Then we will do the same thing for all the modes and all the cylinders step by step and add them up at the end, thus obtaining the whole modal amplitude of the planewaves going outside the system.

2.6.5.1 S_{11} partition formula

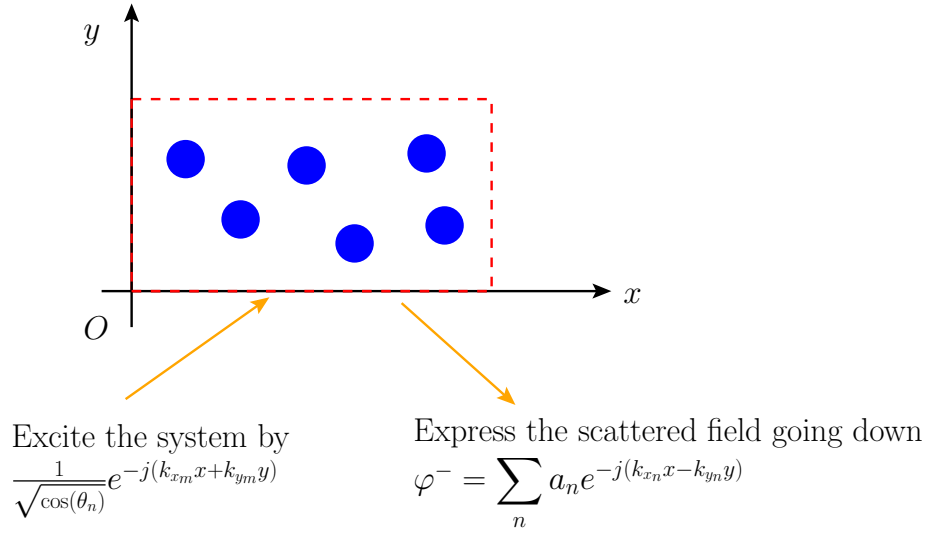


Figure 2.24: Obtaining the modal coefficients of the scattered wave for S_{11} partition.

To get the S_{11} partition's entries, we excite the system by the m -th mode with proper normalization, i.e. $\frac{1}{\sqrt{\cos(\theta_n)}} e^{-j(k_{x_n}x + k_{y_n}y)}$ and express the scattered wave going down in modal expansion like below.

$$\varphi^- = \sum_{n=-N}^N a_n^m e^{-j(k_{x_n}x - k_{y_n}y)} \quad (2.88)$$

where N is the highest mode index.

Let us focus on one cylinder with its periodic counterparts.

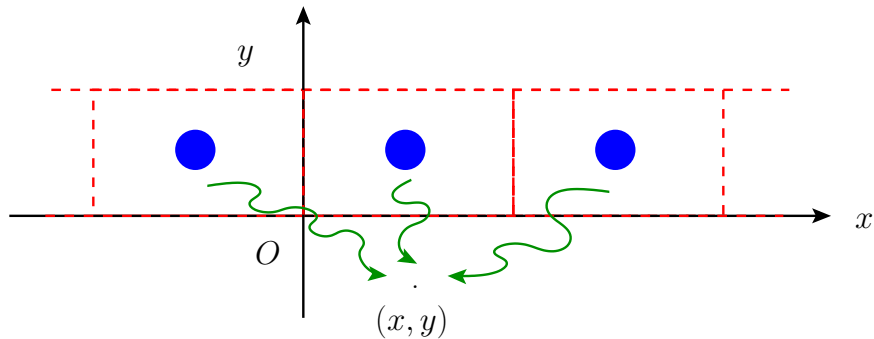


Figure 2.25: To extract the modal coefficients, we have to use the fact that S_{11} partition only considers the waves going down.

Its position in the 0-th system is $cloc = (clocx, clocy)$ and its cm -th coefficient is c_{cm} . The cm -th mode wave arriving at a specific point (x, y) will be like below.

$$\sum_{n=-\infty}^{\infty} c_{cm} H_{cm}^{(2)}(k\Delta\rho_n) e^{-j(cm)\Delta\phi_n} \quad (2.89)$$

where $\Delta\rho_n = \|(x, y) - (cloc + n(L, 0))\|$ and $\Delta\phi_n = \arctan((x, y) - (cloc + n(L, 0)))$. Using the formula Eq. (2.86) to the summation above becomes,

$$(2.86) = \sum_{n=-\infty}^{\infty} c_{cm} \text{sign}(\tilde{y})^{cm} \cdot e^{-jk_{x_n}\tilde{x}} \cdot e^{-jk_{y_n}|\tilde{y}|} \cdot e^{-jcm(\text{sign}(\tilde{y})\cdot\arcsin(\frac{k_{x_n}}{k})-\pi)} \cdot \frac{2}{k_{y_n} \cdot L} \quad (2.90)$$

where $\tilde{x} = x - xloc$, $\tilde{y} = y - yloc$.

Considering the geometrical situation in Fig. 2.25, \tilde{y} is negative. So $|\tilde{y}| = -y + clocy$. Then, Eq. (2.90) becomes,

$$(2.90) = \sum_{n=-\infty}^{\infty} c_{cm} (-1)^{cm} \cdot e^{-jk_{x_n}(x-clocx)} \cdot e^{-jk_{y_n}(-y+clocy)} \cdot e^{-jcm((-1)\cdot\arcsin(\frac{k_{x_n}}{k})-\pi)} \cdot \frac{2}{k_{y_n} \cdot L} \quad (2.91)$$

$$= \sum_{n=-\infty}^{\infty} c_{cm} (-1)^{cm} \cdot e^{jk_{x_n}clocx} \cdot e^{-jk_{y_n}clocy} \cdot e^{-jcm((-1)\cdot\arcsin(\frac{k_{x_n}}{k})-\pi)} \cdot \frac{2}{k_{y_n} \cdot L} \cdot e^{-jk_{x_n}x} \cdot e^{jk_{y_n}y} \quad (2.92)$$

So the n -th mode planewave coefficient from the periodic cm -th cylinder wave becomes,

$$b_n = c_{cm} (-1)^{cm} \cdot e^{jk_{x_n}clocx} \cdot e^{-jk_{y_n}clocy} \cdot e^{-jcm((-1)\cdot\arcsin(\frac{k_{x_n}}{k})-\pi)} \cdot \frac{2}{k_{y_n} \cdot L} \quad (2.93)$$

We stack these b_n s as $\underline{b} = [b_{-N}, \dots, b_N]$ and use this formula repeatedly for all the modes and for all the cylinders, sum them up, normalize the summed result and fill it in the $(m + N + 1)$ -th column of S_{11} .

2.6.5.2 S_{21} partition formula

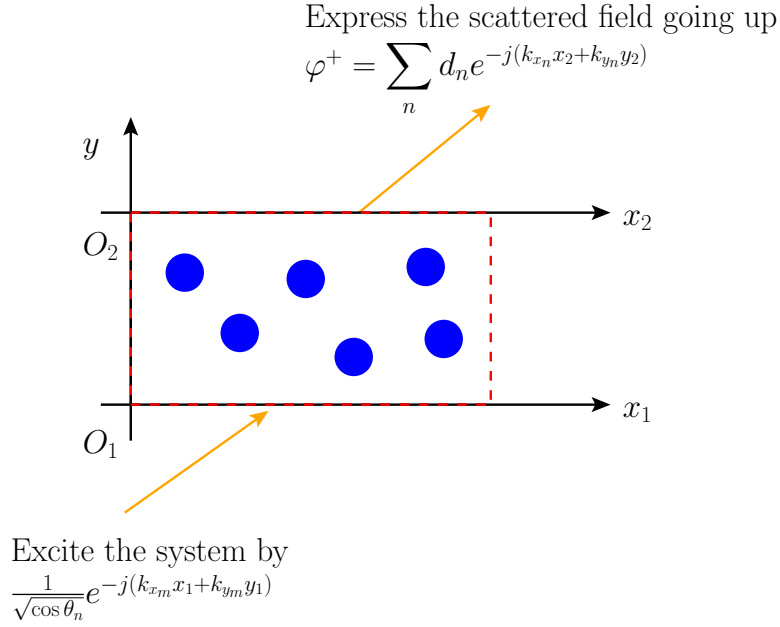


Figure 2.26: Obtaining the modal coefficients of the scattered wave for S_{21} partition. The scattered wave going upwards are based on the coordinate system $O_2(x_2, y_2)$. So we have to be careful since the coordinate system is changing from $O_1(x_1, y_1)$ to $O_2(x_2, y_2)$.

To get the S_{21} partition's entries, we excite the system by the m -th mode with proper normalization, i.e. $\frac{1}{\sqrt{\cos(\theta_n)}} e^{-j(k_{x_n}x_1 + k_{y_n}y_1)}$ and express the scattered wave going up in modal expansion like below.

$$\varphi^+ = \sum_{n=-N}^N d_n e^{-j(k_{x_n}x_2 + k_{y_n}y_2)} \quad (2.94)$$

Note that the coordinate system of the scattered wave becomes $O_2(x_2, y_2)$ and the thickness of the system is D .

Let us focus on one cylinder with its periodic counterparts.

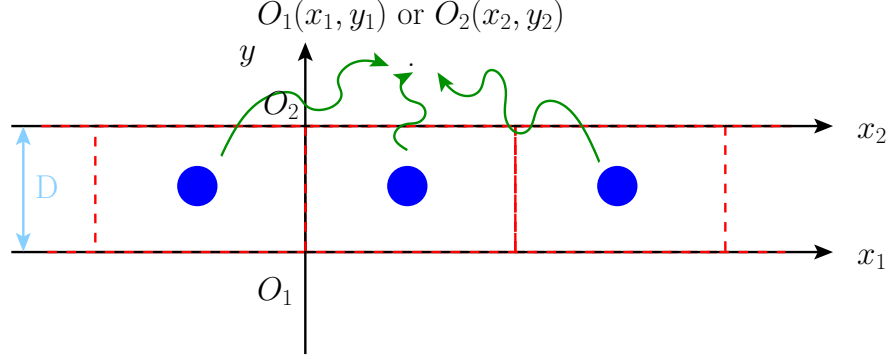


Figure 2.27: To extract the modal coefficients, we have to use the fact that S_{21} partition only considers the waves going up, and we also have to take into account that the coordinate system changes from $O_1(x_1, y_1)$ to $O_2(x_2, y_2)$ where the distance between them are D in the y direction.

Using the same argument and parameters as we did for S_{11} partition, the wave coming from the cm -th mode at a specific point (x, y) will be Eq. (2.89) and applying Eq. (2.86) with careful caution

$$\begin{aligned} \tilde{y} &> 0, \text{ so } |\tilde{y}| = y_1 - cloy \\ y_1 &= y_2 + d \\ \therefore |\tilde{y}| &= y_2 + D - cloy \end{aligned}$$

then we will get

$$\sum_{n=-\infty}^{\infty} c_{cm} (+1)^{cm} \cdot e^{jk_{x_n} clox} \cdot e^{-jk_{y_n} (cloy-D)} \cdot e^{-jcm((+1) \cdot \arcsin(\frac{k_{x_n}}{k}) - \pi)} \cdot \frac{2}{k_{y_n} \cdot L} \cdot e^{-jk_{x_n} x_2} \cdot e^{-jk_{y_n} y_2} \quad (2.95)$$

So the n -th mode planewave coefficient from the cm -th cylinder wave becomes,

$$d_n = c_{cm} e^{jk_{x_n} clox} \cdot e^{jk_{y_n} (cloy-D)} \cdot e^{-jcm(\arcsin(\frac{k_{x_n}}{k}) - \pi)} \cdot \frac{2}{k_{y_n} \cdot L} \quad (2.96)$$

We stack these d_n s as $\underline{d} = [d_{-N}, \dots, d_N]$ and use this formula repeatedly for all the modes and for all the cylinders, sum them up, normalize the summed result, add the incident wave, i.e. $d_m \leftarrow d_m + e^{-jk_{y_m} D}$, and fill it in the $(m + N + 1)$ -th column of S_{21} .

2.6.5.3 S_{12} partition formula

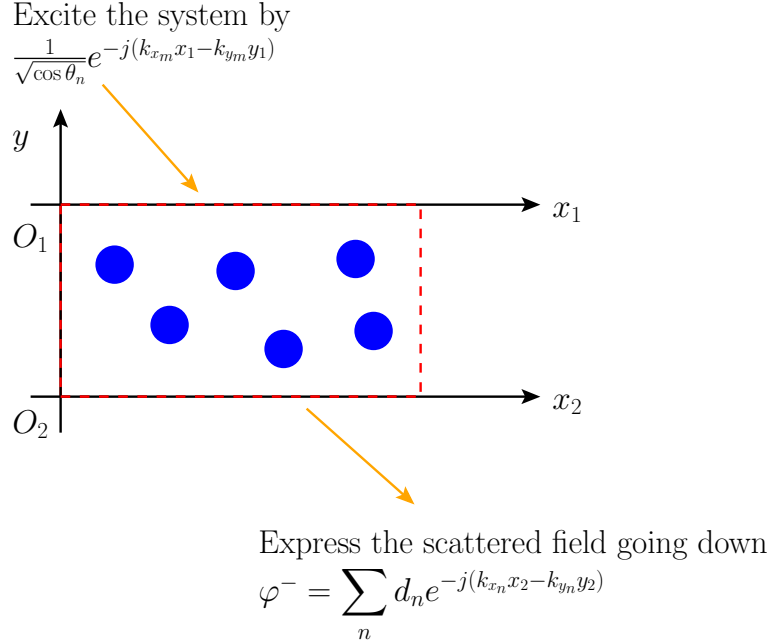


Figure 2.28: Obtaining the modal coefficient of the scattered wave for S_{12} partition. The scattered wave going downwards are based on the coordinate system $O_2(x_2, y_2)$. So we have to be careful since the coordinate system is changing from $O_1(x_1, y_1)$ to $O_2(x_2, y_2)$ which are separated by D in y direction. Note that the cylinders are positioned below the first quadrant of $O_1(x_1, y_1)$. So we have to shift the y positions of all the cylinders by $-D$.

To get the S_{12} partition's entries, we excite the system by the m -th mode with proper normalization, i.e. $\frac{1}{\sqrt{\cos(\theta_n)}} e^{-j(k_{x_n} x_1 - k_{y_n} y_1)}$ and express the scattered wave going down in modal expansion like below.

$$\varphi_+ = \sum_{n=-N}^N d_n e^{-j(k_{x_n} x_2 - k_{y_n} y_2)} \quad (2.97)$$

Note that the coordinate system of the scattered wave becomes $O_2(x_2, y_2)$ and the thickness of the system is D . Also we have to shift the y position of the all the scatterers by $-D$ when we solve the coefficients.

Let us focus on one cylinder with its periodic counterparts.

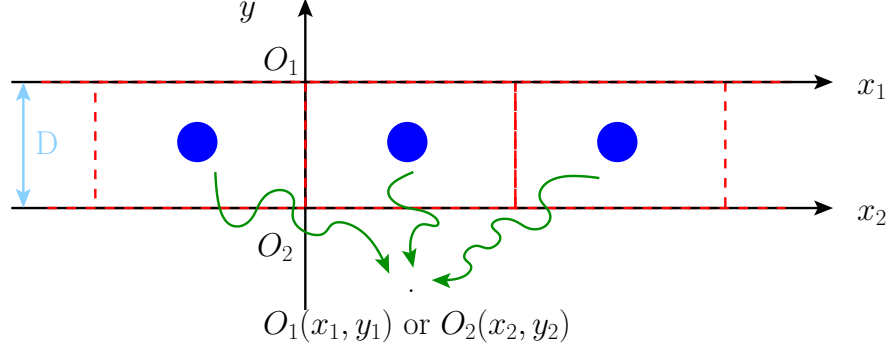


Figure 2.29: To extract the modal coefficients, we have to use the fact that S_{12} partition only considers the waves going down, and we also have to take into account that the coordinate system changes from $O_1(x_1, y_1)$ to $O_2(x_2, y_2)$ where the distance between them are D .

Using the same argument and parameters as we did for S_{11} partition, the wave coming from the cm -th mode at a specific point $O_2(x_2, y_2)$ will be Eq. (2.89) and applying Eq. (2.86) with careful caution

$$\tilde{y} < 0, \text{ so } |\tilde{y}| = -y_1 + clocy \quad (2.98)$$

$$y_1 = y_2 - D \quad (2.99)$$

$$\therefore |\tilde{y}| = -y_2 + D + clocy \quad (2.100)$$

then we will get

$$\sum_{n=-\infty}^{\infty} c_{cm} (-1)^{cm} \cdot e^{jk_{x_n} clocx} \cdot e^{-jk_{y_n} (clocy+D)} \cdot e^{-jcm((-1) \cdot \arcsin(\frac{k_{x_n}}{k}) - \pi)} \cdot \frac{2}{k_{y_n} \cdot L} \cdot e^{-jk_{x_n} x_2} \cdot e^{+jk_{y_n} y_2} \quad (2.101)$$

So the n -th mode planewave coefficient from the cm -th cylinder wave becomes,

$$c_n^m = c^{cm} (-1)^{cm} \cdot e^{jk_{x_n} xloc} \cdot e^{-jk_{y_n} (yloc+d)} \cdot e^{-jcm((-1) \cdot \arcsin(\frac{k_{x_n}}{k}) - \pi)} \cdot \frac{2}{k_{y_n} \cdot L} \quad (2.102)$$

We stack these d_n s as $\underline{d} = [d_{-N}, \dots, d_N]$ and use this formula repeatedly for all the modes and for all the cylinders, sum them up, normalize the summed result, add the incident wave, i.e. $d_m \leftarrow d_m + e^{-jk_{y_m} D}$, and fill it in the $(m + N + 1)$ -th column of S_{12} .

2.6.5.4 S_{22} Partition formula

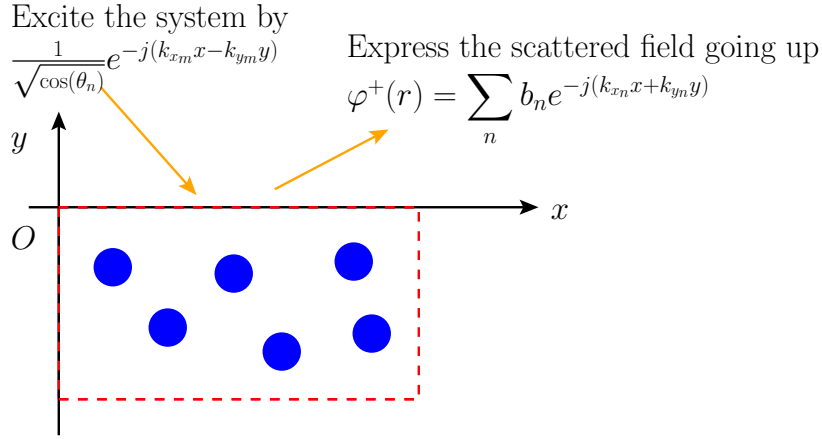


Figure 2.30: Obtaining the modal coefficients of for S_{22} partition. Note that all the cylinders are positioned below the first quadrant.

To get the S_{22} partition's entries, we excite the system by the m -th mode with proper normalization, i.e. $\frac{1}{\sqrt{\cos(\theta_n)}} e^{-j(k_{x_n}x - k_{y_n}y)}$ and express the scattered wave going down in modal expansion like below.

$$\varphi^+ = \sum_{n=-N}^N b_n e^{-j(k_{x_n}x + k_{y_n}y)} \quad (2.103)$$

Note that the thickness of the system is D . So we have to shift the y position of the scatterer by $-D$ when we solve the coefficients.

Let us focus on one cylinder with its periodic counterparts.

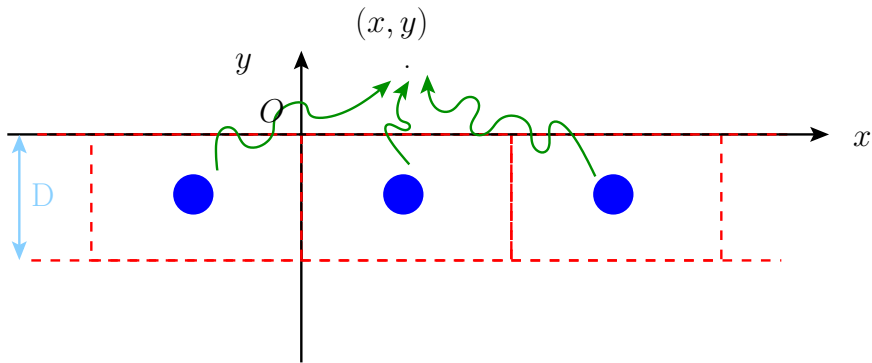


Figure 2.31: To extract the modal amplitude, we have to use the fact that S_{22} partition only considers the waves going up.

Using the same argument and parameters as we did for S_{11} partition, the wave coming from the cm -th mode at a specific point (x, y) will be Eq. (2.89) and applying Eq. (2.86) with careful caution

$$\tilde{y} > 0, \text{ so } |\tilde{y}| = y + clocy \quad (2.104)$$

then we get

$$\sum_{n=-\infty}^{\infty} c_{cm} (+1)^{cm} \cdot e^{jk_{x_n} clox} \cdot e^{jk_{y_n} cloy} \cdot e^{-jcm((+1) \cdot \arcsin(\frac{k_{x_n}}{k}) - \pi)} \cdot \frac{2}{k_{y_n} \cdot L} \cdot e^{-jk_{x_n} x} \cdot e^{-jk_{y_n} y} \quad (2.105)$$

So the n -th mode planewave coefficient from the cm -th cylinder wave becomes,

$$b_n = c_{cm} e^{jk_{x_n} clox} \cdot e^{jk_{y_n} cloy} \cdot e^{-jcm(\arcsin(\frac{k_{x_n}}{k}) - \pi)} \cdot \frac{2}{k_{y_n} \cdot L} \quad (2.106)$$

We stack these b_n s as $\underline{b} = [b_{-N}, \dots, b_N]$ and use this formula repeatedly for all the modes and for all the cylinders, sum them up, normalize the summed result, and fill it in the $(m + N + 1)$ -th column of S_{22} .

2.6.6 Computational Issue - Speed

Main bottleneck for computing the scattering matrix is the computation of the T matrix. The number of elements in the T matrix grows quadratically with respect to the number of cylinders. Moreover, the elements in the T matrix, the *spatial sum* and *self sum*, converge really slowly. Therefore our main technique to speed up the computation is to reduce the computation time of T matrix.

2.6.6.1 Periodicity of T-Matrix

The core of the scattering matrix computing Algorithm 2 is to use the key equation Eq. (2.74) to get the scattered field for all $(4N + 2)$ incident lights. Since T matrix depends on the angle of incident light, we have to generate $(4N + 2)$ number of T matrices in principle. However, T matrix is periodic with respect to the x component of the incident wavevector, k_x^{inc} . We can easily see this from the spatial sum formula for the T matrix,

$$\sum_{n=-\infty}^{\infty} H_{cmso-cmob}^{(2)}(\Delta\rho_n) e^{j(cmso-cmob)\Delta\phi_n} \cdot e^{-jk_x^{inc} n \cdot period} \quad (2.107)$$

The part where the incident angle involves is $e^{-jk_x^{inc} n \cdot L}$. The formula will remain the same if k_x^{inc} changes by integer multiple of $\frac{2\pi}{L}$

$$e^{-j(k_x^{inc} + \frac{2\pi}{L} m)n \cdot L} = e^{-jk_x^{inc} n \cdot L}, \quad \text{where } m \text{ is integer} \quad (2.108)$$

So the T matrix is periodic with respect to k_x^{inc} we use. Therefore, we only have to compute the T matrix at the beginning and reuse it throughout the whole procedure of Algorithm 2.

2.6.6.2 Spectral Method

Now let us deal with the computation of spatial sums, which are slowly converging infinite summations. In practice, we have to add the entries up to some index where we think the series converges to a certain degree of accuracy. However, the spatial sum does not converge quickly and oscillates a lot as we add up the entries. One way to accelerate the convergence of this sum is to express the sum in a different way. Let us compare the left hand side of the cylinder wave to plane wave conversion formula Eq. (2.86) and the spatial sum.

$$\left\{ \begin{array}{l} \text{LHS of conversion formula} \\ \text{Spatial Sum} \end{array} \right. : \begin{array}{l} \sum_{n=-\infty}^{\infty} H_{cm}^{(2)}(k\Delta\rho_n) e^{j(cm)\Delta\phi_n} \cdot e^{-jk_x^{inc}n \cdot L} \\ \sum_{n=-\infty}^{\infty} H_{cmso-cmob}^{(2)}(k\Delta\rho_n) e^{j(cmso-cmob)\Delta\phi_n} \cdot e^{-jk_x^{inc}n \cdot L} \end{array} \quad (2.109)$$

They are basically the same. Applying the conversion formula to the spatial sum by setting $cm = cmso - cmob$, then

$$\begin{aligned} & \sum_{n=-\infty}^{\infty} H_{cmso-cmob}^{(2)}(k\Delta\rho_n) e^{j(cmso-cmob)\Delta\phi_n} \cdot e^{-jk_x^{inc}n \cdot L} \\ &= \sum_{n=-\infty}^{\infty} \text{sign}(\tilde{y})^{cmso-cmob} \cdot e^{-jk_{xn}\tilde{x}} \cdot e^{-jk_{yn}|\tilde{y}|} \cdot e^{-j(cmso-cmob)(\text{sign}(\tilde{y}) \cdot \arcsin(\frac{k_{xn}}{k}) - \pi)} \cdot \frac{2}{k_{yn} \cdot L} \end{aligned} \quad (2.110)$$

The right hand side of this equation is called *spectral sum*. The spectral sum can converge faster than the spatial sum for the following reason. The entries of the spectral sum start to become evanescent waves at $|n| > \lfloor \frac{L}{\lambda} \rfloor$, and if \tilde{y} is positive, the evanescent waves will decay to 0 quickly, thereby the sum will converge quickly after $|n|$ gets larger than $\lfloor \frac{L}{\lambda} \rfloor$. Note that we can not use the same thing for the self-sum because $\tilde{y} = 0$.

2.6.6.3 Shanks Transformation

Now let us deal with the computation of self sums, which can not be accelerated by spectral sum technique. There is a well-known extrapolation method called *Shanks Transformation*. This is basically a *transformation of the sequence of the sum of the series*. It changes the original sequence $A_n = \sum_{m=0}^n a_m$ into a different sequence and this transformed sequence converges quicker to the converged value than the original sequence. So we can apply this technique to the calculation of spatial sum.

Suppose we want to compute,

$$A = \sum_{m=0}^{\infty} a_m \quad (2.111)$$

The k -th order of Shanks Transformation at sequence index n , $B_{k,n}$, can be written by a *Hankel matrix*

$$B_{k,n} = \frac{\begin{vmatrix} A_{n-k} & \cdots & A_{n-1} & A_n \\ \Delta A_{n-k} & \cdots & \Delta A_{n-1} & \Delta A_n \\ \vdots & \ddots & \vdots & \vdots \\ \Delta A_{n-1} & \cdots & \Delta A_{n+k-2} & \Delta A_{n+k-1} \end{vmatrix}}{\begin{vmatrix} 1 & \cdots & 1 & 1 \\ \Delta A_{n-k} & \cdots & \Delta A_{n-1} & \Delta A_n \\ \vdots & \ddots & \vdots & \vdots \\ \Delta A_{n-1} & \cdots & \Delta A_{n+k-2} & \Delta A_{n+k-1} \end{vmatrix}} \quad (2.112)$$

where $A_n = \sum_{m=0}^n a_m$ and $\Delta A_n = A_{n+1} - A_n$.

Under appropriate conditions [29], $\lim_{n \rightarrow \infty} B_{k,n} = A$. Also the convergence of $B_{k,n}$ to A is more rapid than that of A_n . The higher order transformation requires more data and computation, but converges faster. The 1st order Shanks transformation formula is like below,

$$B_{1,n} = \frac{\begin{vmatrix} A_{n-1} & A_n \\ A_n - A_{n-1} & A_{n+1} - A_n \end{vmatrix}}{\begin{vmatrix} 1 & 1 \\ A_n - A_{n-1} & A_{n+1} - A_n \end{vmatrix}} = \frac{A_{n-1}A_{n+1} - A_n^2}{A_{n+1} + A_{n-1} - 2A_n} \quad (2.113)$$

Brief proof on its mechanism is the following.

Proof. We assume that this sum behaves like

$$A_n = A + \alpha q^n \text{ for sufficiently large } n \text{ and } \|q\| < 1$$

We have three unknowns, A , α and q . To solve this problem let us use the following three equations.

$$\begin{cases} A_{n-1} & = A + \alpha q^{n-1} \\ A_n & = A + \alpha q^n \\ A_{n+1} & = A + \alpha q^{n+1} \end{cases} \quad (2.114)$$

From the first equation, we get

$$\alpha = (A_{n-1} - A)q^{-n+1} \quad (2.115)$$

Plugging this into the two last equations, we get

$$\begin{cases} A_n &= A + (A_{n-1} - A)q \\ A_{n+1} &= A + (A_{n-1} - A)q^2 \end{cases} \quad (2.116)$$

$$q^2 = \left(\frac{A_n - A}{A_{n-1} - A} \right)^2 = \frac{A_{n+1} - A}{A_{n-1} - A} \quad (2.117)$$

$$(A_n - A)^2 = (A_{n+1} - A)(A_{n-1} - A) \quad (2.118)$$

$$A_n^2 - 2A_n A + A^2 = A_{n+1}A_{n-1} - A_{n+1}A - AA_{n-1} + A^2 \quad (2.119)$$

$$(A_{n+1} + A_{n-1} - 2A_n)A = A_{n+1}A_{n-1} - A_n^2 \quad (2.120)$$

$$\therefore A = \frac{A_{n+1}A_{n-1} - A_n^2}{A_{n+1} + A_{n-1} - 2A_n} \quad (2.121)$$

□

Shanks transformation generally holds for all converging series. However, the Shanks transformation is stable for oscillatory converging series but unstable for monotonically converging series [30]. Due to this fact, it is not a good idea to apply Shanks transformation to *spectral sum* because this series converges monotonically after its entries become evanescent modes.

Various ways of implementing Shanks transformations exist. We recommend the algorithm called *epsilon algorithm* with *cross-rule*. Detailed description on this algorithm, all the detailed analysis on Shanks transform and furthermore systematic analysis on the topic of *Extrapolation Methods* can be found in [29].

Let us briefly talk about the order of Shanks transformation. In general, the higher order transformation converges in a fewer index than the lower order transformation. So the higher order Shanks transformation can appear to be faster than the lower ones. However, as the order gets higher, the computational time for the transformation increases substantially. So increasing the transformation order blindly is not a good idea. Also, the result starts to be unstable as well. *Recursive* Shanks transformation can be use to avoid these problems but does not improve significantly.

In our simulation environment, the 3rd order Shanks transformation was the most stable and fast order. We checked whether the series has converged by checking the difference between the previous sequence and the current sequence. If the difference is smaller than a threshold, which we called *epsseries*, for *nrepeat* consecutive times, we declared convergence. Our optimal parameter setting is like below,

Optimal parameters for Shanks transformation	
<i>epsseries</i>	10^{-11}
<i>nrepeat</i>	5
Shanks Transformation Order for Spatial Sum	3
Shanks Transformation Order for Spectral Sum	none

Figure 2.32: Optimal parameter setting for Shanks transformation.

2.6.6.4 Quasi-symmetric structure of T matrix

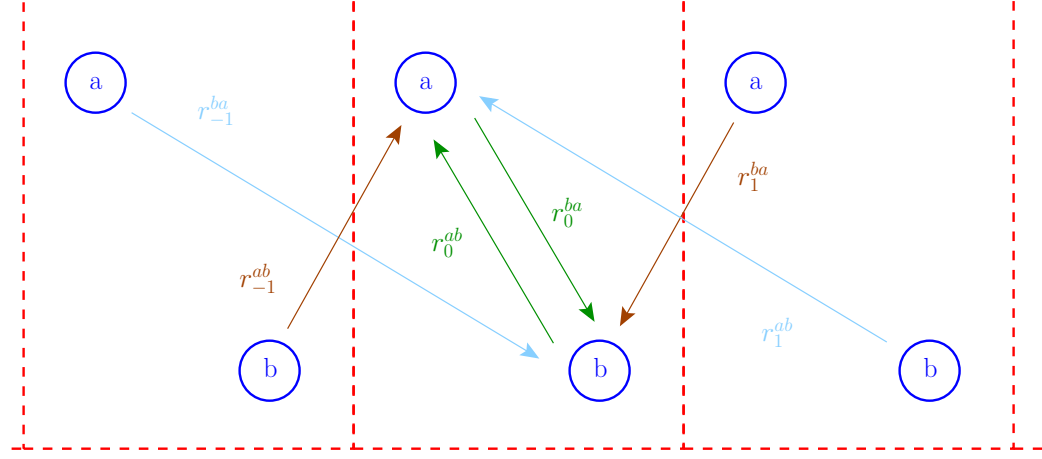
Another way to reduce the computation time of the T matrix is to exploit its structure. Recall the structure of the T matrix,

$$T = \begin{bmatrix} T_{11} & T_{12} & T_{13} & \cdots & T_{1N_{cy}} \\ T_{21} & T_{22} & T_{23} & \cdots & T_{2N_{cy}} \\ \vdots & \vdots & \vdots & \ddots & \vdots \\ T_{N_{cy}1} & T_{N_{cy}2} & T_{N_{cy}3} & \cdots & T_{N_{cy}N_{cy}} \end{bmatrix} \quad (2.122)$$

T_{ab} describes the effect on cylinder a from cylinder b . Entries in T_{ab} and T_{ba} are calculated by

$$\begin{cases} T_{ab} & : \sum_{n=-\infty}^{\infty} H_{cm}^{(2)}(k\Delta\rho_n^{ab}) e^{j(cm)\Delta\phi_n^{ab}} \cdot e^{-jk_x^{inc}n \cdot L} \\ T_{ba} & : \sum_{n=-\infty}^{\infty} H_{cm}^{(2)}(k\Delta\rho_n^{ba}) e^{j(cm)\Delta\phi_n^{ba}} \cdot e^{-jk_x^{inc}n \cdot L} \end{cases} \quad (2.123)$$

We can show that these two are related by the following argument.



$$r_n^{ab} = cloca - (clocb + n \cdot (L, 0))$$

$$\Delta\rho_n^{ab} = \|r_n^{ab}\|_2$$

$$\Delta\phi_n^{ab} = \arctan(r_n^{ab})$$

Figure 2.33: The geometrical relationships between the cylinders makes the T matrix have a quasi-symmetric structure.

From the Fig. 2.33, we can see that

$$\Delta\rho_n^{ab} = \Delta\rho_{-n}^{ba} \quad (2.124)$$

$$\Delta\phi_n^{ab} = \Delta\phi_{-n}^{ba} + \pi \quad (2.125)$$

Also, $e^{-jk_x^{inc} n \cdot period} = 1$ since $k_x^{inc} = \frac{2\pi}{L}n$ for constructing a scattering matrix. Combining everything together,

$$T_{ab} = \sum_{n=-\infty}^{\infty} H_{cm}^{(2)}(k\Delta\rho_n^{ab}) e^{j(cm)\Delta\phi_n^{ab}} \quad (2.126)$$

$$= \sum_{n=-\infty}^{\infty} H_{cm}^{(2)}(k\Delta\rho_{-n}^{ba}) e^{j(cm)(\Delta\phi_{-n}^{ba} + \pi)} \quad (2.127)$$

$$= e^{j(cm)\pi} \sum_{n=-\infty}^{\infty} H_{cm}^{(2)}(k\Delta\rho_n^{ba}) e^{j(cm)\Delta\phi_n^{ba}} \text{ (by changing the index)} \quad (2.128)$$

$$= e^{j(cm)\pi} T_{ba} \quad (2.129)$$

Therefore, after generating T_{ab} , we get T_{ba} as well by

$$T_{ab} = C .*^1 T_{ba}, \quad \text{where } \{C\}_{mn} = (-1)^{(m-n)} \quad (2.130)$$

¹.* is a matlab notation which means multiplying two matrices elementwise.

Thus, this will reduce the calculation time of T matrix about by the factor of 2.

One thing to be careful is that the quasi symmetric structure of T matrix is only true when we illuminate light with $k_{x_n}^{inc} = \frac{2\pi}{L}n$. We can not use this for calculating general periodic scattering situation where $k_{x_n}^{inc}$ can have an offset.

2.6.7 Computational Issue - Accuracy

2.6.7.1 Accuracy of the scattering matrix

We defined the following 5 metrics to check the accuracy of the scattering matrix,

$$\begin{aligned} DOU_1 &= \frac{\|S^H \cdot S\|_{\text{fro}}^2}{4N + 2} \\ DOU_2 &= \|S^H \cdot S^H - I\|_{\text{fro}} \\ DOR_1 &= \|S_{11}^T - F \cdot S_{11} \cdot F\|_{\text{fro}} \\ DOR_2 &= \|S_{22}^T - F \cdot S_{22} \cdot F\|_{\text{fro}} \\ DOR_3 &= \|S_{21}^T - F \cdot S_{12} \cdot F\|_{\text{fro}} \end{aligned}$$

where $\|\cdot\|_{\text{fro}}$ denotes the frobenius norm. DOU stands for the degree of unitariness and DOR stands for the degree of reciprocity.

The accuracy depends on how strictly we checked the convergence of the spatial sum and self sum in T matrix, and the level of strictness was controlled by *epsseries*. In our code, we have set *epsseries* = 10^{-11} and all the metrics listed above was being met to the order of 10^{-10} . This is accurate enough and making this more accurate by making *epsseries* smaller will result in prolonging the simulation time.

2.6.7.2 Accuracy on cascading

In order to have accurate cascading results, we need to include enough buffer at the boundary of the two neighboring systems or include enough amount of evanescent modes to consider all the interaction between the two neighboring systems.

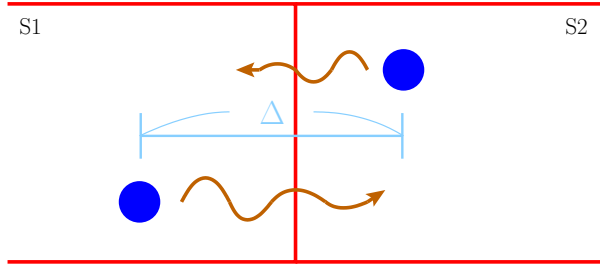


Figure 2.34: When cascading, including enough amount of modes or buffer is important to increase the accuracy of the result. All the modes that have significant activity at the first scatterer they encounter in the neighboring system must be included.

Let tol be the cascade error we want to guarantee and Δ be the distance between the two cylinder nearest to the boundary from the two neighboring systems. Then we can set a criterion for the modes that we have to include like below

$$e^{-\sqrt{\left(\frac{2\pi}{L}n\right)^2 - \left(\frac{2\pi}{\lambda}\right)^2} \Delta} \geq tol \quad (2.131)$$

$$-\sqrt{\left(\frac{2\pi}{L}n\right)^2 - \left(\frac{2\pi}{\lambda}\right)^2} \Delta \geq \ln(tol) \quad (2.132)$$

$$\left(\frac{2\pi}{L}n\right)^2 - \left(\frac{2\pi}{\lambda}\right)^2 \leq \left(\frac{\ln(tol)}{\Delta}\right)^2 \quad (2.133)$$

$$n \leq \frac{L}{2\pi} \sqrt{\left(\frac{\ln(tol)}{\Delta}\right)^2 + \left(\frac{2\pi}{\lambda}\right)^2} \quad (2.134)$$

Therefore, the highest order index to achieve the accuracy of tol will be like below,

$$N = \left\lfloor \frac{L}{2\pi} \sqrt{\left(\frac{\ln(tol)}{\Delta}\right)^2 + \left(\frac{2\pi}{\lambda}\right)^2} \right\rfloor \quad (2.135)$$

CHAPTER III

Transmission Maximization and Focusing of Light

Scattering hinders the passage of light through random media and consequently limits the usefulness of optical techniques for sensing and imaging. Thus, methods for increasing the transmission of light through such random media are of interest. Against this backdrop, recent theoretical and experimental advances have suggested the existence of a few highly transmitting eigen-wavefronts with transmission coefficients close to one in strongly backscattering random media.

In this chapter, we numerically analyze this phenomenon in 2-D with fully spectrally accurate simulators and provide rigorous numerical evidence confirming the existence of these highly transmitting eigen-wavefronts in random media with periodic boundary conditions that is composed of hundreds of thousands of non-absorbing scatterers.

We then develop physically realizable algorithms for increasing the transmission through such random media using backscatter analysis. We show via numerical simulations that the algorithms converge rapidly, yielding a near-optimum wavefront in just a few iterations. We also develop an algorithm that combines the knowledge of these highly transmitting eigen-wavefronts obtained from backscatter analysis, with intensity measurements at a point to produce a near-optimal focus with significantly fewer measurements than a method that does not utilize this information.

The chapter is organized as follows. We describe our setup in Section 3.1. We discuss the problem of transmission maximization and focusing in Section 3.2. To assist in the development of physically realizable algorithms for these applications, we identify physically realizable operations in Section 3.3, and describe iterative, implementable algorithms for finding transmission-maximizing and focusing inputs in Sections 3.4 and 3.5, respectively. We highlight the existence of the eigen-wavefronts with transmission coefficients approaching one, the algorithms' performance and rapid convergence via numerical simulations in Section 3.6, and my paper related to this chapter is [21].

3.1 Setup

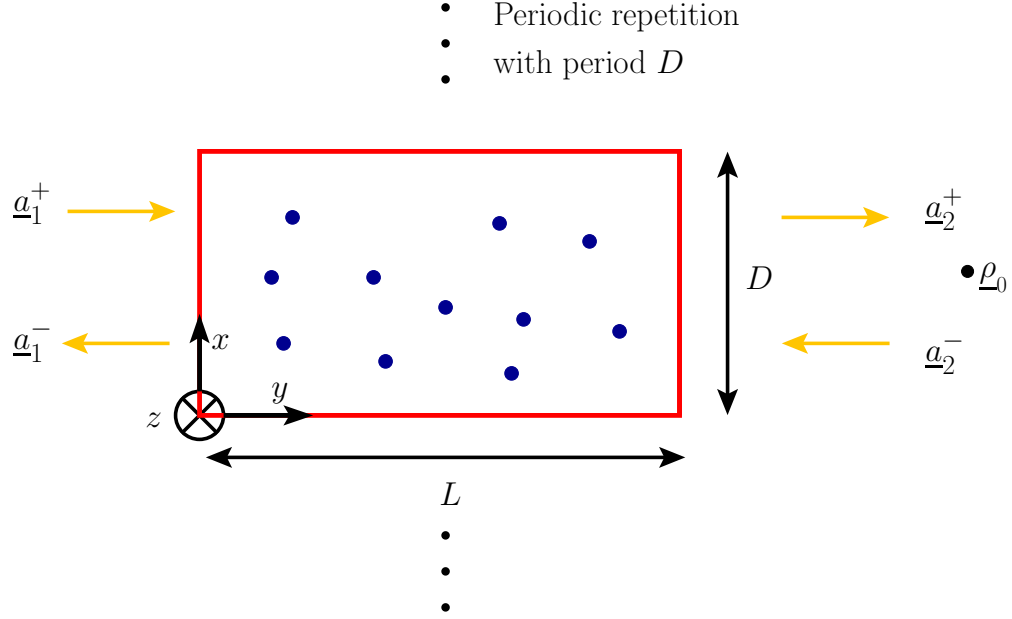


Figure 3.1: Geometry of the scattering system considered.

We study scattering from a two-dimensional (2D) random slab of thickness L and periodicity D ; the slab's unit cell occupies the space $0 \leq x < D$ and $0 \leq y < L$ (Fig. 3.1). The slab contains N_c infinite and z -invariant circular cylinders of radius r that are placed randomly within the cell and assumed either perfect electrically conducting (PEC) or dielectric with refractive index n_d ; care is taken to ensure the cylinders do not overlap. Fields are TM_z polarized: electric fields in the $y < 0$ ($i = 1$) and $y > L$ ($i = 2$) halfspaces are denoted $\underline{e}_i(\underline{\rho}) = e_i(\underline{\rho})\hat{z}$. The field (complex) amplitude $e_i(\underline{\rho})$ can be decomposed in terms of $+y$ and $-y$ propagating waves as $e_i(\underline{\rho}) = e_i^+(\underline{\rho}) + e_i^-(\underline{\rho})$, where

$$e_i^\pm(\underline{\rho}) = \sum_{n=-N}^N h_n a_{i,n}^\pm e^{-jk_n^\pm \cdot \underline{\rho}}. \quad (3.1)$$

In the above expression, $\underline{\rho} = x\hat{x} + y\hat{y} \equiv (x, y)$, $\underline{k}_n^\pm = k_{n,x}\hat{x} \pm k_{n,y}\hat{y} \equiv (k_{n,x}, \pm k_{n,y})$, $k_{n,x} = 2\pi n/D$, $k_{n,y} = 2\pi\sqrt{(1/\lambda)^2 - (n/D)^2}$, λ is the wavelength, and $h_n = \sqrt{\|\underline{k}_n^\pm\|_2/k_{n,y}}$ is a power-normalizing coefficient. We assume $N = \lfloor D/\lambda \rfloor$, i.e., we only model propagating waves and denote $M = 2N + 1$. The modal coefficients $a_{i,n}^\pm$, $i = 1, 2$; $n = -N, \dots, N$ are related by the scattering matrix

$$\begin{bmatrix} \underline{a}_1^- \\ \underline{a}_2^+ \end{bmatrix} = \underbrace{\begin{bmatrix} S_{11} & S_{12} \\ S_{21} & S_{22} \end{bmatrix}}_{=:S} \begin{bmatrix} \underline{a}_1^+ \\ \underline{a}_2^- \end{bmatrix}, \quad (3.2)$$

where $\underline{a}_i^\pm = [a_{i,-N}^\pm \ \dots \ a_{i,0}^\pm \ \dots \ a_{i,N}^\pm]^T$. In what follows, we assume that the slab is only excited from the $y < 0$ halfspace; hence, $\underline{a}_2^- = 0$. For a given incident field amplitude $e_1^+(\rho)$, we define transmission and reflection coefficients as

$$\tau(\underline{a}_1^+) := \frac{\|S_{21} \cdot \underline{a}_1^+\|_2^2}{\|\underline{a}_1^+\|_2^2}, \quad (3.3)$$

and

$$\Gamma(\underline{a}_1^+) := \frac{\|S_{11} \cdot \underline{a}_1^+\|_2^2}{\|\underline{a}_1^+\|_2^2}, \quad (3.4)$$

respectively. We denote the transmission coefficient of a normally incident wavefront by $\tau_{\text{normal}} = \tau([0 \ \dots \ 0 \ 1 \ 0 \ \dots \ 0]^T)$; here T denotes transposition.

3.2 Problem formulation

3.2.1 Transmission maximization

The problem of designing an incident wavefront $\underline{a}_{\text{opt}}$ that maximizes the transmitted power can be stated as

$$\underline{a}_{\text{opt}} = \arg \max_{\underline{a}_1^+} \tau(\underline{a}_1^+) = \arg \max_{\underline{a}_1^+} \frac{\|S_{21} \cdot \underline{a}_1^+\|_2^2}{\|\underline{a}_1^+\|_2^2} = \arg \max_{\|\underline{a}_1^+\|_2=1} \|S_{21} \cdot \underline{a}_1^+\|_2^2 \quad (3.5)$$

where $\|\underline{a}_1^+\|_2 = 1$ represents the incident power constraint.

Let $S_{21} = \sum_{i=1}^M \sigma_i \underline{u}_i \cdot \underline{v}_i^H$ denote the singular value decomposition (SVD) of S_{21} ; σ_i is the singular value associated with the left and right singular vectors \underline{u}_i and \underline{v}_i , respectively. By convention, the singular values are arranged so that $\sigma_1 \geq \dots \geq \sigma_M$ and H denotes complex conjugate transpose. A well-known result in matrix analysis [31] states that

$$\underline{a}_{\text{opt}} = \underline{v}_1. \quad (3.6)$$

When the optimal wavefront $\underline{a}_{\text{opt}}$ is excited, the optimal transmitted power is $\tau_{\text{opt}} := \tau(\underline{a}_{\text{opt}}) = \sigma_1^2$. When the wavefront associated with the i -th right singular vector \underline{v}_i is transmitted, the transmitted power is $\tau(\underline{v}_i) = \sigma_i^2$, which we refer to as the transmission coefficient of the i -th eigen-wavefront of S_{21} . Analogously, we refer to $\Gamma(\underline{v}_i)$ as the reflection coefficient of the i -th eigen-wavefront of S_{21} .

The theoretical distribution [3, 4, 5, 6, 7] of the transmission coefficients for lossless random media has density given by

$$f(\tau) = \lim_{M \rightarrow \infty} \frac{1}{M} \sum_{i=1}^M \delta(\tau - \tau(\underline{v}_i)) = \frac{l}{2L} \frac{1}{\tau \sqrt{1 - \tau}}, \quad \text{for } 4 \exp(-L/2l) \lesssim \tau \leq 1. \quad (3.7)$$

In Eq. (3.7), l is the mean-free path through the medium. Fig. 3.2 shows the theoretical density when $L/l = 3$. From, Eq. (3.7) we expect $\tau_{\text{opt}} = 1$.

From (3.6) it follows that the optimal wavefront can be constructed by measuring the S_{21} matrix and computing its SVD. Techniques for measuring the S_{21} matrix have been developed in recent works by Popoff et al. [9] and others [10, 11]. Kim et al. experimentally measured the S_{21} matrix and demonstrated improved transmission by using the optimal wavefront in Eq. (3.6) [12].

In the lossless setting, the scattering matrix S in Eq. (3.2) will be unitary, i.e., $S^H \cdot S = I$, where I is the identity matrix. Consequently, we have that $S_{11}^H \cdot S_{11} + S_{21}^H \cdot S_{21} = I$, and the optimization problem in Eq. (3.5) can be reformulated as

$$\underline{a}_{\text{opt}} = \arg \max_{\|\underline{a}_1^+\|_2=1} \underbrace{(\underline{a}_1^+)^H \cdot S_{21}^H \cdot S_{21} \cdot \underline{a}_1^+}_{=(\underline{a}_1^+)^H \cdot (I - S_{11}^H \cdot S_{11}) \cdot \underline{a}_1^+} = \arg \min_{\|\underline{a}_1^+\|_2=1} \|S_{11} \cdot \underline{a}_1^+\|_2^2 = \arg \min_{\underline{a}_1^+} \Gamma(\underline{a}_1^+). \quad (3.8)$$

In other words, in a lossless medium the backscatter-minimizing wavefront also maximizes transmission. Let $S_{11} = \sum_{i=1}^M \tilde{\sigma}_i \tilde{\underline{u}}_i \cdot \tilde{\underline{v}}_i^H$ denote the SVD of S_{11} ; $\tilde{\sigma}_i$ is the singular value associated with the left and right singular vectors $\tilde{\underline{u}}_i$ and $\tilde{\underline{v}}_i$, respectively. Then from [31] it follows that

$$\underline{a}_{\text{opt}} = \tilde{\underline{v}}_M. \quad (3.9)$$

When this optimal wavefront is excited and the medium is lossless, $\tau_{\text{opt}} = 1 - \Gamma(\underline{a}_{\text{opt}}) = 1 - \tilde{\sigma}_M^2 = \sigma_1^2$. When the wavefront associated with the i -th right singular vector $\tilde{\underline{v}}_i$ is excited, the transmitted power is given by $\tau(\tilde{\underline{v}}_i) = 1 - \Gamma(\tilde{\underline{v}}_i) = 1 - \tilde{\sigma}_i^2$, which we refer to as the transmission coefficient of the i -th eigen-wavefront of S_{11} . Analogously, we refer to $\Gamma(\tilde{\underline{v}}_i)$ as the reflection coefficient of the i -th eigen-wavefront of S_{11} .

A technique for increasing transmission via backscatter analysis would require measurement of the S_{11} matrix and the computation of $\underline{a}_{\text{opt}}$ as in Eq. (3.9). Our objective is to develop fast, physically realizable, iterative algorithms that converge to $\underline{a}_{\text{opt}}$ by utilizing significantly fewer backscatter field measurements than the $O(M)$ measurements it would take to first estimate S_{11} and then compute its SVD to determine $\tilde{\underline{v}}_M$. Here, we are motivated by applications where it is not possible to measure the transmitted field so that it will not be feasible to measure the S_{21} matrix and compute the optimal wavefront as in Eq. (3.6).

3.2.2 Focusing

From Eq. (3.1) and using the fact that that $\underline{a}_2^+ = S_{21} \cdot \underline{a}_1^+$ (since $\underline{a}_2^- = 0$), the field at point $\underline{\rho}_0$ is

$$\underline{e}_2^+(\underline{\rho}_0) = \underbrace{\begin{bmatrix} h_{-N} e^{-j\mathbf{k}_{-N}^+ \cdot \underline{\rho}_0} & \dots & h_N e^{-j\mathbf{k}_N^+ \cdot \underline{\rho}_0} \end{bmatrix}}_{=: \underline{f}(\underline{\rho}_0)^H} \cdot S_{21} \cdot \underline{a}_1^+. \quad (3.10)$$

The problem of designing an incident wavefront that maximizes the intensity (or amplitude squared) of the field at $\underline{\rho}_0$ is equivalent to the problem

$$\underline{a}_{\text{foc}} = \arg \max_{\underline{a}_1^+} \frac{\|\underline{e}_2^+(\underline{\rho}_0)\|_2^2}{\|\underline{a}_1^+\|_2^2} = \arg \max_{\|\underline{a}_1^+\|_2=1} \|\underbrace{\underline{f}^H(\underline{\rho}_0) \cdot S_{21} \cdot \underline{a}_1^+}_{=: \underline{c}(\underline{\rho}_0)^H}\|_2^2, \quad (3.11)$$

whose solution is

$$\underline{a}_{\text{foc}} = \frac{\underline{c}(\underline{\rho}_0)}{\|\underline{c}(\underline{\rho}_0)\|_2} = \frac{S_{21}^H \cdot \underline{f}(\underline{\rho}_0)}{\|S_{21}^H \cdot \underline{f}(\underline{\rho}_0)\|_2}. \quad (3.12)$$

Thus the optimal wavefront equals the vector $\underline{c}(\underline{\rho}_0)$ with normalization to satisfy the power constraint. It can be shown that this wavefront may be obtained by time-reversing the wavefront received by placing a source at $\underline{\rho}_0$ [32]. This fact was exploited in recent work by Cui and collaborators [33, 34].

In Vellekoop and Mosk’s breakthrough work [8, 1, 35], a coordinate descent method was employed for constructing the optimal wavefront. The coordinate descent approach finds the amplitude and phase of a single mode that maximize the intensity at $\underline{\rho}_0$ while keeping the amplitudes and phases of the other modes fixed and then repeating this procedure for the remaining modes, one mode at a time. In Vellekoop and Mosk’s experiments [8, 1, 35], they kept the amplitude constant for all the modes and considered phase-only modifications of the incident wavefront. While this reduces the complexity of the algorithm, this approach still requires $O(M)$ intensity measurements at $\underline{\rho}_0$ to construct the optimal wavefront. When M is large, the time for convergence will also be large.

This has motivated recent work [15, 16, 17] for faster determination of the optimal wavefront. Cui [15, 16] considers an approach using multiple frequencies to find the optimal phases of modes simultaneously, while Stockbridge et al. [17] have proposed a coordinate descent approach using 2D Walsh functions as a basis set. These methods have accelerated the experimental convergence, but the reported results are still for small M (between 441 and 1024).

Expressing the optimal wavefront in terms of the singular vectors of S_{21} yields the expression

$$\underline{a}_{\text{foc}} \propto S_{21}^H \cdot \underline{f}(\underline{\rho}_0) = \sum_{i=1}^M \sigma_i \underbrace{(\underline{u}_i^H \cdot \underline{f}(\underline{\rho}_0))}_{=: w_i} \underline{v}_i = \sum_{i=1}^M \sigma_i w_i \underline{v}_i. \quad (3.13)$$

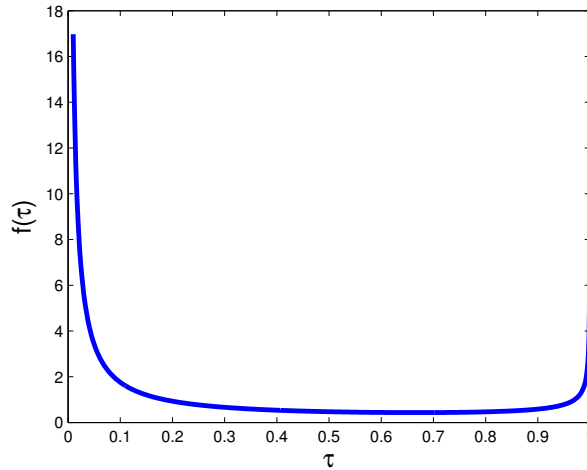


Figure 3.2: Theoretical distribution in (3.7) for $L/l = 3$.

Recall that $\sigma_i^2 = \tau(\underline{v}_i)$; thus an important insight from Eq. (3.7) and Fig. 3.2 is that most of the singular values in Eq. (3.13) are close to zero. However, there typically are $K \ll M$ singular values close to one. It is the superposition of these K eigen-wavefronts of S_{21} having transmission coefficients close to one whose constructive interference yields the maximal transmission that contributes to maximal intensity.

In the lossless setting, when the scattering matrix S is unitary, we have that $\tau(\underline{v}_i) = 1 - \Gamma(\tilde{\underline{v}}_{M-i+1})$. Hence, the K eigen-wavefronts of S_{21} that have transmission coefficients close to one correspond precisely to the K eigen-wavefronts associated with S_{11} that have reflection coefficients close to zero. By using $O(K)$ backscatter field measurements to measure the K eigen-wavefronts of S_{11} with small reflection coefficients and $O(K)$ intensity measurements at $\underline{\rho}_0$, we might expect to approximate $\underline{a}_{\text{foc}}$ in Eq. (3.13) and yield a near-optimal focus using just $O(K)$ measurements (we expect $K \ll M$).

Our objective is to develop a fast, physically realizable, iterative algorithm that utilizes backscatter field measurements and intensity measurements at $\underline{\rho}_0$ to construct a near-optimal focusing wavefront using significantly fewer measurements than are required by coordinate descent methods that only employ intensity measurements at $\underline{\rho}_0$. The emphasis here is on accelerating the convergence behavior; we do not improve the quality of the focus.

3.3 Recognizing physically realizable matrix-vector operations

The iterative algorithms we will develop in Sections 3.4 and 3.5 build on the vast literature of iterative methods in numerical linear algebra [36, 37]. The algorithms are based on three matrix-vector operations, $S_{11} \cdot \underline{a}_1^+$, $F \cdot (\underline{a}_1^-)^*$, and $S_{11}^H \cdot \underline{a}_1^-$. These operations can be performed mathematically, but the measurement corresponding to these operations in a physical setting is not obvious. Here, we dwell on mapping these matrix-vector operations into their physical counterparts, thus making our algorithms physically realizable.

The first operation, $S_{11} \cdot \underline{a}_1^+$, can be realized by measuring the backscattered wave. In an experimental setting, the modal coefficient vector of the backscattered wave would be extracted from the backscatter intensity measurement by digital holography techniques described in, for example [38]. We also assume that it is possible to modulate the amplitude and phase of a wavefront, using the methods described in [20]. Thus, the matrix-vector multiplicative operation $S_{11} \cdot \underline{a}_1^+$ corresponds to sending an incident wavefront with modal coefficient vector \underline{a}_1^+ and measuring the modal coefficient vector of the backscattered wavefront. Furthermore, we assume that these modal coefficient vectors can be recovered perfectly, and the amplitude and the phase can be perfectly modulated, so that we might investigate the best-case performance of the algorithms.

The second operation, $F \cdot (\underline{a}_1^-)^*$, can be realized by time-reversing the wave. Let $\text{flipud}(\cdot)$ represent the operation of flipping a vector or a matrix argument upside

down so that the first row becomes the last row and so on, and let $*$ denote complex conjugation. We define $F = \text{flipud}(I)$, where I is the identity matrix; then the operation $F \cdot (\underline{a}_1^-)^*$ represents time-reversing the wave corresponding to \underline{a}_1^- . This can be explained as follows. The expression for time-reversed wave of \underline{a}_1^- is

$$\begin{aligned} (e_1^-(\underline{\rho}))^* &= \left(\sum_{n=-N}^N h_n a_{1,n}^- e^{-j\mathbf{k}_n^- \cdot \underline{\rho}} \right)^* = \sum_{n=-N}^N h_n^* (a_{1,n}^-)^* e^{j\mathbf{k}_n^- \cdot \underline{\rho}} \\ &= \sum_{n=-N}^N h_n (a_{1,-n}^-)^* e^{-j\mathbf{k}_n^+ \cdot \underline{\rho}}. \end{aligned} \quad (3.14)$$

Note that we have used the fact that $h_{-n}^* = h_n$ and $\mathbf{k}_{-n}^- = -\mathbf{k}_n^+$. From Eq. (3.14), we see that the modal coefficient vector representation of the time-reversed wave of \underline{a}_1^- is $\left[(a_N^-)^* \ (a_{N-1}^-)^* \ \dots \ (a_{-N+1}^-)^* \ (a_{-N}^-)^* \right]^T = F \cdot (\underline{a}_1^-)^*$. Furthermore, we emphasize that the operation $F \cdot (\underline{a}_1^-)^*$ can be physically realized via phase-conjugate mirroring (PCM) [32].

The third operation, $S_{11}^H \cdot \underline{a}_1^-$, can be realized by using reciprocity. In a scattering medium that exhibits reciprocity, there are relationships [39, 26, 40, 41, 42] between the incident and scattered wavefronts. Consequently, reciprocity requires the reflection matrix S_{11} to satisfy

$$S_{11}^H = F \cdot S_{11}^* \cdot F, \quad (3.15)$$

which is proven in subsection 2.4.3. This means that if \underline{a} is an input to the system that produces a backscattered wave of \underline{b} , then sending $F \cdot (\underline{a})^*$ will produce backscattered wave of $F \cdot (\underline{b})^*$ in a medium whose reflection matrix corresponds to S_{11}^H . (Fig. 3.3)



Figure 3.3: The relationship between wavefronts in a medium that exhibits reciprocity. Reciprocity tells us that $S_{11}^H \cdot \underline{a}$ is obtained by time-reversing the wave *before and after* sending \underline{a} into the medium, and we call this sequence of operations *double phase conjugation*.

An important implication of this equation is that the matrix-vector operation $S_{11}^H \cdot \underline{a}_1^-$ can be cast in terms of physically realizable operations. Note that $S_{11}^H \cdot \underline{a}_1^-$ can be expressed as

$$S_{11}^H \cdot \underline{a}_1^- = F \cdot S_{11}^* \cdot F \cdot \underline{a}_1^- = F \cdot (S_{11} \cdot (F \cdot (\underline{a}_1^-)^*))^*.$$

From the last expression, we see that the operation $S_{11}^H \cdot \underline{a}_1^-$ can be physically realized in a sequence of two steps:

1. Time-reverse the wavefront whose modal coefficient vector is \underline{a}_1^- , and send it to the scattering system.
2. Time-reverse the resulting backscattered wavefront.

We call this sequence of operations as *double phase conjugation*, and we shall leverage it extensively in what follows.

3.4 Iterative, physically realizable algorithms for transmission maximization

We now develop iterative, physically realizable algorithms for transmission maximization that converge to $\underline{a}_{\text{opt}}$ in Eq. (3.9), by utilizing significantly fewer backscatter field measurements than the $O(M)$ measurements it would take to first estimate S_{11} and then compute its SVD to determine $\tilde{\underline{v}}_M$.

3.4.1 Steepest descent method

The backscatter minimization problem involves optimization with respect to the objective function $\|S_{11} \cdot \underline{a}_1^+\|_2^2$ that appears on the right hand side of Eq. (3.8). The objective function's negative gradient is used as a search direction to correct the previous input as

$$\underline{a}_{1,(k+1)}^+ = \underline{a}_{1,(k)}^+ - \mu \left. \frac{\partial \|S_{11} \cdot \underline{a}_1^+\|_2^2}{\partial \underline{a}_1^+} \right|_{\underline{a}_1^+ = \underline{a}_{1,(k)}^+} = \underline{a}_{1,(k)}^+ - 2\mu S_{11}^H \cdot S_{11} \cdot \underline{a}_{1,(k)}^+,$$

where $\underline{a}_{1,(k)}^+$ represents the modal coefficient vector of the wavefront produced at the k -th iteration of the algorithm and μ is a positive stepsize. This yields Algorithm 3 which iteratively refines the wavefront $\underline{a}_{1,(k+1)}^+$ until the backscattered intensity $\|S_{11} \cdot \underline{a}_{1,(k)}^+\|_2^2$ drops below a preset threshold ϵ , and we call this steepest descent method.

Algorithm 3 Steepest descent algorithm for finding $\underline{a}_{\text{opt}}$

- 1: Input: $\underline{a}_{1,(0)}^+$ = Initial random vector with unit norm
 - 2: Input: $\mu > 0$ = step size
 - 3: Input: ϵ = Termination condition
 - 4: $k = 0$
 - 5: **while** $\|S_{11} \cdot \underline{a}_{1,(k)}^+\|_2^2 > \epsilon$ **do**
 - 6: $\tilde{\underline{a}}_{1,(k)}^+ = \underline{a}_{1,(k)}^+ - 2\mu S_{11}^H \cdot S_{11} \cdot \underline{a}_{1,(k)}^+$
 - 7: $\underline{a}_{1,(k+1)}^+ = \tilde{\underline{a}}_{1,(k)}^+ / \|\tilde{\underline{a}}_{1,(k)}^+\|_2$
 - 8: $k = k + 1$
 - 9: **end while**
-

This is also called as gradient projection method in the iterative methods literature because the method projects the iterated solution onto the l_2 ball after the update at each iteration.

By viewing Algorithm 3 as a variant of the *power method*, we obtain the following characterization of its rate of convergence.

Theorem 4. Let S_{11} be a $M \times M$ reflection matrix and the reflection coefficients of the scattering system, $\tilde{\sigma}_1^2 \geq \tilde{\sigma}_2^2 \geq \dots \geq \tilde{\sigma}_{M-1}^2 > \tilde{\sigma}_M^2$, be the eigenvalues of $S_{11}^H \cdot S_{11}$. Then if $\underline{a}_{\text{opt}}^H \cdot \underline{a}_{1,(0)}^+ \neq 0$,

$$\|\underline{a}_{1,(k)}^+ - \underline{a}_{\text{opt}}\|_2 = \begin{cases} O(|\frac{1-2\mu\tilde{\sigma}_{M-1}^2}{1-2\mu\tilde{\sigma}_M^2}|^k), & 0 < \mu \leq \frac{1}{\tilde{\sigma}_1^2 + \tilde{\sigma}_{M-1}^2} \\ O(|\frac{-1+2\mu\tilde{\sigma}_1^2}{1-2\mu\tilde{\sigma}_M^2}|^k), & \frac{1}{\tilde{\sigma}_1^2 + \tilde{\sigma}_{M-1}^2} \leq \mu < \frac{1}{\tilde{\sigma}_1^2 + \tilde{\sigma}_M^2} \end{cases}$$

as $k \rightarrow \infty$. Optimal convergence rate is $O(|\frac{\tilde{\sigma}_1^2 - \tilde{\sigma}_{M-1}^2}{\tilde{\sigma}_1^2 + \tilde{\sigma}_{M-1}^2 - 2\tilde{\sigma}_M^2}|^k)$ when $\mu = \mu_{\text{opt}} = \frac{1}{\tilde{\sigma}_1^2 + \tilde{\sigma}_{M-1}^2}$.

Note that the gap between the smallest two reflection coefficients $|\tilde{\sigma}_{M-1}^2 - \tilde{\sigma}_M^2|$ is a crucial quantity to guarantee numerical stability and a fast convergence rate.

Proof. Algorithm 3 mainly performs

$$\underline{a}_{1,(k)}^+ = \frac{1}{c_k} (I - 2\mu S_{11}^H \cdot S_{11})^k \cdot \underline{a}_{1,(0)}^+,$$

where c_k is the normalization coefficient at the k -th iteration. From this perspective the algorithm can be viewed as *power method* which is an algorithm that finds the eigenvector of the matrix whose corresponding eigenvalue has the largest magnitude. The eigenvalue decomposition of the matrix $S_{11}^H \cdot S_{11}$ can be written as $S_{11}^H \cdot S_{11} = V \cdot R \cdot V^H$, where $V = [\underline{v}_1, \underline{v}_2, \dots, \underline{v}_M]$ and $R = \text{diag}(\tilde{\sigma}_1^2, \tilde{\sigma}_2^2, \dots, \tilde{\sigma}_M^2)$ such that $\tilde{\sigma}_1^2 \geq \tilde{\sigma}_2^2 \geq \dots > \tilde{\sigma}_M^2$. (Note that $\underline{a}_{\text{opt}} = \underline{v}_M$.) Then the previous equation becomes

$$\begin{aligned} \underline{a}_{1,(k)}^+ &= \frac{1}{c_k} V \cdot (I - 2\mu R)^k \cdot V^H \cdot \underline{a}_{1,(0)}^+ \\ &= \frac{1}{c_k} \sum_{i=1}^M \tilde{a}_i \lambda_i^k \underline{v}_i \end{aligned}$$

where $\tilde{a}_i = \underline{v}_i^H \cdot \underline{a}_{1,(0)}^+$, $\lambda_i = (1 - 2\mu\tilde{\sigma}_i^2)$ and $c_k^2 = \sum_{i=1}^M |\tilde{a}_i|^2 \lambda_i^{2k}$.

To guarantee the convergence of $\underline{a}_{1,(k)}^+ \rightarrow \underline{a}_{\text{opt}}$, the following condition must hold

$$\max_i |\lambda_i| = |\lambda_M| \quad (3.16)$$

so that

$$\begin{aligned} \underline{a}_{1,(k)}^+ &= \frac{|\lambda_M|^k}{c_k} (\tilde{a}_M \frac{\lambda_M^k}{|\lambda_M|^k} \underline{v}_M + \sum_{i=1}^{M-1} \tilde{a}_i \frac{\lambda_i^k}{|\lambda_M|^k} \underline{v}_i) \\ &\simeq \frac{\tilde{a}_M \lambda_M^k}{c_k} \underline{v}_M \quad (\text{for large } k) \end{aligned} \quad (3.17)$$

$\lambda(r) = |1 - 2\mu r|$ is symmetric and minimal at $r = \frac{1}{2\mu}$. So if the minimum point $r = \frac{1}{2\mu}$ is larger than $\frac{\tilde{\sigma}_1^2 + \tilde{\sigma}_M^2}{2}$, then the condition (3.16) will be satisfied. The condition can be simplified as below

$$\mu < \frac{1}{\tilde{\sigma}_1^2 + \tilde{\sigma}_M^2}$$

Convergence rate of $\|\underline{a}_{1,(k)}^+ - \underline{a}_{\text{opt}}\|_2$ depends on how fast the second largest component decays in (3.17),

$$\|\underline{a}_{1,(k)}^+ - \frac{\tilde{a}_M \lambda_M^k}{c_k} \underline{v}_M\|_2 = O\left(\frac{\tilde{a}_M \lambda_M^k}{c_k} \left| \frac{\max\{|\lambda_1|, |\lambda_{M-1}|\}}{|\lambda_M|} \right|^k\right).$$

Note that the function $\max\{|\lambda_1|, |\lambda_{M-1}|\}$ behaves like below in the interval $0 < \mu < \frac{1}{\tilde{\sigma}_1^2 + \tilde{\sigma}_M^2}$,

$$\max\{|\lambda_1|, |\lambda_{M-1}|\} = \begin{cases} \lambda_{M-1}, & 0 < \mu \leq \frac{1}{\tilde{\sigma}_1^2 + \tilde{\sigma}_{M-1}^2} \\ -\lambda_1, & \frac{1}{\tilde{\sigma}_1^2 + \tilde{\sigma}_{M-1}^2} \leq \mu < \frac{1}{\tilde{\sigma}_1^2 + \tilde{\sigma}_M^2} \end{cases}$$

Depending on the choice of μ , the convergence rate will be like below as $k \rightarrow \infty$,

$$\|\underline{a}_{1,(k)}^+ - \underline{v}_M\|_2 = \begin{cases} O\left(\frac{|\lambda_{M-1}|^k}{\lambda_M}\right), & 0 < \mu \leq \frac{1}{\tilde{\sigma}_1^2 + \tilde{\sigma}_{M-1}^2} \\ O\left(\frac{|\lambda_1|^k}{\lambda_M}\right), & \frac{1}{\tilde{\sigma}_1^2 + \tilde{\sigma}_{M-1}^2} \leq \mu < \frac{1}{\tilde{\sigma}_1^2 + \tilde{\sigma}_M^2} \end{cases}$$

The optimal convergence rate is achieved when $\mu = \mu_{\text{opt}} = \frac{1}{\tilde{\sigma}_1^2 + \tilde{\sigma}_{M-1}^2}$ and it is $O\left(\left|\frac{\tilde{\sigma}_1^2 - \tilde{\sigma}_{M-1}^2}{\tilde{\sigma}_1^2 + \tilde{\sigma}_{M-1}^2 - 2\tilde{\sigma}_M^2}\right|^k\right)$.

Furthermore, let us discuss about the convergence of the reflected power. The reflected power at the k -th iteration $\tilde{\sigma}_{(k)}^2$ is

$$\tilde{\sigma}_{(k)}^2 = \|\mathcal{S}_{11} \cdot \underline{a}_{1,(k)}^+\|_2^2 = \frac{1}{c_k^2} \sum_{i=1}^M \tilde{\sigma}_i^2 \lambda_i^{2k} |\tilde{a}_i|^2$$

Using the same argument as we did for $\underline{a}_{1,(k)}^+$, convergence rate of $|\tilde{\sigma}_{(k)}^2 - \tilde{\sigma}_M^2|$ becomes,

$$|\tilde{\sigma}_{(k)}^2 - \frac{|\tilde{a}_M|^2 \lambda_M^{2k}}{c_k^2} \tilde{\sigma}_M^2| = O\left(\frac{|\tilde{a}_M|^2 \lambda_M^{2k}}{c_k^2} \left| \frac{\max\{|\lambda_1|, |\lambda_{M-1}|\}}{|\lambda_M|} \right|^{2k}\right).$$

So depending on the choice of μ , the convergence rate will be like below,

$$|\tilde{\sigma}_{(k)}^2 - \tilde{\sigma}_M^2|_2 = \begin{cases} O\left(\left|\frac{1-2\mu\tilde{\sigma}_{M-1}^2}{1-2\mu\tilde{\sigma}_M^2}\right|^{2k}\right), & 0 < \mu \leq \frac{1}{\tilde{\sigma}_1^2 + \tilde{\sigma}_{M-1}^2} \\ O\left(\left|\frac{-1+2\mu\tilde{\sigma}_1^2}{1-2\mu\tilde{\sigma}_M^2}\right|^{2k}\right), & \frac{1}{\tilde{\sigma}_1^2 + \tilde{\sigma}_{M-1}^2} \leq \mu < \frac{1}{\tilde{\sigma}_1^2 + \tilde{\sigma}_M^2} \end{cases}$$

as $k \rightarrow \infty$. Optimal convergence rate is $O\left(\left|\frac{\tilde{\sigma}_1^2 - \tilde{\sigma}_{M-1}^2}{\tilde{\sigma}_1^2 + \tilde{\sigma}_{M-1}^2 - 2\tilde{\sigma}_M^2}\right|^{2k}\right)$ when $\mu = \mu_{\text{opt}} = \frac{1}{\tilde{\sigma}_1^2 + \tilde{\sigma}_{M-1}^2}$. \square

Armed with the relationship in Eq. (3.15), step 6 in Algorithm 3 can be expressed as

$$\tilde{\underline{a}}_{1,(k)}^+ = \underline{a}_{1,(k)}^+ - 2\mu S_{11}^H \cdot S_{11} \cdot \underline{a}_{1,(k)}^+ = \underline{a}_{1,(k)}^+ - 2\mu F \cdot S_{11}^* \cdot F \cdot S_{11} \cdot \underline{a}_{1,(k)}^+. \quad (3.18)$$

This allows us to recast each step of Algorithms 3 into the counterparts of the physical operations in the second column of Table 3.1.

Vector Operation	Physical Operation
1 : $\underline{a}_1^- = S_{11} \cdot \underline{a}_{1,(k)}^+$	1 : $\underline{a}_{1,(k)}^+ \xrightarrow{\text{Backscatter}} \underline{a}_1^-$
2 : $\underline{a}_1^+ = F \cdot (\underline{a}_1^-)^*$	2 : $\underline{a}_1^- \xrightarrow{\text{PCM}} \underline{a}_1^+$
3 : $\underline{a}_1^- = S_{11} \cdot \underline{a}_1^+$	3 : $\underline{a}_1^+ \xrightarrow{\text{Backscatter}} \underline{a}_1^-$
4 : $\underline{a}_1^+ = F \cdot (\underline{a}_1^-)^*$	4 : $\underline{a}_1^- \xrightarrow{\text{PCM}} \underline{a}_1^+$
5 : $\tilde{\underline{a}}_1^+ = \underline{a}_{1,(k)}^+ - 2\mu \underline{a}_1^+$	5 : $\tilde{\underline{a}}_1^+ = \underline{a}_{1,(k)}^+ - 2\mu \underline{a}_1^+$
6 : $\underline{a}_{1,(k+1)}^+ = \tilde{\underline{a}}_1^+ / \ \tilde{\underline{a}}_1^+\ _2$	6 : $\tilde{\underline{a}}_1^+ \xrightarrow{\text{Normalization}} \underline{a}_{1,(k+1)}^+$

Table 3.1: Steepest descent algorithm for transmission maximization. The first column represents vector operations in Algorithm 3. The second column represents the physical (or experimental) counterpart. The operation $\underline{a}_1^- \mapsto F \cdot (\underline{a}_1^-)^*$ can be realized via the use of a phase-conjugating mirror (PCM). The algorithm terminates when the backscatter intensity falls below a preset threshold ϵ .

The sequence of steps 1 – 4 in Table 3, which involves *double phase conjugation*, amplifies the highly-backscattering component in the wavefront, analogous to the operations for time-reversal focusing [43, 44, 32, 45]. In step 5, this component is subtracted leading to a refined wavefront that will backscatter less. This process is repeated till convergence. A consequence of this technique is that the backscatter field intensity will typically decrease monotonically. This makes the measurement of the backscatter modal coefficient vector increasingly difficult as the iteration progresses. An additional disadvantage of this method is the obvious need to carefully set μ to guarantee convergence, $0 < \mu < \frac{1}{\sigma_1^2 + \sigma_M^2} \approx 1$. In an experimental setting, the step size μ is chosen by a simple line search, i.e., by scanning a set of discretized values and selecting the one that results in the smallest backscatter intensity after a fixed number of iterations.

We describe a method next, which maintains high backscatter field intensity throughout the process and does not require selection of any other auxiliary parameters to guarantee convergence.

3.4.2 Conjugate gradient method

Consider an iterative solution to Eq. (3.8) where the iterate (before normalization for power) is formed as

$$\underline{a}_{1,(k+1)}^+ = \underline{a}_{1,(k)}^+ + \mu^{(k+1)} \underline{d}_{(k)}, \quad (3.19)$$

where $\mu^{(k+1)}$ is a stepsize and $\underline{d}_{(k)}$ is the search direction. In this framework, Algorithm 3 results from setting $\mu^{(k+1)} = \mu$ and $\underline{d}_{(k)} = -2S_{11}^H \cdot S_{11} \cdot \underline{a}_{1,(k)}^+$.

The conjugate gradients method (see [36, Chapter 5] for a detailed derivation) results from choosing the stepsize

$$\mu^{(k+1)} = \|\underline{r}_{(k)}\|_2^2 / \|S_{11} \cdot \underline{d}_{(k)}\|_2^2, \quad (3.20a)$$

with the search direction given by

$$\underline{d}_{(k+1)} = \underline{r}_{(k+1)} + \beta^{(k+1)} \underline{d}_{(k)}, \quad (3.20b)$$

and

$$\beta^{(k+1)} = \|\underline{r}_{(k+1)}\|_2^2 / \|\underline{r}_{(k)}\|_2^2. \quad (3.20c)$$

Here, the residual vector is

$$\underline{r}_{(k+1)} = -S_{11}^H \cdot S_{11} \cdot \underline{a}_{1,(k+1)}^+. \quad (3.20d)$$

The iteration terminates when $\|\underline{r}_{(k+1)}\|_2 < \epsilon$, a preset threshold.

Plugging Eq. (3.19) into Eq. (3.20d) and substituting the expressions in Eqs.(3.20a) - (3.20c) gives us an alternate expression for the residual vector

$$\underline{r}_{(k+1)} = \underline{r}_{(k)} - \mu^{(k+1)} S_{11}^H \cdot S_{11} \cdot \underline{d}_{(k)}, \quad (3.21a)$$

or, equivalently

$$\underline{r}_{(k+1)} = \underline{r}_{(k)} - \frac{\|\underline{r}_{(k)}\|_2^2}{\|S_{11} \cdot \underline{d}_{(k)}\|_2^2} S_{11}^H \cdot S_{11} \cdot \underline{d}_{(k)}. \quad (3.21b)$$

The utility of Eq. (3.21b) will become apparent shortly. The convergence rate of conjugate gradient algorithm can be written as follows.

Theorem 5. Let S_{11} be a $M \times M$ reflection matrix and the reflection coefficients of the scattering system, $\tilde{\sigma}_1^2 \geq \tilde{\sigma}_2^2 \geq \dots \geq \tilde{\sigma}_{M-1}^2 \geq \tilde{\sigma}_M^2$, be the eigenvalues of $S_{11}^H \cdot S_{11}$. Then if we have highly-scattering systems where most of the reflection coefficients are clustered near one,

$$\|\underline{a}_{1,(k)}^+ - \underline{a}_{\text{opt}}\|_2 = O \left(\left| \frac{\sqrt{\tilde{\sigma}_1^2} - \sqrt{\tilde{\sigma}_{M-1}^2}}{\sqrt{\tilde{\sigma}_1^2} + \sqrt{\tilde{\sigma}_{M-1}^2}} \right|^k \right)$$

at the initial stage of the iteration.

Proof. The Krylov subspace algorithm minimizes the residual error at each iteration by finding the optimal direction with the optimal stepsize. The residual at each iteration can be written as follows,

$$\begin{aligned}
& \min_{\underline{a}_{1,(k)}^+} \|\tilde{\sigma}_M^2 \underline{a}_{\text{opt}} - S_{11}^H \cdot S_{11} \cdot \underline{a}_{1,(k)}^+\|_2 \\
&= \min_{p_k} \|p_k(S_{11}^H \cdot S_{11}) \cdot \underline{a}_{1,(0)}^+\|_2 \\
&\leq \min_{p_k} \|p_k(S_{11}^H \cdot S_{11})\|_2 \|\underline{a}_{1,(0)}^+\|_2 \\
&\leq \min_{p_k} \max_{\tilde{\sigma}_i^2} |p_k(\tilde{\sigma}_i^2)| \tag{3.22}
\end{aligned}$$

where p_k is a polynomial of order less or equal to k with $p_k(0) = 1$ and at the end we used the fact that $\|\underline{a}_{1,(k)}^+\|_2 = 1$. This tells us that Krylov subspace algorithm seeks the polynomial whose maximum height is minimum on the spectrum of $S_{11}^H \cdot S_{11}$. From this point of view, we can get a tight bound for the residual error by using variation of Chebyshev polynomial which has minimum $\|\cdot\|_\infty$ norm on the spectrum. Assuming that most of the reflection coefficients are concentrated near one and we have few near zero (highly-scattering system assumption), we set p_k as below,

$$p_k(z) = (1 - z/\tilde{\sigma}_M^2) \frac{T_{k-1}((\frac{\tilde{\sigma}_1^2 + \tilde{\sigma}_M^2}{2} - z)/(\frac{\tilde{\sigma}_1^2 - \tilde{\sigma}_M^2}{2}))}{T_{k-1}(\frac{\tilde{\sigma}_1^2 + \tilde{\sigma}_M^2}{\tilde{\sigma}_1^2 - \tilde{\sigma}_M^2})}.$$

where T_k is the Chebyshev polynomial of order k .

Proceeding with this polynomial, (3.22) becomes

$$\begin{aligned}
& \min_{\underline{a}_{1,(k)}^+} \|\tilde{\sigma}_M^2 \underline{a}_{\text{opt}} - S_{11}^H \cdot S_{11} \cdot \underline{a}_{1,(k)}^+\|_2 \\
&\leq \max_{\tilde{\sigma}_1^2, \dots, \tilde{\sigma}_{M-1}^2} \left| (1 - z/\tilde{\sigma}_M^2) \frac{T_{k-1}((\frac{\tilde{\sigma}_1^2 + \tilde{\sigma}_M^2}{2} - z)/(\frac{\tilde{\sigma}_1^2 - \tilde{\sigma}_M^2}{2}))}{T_{k-1}(\frac{\tilde{\sigma}_1^2 + \tilde{\sigma}_M^2}{\tilde{\sigma}_1^2 - \tilde{\sigma}_M^2})} \right| \\
&\leq \max_{\tilde{\sigma}_1^2, \dots, \tilde{\sigma}_{M-1}^2} \left| \frac{1}{T_{k-1}(\frac{\tilde{\sigma}_1^2 + \tilde{\sigma}_M^2}{\tilde{\sigma}_1^2 - \tilde{\sigma}_M^2})} \right|, \quad (\because (1 - z/\tilde{\sigma}_M^2) \leq 1 \text{ and } T_{k-1}(z) \leq 1) \\
&\leq \max_{\tilde{\sigma}_1^2, \dots, \tilde{\sigma}_{M-1}^2} \left| \frac{1}{T_{k-1}(\frac{\kappa+1}{\kappa-1})} \right|, \quad (\because \kappa \triangleq \frac{\tilde{\sigma}_1^2}{\tilde{\sigma}_{M-1}^2}) \\
&= \frac{2}{(\frac{\sqrt{\kappa+1}}{\sqrt{\kappa-1}})^{k-1} + (\frac{\sqrt{\kappa+1}}{\sqrt{\kappa-1}})^{-k+1}} \\
&\leq 2 \left(\frac{\sqrt{\kappa} - 1}{\sqrt{\kappa} + 1} \right)^{k-1}
\end{aligned}$$

Note that the set on which we maximize the value above does not include $\tilde{\sigma}_M^2$ since the polynomial we are using will be 0 at $z = \tilde{\sigma}_M^2$ and this gives us a reduced spectrum

to maximize on and thus giving us a tighter bound than that from the entire spectrum.

Using the bounds

$$\begin{aligned} \|\tilde{\sigma}_M^2 \underline{a}_{\text{opt}} - S_{11}^H \cdot S_{11} \cdot \underline{a}_{1,(k)}^+\|_2 &\leq O\left(\left|\frac{\sqrt{\tilde{\sigma}_1^2} - \sqrt{\tilde{\sigma}_{M-1}^2}}{\sqrt{\tilde{\sigma}_1^2} + \sqrt{\tilde{\sigma}_{M-1}^2}}\right|^k\right) \\ \|S_{11}^H \cdot S_{11} \cdot (\underline{a}_{\text{opt}} - \underline{a}_{1,(k)}^+)\|_2 &\leq O\left(\left|\frac{\sqrt{\tilde{\sigma}_1^2} - \sqrt{\tilde{\sigma}_{M-1}^2}}{\sqrt{\tilde{\sigma}_1^2} + \sqrt{\tilde{\sigma}_{M-1}^2}}\right|^k\right) \end{aligned}$$

By the highly-scattering system assumption, we conclude

$$\|\underline{a}_{\text{opt}} - \underline{a}_{1,(k)}^+\|_2 \leq O\left(\left|\frac{\sqrt{\tilde{\sigma}_1^2} - \sqrt{\tilde{\sigma}_{M-1}^2}}{\sqrt{\tilde{\sigma}_1^2} + \sqrt{\tilde{\sigma}_{M-1}^2}}\right|^k\right)$$

Note that this convergence rate only holds for the initial stage of the algorithm. The converging speed will accelerate as the iteration goes on since the algorithm will locate the extreme reflection coefficients and shorten the spectrum they maximize on. \square

To summarize: we described an iterative method for refining the wavefront $\underline{a}_{1,(k)}^+$ via Eq. (3.19). Inspection of the update Eqs. (3.20a)-(3.20c) and Eq. (3.21b) reveals that matrix-vector operation $S_{11} \cdot \underline{d}_{(k)}$ appears in Eq. (3.20a) while $S_{11}^H \cdot S_{11} \cdot \underline{d}_{(k)}$ appears in Eq. (3.21b). This means that the vector $\underline{d}_{(k)}$ is transmitted and the associated backscatter is measured. Note that these measurements are used to iteratively refine the vector $\underline{a}_{1,(k)}^+$, but $\underline{a}_{1,(k)}^+$ is *never actually transmitted* until the termination condition $\|\underline{r}_{(k+1)}\|_2 < \epsilon$ is met. This is reflected in the physical description of the proposed algorithm in Table 3.2. Also, note that we start with a random unit vector $\underline{a}_{1,(0)}^+$, and set $\underline{d}_{(0)}$ and $\underline{r}_{(0)}$ to $-S_{11}^H \cdot S_{11} \cdot \underline{a}_{1,(0)}^+$, since we are using conjugate gradient for finding the input that minimizes reflection, *i.e.*,

$$-\underline{a}_{1,(0)}^+ \xrightarrow{\text{Backscatter}} \underline{a}_1^- \xrightarrow{\text{PCM}} \underline{a}_1^+ \xrightarrow{\text{Backscatter}} \underline{a}_1^- \xrightarrow{\text{PCM}} \underline{d}_{(0)} = \underline{r}_{(0)}.$$

Vector Operation	Physical Operation
1 : $\underline{d}_1^- = S_{11} \cdot \underline{d}_{(k)}$	1 : $\underline{d}_{(k)} \xrightarrow{\text{Backscatter}} \underline{d}_1^-$
2 : $\underline{d}_1^+ = F \cdot (\underline{a}_1^-)^*$	2 : $\underline{d}_1^- \xrightarrow{\text{PCM}} \underline{d}_1^+$
3 : $\underline{d}_1^- = S_{11} \cdot \underline{d}_1^+$	3 : $\underline{d}_1^+ \xrightarrow{\text{Backscatter}} \underline{d}_1^-$
4 : $\underline{d} = F \cdot (\underline{d}_1^-)^*$	4 : $\underline{d}_1^- \xrightarrow{\text{PCM}} \underline{d}$
5 : $\mu_{(k+1)} = \ \underline{r}_{(k)}\ _2^2 / (\underline{d}_{(k)}^H \cdot \underline{d})$	5 : $\mu_{(k+1)} = \ \underline{r}_{(k)}\ _2^2 / (\underline{d}_{(k)}^H \cdot \underline{d})$
6 : $\underline{r}_{(k+1)} = \underline{r}_{(k)} - \mu_{(k+1)} \underline{d}$	6 : $\underline{r}_{(k+1)} = \underline{r}_{(k)} - \mu_{(k+1)} \underline{d}$
7 : $\beta_{(k+1)} = \ \underline{r}_{(k+1)}\ _2^2 / \ \underline{r}_{(k)}\ _2^2$	7 : $\beta_{(k+1)} = \ \underline{r}_{(k+1)}\ _2^2 / \ \underline{r}_{(k)}\ _2^2$
8 : $\underline{d}_{(k+1)} = \underline{r}_{(k+1)} + \beta_{(k+1)} \underline{d}_{(k)}$	8 : $\underline{d}_{(k+1)} = \underline{r}_{(k+1)} + \beta_{(k+1)} \underline{d}_{(k)}$

Table 3.2: Conjugate gradient algorithm for transmission maximization. The first column represents iterates of the conjugate gradients method. The second column represents the physical (or experimental) counterpart. The operation $\underline{a}_1^- \mapsto F \cdot (\underline{a}_1^-)^*$ can be realized via the use of a phase-conjugating mirror (PCM). The algorithm terminates when the residual vector $\|\underline{r}_{(k+1)}\|_2 < \epsilon$, a preset threshold at which point the optimal backscatter minimizing wavefront is constructed as $\underline{a}_{1,(k+1)}^+ = \underline{a}_{1,(k)}^+ + \mu_{(k+1)} \underline{d}_{(k)}$ followed by a power normalization $\underline{a}_{1,(k+1)}^+ = \underline{a}_{1,(k+1)}^+ / \|\underline{a}_{1,(k+1)}^+\|_2$.

A feature of the conjugate gradient method is that the intensity of the backscatter measurement $S_{11} \cdot \underline{d}_{(k)}$ is expected to remain relatively high (for a strongly backscattering medium) throughout the process. It is only when the wavefront corresponding to $\underline{a}_{1,(k+1)}^+$ is excited that a strong transmission (with minimized backscatter) is obtained - this might be a desirable feature for communication or covert sensing applications. Consequently, the algorithm will produce high intensity backscatter measurements, thereby facilitating accurate estimation of the backscatter modal coefficient vectors that are an important component of the proposed algorithm. This makes the conjugate gradient method less susceptible to measurement noise than the steepest descent method where the backscatter intensity decreases with every iteration.

3.5 An iterative, physically realizable focusing algorithm

We first describe a generalized coordinate descent method for amplitude and phase optimization. Assume we are given a $M \times N_B$ matrix $B = [\underline{b}_1 \ \dots \ \underline{b}_{N_B}]$ whose columns are orthonormal so that $B^H \cdot B = I_{N_B}$. Thus N_B denotes the number of (orthonormal) bases vectors.

The key idea here is to expand \underline{a}_1^+ on the right hand side of Eq. (3.11) in terms

of the bases vectors given by the columns of B as

$$\underline{a}_1^+ = \sum_{l=1}^{N_B} p_l e^{j\phi_l} \underline{b}_l, \quad (3.23)$$

where $p_l \geq 0$ and $\phi_l \in [-\pi, \pi]$ are the unknown amplitudes and phases, respectively.

The optimal amplitudes can be estimated by transmitting $\underline{a}_1^+ = \underline{b}_l$ for every $l = 1, \dots, N_B$, measuring the corresponding intensity \mathcal{I}_l at the target, and setting $p_l = \sqrt{\mathcal{I}_l}$. This can be accomplished with $O(N_B)$ measurements.

The phases can be estimated by first setting $\phi_1, \dots, \phi_{N_B}$ randomly and then for $l = 1, \dots, N_B$, sequentially finding the phase that optimizes measured intensity. This can be done via a simple line search, i.e., by scanning the measured intensity over a fixed set of discretized values of the phase or by using more sophisticated algorithms such as golden section search algorithm with parabolic interpolation [46, Section 10.2]. This too requires $O(N_B)$ measurements.

Setting $N_B = M$ and $B = I$ yields the coordinate descent approach used by Vellekoop and Mosk [8, 1, 35]. This corresponds to exciting one plane wave mode at a time and inferring the optimal phase and amplitude one mode at time. Such an algorithm requires $O(M)$ iterations to yield the optimal focusing wavefront. Setting B to the 2D Walsh function basis matrix yields the method proposed by Stockbridge et al. in [17].

An important insight from Eq. (3.13) is that if we were to express the optimal focusing wavefront as a superposition of eigen-wavefronts of S_{21} , then typically only $K \ll M$ of the combining coefficients will be large. Thus only K of the p_l coefficients in Eq. (3.23) will be significant if we set B to be the right singular vectors of S_{21} . In the lossless setting, the K eigen-wavefronts of S_{21} that have transmission coefficients close to one correspond precisely to the K eigen-wavefronts associated with S_{11} that have reflection coefficients close to zero. Hence, we can set B to be the right singular vectors of S_{11} and expect only K of the p_l coefficients in Eq. (3.23) to be significant as well. Thus, we need to measure the K singular vectors of S_{11} associated with its K smallest singular values.

The Lanczos algorithm is an iterative algorithm for accomplishing just that [36, 37]. The key idea is to create a tridiagonal matrix H whose eigenvalues and eigenvectors (referred to as the Ritz values and vectors) are approximations of the eigenvalues and eigenvectors of $S_{11}^H \cdot S_{11}$. The algorithm is summarized in the first column of Table 3.3; its physical counterpart is described in the second column. The matrix B in Eq. (3.23) is obtained as

$$B = Q \cdot U, \quad (3.24)$$

where $Q = \begin{bmatrix} \underline{q}_{(1)} & \dots & \underline{q}_{(N_B)} \end{bmatrix}$ are the N_B vectors produced by the algorithm (see Table 3.3) and $U = \begin{bmatrix} \underline{u}_{(1)} & \dots & \underline{u}_{(N_B)} \end{bmatrix}$ are the N_B eigenvectors of H associated with the N_B smallest eigenvalues.

The convergence theory [37] of the Lanczos algorithms predicts that the eigenvector estimates will rapidly converge to the K eigenvectors of $S_{11}^H \cdot S_{11}$ associated with

the eigen-wavefronts of S_{11} with the smallest reflection coefficients; hence, setting $N_B = O(K)$ will suffice. An estimate of K can be formed from the eigenvalues of H by counting how many of the converged eigenvalues of H are below a preset threshold ϵ .

Estimating these K right singular vectors will require $O(K)$ measurements and when $K \ll M$, we shall obtain a near-optimal focusing wavefront using significantly fewer measurements than the $O(M)$ measurements required by the coordinate descent when $B = I$. We shall corroborate this convergence behavior using numerical simulations next.

Vector Operation	Physical Operation
1 : $\underline{q}_1^- = S_{11} \cdot \underline{q}_{(k)}$	1 : $\underline{q}_{(k)} \xrightarrow{\text{Backscatter}} \underline{q}_1^-$
2 : $\underline{q}_1^+ = F \cdot (\underline{q}_1^-)^*$	2 : $\underline{q}_1^- \xrightarrow{\text{PCM}} \underline{q}_1^+$
3 : $\underline{q}_1^- = S_{11} \cdot \underline{q}_1^+$	3 : $\underline{q}_1^+ \xrightarrow{\text{Backscatter}} \underline{q}_1^-$
4 : $\underline{v} = F \cdot (\underline{q}_1^-)^*$	4 : $\underline{q}_1^- \xrightarrow{\text{PCM}} \underline{v}$
5 : $H_{k,k} = \underline{q}_{(k)}^H \cdot \underline{v}$	5 : $H_{k,k} = \underline{q}_{(k)}^H \cdot \underline{v}$
6 : $\underline{v} = \underline{v} - H_{k,k} \underline{q}_{(k)} - s_{(k-1)} \underline{q}_{(k-1)}$	6 : $\underline{v} = \underline{v} - H_{k,k} \underline{q}_{(k)} - s_{(k-1)} \underline{q}_{(k-1)}$
7 : $H_{k+1,k} = H_{k,k+1} = s_{(k)} = \ \underline{v}\ _2$	7 : $H_{k+1,k} = H_{k,k+1} = s_{(k)} = \ \underline{v}\ _2$
8 : $\underline{q}_{(k+1)} = \underline{v} / s_{(k)}$	8 : $\underline{q}_{(k+1)} = \underline{v} / s_{(k)}$

Table 3.3: The Lanczos algorithm and its physical counterpart which computes a tridiagonal matrix H whose eigenvalues and eigenvectors are closely related to the eigenvalues and eigenvectors of $S_{11}^H \cdot S_{11}$. Note that we initialize the algorithm by setting $k = 1$, $\underline{q}_{(1)}$ to a random unit norm vector, and $s_{(0)} = 0$.

3.6 Numerical simulations and validation of the existence of highly transmitting eigen-wavefronts

To validate the proposed algorithms, we compute the scattering matrices in Eq. (3.2) via a spectrally accurate, T-matrix inspired integral equation solver that characterizes fields scattered from each cylinder in terms of their traces expanded in series of azimuthal harmonics. Interactions between cylinders are modeled using 2D periodic Greens functions. The method constitutes a generalization of that in [47], in that it does not force cylinders in a unit cell to reside on a line but allows them to be freely distributed throughout the cell. All periodic Greens functions/lattice sums are rapidly evaluated using a recursive Shank's transform as in [48, 29]. Our method exhibits exponential convergence in the number of azimuthal harmonics used in the description of the field scattered by each cylinder. In the numerical experiments below, care was taken to ensure 11-th digit accuracy in the entries of the computed

scattering matrices.

Fig. 3.4 shows the empirical transmission coefficient distribution, i.e., the singular value squared of the S_{21} matrix of a slab with $D = 197\lambda$, $L = 1.2 \times 10^4\lambda$, $r = 0.11\lambda$, $N_c = 14,000$ (Dielectric), $n_d = 1.3$, $M = 395$ and $\bar{l} = 6.7\lambda$, where \bar{l} is the mean of the minimum-inter-scatterer-distances. The computation validates the bimodal shape of the theoretical distribution in Fig. 3.2.

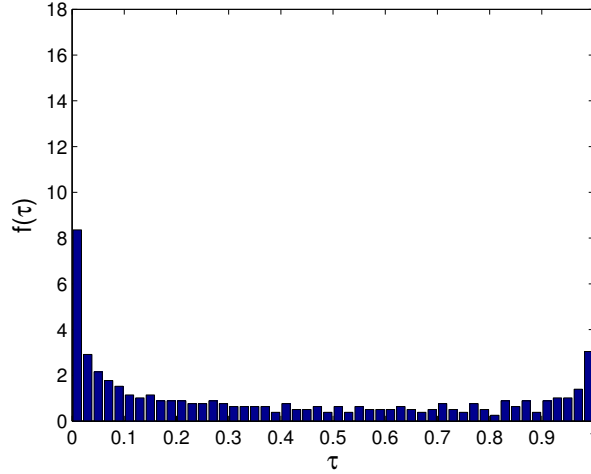
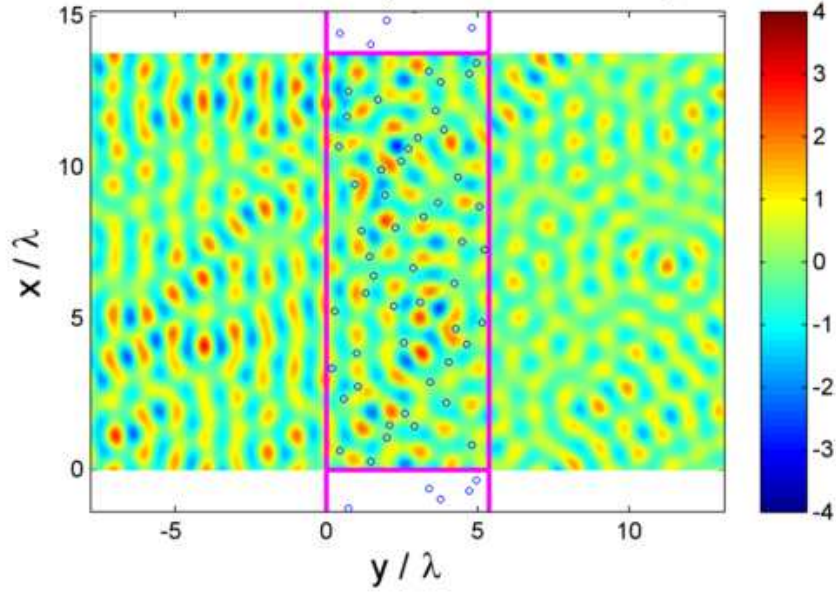
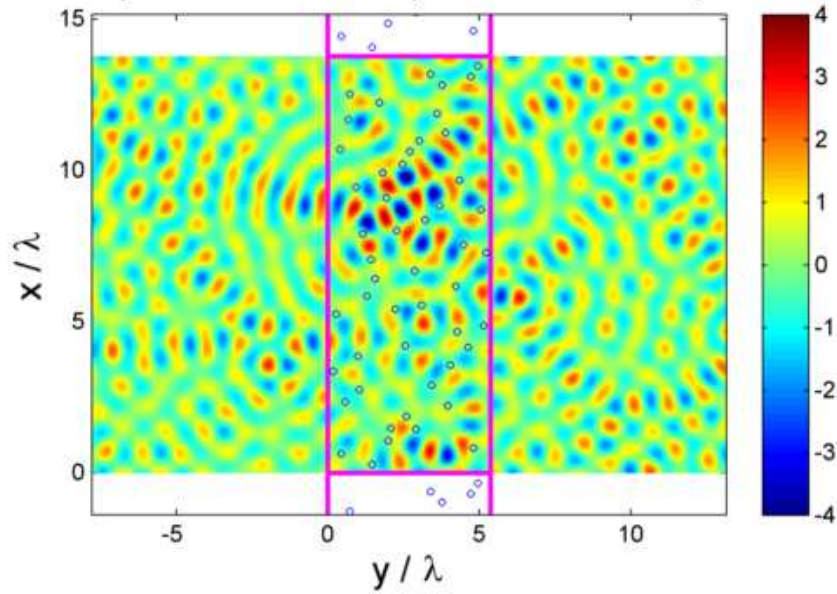


Figure 3.4: Empirical transmission coefficients distribution from a scattering system with $D = 197\lambda$, $L = 1.2 \times 10^4\lambda$, $r = 0.11\lambda$, $N_c = 14,000$ (Dielectric), $n_d = 1.3$, $M = 395$, $\bar{l} = 6.7\lambda$, where \bar{l} is the mean of the minimum-inter-scatterer-distances.

Next, we consider scattering system with $D = 14\lambda$, $L = 5.4\lambda$, $r = 0.11\lambda$, $N_c = 50$ (PEC), $M = 27$, and $\bar{l} = 0.8\lambda$. Here $\tau_{\text{normal}} = 0.483$ while $\tau_{\text{opt}} = 0.9997$ so that wavefront optimization produces a two-fold increase in transmitted power. Fig. 3.5 shows the wavefield produced by a normally incident wavefront and the optimal wavefront, respectively. Fig. 3.6 shows the modal coefficients of the optimal wavefront corresponding to Fig. 3.5.



(a) Wavefield produced by a normally incident wavefront.



(b) Wavefield produced by the optimal wavefront.

Figure 3.5: Wavefield plot of the incident-plus-backscatter wave corresponding to (a) normally incident and the (b) optimal wavefront, which were sent to a scattering system with $D = 14\lambda$, $L = 5.4\lambda$, $r = 0.11\lambda$, $N_c = 50$ PEC, $M = 27$, $\bar{l} = 0.8\lambda$. The normally incident wavefront has $\tau_{\text{normal}} = 0.483$ while the optimal wavefront yields $\tau_{\text{opt}} = 0.9997$.

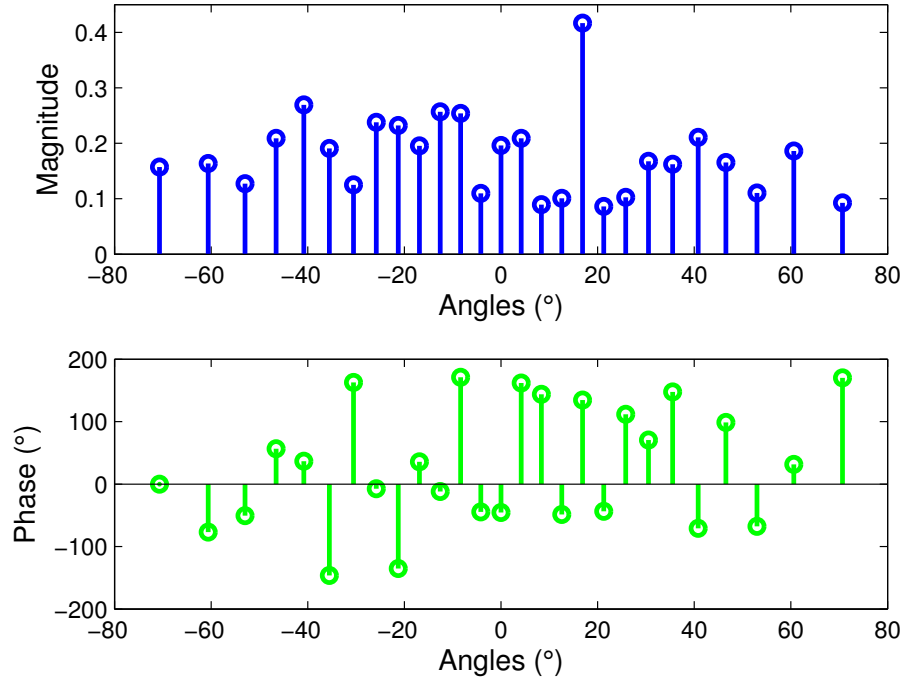


Figure 3.6: The modal coefficients of the optimal wavefront corresponding to Fig. 3.5 (b) are shown.

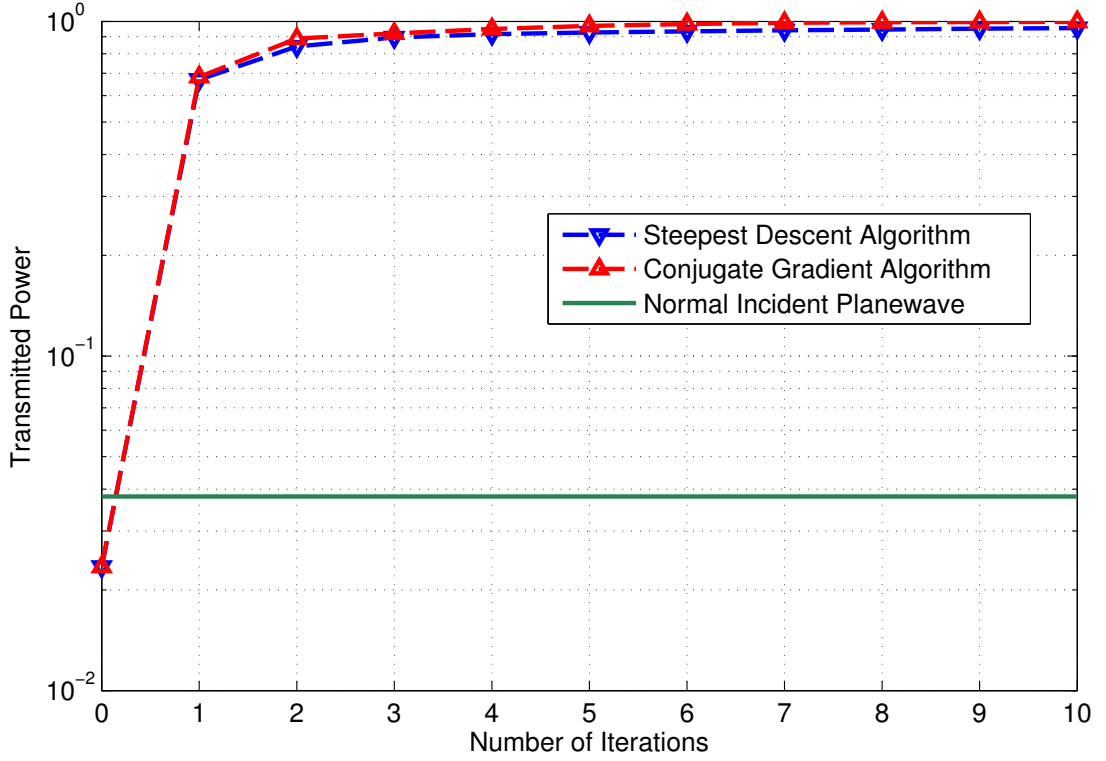


Figure 3.7: The transmitted power versus the number of iterations is shown for steepest descent algorithm with $\mu = 0.5037$ and for conjugate gradient in the setting with $D = 197\lambda$, $L = 3.4 \times 10^5\lambda$, $r = 0.11\lambda$, $N_c = 430,000$ dielectric cylinders with $n_d = 1.3$, $M = 395$, $\bar{l} = 6.69\lambda$. The conjugate gradient algorithm converged to the optimal transmitted power slightly faster than the steepest descent algorithm. However, since the steepest descent algorithm requires a line search for setting the optimal step size μ , it requires more measurements than the conjugate gradient method which does not require any parameters to be set.

Fig. 3.7 displays the rate of convergence of the algorithm's developed for a setting with $D = 197\lambda$, $L = 3.4 \times 10^5\lambda$, $r = 0.11\lambda$, $N_c = 430,000$ (Dielectric), $n_d = 1.3$, $M = 395$ and, $\bar{l} = 6.69\lambda$; this slab has a comparable (slightly lower) packing density than that in Fig. 3.5.

A normally incident wavefront results in a transmission of $\tau_{\text{normal}} = 0.038$. The optimal wavefront yields $\tau_{\text{opt}} = 0.9973$ corresponding to a 26-fold increase in transmission. Steepest descent algorithm and conjugate gradient algorithm produce wavefronts that converge to the near optimum in about 5 – 10 iterations, as shown in Fig. 3.7.

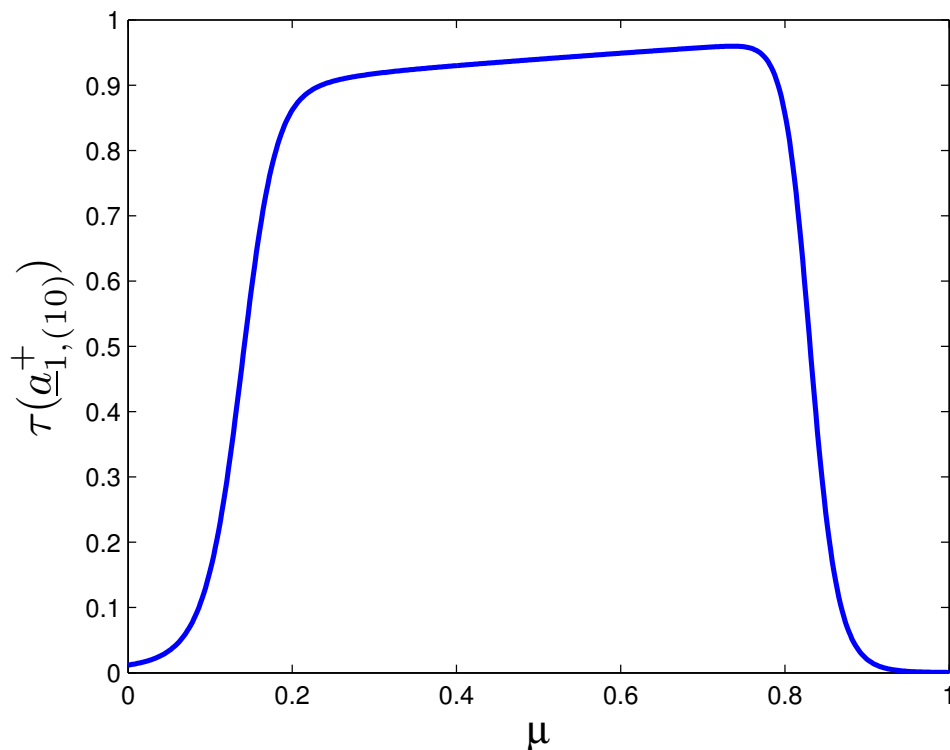


Figure 3.8: The transmitted power at the 10-th iteration as a function of the stepsize μ used in Algorithm 1 for the same setting as in Fig. 3.7.

Fig. 3.8 plots the transmitted power after the 10-th iteration of steepest descent algorithm for different choices of μ . Fig. 3.8 reveals that there is broad range of μ for which the algorithm converges in a handful of iterations. We have found that setting $\mu \approx 0.5$ yields fast convergence.

The conjugate gradient algorithm converges slightly faster than the steepest descent algorithm in the setting where we chose the optimal $\mu = 0.5037$ for steepest descent algorithm by a line search; i.e., we ran steepest descent algorithm over a fixed set of discretized values of μ between 0 and 1, and chose the optimal μ that gives the fastest convergence result. In an experimental setting, the line search for finding the optimal μ for the steepest descent algorithm will require additional measurements. Thus, conjugate gradient algorithm will require fewer measurements than steepest descent algorithm with the additional advantage of not requiring any auxiliary parameters to be set.

Next, we consider the setting where a subset of the propagation modes are controlled so that the summation in (3.1) is from $-N_{\text{ctrl}}$ to N_{ctrl} . Thus the number of controlled modes is given by $M_{\text{ctrl}} = 2N_{\text{ctrl}} + 1$.

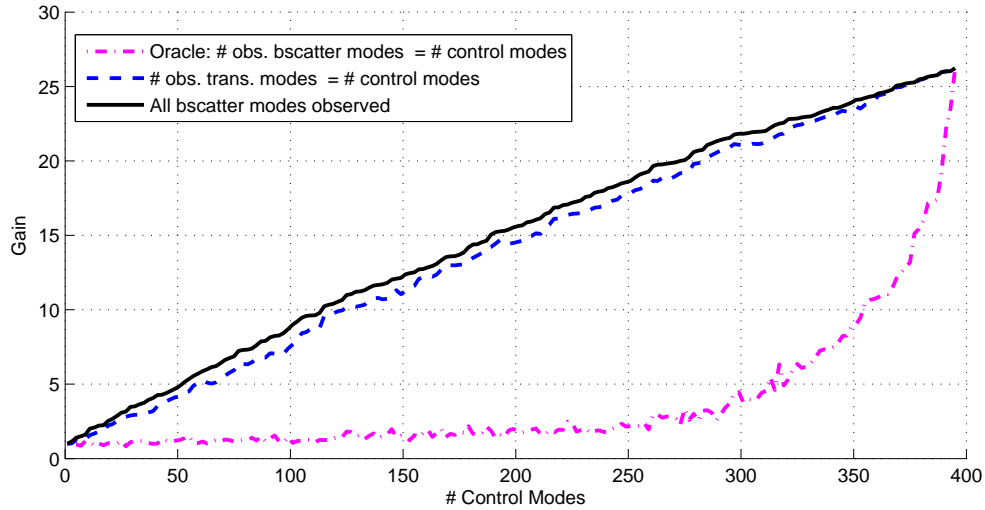


Figure 3.9: Gain ($=:\tau_{\text{opt}}/\tau_{\text{normal}}$) versus the number of control modes for the same setting as in Fig. 3.7. Here we compute the realized gain for algorithms that control only part of the total number of modes but capture, 1) all modes in the backscatter field, 2) only as many modes in the transmitted field as the number of control modes, and 3) only as many modes in the backscatter field as the number of control modes. For the last algorithm, we transmit the eigen-wavefront of the (portion of the) S_{11} matrix that yields the highest transmission.

Fig. 3.9 shows the realized gain (relative to a normally incident wavefront) for three different approaches versus the number of control modes in the same setting as in Fig. 3.7. Here we compute the realized gain for algorithms that control only part of the total number of modes but capture, 1) all modes in the backscatter field, 2) only as many modes in the transmitted field as the number of control modes, and 3) only as many modes in the backscatter field as the number of control modes. For the last algorithm, we transmit the eigen-wavefront of the (portion of the) S_{11} matrix that yields the highest transmission. Fig. 3.9 shows that if the backscatter field is fully sampled, then it is possible to realize increased transmission with a limited number of control modes. It also emphasizes the important point that when the backscatter field is not fully sampled then the principle of minimizing backscatter might produce ‘transmission’ into the unsampled portion of the backscatter field instead of producing forward transmission.

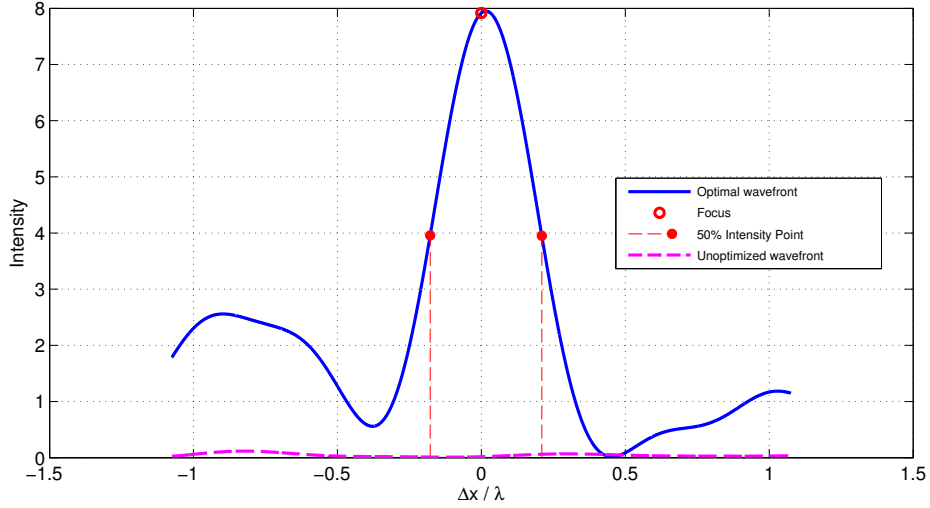
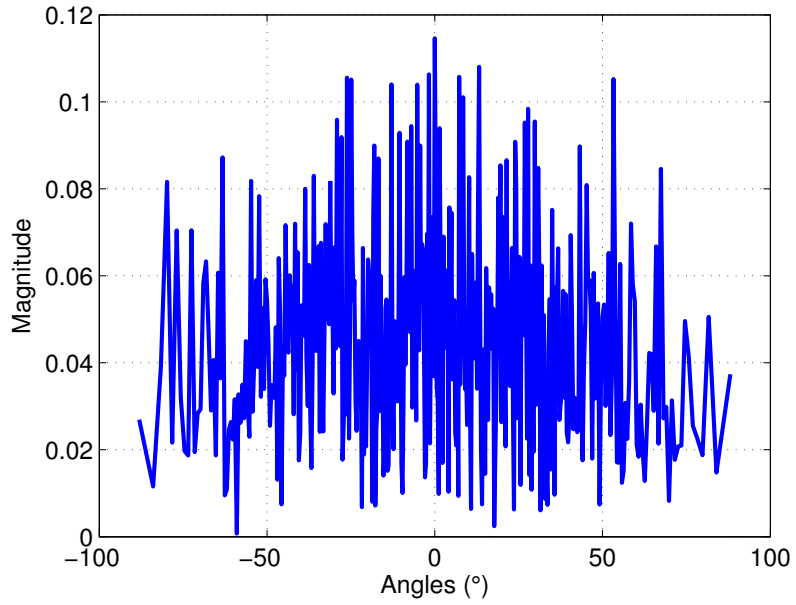
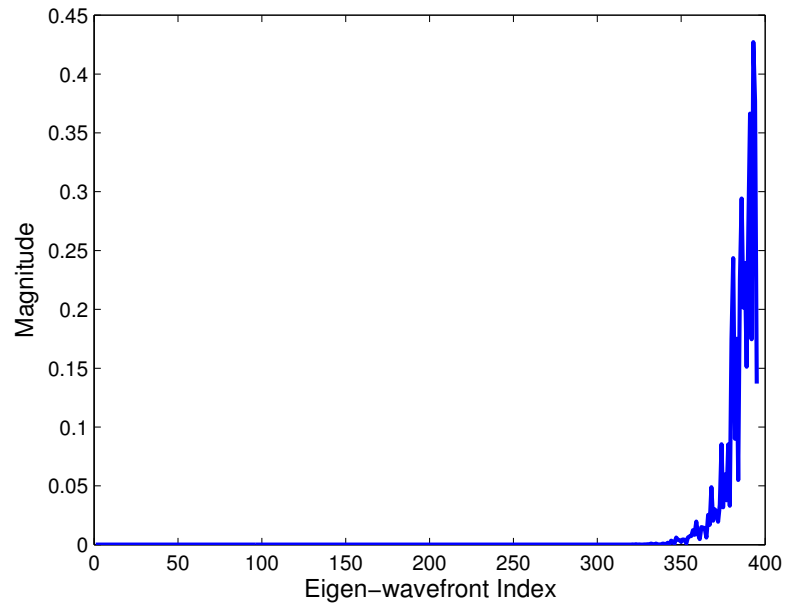


Figure 3.10: Intensity plot around the target at $(D/2, L + 5.4\lambda)$ for the scattering system defined in Fig. 3.7. The optimal focusing wavefront forms a sharp focus of 1λ around the target. The unoptimized wavefront solution corresponds to an incident wavefront that would have produced a focus at the target if there were no intervening scattering medium.

Fig. 3.10 considers the same setup as in Fig. 3.7 with a target at $(D/2, L + 5.4\lambda)$ and plots the focus achieved at the target by exciting a focusing wavefront as in (3.12). The modal coefficients are plotted in Fig. 3.11. Fig. 3.11 shows the sparsity of the modal coefficients of the optimal focusing wavefront when expressed in terms of the basis given by the right singular vectors of the S_{11} matrix or equivalently, the eigenvectors of $S_{11}^H \cdot S_{11}$.



(a) Identity base decomposition.



(b) Eigen-mode base decomposition.

Figure 3.11: Here, we depict the magnitude of the coefficients of the optimal focusing wavefront, corresponding to the situation in Fig. 3.10, in terms of two choices of bases vectors. In (a) we decompose the optimal focusing wavefront with respect to the bases vectors corresponding to plane waves; in (b) decompose the optimal focusing wavefront with respect to the bases vectors associated with the eigen-wavefronts of the S_{11} matrix. A particular important observation is that the eigen-wavefront decomposition yields a sparse representation of the optimal focusing wavefront.

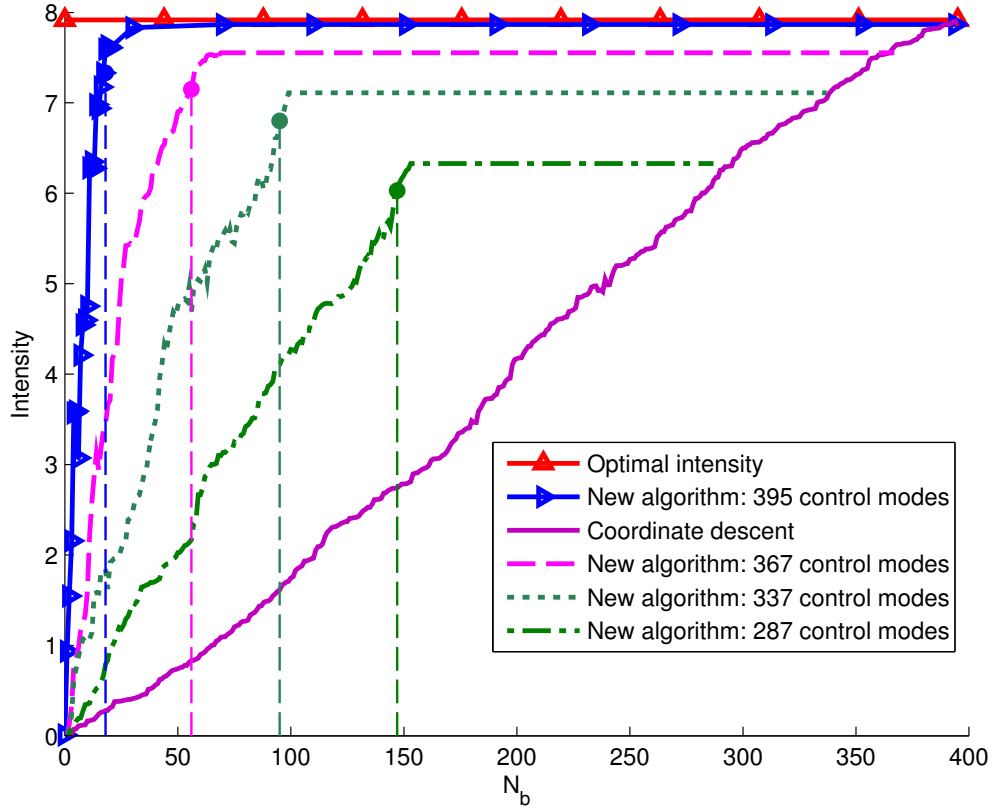


Figure 3.12: Intensity at target as a function of the number of bases vectors for the new algorithm (which uses the bases vectors estimated using (3.24) and the algorithm described in Table 3.3) for different number of control modes versus the standard coordinate descent method which uses the plane wave associated bases vectors (see Section 3.5) for the same setting as in Fig. 3.10. The sparsity of the optimal wavefront’s modal coefficient vector when expressed using the bases of the eigen-wavefronts (shown in Fig. 3.11) leads to the rapid convergence observed. The optimal wavefront was constructed as described in Section 3.2.2 using time-reversal. The number of bases vectors needed to attain 95% of the optimal focus intensity for a given number of control modes is indicated with a vertical line highlighting the fast convergence of the algorithm and the ability to get a near-optimal focus using significantly fewer measurements than the coordinate descent approach.

Fig. 3.12 plots the intensity achieved when using N_B bases vectors for the algorithms described in Section 3.5 in the same setup as in Fig. 3.10. The new algorithm which computes the bases B from the eigenvectors of $S_{11}^H \cdot S_{11}$ associated with its smallest eigenvalues reaches 95% of the optimal intensity with significantly fewer iterations than the coordinate descent algorithm. This fast convergence to the near-optimum

is the principal advantage of the proposed method. Figure 3.12 shows that this convergence behavior is retained even when the number of control modes is reduced. We obtain similar gains for the setting where there are multiple focusing points.

Finally, we consider the setting where the scatterers are absorptive. Here, backscatter minimization as a general principle for increasing transmission is clearly sub-optimal since an input with significant absorption can also minimize backscatter. We defined gain as $\tau_{\text{opt}}/\tau_{\text{normal}}$. Here we have $D = 197\lambda$, $L = 3.4 \times 10^5\lambda$, $r = 0.11\lambda$, $N_c = 4.3 \times 10^5$ (Absorbing Dielectric), $n_d = 1.3 - j\kappa$, $M = 395$, and $\bar{l} = 6.69\lambda$. In Fig. 3.13, we compare the gain obtained by using the backscatter minimizing wavefront to the gain obtained by the optimal wavefront (that utilizes information from the S_{21} matrix) for various κ , as the thickness of the scattering system increases. We obtain an increase in transmission and the methods described again produce dramatic gains whenever the scatterers are weakly absorptive.

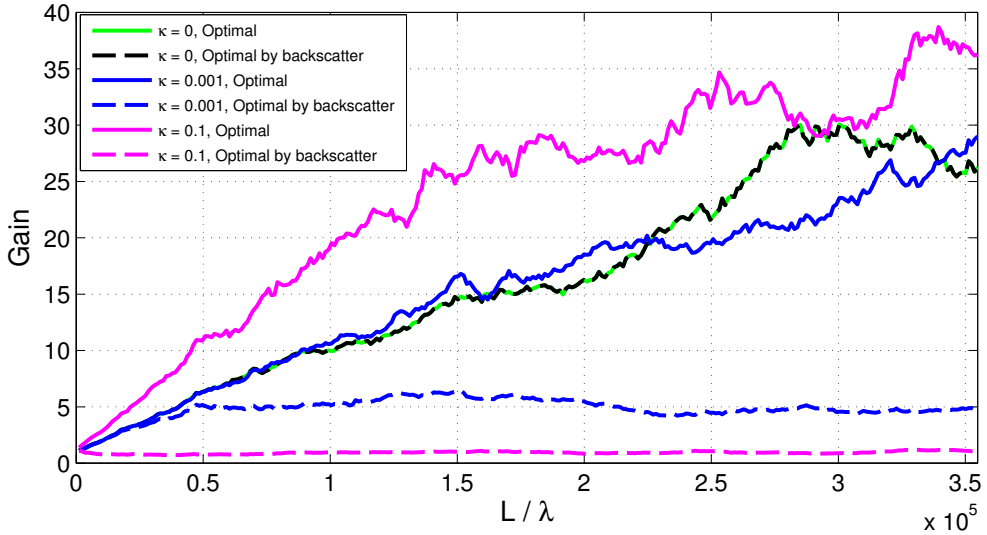


Figure 3.13: Gain ($=:\tau_{\text{opt}}/\tau_{\text{normal}}$) versus the thickness L/λ in a setting with $D = 197\lambda$, $r = 0.11\lambda$, $N_c = 430,000$ Absorbing Dielectric, $n_d = 1.3 - j\kappa$, $M = 395$, $\bar{l} = 6.69\lambda$, for different values of κ . The solid line represents the maximum possible gain and the dashed line represents the gain obtained by using backscatter minimizing algorithm discussed in Section 3.4.

CHAPTER IV

Phase-only Algorithms for Transmission Maximization

Recent theoretical and experimental advances have shed light on the existence of so-called ‘perfectly transmitting’ wavefronts with transmission coefficients close to 1 in strongly backscattering random media. These perfectly transmitting eigen-wavefronts can be synthesized by spatial amplitude and phase modulation.

Here, we consider the problem of transmission enhancement using phase-only modulated wavefronts. Motivated by bio-imaging applications in which it is not possible to measure the transmitted fields, we develop physically realizable iterative and non-iterative algorithms for increasing the transmission through such random media using backscatter analysis. We theoretically show that, despite the phase-only modulation constraint, the non-iterative algorithms will achieve at least about $25\pi\% \approx 78.5\%$ transmission assuming there is at least one perfectly transmitting eigen-wavefront and that the singular vectors of the transmission matrix obey a maximum entropy principle so that they are isotropically random.

We numerically analyze the limits of phase-only modulated transmission in 2-D with fully spectrally accurate simulators and provide rigorous numerical evidence confirming our theoretical prediction in random media with periodic boundary conditions that is composed of hundreds of thousands of non-absorbing scatterers. We show via numerical simulations that the iterative algorithms we have developed converge rapidly, yielding highly transmitting wavefronts using relatively few measurements of the backscatter field. Specifically, the best performing iterative algorithm yields $\approx 70\%$ transmission using just 15 – 20 measurements in the regime where the non-iterative algorithms yield $\approx 78.5\%$ transmission but require measuring the entire modal reflection matrix. Our theoretical analysis and rigorous numerical results validate our prediction that phase-only modulation with a given number of spatial modes will yield higher transmission than amplitude and phase modulation with half as many modes.

The chapter is organized as follows. We describe our setup in Section 4.1. We discuss the problem of transmission maximization using phase-only modulated wavefronts in Section 4.2. We describe physically realizable, non-iterative and iterative algorithms for transmission maximization in Section 4.3 and in Section 4.5, respectively. We identify fundamental limits of phase-only modulated transmission in Sec-

tion 4.4, validate the predictions and the rapid convergence behavior of the iterative algorithms in Section 4.6.

4.1 Setup

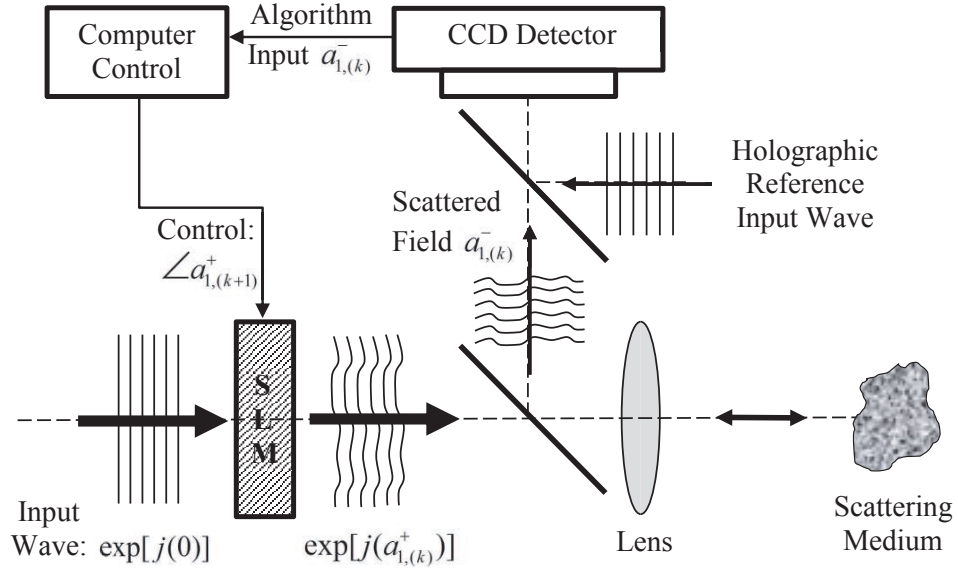


Figure 4.1: Schematic for the experimental setup considered. (Figure from Steve C. Rand)

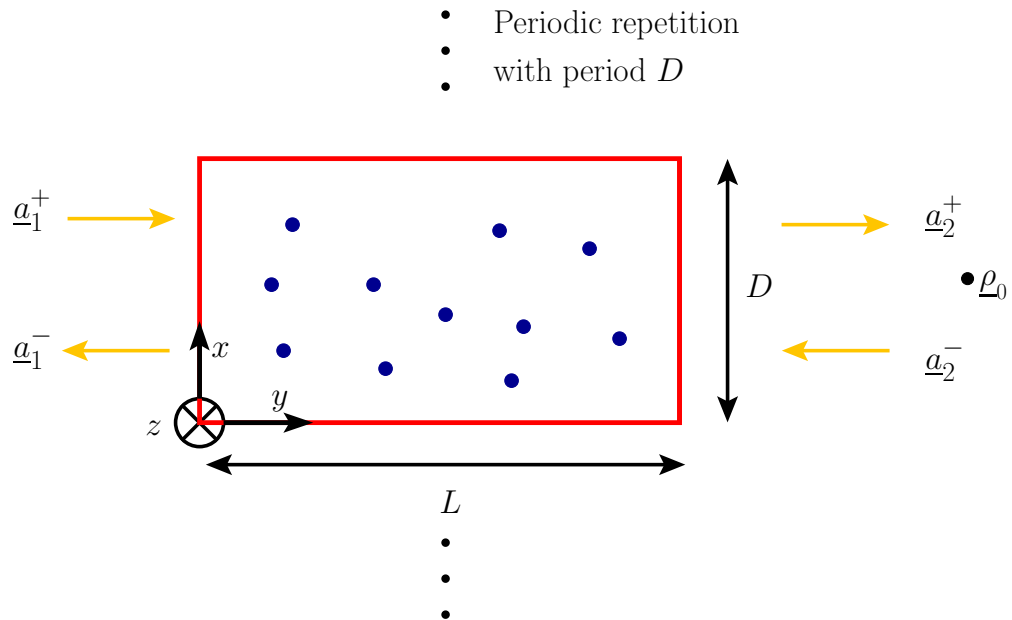


Figure 4.2: Geometry of the scattering system considered.

We study scattering from a two-dimensional (2D) periodic slab of thickness L and periodicity D . The slab's unit cell occupies the space $0 \leq x < D$ and $0 \leq y < L$ (Fig. 4.2) and contains N_c infinite and z -invariant circular cylinders of radius r that are placed randomly within the cell and assumed either perfect electrically conducting (PEC) or dielectric with refractive index n_d . Care is taken to ensure the cylinders do not overlap. All fields are TM_z polarized: electric fields in the $y < 0$ ($i = 1$) and $y > L$ ($i = 2$) halfspaces are denoted $\underline{e}_i(\underline{\rho}) = e_i(\underline{\rho})\hat{z}$. These fields (complex) amplitudes $e_i(\underline{\rho})$ can be decomposed in terms of $+y$ and $-y$ propagating waves as $e_i(\underline{\rho}) = e_i^+(\underline{\rho}) + e_i^-(\underline{\rho})$, where

$$e_i^\pm(\underline{\rho}) = \sum_{n=-N}^N h_n a_{i,n}^\pm e^{-jk_n^\pm \cdot \underline{\rho}}. \quad (4.1)$$

In the above expression, $\underline{\rho} = x\hat{x} + y\hat{y} \equiv (x, y)$, $\underline{k}_n^\pm = k_{n,x}\hat{x} \pm k_{n,y}\hat{y} \equiv (k_{n,x}, \pm k_{n,y})$, $k_{n,x} = 2\pi n/D$, $k_{n,y} = 2\pi\sqrt{(1/\lambda)^2 - (n/D)^2}$, λ is the wavelength, and $h_n = \sqrt{\|\underline{k}_n^\pm\|_2/k_{n,y}}$ is a power-normalizing coefficient. We assume $N = \lfloor D/\lambda \rfloor$, i.e., we only model propagating waves and denote $M = 2N + 1$. The modal coefficients $a_{i,n}^\pm$, $i = 1, 2$; $n = -N, \dots, N$ are related by the scattering matrix

$$\begin{bmatrix} \underline{a}_1^- \\ \underline{a}_2^+ \end{bmatrix} = \underbrace{\begin{bmatrix} S_{11} & S_{12} \\ S_{21} & S_{22} \end{bmatrix}}_{=:S} \begin{bmatrix} \underline{a}_1^+ \\ \underline{a}_2^- \end{bmatrix}, \quad (4.2)$$

where $\underline{a}_i^\pm = [a_{i,-N}^\pm \ \dots \ a_{i,0}^\pm \ \dots \ a_{i,N}^\pm]^T$ and T denotes transposition. In what follows, we assume that the slab is only excited from the $y < 0$ halfspace; hence, $\underline{a}_2^- = 0$. For a given incident field amplitude $e_1^+(\underline{\rho})$, we define transmission and reflection coefficients as

$$\tau(\underline{a}_1^+) := \frac{\|S_{21} \cdot \underline{a}_1^+\|_2^2}{\|\underline{a}_1^+\|_2^2}, \quad (4.3)$$

and

$$\Gamma(\underline{a}_1^+) := \frac{\|S_{11} \cdot \underline{a}_1^+\|_2^2}{\|\underline{a}_1^+\|_2^2}, \quad (4.4)$$

respectively. We denote the transmission coefficient of a normally incident wavefront by $\tau_{\text{normal}} = \tau([0 \ \dots \ 0 \ 1 \ 0 \ \dots \ 0]^T)$.

4.2 Problem formulation

We define the phase-vector of the modal coefficient vector \underline{a}_1^+ , as

$$\angle \underline{a}_1^+ = \left[\angle a_{1,-N}^+ \ \dots \ \angle a_{1,0}^+ \ \dots \ \angle a_{1,N}^+ \right]^T,$$

where for $n = -N, \dots, N$, $a_{1,n}^+ = |a_{1,n}^+| \exp(j \angle a_{1,n}^+)$ and $|a_{1,n}^+|$ and $\angle a_{1,n}^+$ denote the magnitude and phase of $a_{1,n}^+$, respectively. For a real-valued constant $c > 0$, let P_c^M denote vectors of the form

$$\underline{p}(\underline{\theta}; c) = \sqrt{\frac{c}{M}} \left[e^{j\theta_{-N}} \quad \dots \quad e^{j\theta_0} \quad \dots \quad e^{j\theta_N} \right]^T, \quad (4.5)$$

where $\underline{\theta} = \left[\theta_{-N} \quad \dots \quad \theta_0 \quad \dots \quad \theta_N \right]^T$ is a $2N + 1 =: M$ -vector of phases. Then, the problem of designing a phase-only modulated incident wavefront that maximizes the transmitted power can be stated as

$$\underline{a}_{\text{opt}} = \arg \max_{\underline{a}_1^+ \in P_c^M} \tau(\underline{a}_1^+) = \arg \max_{\underline{a}_1^+ \in P_c^M} \frac{\|S_{21} \cdot \underline{a}_1^+\|_2^2}{\|\underline{a}_1^+\|_2^2} = \arg \max_{\underline{a}_1^+ \in P_1^M} \|S_{21} \cdot \underline{a}_1^+\|_2^2. \quad (4.6)$$

Henceforth, let $\underline{p}(\underline{\theta}) := \underline{p}(\underline{\theta}; 1)$ denote the setting where $c = 1$ in Eq. (4.5). Consider the optimization problem

$$\underline{\theta}_{\text{opt}} = \arg \max_{\underline{\theta}} \|S_{21} \cdot \underline{p}(\underline{\theta})\|_2^2. \quad (4.7)$$

Then, from Eq. (4.6), the optimal wavefront is given by

$$\underline{a}_{\text{opt}} = \underline{p}(\underline{\theta}_{\text{opt}}). \quad (4.8)$$

In the lossless setting, the scattering matrix S in Eq. (4.2) will be unitary, i.e., $S^H \cdot S = I$, where I is the identity matrix. Consequently, we have that $S_{11}^H \cdot S_{11} + S_{21}^H \cdot S_{21} = I$, and the optimization problem in Eq. (4.7) can be reformulated as

$$\underline{\theta}_{\text{opt}} = \arg \max_{\underline{\theta}} \underbrace{(p(\underline{\theta}))^H \cdot S_{21}^H \cdot S_{21} \cdot p(\underline{\theta})}_{=(p(\underline{\theta}))^H \cdot (I - S_{11}^H \cdot S_{11}) \cdot p(\underline{\theta})} = \arg \min_{\underline{\theta}} \|S_{11} \cdot \underline{p}(\underline{\theta})\|_2^2 = \arg \min_{\underline{\theta}} \Gamma(\underline{p}(\underline{\theta})). \quad (4.9)$$

Thus the phase-only modulated wavefront that maximizes transmission will also minimize backscatter. The phase-only modulating constraint leads to non-convex cost functions in Eqs. (4.7) and (4.9) for which there is no closed-form solution for $\underline{\theta}_{\text{opt}}$ or $\underline{a}_{\text{opt}}$.

4.3 Non-iterative, phase-only modulating algorithms for transmission maximization

We first consider algorithms for increasing transmission by backscatter minimization using phase-only modulated wavefronts that utilize measurements of the reflection matrix S_{11} . We assume that this matrix can be measured using the experimental techniques described in [9, 10, 11, 12] by, in essence, transmitting $K > M$ incident wavefronts $\{\underline{a}_{1,i}^+\}_{i=1}^K$, measuring the (modal decomposition of the) backscattered wavefronts $\{\underline{a}_{1,i}^-\}_{i=1}^K$ and estimating S_{11} by solving the system of equations

$\{\underline{a}_{1,i}^- = S_{11} \cdot \underline{a}_{1,i}^+\}_{i=1}^K$. We note that, even if the S_{11} matrix has been measured perfectly, the optimization problem

$$\underline{a}_{\text{opt}} = \arg \min_{\underline{a}_1^+ \in P_1^M} \|S_{11} \cdot \underline{a}_1^+\|_2^2, \quad (4.10)$$

is computationally intractable. In the simplest setting where the elements of \underline{a}_1^+ are restricted to be $\pm 1/\sqrt{M}$ instead of continuous values, the optimization problem in (4.10) is closely related to the binary quadratic programming (BQP) problem which is known to be NP-hard [49].

We can make the problem computationally tractable by relaxing the phase-only constraint in Eq. (4.10) and allowing the elements of \underline{a}_1^+ to take on arbitrary amplitudes and phases while imposing the power constraint $\|\underline{a}_1^+\|_2^2 = 1$. This yields the optimization problem

$$\underline{a}_{\text{svd}} = \arg \min_{\|\underline{a}_1^+\|_2=1} \|S_{11} \cdot \underline{a}_1^+\|_2^2, \quad (4.11)$$

where we have relaxed the difficult constraint $\underline{a}_1^+ \in P_1^M$ into the spherical constraint $\|\underline{a}_1^+\|_2 = 1$. Although the original unrelaxed backscatter minimization problem in Eq. (4.9) is hard to solve, the relaxed problem in Eq. (4.11) is much easier and can be solved exactly.

Let $S_{21} = \sum_{i=1}^M \sigma_i \underline{u}_i \cdot \underline{v}_i^H$ and $S_{11} = \sum_{i=1}^M \tilde{\sigma}_i \tilde{\underline{u}}_i \cdot \tilde{\underline{v}}_i^H$ denote the singular value decompositions (SVD) of S_{21} and S_{11} , respectively. Here σ_i (resp. $\tilde{\sigma}_i$) is the singular value associated with the left and right singular vectors \underline{u}_i and \underline{v}_i (resp. $\tilde{\underline{u}}_i$ and $\tilde{\underline{v}}_i$), respectively. By convention, the singular values are arranged so that $\sigma_1 \geq \dots \geq \sigma_M$ and $\tilde{\sigma}_1 \geq \dots \geq \tilde{\sigma}_M$ and H denotes the complex conjugate transpose. In the lossless setting we have that $S_{11}^H \cdot S_{11} + S_{21}^H \cdot S_{21} = I$ so that $\underline{v}_i = \tilde{\underline{v}}_{M-i+1}$. Then, a well-known result in matrix analysis [31] states that

$$\underline{a}_{\text{svd}} = \tilde{\underline{v}}_M = \underline{v}_1. \quad (4.12)$$

This is an exact solution to the relaxed backscatter minimization problem in Eq. (4.11).

To get an approximation of the solution to the original unrelaxed problem in Eq. (4.10) we construct a highly-transmitting wavefront as

$$\underline{a}_{\text{opt,svd}} = \underline{p}(\underline{a}_{\text{svd}}). \quad (4.13)$$

Note that $\underline{a}_{\text{opt,svd}}$ given by Eq. (4.13) is an approximation to the solution of Eq. (4.10). It is not guaranteed to be the phase-only modulated wavefront that yields the highest transmission. It does, however, provide a lower bound on the amount of transmission that can be achieved using phase-only modulated wavefronts. As we shall see in Section 4.6, it produces highly transmitting wavefronts for the scattering systems considered here.

The spherical relaxation that yields the optimization problem in Eq. (4.11) includes all the phase-only wavefronts in the original problem, but also includes many other wavefronts as well. We now consider a ‘tighter’ relaxation that includes all the

phase-only wavefronts in the original problem but fewer other wavefronts than the spherical relaxation does.

We begin by examining the objective function on the right hand side of Eq. (4.11). Note that

$$\|S_{11} \cdot \underline{a}_1^+\|_2^2 = ((\underline{a}_1^+)^H \cdot S_{11}^H \cdot S_{11} \cdot \underline{a}_1^+) = \text{Tr} (S_{11}^H \cdot S_{11} \cdot \underline{a}_1^+ \cdot (\underline{a}_1^+)^H), \quad (4.14)$$

where $\text{Tr}(\cdot)$ denotes the trace of its matrix argument. Let us define a new matrix-valued variable $A = \underline{a}_1^+ \cdot (\underline{a}_1^+)^H$. We note that A is a Hermitian, positive semi-definite matrix with rank 1 and $A_{ii} = 1/M$ whenever $\underline{a}_1^+ \in P_1^M$, where A_{ii} denotes the i th diagonal element of the matrix A . Consequently, from Eq. (4.14), we can derive the modified optimization problem

$$\begin{aligned} A_{\text{opt}} &= \arg \min_{A \in \mathbb{C}^{M \times M}} \text{Tr} (S_{11}^H \cdot S_{11} \cdot A) \\ &\text{subject to } A = A^H, A \succeq 0, \text{rank}(A) = 1 \text{ and } A_{ii} = 1/M \text{ for } i = 1, \dots, M, \end{aligned} \quad (4.15)$$

where the conditions $A = A^H$ and $A \succeq 0$ imply that A is a Hermitian, positive semi-definite matrix. If we can solve Eq. (4.15) exactly, then by construction, since A_{opt} is rank 1, we must have that $A_{\text{opt}} = \underline{a}_{\text{opt,eig}} \cdot \underline{a}_{\text{opt,eig}}^H$ with $\underline{a}_{\text{opt,eig}} \in P_1^M$ so we would have solved Eq. (4.10) exactly. Alas, the rank constraint in Eq. (4.15) makes the problem computationally intractable.

Eliminating the difficult rank constraint yields the semi-definite programming (SDP) problem [50]

$$\begin{aligned} A_{\text{sdp}} &= \arg \min_{A \in \mathbb{C}^{M \times M}} \text{Tr} (S_{11}^H \cdot S_{11} \cdot A) \\ &\text{subject to } A = A^H, A \succeq 0, \text{ and } A_{ii} = 1/M \text{ for } i = 1, \dots, M, \end{aligned} \quad (4.16)$$

which can be efficiently solved in polynomial-time [49] using off-the shelf solvers such as CVX [51, 52] or SDPT3 [53]. Specifically, the solution to Eq. (4.16) can be computed in MATLAB using the CVX package by invoking the following sequence of commands:

```
cvx_begin sdp
    variable A(M,M) hermitian
    minimize trace(S11'*S11*A)
    subject to
        A >= 0;
        diag(A) == ones(M,1)/M;
cvx_end
Asdp = A; % return optimum in variable Asdp
```

For settings where $M > 100$, we recommend using the SDPT3 solver. The solution to Eq. (4.16) can be computed in MATLAB using the SDPT3 package by invoking the following sequence of commands:

```

cost_function = S11'*S11;
e = ones(M,1); b = e/M;
num_params = M*(M-1)/2;
C{1} = cost_function;
A = cell(1,M); for j = 1:M, A{j} = sparse(j,j,1,M,M); end
blk{1,1} = 's'; blk{1,2} = M; Avec = svec(blk(1,:),A,1);
[obj,X,y,Z] = sqlp(blk,Avec,C,b);
Asdp = cell2mat(X); % return optimum in variable Asdp

```

We note that A_{sdp} is the solution to the relaxed backscatter minimization problem in Eq. (4.16). If A_{sdp} thus obtained has rank 1 then we will have solved the original unrelaxed problem in Eq. (4.10) exactly as well. Typically, however, the matrix A_{sdp} will not be rank one so we describe a procedure next for obtaining an approximation to the original unrelaxed problem in Eq. (4.10).

Let $A_{\text{sdp}} = \sum_{i=1}^M \lambda_i \underline{u}_{i,\text{sdp}} \cdot \underline{u}_{i,\text{sdp}}^H$ denote the eigenvalue decomposition of A_{sdp} with the eigenvalues arranged so that $\lambda_1 \geq \dots \lambda_M \geq 0$. Then we can construct a highly-transmitting phase modulated wavefront as

$$\underline{a}_{\text{opt,sdp}} = \underline{p}(\underline{u}_{1,\text{sdp}}). \quad (4.17)$$

Note that $\underline{a}_{\text{opt,sdp}}$ given by Eq. (4.17) is an approximation to the solution of Eq. (4.10). It is not guaranteed to be the phase-only modulated wavefront that yields the highest transmission. It does however provide a lower bound on the amount of transmission that can be achieved. Since the SDP relaxation is a tighter relaxation than the spherical relaxation [49], we expect $\underline{a}_{\text{opt,sdp}}$ to result in higher transmission than $\underline{a}_{\text{opt,svd}}$.

We note that the computational cost of solving Eq. (4.16) and obtaining A_{sdp} is $O(M^{4.5})$ [49] while the computational cost for obtaining $\underline{a}_{\text{opt,svd}}$ using the Lanczos method for computing only the leading singular vector is $O(M^2)$ [54]. Thus when $M > 1000$, there is a significant extra computational burden in obtaining the SDP solution. Hence, the question of when the extra computational burden of solving the SDP relaxation yields ‘large enough’ gains relative to the spherical relaxation is of interest. We provide an answer using extensive numerical simulations in Section 4.6.

We have described two non-iterative techniques for increasing transmission via backscatter analysis that first require the S_{11} to be measured and then compute $\underline{a}_{\text{opt,svd}}$ or $\underline{a}_{\text{opt,sdp}}$ using Eq. (4.13) and Eq. (4.17), respectively. We now provide a theoretical analysis of the transmission power we can expect to achieve using these phase-only modulated wavefronts.

4.4 Theoretical limit of phase-only modulated light transmission

When the wavefront $\underline{a}_{\text{svd}}$ is excited, the optimal transmitted power is $\tau_{\text{opt}} := \tau(\underline{a}_{\text{opt}}) = \sigma_1^2$. Similarly, when the wavefront associated with the i -th right singular vector \underline{v}_i is transmitted, the transmitted power is $\tau(\underline{v}_i) = \sigma_i^2$, which we refer to as

the transmission coefficient of the i -th eigen-wavefront of S_{21} . Analogously, we refer to $\Gamma(\underline{v}_i)$ as the reflection coefficient of the i -th eigen-wavefront of S_{21} .

The theoretical distribution [3, 4, 5, 6, 7] of the transmission coefficients for lossless random media (referred to as the DMPK distribution) has density given by

$$f(\tau) = \lim_{M \rightarrow \infty} \frac{1}{M} \sum_{i=1}^M \delta(\tau - \tau(\underline{v}_i)) = \frac{l}{2L} \frac{1}{\tau \sqrt{1 - \tau}}, \quad \text{for } 4 \exp(-L/2l) \lesssim \tau \leq 1. \quad (4.18)$$

In Eq. (4.18), l is the mean-free path through the medium. This implies that in the regime where the DMPK distribution is valid, we expect $\tau(\underline{a}_{\text{opt}}) \approx 1$ so that (near) perfect transmission is possible using amplitude and phase modulation. We now analyze the theoretical limit of phase-only modulation in the setting where the S_{21} (or S_{11}) matrix has been measured and we have computed $\underline{a}_{\text{opt,svd}}$ or $\underline{a}_{\text{opt,sdp}}$ as in Eq. (4.13) and Eq. (4.17), respectively. In what follows, we prove a lower bound on the transmission we expect to achieve in the regime where the DMPK distribution is valid.

We begin by considering the wavefront $\underline{a}_{\text{opt,svd}}$ which yields a transmission power given by

$$\tau(\underline{a}_{\text{opt,svd}}) = \tau(\underline{p}(\underline{v}_{\underline{a}_{\text{opt,svd}}})) = \|S_{21} \cdot \underline{p}(\underline{v}_{\underline{a}_{\text{opt,svd}}})\|_2^2 \quad (4.19)$$

$$= \|U \cdot \Sigma \cdot V^H \cdot \underline{p}(\underline{v}_{\underline{a}_{\text{opt,svd}}})\|_2^2 = \|\Sigma \cdot V^H \cdot \underline{p}(\underline{v}_{\underline{a}_{\text{opt,svd}}})\|_2^2. \quad (4.20)$$

Define $\tilde{\underline{p}}(\underline{v}_{\underline{a}_{\text{opt,svd}}}) = V^H \cdot \underline{p}(\underline{v}_{\underline{a}_{\text{opt,svd}}})$. Then from Eq. (4.20), we have that

$$\tau(\underline{a}_{\text{opt,svd}}) = \|\Sigma \cdot \tilde{\underline{p}}(\underline{v}_{\underline{a}_{\text{opt,svd}}})\|_2^2 \quad (4.21)$$

$$= \sum_{i=1}^M \sigma_i^2 |\tilde{p}_i(\underline{v}_{\underline{a}_{\text{opt,svd}}})|^2 \geq \sigma_1^2 |\tilde{p}_1(\underline{v}_{\underline{a}_{\text{opt,svd}}})|^2. \quad (4.22)$$

In the DMPK regime, we have that $\sigma_1^2 \approx 1$ from which we can deduce that

$$\tau(\underline{a}_{\text{opt,svd}}) \gtrsim |\tilde{p}_1(\underline{v}_{\underline{a}_{\text{opt,svd}}})|^2. \quad (4.23)$$

From Eq. (4.12), we have that $\underline{a}_{\text{svd}} = \underline{v}_1 = \tilde{\underline{v}}_M$ so that if

$$\underline{v}_1^H = \left[|v_{1,1}| e^{-j\angle v_{1,1}} \quad \dots \quad |v_{1,M}| e^{-j\angle v_{1,M}} \right],$$

then

$$\tilde{p}_1(\underline{v}_{\underline{a}_{\text{opt,svd}}}) = \underline{v}_1^H \cdot \underline{p}(\underline{v}_1) = \frac{1}{\sqrt{M}} \sum_{i=1}^M |v_{1,i}|, \quad (4.24)$$

and

$$|\tilde{p}_1(\underline{v}_{\underline{a}_{\text{opt,svd}}})|^2 = \frac{1}{M} \sum_{i=1}^M |v_{1,i}|^2 + \frac{2}{M} \sum_{i < j} |v_{1,i}| \cdot |v_{1,j}|. \quad (4.25)$$

Substituting Eq. (4.25) into Eq. (4.23) gives

$$\tau(\underline{a}_{\text{opt,svd}}) \gtrsim \frac{1}{M} \sum_{i=1}^M |v_{1,i}|^2 + \frac{2}{M} \sum_{i < j} |v_{1,i}| \cdot |v_{1,j}|. \quad (4.26)$$

Taking expectations on both sides of Eq. (4.26) and invoking the linearity of the expectation operator gives us

$$\mathbb{E} [\tau(\underline{a}_{\text{opt,svd}})] \gtrsim \frac{1}{M} \sum_{i=1}^M \mathbb{E} [|v_{1,i}|^2] + \frac{2}{M} \sum_{i < j} \mathbb{E} [|v_{1,i}| \cdot |v_{1,j}|]. \quad (4.27)$$

We now invoke the maximum-entropy principle as in Pendry's derivation [4, 5] and assume that the vector \underline{v}_1 , is uniformly distributed on the unit hypersphere. Since the uniform distribution is symmetric, for any indices i and j , we have that $\mathbb{E} [|v_{1,i}|^2] = \mathbb{E} [|v_{1,1}|^2]$ and $\mathbb{E} [|v_{1,i}| \cdot |v_{1,j}|] = \mathbb{E} [|v_{1,1}| \cdot |v_{1,2}|]$. Consequently Eq. (4.27) simplifies to

$$\mathbb{E} [\tau(\underline{a}_{\text{opt,svd}})] \gtrsim \mathbb{E} [|v_{1,1}|^2] + \frac{2M(M-1)}{2M} \mathbb{E} [|v_{1,1}| \cdot |v_{1,2}|] \quad (4.28)$$

Since $\|\underline{v}_1\|_2^2 = \sum_{i=1}^M |v_{1,i}|^2 = 1$, we have that

$$\mathbb{E} [|v_{1,1}|^2] = O\left(\frac{1}{M}\right). \quad (4.29)$$

Substituting Eq. (4.29) into Eq. (4.28) gives

$$\mathbb{E} [\tau(\underline{a}_{\text{opt,svd}})] \gtrsim (M-1) \mathbb{E} [|v_{1,1}| \cdot |v_{1,2}|] + O\left(\frac{1}{M}\right). \quad (4.30)$$

We now note that

$$\mathbb{E} [|v_{1,1}| \cdot |v_{1,2}|] = \mathbb{E} [|v_{1,1}|] \cdot \mathbb{E} [|v_{1,2}|] + \text{cov}(|v_{1,1}|, |v_{1,2}|), \quad (4.31)$$

$$= \mathbb{E}^2 [|v_{1,1}|] + \text{cov}(|v_{1,1}|, |v_{1,2}|), \quad (4.32)$$

where

$$\text{cov}(|v_{1,1}|, |v_{1,2}|) = \mathbb{E} [\{|v_{1,1}| - \mathbb{E}[|v_{1,1}|]\} \cdot \{|v_{1,2}| - \mathbb{E}[|v_{1,2}|]\}], \quad (4.33)$$

is the covariance between the random variables $|v_{1,1}|$ and $|v_{1,2}|$. A useful fact that will facilitate analytical progress is that the complex-valued random variable $v_{1,1}$ has the same distribution [55, Chap. 3a] as the vector

$$\frac{g_1}{\sqrt{|g_1|^2 + \dots + |g_M|^2}},$$

where $g_i = x_i + \sqrt{-1}y_i$ and x_i and y_i are i.i.d. normally distributed variables with mean zero and variance $1/(2M)$. This implies that the variable $|v_{1,1}|^2$ is beta distributed since $|g_1|^2$ and $|g_1|^2 + \dots + |g_M|^2$ are chi-square distributed. Hence, it can be easily seen that

$$\text{cov}(|v_{1,1}|, |v_{1,2}|) = O\left(\frac{1}{M^2}\right) \quad (4.34)$$

and

$$\mathbb{E}[|v_{1,1}|] = \sqrt{\frac{\pi}{4M}} + O\left(\frac{1}{M}\right), \quad (4.35)$$

where the first term on the righthand side of Eq. (4.35) equals $\mathbb{E}[|g_i|]$. Substituting Eq. (4.34) and Eq. (4.35) into Eq. (4.32) gives us an expression for $\mathbb{E}[|v_{1,1}| \cdot |v_{1,2}|]$, which on substituting into the right-hand side of Eq. (4.30) yields the inequality

$$\mathbb{E}[\tau(\underline{a}_{\text{opt,svd}})] \gtrsim \frac{\pi}{4} + O\left(\frac{1}{M}\right). \quad (4.36)$$

Since $\tau(\underline{a}_{\text{opt,sdp}}) \geq \tau(\underline{a}_{\text{opt,svd}})$, Eq. (4.36) yields the inequality

$$\mathbb{E}[\tau(\underline{a}_{\text{opt,sdp}})] \geq \mathbb{E}[\tau(\underline{a}_{\text{opt,svd}})] \gtrsim \frac{\pi}{4} + O\left(\frac{1}{M}\right). \quad (4.37)$$

Letting $M \rightarrow \infty$ on both sides on Eq. (4.37) gives us

$$\lim_{M \rightarrow \infty} \mathbb{E}[\tau(\underline{a}_{\text{opt,sdp}})] \geq \lim_{M \rightarrow \infty} \mathbb{E}[\tau(\underline{a}_{\text{opt,svd}})] \gtrsim \frac{\pi}{4}. \quad (4.38)$$

From Eq. (4.38) we expect to achieve at least 25 $\pi\%$ when the S_{21} (or S_{11}) matrix has been measured and we compute the phase-only modulated wavefront using $\underline{a}_{\text{opt,svd}}$ or $\underline{a}_{\text{opt,sdp}}$. In contrast, amplitude and phase modulation yields (nearly) 100% transmission; thus the phase-only modulation incurs an (average) loss of at most 22%.

We now develop rapidly-converging, physically-realizable, iterative algorithms for increasing transmission by backscatter minimization that utilize significantly fewer measurements than the $O(M)$ measurements it would take to first estimate S_{11} and subsequently construct $\underline{a}_{\text{opt,svd}}$ or $\underline{a}_{\text{opt,sdp}}$.

4.5 Iterative, phase-only modulated algorithms for transmission maximization

4.5.1 Steepest Descent Method

We first consider an iterative method, based on the method of steepest descent, for finding the wavefront \underline{a}_1^+ that minimizes the objective function $\|S_{11} \cdot \underline{a}_1^+\|_2^2$. At this stage, we consider arbitrary vectors \underline{a}_1^+ instead of phase-only modulated vectors $\underline{a}_1^+ \in P_1^M$. The algorithm utilizes the negative gradient of the objective function to update the incident wavefront as

$$\tilde{\underline{a}}_{1,(k)}^+ = \underline{a}_{1,(k)}^+ - \mu \left. \frac{\partial \|S_{11} \cdot \underline{a}_1^+\|_2^2}{\partial \underline{a}_1^+} \right|_{\underline{a}_1^+ = \underline{a}_{1,(k)}^+} \quad (4.39)$$

$$= \underline{a}_{1,(k)}^+ - 2\mu S_{11}^H \cdot S_{11} \cdot \underline{a}_{1,(k)}^+, \quad (4.40)$$

where $\underline{a}_{1,(k)}^+$ represents the modal coefficient vector of the incident wavefront produced at the k -th iteration of the algorithm and μ is a positive stepsize. If we renormalize

$\tilde{\underline{a}}_{1,(k)}^+$ to have $\|\tilde{\underline{a}}_{1,(k)}^+\|_2 = 1$, then we obtain Algorithm 3 which was already discussed in Chapter III. In the limit of $k \rightarrow \infty$, the incident wavefront $\underline{a}_{1,(k+1)}^+$ will converge to $\underline{a}_{\text{svd}}$.

We now describe how the update equation given by Eq. (4.40), which requires computation of the gradient $S_{11}^H \cdot S_{11} \cdot \underline{a}_{1,(k)}^+$, can be physically implemented even though we have not measured S_{11} a priori.

Let $\text{flipud}(\cdot)$ represent the operation of flipping a vector or a matrix argument upside down so that the first row becomes the last row and so on. Let $F = \text{flipud}(I)$ where I is the identity matrix, and let $*$ denote complex conjugation. In subsection 2.4.3, we showed that reciprocity of the scattering system implies that

$$S_{11}^H = F \cdot S_{11}^* \cdot F, \quad (4.41)$$

which can be exploited to make the gradient vector $S_{11}^H \cdot S_{11} \cdot \underline{a}_{1,(k)}^+$ physically measurable. To that end, we note that Eq. (4.41) implies that

$$S_{11}^H \cdot \underline{a}_1^- = F \cdot S_{11}^* \cdot F \cdot \underline{a}_1^- = F \cdot (S_{11} \cdot (F \cdot (\underline{a}_1^-)^*))^*. \quad (4.42)$$

where $\underline{a}_1^- = S_{11} \cdot \underline{a}_{1,(k)}^+$. Thus, we can physically measure $S_{11}^H \cdot S_{11} \cdot \underline{a}_{1,(k)}^+$, by performing the following sequence of operations and the accompanying measurements:

1. Transmit $\underline{a}_{1,(k)}^+$ and measure the backscattered wavefront $\underline{a}_1^- = S_{11} \cdot \underline{a}_{1,(k)}^+$.
2. Transmit the wavefront obtained by time-reversing the wavefront whose modal coefficient vector is \underline{a}_1^- or equivalently transmitting the wavefront $F \cdot (\underline{a}_1^-)^*$.
3. Measure the resulting backscattered wavefront corresponding to $S_{11} \cdot (F \cdot (\underline{a}_1^-)^*)$ and time-reverse it to yield the desired gradient vector $S_{11}^H \cdot S_{11} \cdot \underline{a}_{1,(k)}^+$ as shown in Eq. (4.42).

The above represents a physically realizable scheme for measuring the gradient vector, which we proposed in our previous paper [21]. Since time-reversal can be implemented using phase-conjugating mirror [32], we referred to our algorithm a *double phase-conjugating method*.

For the setting considered here, we have the additional physically-motivated restriction that all transmitted wavefronts $\underline{a}_1^+ \in P_1^M$. However, the wavefront \underline{a}_1^- can have arbitrary amplitudes and so will the wavefront obtained by time-reversing it (as in Step 2 above) thereby violating the phase-only modulating restriction and making Algorithm ??, physically unrealizable. This is also why algorithms of the sort considered by others in array processing [56] cannot be directly applied here.

This implies that even though Algorithm ?? probably converges to $\underline{a}_{\text{svd}}$, it cannot be used to compute $\underline{a}_{\text{opt,svd}}$ as in Eq. (4.13) because it is not physically implementable given the phase-only modulation constraint. To mitigate this problem, we propose modifying the update step in Eq. (4.40) to

$$\tilde{\underline{a}}_{1,(k)}^+ = \underline{p} \left(\underline{a}_{1,(k)}^+ - 2\mu\bar{a} S_{11}^H \cdot \underline{p}(\underline{S}_{11} \cdot \underline{a}_{1,(k)}^+) \right), \quad (4.43)$$

Vector Operation	Physical Operation
1 : $\underline{a}_1^- = S_{11} \cdot \underline{a}_{1,(k)}^+$	1 : $\underline{a}_{1,(k)}^+ \xrightarrow{\text{Backscatter}} \underline{a}_1^-$
2 : $\bar{a} = \frac{\sum_{n=-N}^N a_{1,n}^- }{\sqrt{M}}$	2 : $\bar{a} = \frac{\sum_{n=-N}^N a_{1,n}^- }{\sqrt{M}}$
3 : $\underline{a}_1^- \leftarrow \underline{p}(\underline{a}_1^-)$	3 : $\underline{a}_1^- \leftarrow \underline{p}(\underline{a}_1^-)$
4 : $\underline{a}_1^+ = F \cdot (\underline{a}_1^-)^*$	4 : $\underline{a}_1^- \xrightarrow{\text{PCM}} \underline{a}_1^+$
5 : $\underline{a}_1^- = S_{11} \cdot \underline{a}_1^+$	5 : $\underline{a}_1^+ \xrightarrow{\text{Backscatter}} \underline{a}_1^-$
6 : $\underline{a}_1^+ = F \cdot (\underline{a}_1^-)^*$	6 : $\underline{a}_1^- \xrightarrow{\text{PCM}} \underline{a}_1^+$
7 : $\tilde{\underline{a}}_1^+ = \underline{a}_{1,(k)}^+ - 2\mu\bar{a}\underline{a}_1^+$	7 : $\tilde{\underline{a}}_1^+ = \underline{a}_{1,(k)}^+ - 2\mu\bar{a}\underline{a}_1^+$
8 : $\underline{a}_{1,(k+1)}^+ = \underline{p}(\underline{\tilde{a}}_1^+)$	8 : $\underline{a}_{1,(k+1)}^+ = \underline{p}(\underline{\tilde{a}}_1^+)$

Table 4.1: Steepest descent algorithm for refining a highly transmitting phase-only modulated wavefront. The first column represents vector operations. The second column represents the physical (or experimental) counterpart. The operation $\underline{a}_1^- \mapsto F \cdot (\underline{a}_1^-)^*$ can be realized via the use of a phase-conjugating mirror (PCM). The algorithm terminates when the backscatter intensity falls below a preset threshold ϵ .

where \bar{a} is chosen such that all magnitudes of modal coefficients of $\bar{a}\underline{p}(\underline{a}_1^-)$ are set to the average magnitude of modal coefficients of \underline{a}_1^- . Then, by applying Eq. (4.41) as before, we can physically measure $\bar{a} S_{11}^H \cdot \underline{p}(\underline{S}_{11} \cdot \underline{a}_{1,(k)}^+)$ by performing the following sequence of operations and the accompanying measurements:

1. Transmit $\underline{a}_{1,(k)}^+$ and measure the backscattered wavefront $\underline{a}_1^- = S_{11} \cdot \underline{a}_{1,(k)}^+$.
2. Compute the scalar $\bar{a} = \frac{\sum_{n=-N}^N |a_{1,n}^-|}{\sqrt{M}}$.
3. Transmit the (phase-only modulated) wavefront obtained by time-reversing the wavefront whose modal coefficient vector is $\underline{p}(\underline{a}_1^-)$.
4. Measure the resulting backscattered wavefront, time-reverse it, and scale it with \bar{a} to yield the desired gradient vector.

This modified iteration in Eq. (4.43) leads to the algorithm in the left column of Table 4.1 and its physical counterpart in the right column of Table 4.1.

4.5.2 Gradient Method

The wavefront updating step for the algorithm described in Table 4.1 first updates both the amplitude and phase of the incident wavefront (in Step 7) and then ‘projects

it' onto the set of phase-only modulated wavefronts (in Step 8). We now develop a gradient-based method that only updates the phase of the incident wavefront. From Eq. (4.9), the objective function of interest is $\|S_{11} \cdot \underline{p}(\underline{\theta})\|_2^2$ which depends on the phase-only modulated wavefront. The algorithm utilizes the negative gradient of the objective function with respect to the phase vector to update the phase vector of the incident wavefront as

$$\underline{\theta}_{1,(k+1)}^+ = \underline{\theta}_{1,(k)}^+ - \sqrt{M}\mu \left. \frac{\partial \|S_{11} \cdot \underline{p}(\underline{\theta})\|_2^2}{\partial \underline{\theta}} \right|_{\underline{\theta}=\underline{\theta}_{1,(k)}^+}, \quad (4.44)$$

where $\underline{\theta}_{1,(k)}^+$ represents the phase vector of the wavefront produced at the k -th iteration of the algorithm and μ is a positive stepsize. We have separated the \sqrt{M} factor from the stepsize so that μ can be $O(1)$ and independent of M . In Appendix VI, we show that

$$\left. \frac{\partial \|S_{11} \cdot \underline{p}(\underline{\theta})\|_2^2}{\partial \underline{\theta}} \right|_{\underline{\theta}=\underline{\theta}_{1,(k)}^+} = 2\text{Im} \left[\text{diag}\{\underline{p}(-\underline{\theta}_{1,(k)}^+)\} \cdot S_{11}^H \cdot S_{11} \cdot \underline{p}(\underline{\theta}_{1,(k)}^+) \right], \quad (4.45)$$

where $\text{diag}\{\underline{p}(-\underline{\theta}_{1,(k)}^+)\}$ denotes a diagonal matrix with entries $\underline{p}(-\underline{\theta}_{1,(k)}^+)$ along its diagonal. Substituting Eq. (4.45) into the right-hand side of Eq. (4.44) yields the iteration

$$\underline{\theta}_{1,(k+1)}^+ = \underline{\theta}_{1,(k)}^+ - 2\sqrt{M}\mu \text{Im} \left[\text{diag}\{\underline{p}(-\underline{\theta}_{1,(k)}^+)\} \cdot S_{11}^H \cdot S_{11} \cdot \underline{p}(\underline{\theta}_{1,(k)}^+) \right]. \quad (4.46)$$

To evaluate the update Eq. (4.46), it is necessary to measure the gradient vector $S_{11}^H \cdot S_{11} \cdot \underline{p}(\underline{\theta}_{1,(k)}^+)$. For the same reason as in the steepest descent scheme, we cannot use double-phase conjugation introduced in our previous paper because of the phase-only modulating restriction. Therefore, we propose modifying the update step in Eq. (4.46) to

$$\underline{\theta}_{1,(k+1)}^+ = \underline{\theta}_{1,(k)}^+ - 2\sqrt{M}\mu \bar{a} \text{Im} \left[\text{diag}\{\underline{p}(-\underline{\theta}_{1,(k)}^+)\} \cdot S_{11}^H \cdot \underline{p}(\underline{S}_{11} \cdot \underline{p}(\underline{\theta}_{1,(k)}^+)) \right], \quad (4.47)$$

and we use the modified double-phase conjugation as

1. Transmit $\underline{p}(\underline{\theta}_{1,(k)}^+)$ and measure the backscattered wavefront $\underline{a}_1^- = S_{11} \cdot \underline{p}(\underline{\theta}_{1,(k)}^+)$;
2. Compute the scalar $\bar{a} = \frac{\sum_{n=-N}^N |a_{1,n}^-|}{\sqrt{M}}$;
3. Transmit the phase-only modulated wavefront obtained by time-reversing the wavefront whose modal coefficient vector is $\underline{p}(\underline{a}_1^-)$;
4. Measure the resulting backscattered wavefront, time-reverse it, and scale it with \bar{a} to yield the desired gradient vector.

The phase-updating iteration in Eq. (4.47) leads to the algorithm in the left column of Table 4.2 and its physical counterpart in the right column of Table 4.1.

Vector Operation	Physical Operation
1 : $\underline{a}_1^- = S_{11} \cdot \underline{p}(\theta_{1,(k)}^+)$	1 : $\underline{p}(\theta_{1,(k)}^+) \xrightarrow{\text{Backscatter}} \underline{a}_1^-$
2 : $\bar{a} = \frac{\sum_{n=-N}^N a_{1,n}^- }{\sqrt{M}}$	2 : $\bar{a} = \frac{\sum_{n=-N}^N a_{1,n}^- }{\sqrt{M}}$
3 : $\underline{a}_1^- \leftarrow \underline{p}(\underline{a}_1^-)$	3 : $\underline{a}_1^- \leftarrow \underline{p}(\underline{a}_1^-)$
4 : $\underline{a}_1^+ = F \cdot (\underline{a}_1^-)^*$	4 : $\underline{a}_1^- \xrightarrow{\text{PCM}} \underline{a}_1^+$
5 : $\underline{a}_1^- = S_{11} \cdot \underline{a}_1^+$	5 : $\underline{a}_1^+ \xrightarrow{\text{Backscatter}} \underline{a}_1^-$
6 : $\underline{a}_1^+ = F \cdot (\underline{a}_1^-)^*$	6 : $\underline{a}_1^- \xrightarrow{\text{PCM}} \underline{a}_1^+$
7 : $\theta_{1,(k+1)}^+ = \theta_{1,(k)}^+ - 2\sqrt{M}\mu\bar{a}\text{Im} \left[\text{diag}\{\underline{p}(-\theta_{1,(k)}^+)\} \cdot \underline{a}_1^+ \right]$	

Table 4.2: Gradient descent algorithm for transmission maximization. The first column contains the updating iteration in Eq. (4.47) split into a series of individual updates so that they may be mapped into their physical (or experimental) counterparts in the column to their right. The operation $\underline{a}_1^- \mapsto F \cdot (\underline{a}_1^-)^*$ can be realized via the use of a phase-conjugating mirror (PCM). The algorithm terminates when the backscatter intensity falls below a preset threshold ϵ .

4.6 Numerical simulations

To validate the proposed algorithms and the theoretical limits of phase-only wavefront optimization, we adopt the numerical simulation protocol described in [21]. Specifically, we compute the scattering matrices in Eq. (4.2) via a spectrally accurate, T-matrix inspired integral equation solver that characterizes fields scattered from each cylinder in terms of their traces expanded in series of azimuthal harmonics. As in [21], interactions between cylinders are modeled using 2D periodic Green's functions. The method constitutes a generalization of that in [47], in that it does not force cylinders in a unit cell to reside on a line but allows them to be freely distributed throughout the cell. As in [21], all periodic Green's functions/lattice sums are rapidly evaluated using a recursive Shank's transform using the methods described in [48, 29]. Our method exhibits exponential convergence in the number of azimuthal harmonics used in the description of the field scattered by each cylinder. As in [21], in the numerical experiments below, care was taken to ensure 11-digit accuracy in the entries of the computed scattering matrices.

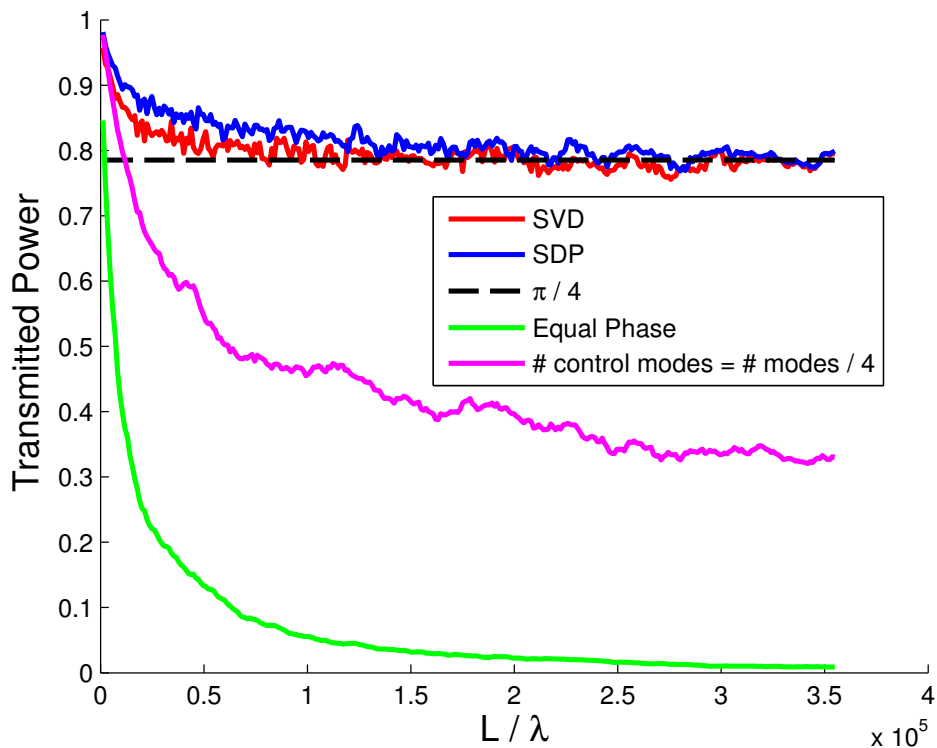


Figure 4.3: Plot of transmitted power obtained by SVD or SDP versus the thickness L/λ in a setting with $D = 197\lambda$, $r = 0.11\lambda$, $N_c = 430,000$, $n_d = 1.3$, $M = 395$, $\bar{l} = 6.69\lambda$. SDP had 2.5% improvement compared to SVD on average.

First we compare the transmission power achieved by the non-iterative algorithms that utilize measurements of the S_{11} matrix to compute the wavefronts $\underline{a}_{\text{opt,svd}}$ and $\underline{a}_{\text{opt,sdp}}$ given by Eq. (4.13) and Eq. (4.17), respectively. Here we have a scattering system with $D = 197\lambda$, $r = 0.11\lambda$, $N_c = 430,000$, $n_d = 1.3$, $M = 395$ and $\bar{l} = 6.69\lambda$, where \bar{l} is the average distance to the nearest scatterer. Fig. 4.3 plots transmitted power for the SVD and SDP based algorithms as a function of the thickness L/λ of the scattering system.

As expected, the wavefront $\underline{a}_{\text{opt,sdp}}$ realizes increased transmission relative to the wavefront $\underline{a}_{\text{opt,svd}}$. However, as the thickness of the medium increases, the gain vanishes. Typically $\underline{a}_{\text{opt,sdp}}$ increases transmission by about 1–5% relative to $\underline{a}_{\text{opt,svd}}$. Fig. 4.3 also shows the accuracy of our theoretical prediction of $25\pi\% \approx 78.5\%$ transmission using phase-only modulation for highly backscattering (or thick) random media in the same regime where the DMPK theory predicts perfect transmission using amplitude and phase modulated wavefronts.

Fig. 4.3 also plots the transmitted power achieved by an ‘equal phase’ wavefront with a modal coefficient vector $1/\sqrt{M} [1 \dots 1]^T$. Both the SVD and the SDP based algorithms realized significant gains relative to this vector.¹

¹A normally incident wavefront also yields about the same transmitted power. Note that a

Recall that the computational cost of computing $\underline{a}_{\text{opt,sdp}}$ is $O(M^{4.5})$ while the cost for computing $\underline{a}_{\text{opt,svd}}$ is $O(M^2)$. Fig. 4.3 suggests that for large M , the significant extra computational effort for computing $\underline{a}_{\text{opt,sdp}}$ might not be worth the effort for strongly scattering random media.

We also plot the transmitted power achieved by undersampling the number of control modes by a factor of 4, computing the resulting S_{21} matrix, and constructing the amplitude and phase modulated eigen-wavefront associated with the largest right singular vector. This is what would happen if we were to implement the ‘superpixel’-based amplitude and phase modulation scheme described in [20] in the framework of a system with periodic boundary conditions. As can be seen, phase-only modulation yields higher transmission than amplitude and phase modulation with undersampled modes. We are presently studying whether the same result holds true in systems without periodic boundary conditions as considered in [18].

normally incident wavefront cannot be synthesized using phase-only modulation using the setup in Fig. 4.1.

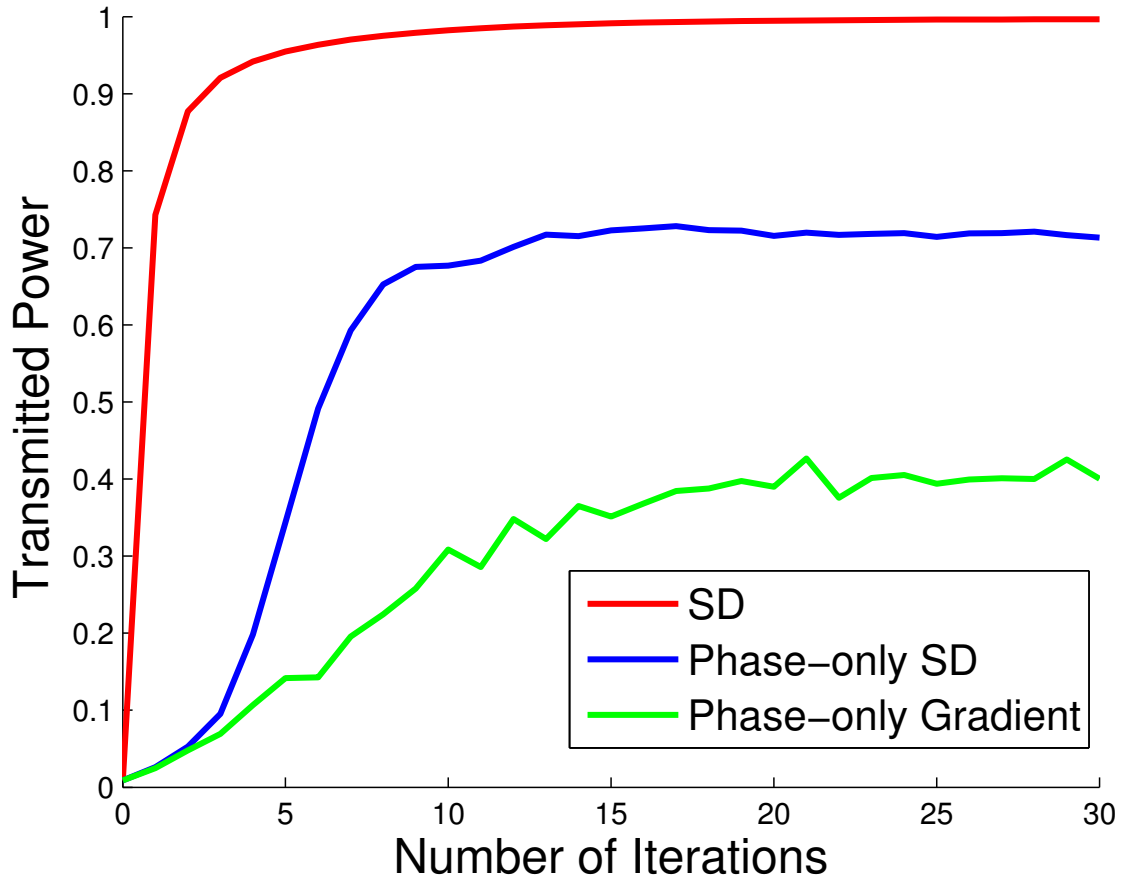


Figure 4.4: The transmitted power versus the number of iterations is shown for steepest descent algorithm with $\mu = 0.5059$, for phase-only steepest descent algorithm with $\mu = 0.6574$ and for phase-only gradient algorithm with $\mu = 1.4149$ in the setting with $D = 197\lambda$, $L = 3.4 \times 10^5\lambda$, $r = 0.11\lambda$, $N_c = 430,000$ dielectric cylinders with $n_d = 1.3$, $M = 395$, $\bar{l} = 6.69\lambda$. The phase-only steepest descent algorithm converged to the optimal transmitted power faster than the phase-only gradient algorithm.

Fig. 4.4 compares the rate of convergence of the phase-only modulated steepest descent (with $\mu = 0.6574$) and gradient descent (with $\mu = 1.4149$)-based algorithms and the rate of convergence of the amplitude and phase-only modulated steepest descent (with $\mu = 0.5059$) based algorithm from [21, Algorithm 1]. Here we are in a setting with $D = 197\lambda$, $L = 3.4 \times 10^5\lambda$, $r = 0.11\lambda$, $N_c = 430,000$ dielectric cylinders with $n_d = 1.3$, $M = 395$, $\bar{l} = 6.69\lambda$. In this setting, a normally incident wavefront results in a transmission of $\tau_{\text{normal}} = 0.038$. The wavefront $\underline{a}_{\text{svd}}$ yields $\tau_{\text{opt}} = 0.9973$ corresponding to a 26-fold increase in transmission. The amplitude and phase modulated steepest descent algorithm produces a wavefront that converges to 95% of the near optimum in about 5 – 10 iterations as shown in Fig. 4.4. The phase-only modulated steep-

est descent algorithm yields an 19-fold increase in transmission and converges within 5 – 10 iterations. The phase-only modulated gradient descent algorithm yields a 13-fold increase in transmission and converges in 15 – 20 iterations. The fast convergence properties of the steepest descent based method make it suitable for use in an experimental setting where it might be infeasible to measure the S_{11} matrix first.

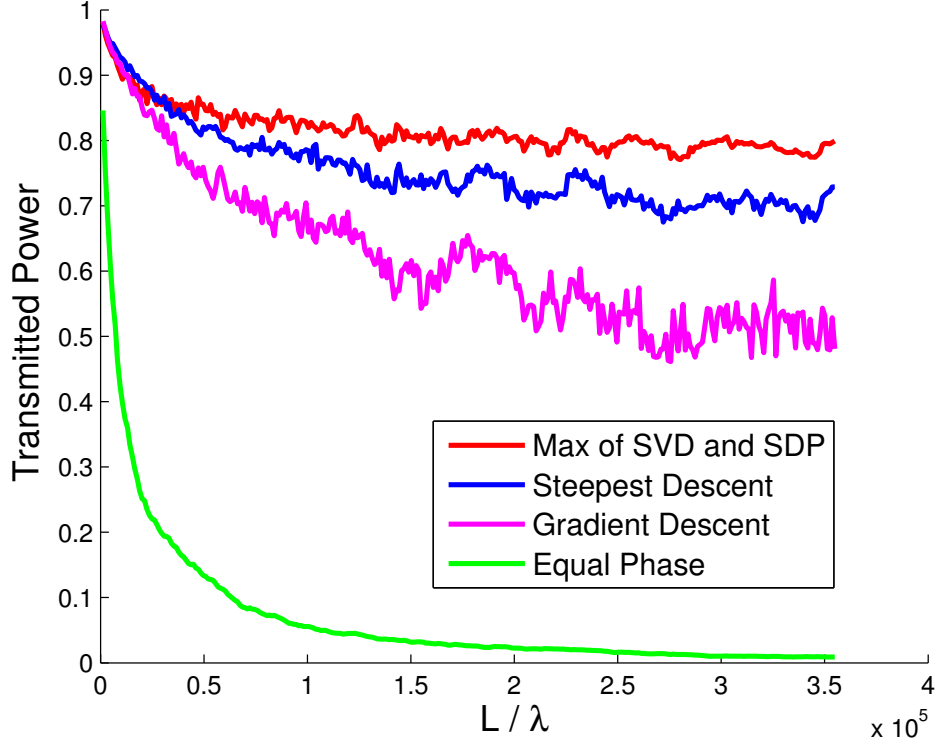


Figure 4.5: Maximum transmitted power in 50 iterations of SVD and SDP method, steepest descent, gradient descent and equal-phase input versus the thickness L/λ in a setting with $D = 197\lambda, r = 0.11\lambda, N_c = 430,000, n_d = 1.3, M = 395, \bar{l} = 6.69\lambda$. Max of SDP and SVD had 8.3% improvement compared to SD on average.

Fig. 4.5 compares the maximum transmitted power achieved after 50 iterations as a function of thickness L/λ for the iterative, phase-only modulated steepest descent and gradient descent methods and the non-iterative SVD and SDP methods. The non-iterative methods increase transmission by 8.3% relative to the steepest descent method. The gradient descent method performs poorly relative to the steepest descent method but still achieves increased transmission relative to the non-adaptive ‘equal-phase’ wavefront.

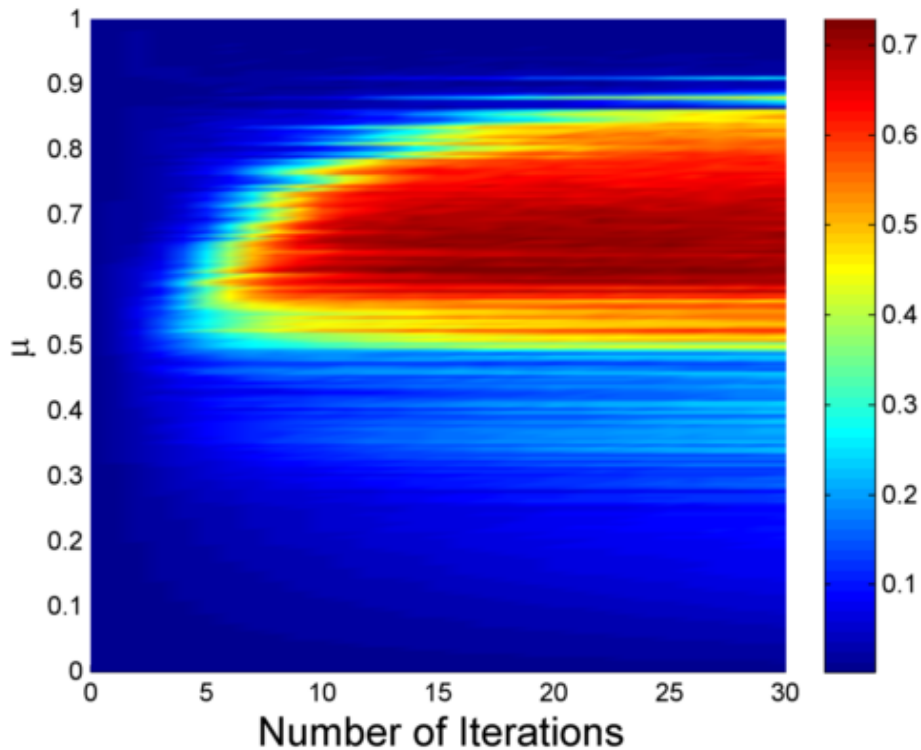


Figure 4.6: Heatmap of the transmitted power on the plane of number of iterations and stepsize μ used in steepest descent method for the same setting as in Fig. 4.4.

We next investigate the choice of stepsize μ on the performance of the algorithms. Fig. 4.4 shows the performance with the optimal μ for the phase-only modulated steepest descent and gradient descent algorithms. The optimal μ was obtained by a line search, i.e., by running the algorithms over a fixed set of discretized values of μ between 0 and μ_{\max} , and choosing the μ that produces the fastest convergence. In an experimental setting, the line search for finding the optimal μ for the steepest descent algorithm could require additional measurements. Fig. 4.6 plots the transmitted power as a function of the number of iterations and the stepsize μ for the phase-only modulated steepest descent algorithm. This plot reveals that there is a broad range of μ for which the converges in a handful of iterations. We have found that setting $\mu \approx 0.65$ yields fast convergence about 15 – 20 iterations under a broad range of conditions.

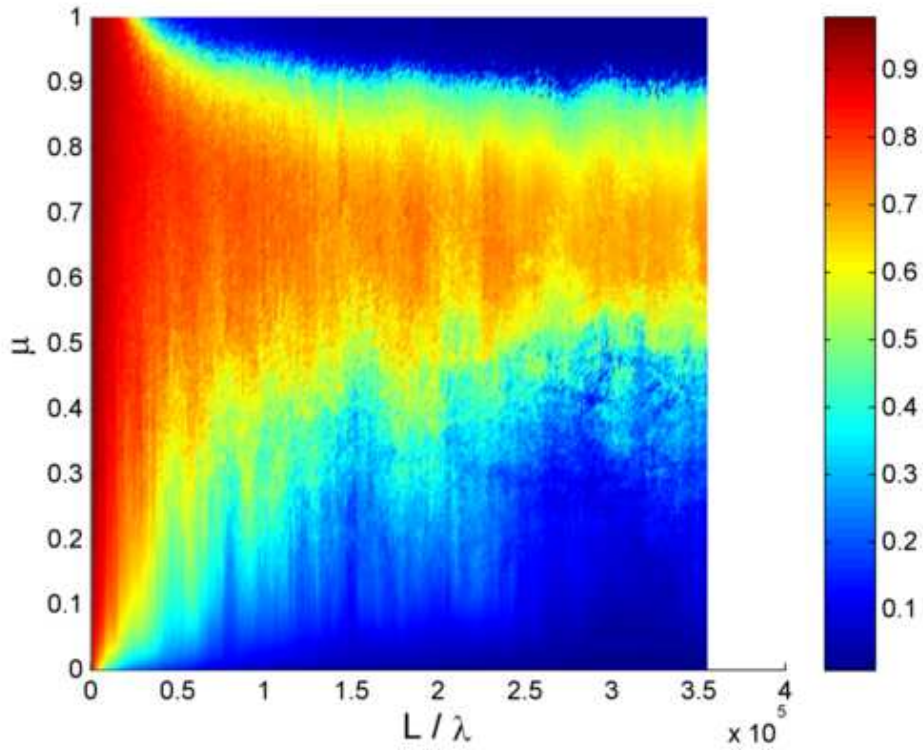


Figure 4.7: Heatmap of the maximum transmitted power in 50 iterations of steepest descent on the plane of stepsize and the thickness L/λ in a setting with $D = 197\lambda$, $r = 0.11\lambda$, $N_c = 430,000$, $n_d = 1.3$, $M = 395$, $\bar{l} = 6.69\lambda$.

Fig. 4.7 shows the transmitted power achieved after 50 iterations of the phase-only modulated steepest descent algorithm as a function of the stepsize μ and the thickness L/λ of the scattering system. There is a wide range of allowed values for μ where the steepest descent algorithm performs well.

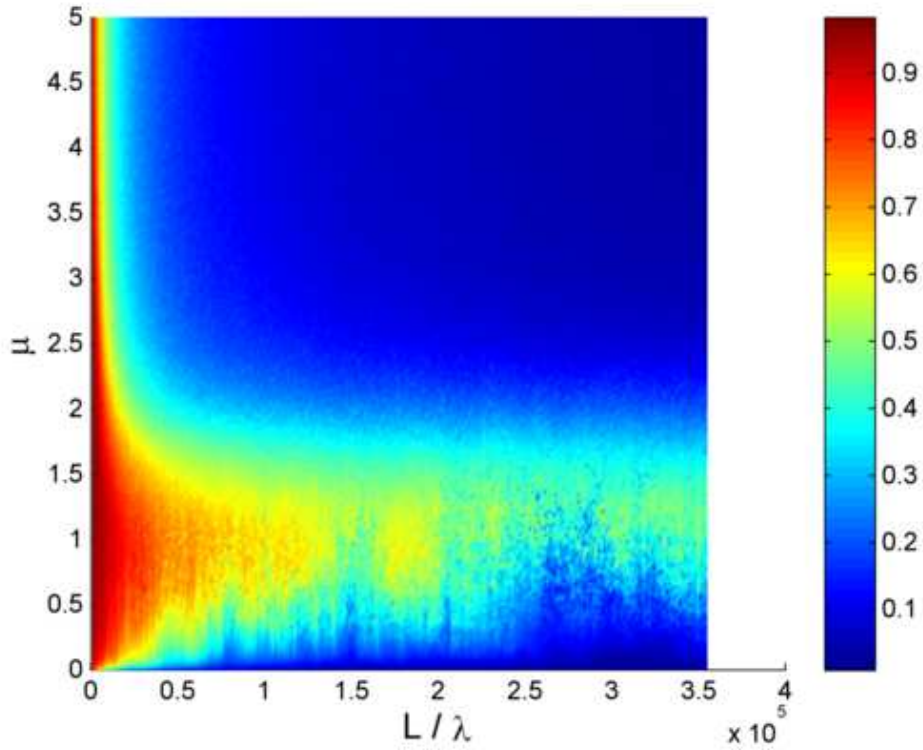


Figure 4.8: Heatmap of the maximum transmitted power in 50 iterations of gradient descent on the plane of stepsize and the thickness L/λ in a setting with $D = 197\lambda$, $r = 0.11\lambda$, $N_c = 430,000$, $n_d = 1.3$, $M = 395$, $\bar{l} = 6.69\lambda$.

Fig. 4.8 plots the transmitted power after 50 iterations of the phase-only modulated gradient descent algorithm a function of the stepsize μ and the thickness L/λ of the scattering system. In contrast to the steepest descent algorithm, the performance of the gradient descent algorithm is much more erratic. A μ of about 1.1 is a good choice for the gradient descent based method.

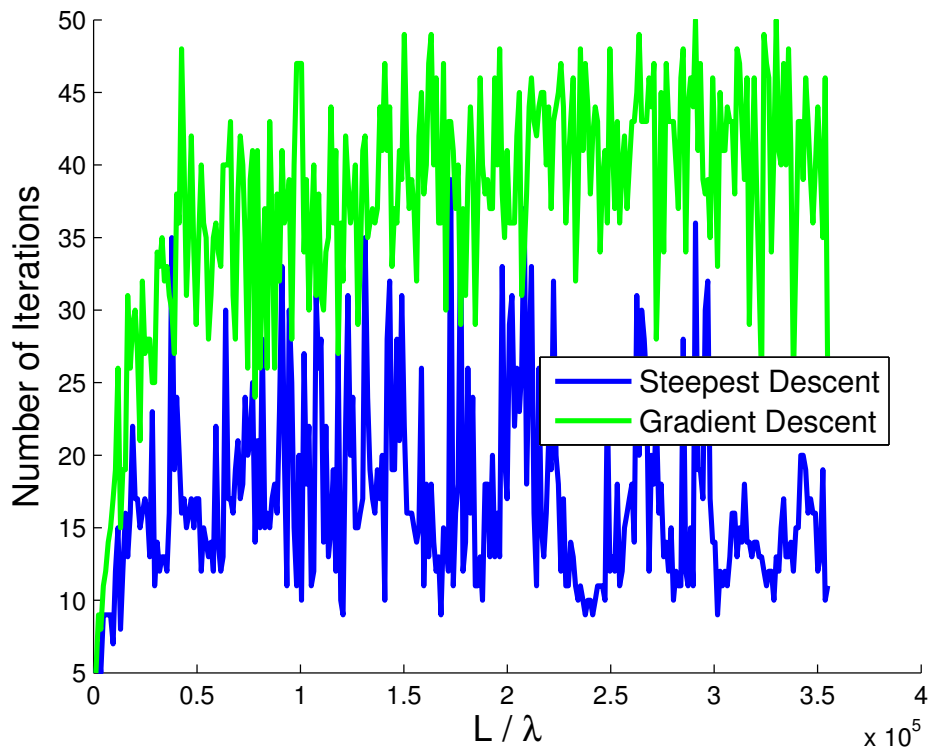


Figure 4.9: Number of iterations to get 95% of the respective maximum transmitted power for steepest descent and gradient descent algorithms versus thickness L/λ in a setting with $D = 197\lambda$, $r = 0.11\lambda$, $N_c = 430,000$, $n_d = 1.3$, $M = 395$, $\bar{l} = 6.69\lambda$.

Finally, Fig. 4.9 plots the average number of iterations required to reach 95% of the respective optimas for the phase-only modulated steepest descent and gradient descent algorithms as a function of the thickness L/λ of the scattering system. On average the steepest descent algorithm converges in about 15–20 iterations while the gradient descent algorithm converges in about 35–45 iterations. Here, we selected the optimal μ 's for the steepest descent algorithm and for the gradient descent algorithm for each depth in the medium.

Since the steepest descent algorithm converges faster and realizes 15–20% greater transmitted power, but only loses 10% transmission relative to the non-iterative phase-only modulated SVD and SDP algorithms, it is the best option for use in an experimental setting.

CHAPTER V

Theory of Perfect Transmission

5.1 Setup

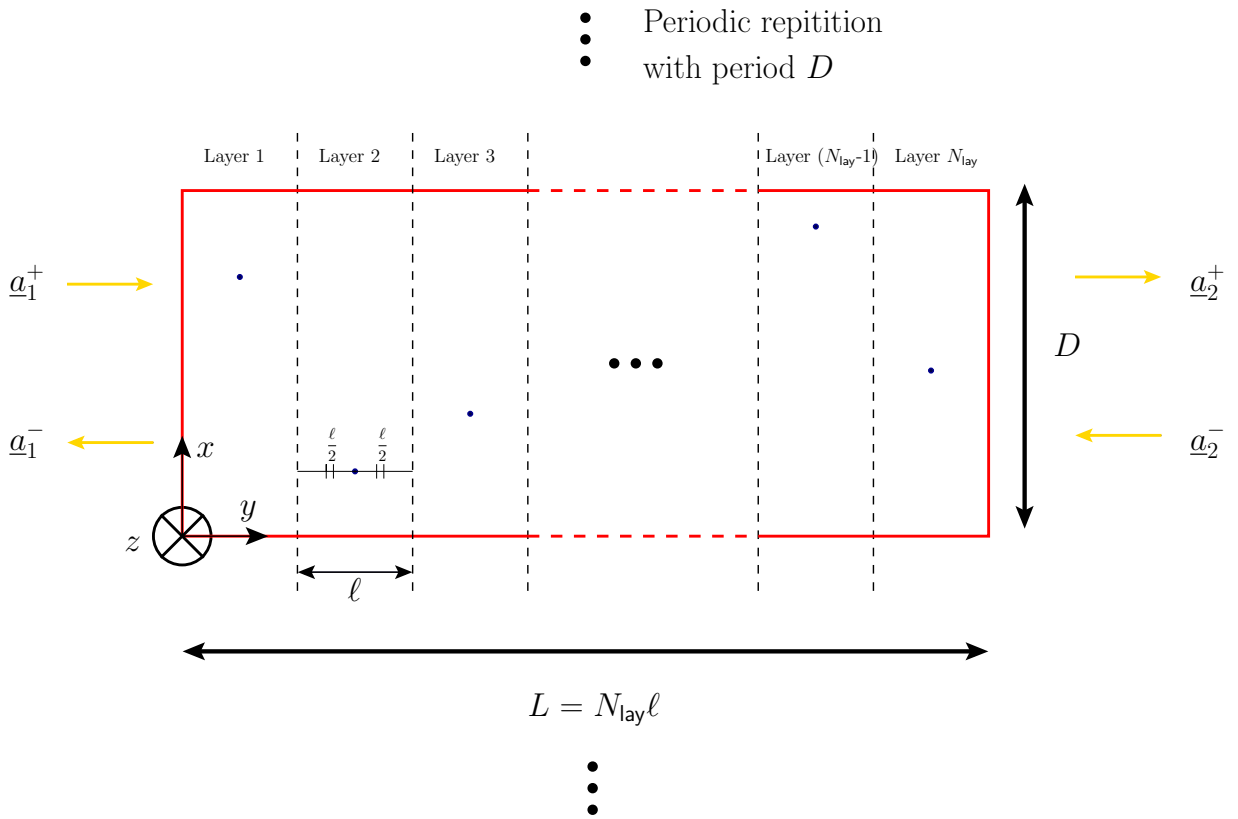


Figure 5.1: Setup.

We study scattering from a two-dimensional (2D) random slab of thickness L and periodicity D ; the slab's unit cell occupies the space $0 \leq x < D$ and $0 \leq y < L$ (Fig. 5.1). The slab contains N_{lay} infinite and z -invariant circular cylinders of radius r that are placed randomly within the cell, as described shortly. The cylinders are

assumed to be dielectric with refractive index n_d ; care is taken to ensure the cylinders do not overlap. The radius of the cylinders is chosen to be sufficiently smaller than the wavelength λ so that the cylinders can be treated as pointer scatterers.

For $i_c = 1, 2, \dots, N_{lay}$, the x and y position of the center of the i_c -th cylinder is $u_{i_c}, \frac{\ell}{2} + (i_c - 1)\ell$, where u_{i_c} 's are i.i.d. uniform random variables on $[r, D - r]$ and ℓ is the y -displacement between the neighboring cylinders; ℓ is chosen to be larger than $\sqrt{D\lambda}$ to ensure that the cascading error can be controlled as described in section (2.6.7.2). Each cylinder's refractive index n_{i_c} is drawn independently from the same distribution of refractive indices $\eta(n)$.

Fields are TM_z polarized: electric fields in the $y < 0$ ($i = 1$) and $y > L$ ($i = 2$) halfspaces are denoted $\underline{e}_i(\underline{\rho}) = e_i(\underline{\rho})\hat{z}$. The field (complex) amplitude $e_i(\underline{\rho})$ can be decomposed in terms of $+y$ and $-y$ propagating waves as $e_i(\underline{\rho}) = e_i^+(\underline{\rho}) + e_i^-(\underline{\rho})$, where

$$e_i^\pm(\underline{\rho}) = \sum_{n=-N}^N h_n a_{i,n}^\pm e^{-jk_n^\pm \cdot \underline{\rho}}. \quad (5.1)$$

In the above expression, $\underline{\rho} = x\hat{x} + y\hat{y} \equiv (x, y)$, $\underline{k}_n^\pm = k_{n,x}\hat{x} \pm k_{n,y}\hat{y} \equiv (k_{n,x}, \pm k_{n,y})$, $k_{n,x} = 2\pi n/D$, $k_{n,y} = 2\pi\sqrt{(1/\lambda)^2 - (n/D)^2}$, λ is the wavelength, and $h_n = \sqrt{\|\underline{k}_n^\pm\|_2/k_{n,y}}$ is a power-normalizing coefficient. We assume $N = \lfloor D/\lambda \rfloor$, i.e., we only model propagating waves and denote $M = 2N + 1$. The modal coefficients $a_{i,n}^\pm$, $i = 1, 2$; $n = -N, \dots, N$ are related by the scattering matrix

$$\begin{bmatrix} \underline{a}_1^- \\ \underline{a}_2^+ \end{bmatrix} = \underbrace{\begin{bmatrix} S_{11} & S_{12} \\ S_{21} & S_{22} \end{bmatrix}}_{=:S} \begin{bmatrix} \underline{a}_1^+ \\ \underline{a}_2^- \end{bmatrix}, \quad (5.2)$$

where $\underline{a}_i^\pm = [a_{i,-N}^\pm \ \dots \ a_{i,0}^\pm \ \dots \ a_{i,N}^\pm]^T$ and T denotes transposition. In what follows, we assume that the slab is only excited from the $y < 0$ halfspace; hence, $\underline{a}_2^- = 0$. For a given incident field amplitude $e_1^+(\underline{\rho})$, we define transmission and reflection coefficients as

$$\tau(\underline{a}_1^+) := \frac{\|S_{21} \cdot \underline{a}_1^+\|_2^2}{\|\underline{a}_1^+\|_2^2}, \quad (5.3)$$

and

$$\Gamma(\underline{a}_1^+) := \frac{\|S_{11} \cdot \underline{a}_1^+\|_2^2}{\|\underline{a}_1^+\|_2^2}, \quad (5.4)$$

respectively. We denote the transmission coefficient of a normally incident wavefront by $\tau_{\text{normal}} = \tau(\begin{bmatrix} 0 & \dots & 0 & 1 & 0 & \dots & 0 \end{bmatrix}^T)$.

Similarly, the modal coefficients $a_{i,n}^\pm$, $i = 1, 2$; $n = -N, \dots, N$ are related by the transfer matrix,

$$\begin{bmatrix} \underline{a}_2^+ \\ \underline{a}_2^- \end{bmatrix} = \underbrace{\begin{bmatrix} T_{11} & T_{12} \\ T_{21} & T_{22} \end{bmatrix}}_{=:T} \begin{bmatrix} \underline{a}_1^+ \\ \underline{a}_1^- \end{bmatrix}. \quad (5.5)$$

Since the transfer matrix relates the current on the left side to the current on the right side, it is very simple to cascade transfer matrices; the transfer matrix of the entire scattering system is the product of transfer matrices of slices of the scattering system as discussed in section 2.5.1.2.

5.2 Problem Formulation

Let $S_{21} = \sum_{i=1}^M \sigma_i \underline{u}_i \cdot \underline{v}_i^H$ denote the singular value decomposition (SVD) of S_{21} ; σ_i is the singular value associated with the left and right singular vectors \underline{u}_i and \underline{v}_i , respectively. By convention, the singular values are arranged so that $\sigma_1 \geq \dots \geq \sigma_M$ and H denotes complex conjugate transpose. When the wavefront associated with the i -th right singular vector \underline{v}_i is transmitted, the transmitted power is $\tau_i := \tau(\underline{v}_i) = \sigma_i^2$, which we refer to as the transmission coefficient of the i -th eigen-wavefront of S_{21} .

Let us denote the empirical (eigen) transmission coefficient distribution from a p th realization and N_{lay} layers of a system described in (Fig. 5.1) with M modes as

$$f_{M,p}^{N_{\text{lay}}}(\tau) = \frac{1}{M} \sum_{i=1}^M \delta(\tau - \tau(\underline{v}_{i,p})) = \frac{1}{M} \sum_{i=1}^M \delta(\tau - \sigma_{i,p}^2) \quad (5.6)$$

where $\underline{v}_{i,p}$ denotes the i th right singular vector of the S_{21} of the p th realization associated with $\sigma_{i,p}$, the i th singular value of the S_{21} of the p th realization.

Furthermore, we define the average transmission coefficient distribution as

$$f_M^{N_{\text{lay}}}(\tau) = \lim_{P \rightarrow \infty} \frac{1}{P} \sum_{p=1}^P f_{M,p}^{N_{\text{lay}}}(\tau) = \lim_{P \rightarrow \infty} \frac{1}{P} \sum_{p=1}^P \sum_{i=1}^M \delta(\tau - \tau(\underline{v}_{i,p})) = \lim_{P \rightarrow \infty} \frac{1}{P} \sum_{p=1}^P \sum_{i=1}^M \delta(\tau - \sigma_{i,p}^2) \quad (5.7)$$

where P is the total number of realizations.

Note that there are three parameters that will determine the shape of the distribution, N_{lay} , M and $\eta(n)$. The distribution will have less weight on $\tau = 1$ if N_{lay} increases due to the increasing number of scatterers. Similarly, the distribution will have more weight on $\tau = 1$ if M increases due to the increasing number of modes that we can control. Since N_{lay} and M determine the shape of the distribution in an inversely way, we define $c = \frac{N_{\text{lay}}}{M}$, which quantifies the degree of scattering of the defined scattering system as in (Fig. 5.1). Also, the the distribution of the index of refraction of the scatterer, $\eta(n)$, will determine the shape of the transmission coefficient distribution.

The objective of this chapter is to derive the average transmission coefficient distribution analytically as a function of $c, \eta(n)$,

$$f(\tau; c, \eta(n)) = \lim_{\substack{N_{\text{lay}}, M \rightarrow \infty \\ N_{\text{lay}}/M \rightarrow c}} f_M^{N_{\text{lay}}}(\tau).$$

We contrast it with the distribution [3, 4, 5, 6, 7] of the transmission coefficients for lossless random media has density given by

$$f(\tau) = \lim_{M \rightarrow \infty} \frac{1}{M} \sum_{i=1}^M \delta(\tau - \tau(\underline{v}_i)) = \frac{l}{2L} \frac{1}{\tau \sqrt{1 - \tau}}, \quad \text{for } 4 \exp(-L/2l) \lesssim \tau \leq 1. \quad (5.8)$$

In Eq. (5.8), l is the mean-free path through the medium.

Since the cascade formula for scattering matrices has a more complicated form than the transfer matrix's, the approach we will take is to use transfer matrix approach, which will allow us to express the entire scattering system as a product of i.i.d. random matrices as below,

$$T = \prod_{n=1}^{N_{\text{lay}}} T_n, \quad (5.9)$$

where T_n denotes the transfer matrix of the n th layer in the scattering system we defined in (Fig. 5.1). From here we will use random matrix theory to derive the closed form for the average transmission coefficient distribution. Let us denote $h(\lambda)$ as the average distribution of the singular value squared of the transfer matrix T . Then, the objective of this chapter can be restated specifically as below,

$$f(\tau) = h(\lambda) \left| \frac{d\lambda}{d\tau} \right|. \quad (5.10)$$

This equation suggests that there are two parts we need to deal with. First, from $h(\lambda)$, we need to predict the singular value squared of the distribution of the transfer matrix which can be accomplished by using free probability from random matrix theory, and we will cover the basics in section 5.3.2. Second, from $\left| \frac{d\lambda}{d\tau} \right|$, we need to find the relationship between τ and λ , and this will be covered in section 5.3.1.

5.3 Basics

5.3.1 Relationship between τ and λ

Here, we uncover the relationship between the singular value squared of S_{21} , τ , and the singular value squared of T , λ .

5.3.1.1 Unitary Decomposition of $T^H \cdot T$

Since the eigenvalue of $T \cdot T$ is equal to the singular value squared of T , let us first expand $T^H \cdot T$ in terms of submatrices of the scattering matrix as below using the formulas we derived in appendix VI,

$$\begin{aligned} T^H \cdot T &= \begin{bmatrix} S_{21}^H - S_{11}^H \cdot S_{12}^{-H} \cdot S_{22}^H & -S_{11}^H \cdot S_{12}^{-H} \\ S_{12}^{-H} \cdot S_{22}^H & S_{12}^{-H} \end{bmatrix} \cdot \begin{bmatrix} S_{21} - S_{22} \cdot S_{12}^{-1} \cdot S_{11} & S_{22} \cdot S_{12}^{-1} \\ -S_{12}^{-1} \cdot S_{11} & S_{12}^{-1} \end{bmatrix} \\ &= \begin{bmatrix} I + 2S_{11}^H \cdot S_{12}^{-H} \cdot S_{12}^{-1} \cdot S_{11} & -2S_{11}^H \cdot S_{12}^{-H} \cdot S_{12}^{-1} \\ -2S_{12}^{-H} \cdot S_{12}^{-1} \cdot S_{11} & 2S_{12}^{-H} \cdot S_{12}^{-1} - I \end{bmatrix}, \end{aligned} \quad (5.11)$$

where unitary conditions $S^H \cdot S = I$ was used. To simplify the last equation Eq. (5.11) furthermore, let us use a general form of scattering matrix below,

$$\begin{aligned} S_{21} &= U \cdot \Sigma \cdot V^H \\ S_{11} &= F \cdot V^* \cdot \sqrt{I - \Sigma^2} \cdot V^H \\ S_{12} &= F \cdot S_{21}^T \cdot F = F \cdot V^* \cdot \Sigma \cdot (F \cdot U^*)^H \\ S_{22} &= U \cdot \tilde{F} \cdot \sqrt{I - \Sigma^2} \cdot (F \cdot U^*)^H, \end{aligned}$$

where $\tilde{F} = \text{diag}(\{e^{j\phi_n}\}_n)$ and $\phi_n \in [0, 2\pi]$, and \tilde{F} represents the phase ambiguity between the singular spaces. Note that this general form satisfies all the conditions for a scattering matrix discussed in section 2.4. Using this form, the equation Eq. (5.11) becomes

$$\begin{aligned} T^H \cdot T &= \begin{bmatrix} V \cdot (2\Sigma^{-2} - I) \cdot V^H & -2V \cdot \sqrt{I - \Sigma^2} \cdot \Sigma^{-2} \cdot (F \cdot V^*)^H \\ -2F \cdot V^* \cdot \sqrt{I - \Sigma^2} \cdot \Sigma^{-2} \cdot V^H & F \cdot V^* \cdot (2\Sigma^{-2} - I) \cdot (F \cdot V^*)^H \end{bmatrix} \\ &= \begin{bmatrix} V & 0 \\ 0 & F \cdot V^* \end{bmatrix} \cdot \begin{bmatrix} 2\Sigma^{-2} - I & -2\sqrt{I - \Sigma^2} \cdot \Sigma^{-2} \\ -2\sqrt{I - \Sigma^2} \cdot \Sigma^{-2} & 2\Sigma^{-2} - I \end{bmatrix} \cdot \begin{bmatrix} V & 0 \\ 0 & F \cdot V^* \end{bmatrix}^H \end{aligned} \quad (5.12)$$

Note that the matrix in the middle is composed of diagonal matrices and the eigenvalues of this matrix are the singular value squared of T .

5.3.1.2 Eigenvalues of Matrix of Diagonal Matrices

Let us compute the eigenvalues of $\begin{bmatrix} D_1 & D_2 \\ D_3 & D_4 \end{bmatrix}$, where $D_1 = \text{diag}(\{d_{1,i}\}_{i=1}^M)$, $D_2 = \text{diag}(\{d_{2,i}\}_{i=1}^M)$, $D_3 = \text{diag}(\{d_{3,i}\}_{i=1}^M)$ and $D_4 = \text{diag}(\{d_{4,i}\}_{i=1}^M)$. Eigenvalues are the solutions to the characteristic equation,

$$\det \left(\begin{bmatrix} D_1 - zI & D_2 \\ D_3 & D_4 - zI \end{bmatrix} \right) = 0$$

where z denotes the eigenvalue. Since the eigenvalues will not be the same as $d_{1,i}$ s, $D_1 - zI$ will be invertible; thereby the characteristic equation can be written as,

$$\begin{aligned} \det(D_1 - zI) \cdot \det(D_4 - zI - D_3 \cdot (D_1 - zI)^{-1} \cdot D_2) &= 0 \\ \prod_{i=1}^M (d_{1,i} - z) \cdot \prod_{i=1}^M \left(d_{4,i} - z - \frac{d_{2,i}d_{3,i}}{d_{1,i} - z} \right) &= 0 \\ \prod_{i=1}^M \{ z^2 - (d_{1,i} + d_{4,i})z + d_{1,i}d_{4,i} - d_{2,i}d_{3,i} \} &= 0 \end{aligned}$$

Therefore,

$$\therefore z = \frac{d_{1,i} + d_{4,i} \pm \sqrt{(d_{1,i} + d_{4,i})^2 - 4(d_{1,i}d_{4,i} - d_{2,i}d_{3,i})}}{2} \quad \text{for } i = 1, \dots, M. \quad (5.13)$$

Note that each diagonal element of D_1, D_2, D_3 and D_5 will produce two corresponding eigenvalues z .

5.3.1.3 Relationship between the singular values of T and S_{21}

Using formula (5.13) into Eq. (5.12), we can compute the eigenvalues of $T^H \cdot T$. Let us denote i -th entry of Σ^2 as τ_i , and the corresponding eigenvalue of $T^H \cdot T$ as λ_i . Then,

$$\lambda_i = \frac{(2\tau_i^{-1} - 1) + (2\tau_i^{-1} - 1) \pm \sqrt{(4\tau_i^{-1} - 2)^2 - 4((2\tau_i^{-1} - 1)^2 - 4(1 - \tau_i)\tau_i^{-2})}}{2} \quad (5.14)$$

$$= 2\tau_i^{-1} - 1 \pm 2\sqrt{\tau_i^{-2} - \tau_i^{-1}} \quad (5.15)$$

Note that $\lambda_i^{-1} = 2\tau_i^{-1} - 1 \mp 2\sqrt{\tau_i^{-2} - \tau_i^{-1}}$. This tells us that the singular values of the transfer matrix come with reciprocal pairs, i.e. if the singular values above one are known, the singular values below one can be obtained as well. Furthermore, the determinant of the transfer matrix is one whether the scattering systems is lossless or lossy, which is proven in appendix VI. Using this reciprocal relationship, the singular values of the transfer matrix and the singular value of the transmission matrix can be stated as follows,

$$\lambda + \lambda^{-1} = 4\tau_i^{-1} - 2 \quad (5.16)$$

$$\therefore \tau_i = \frac{4}{\lambda + \lambda^{-1} + 2} \quad (5.17)$$

$$= \frac{1}{\cosh(x)^2}, \quad (5.18)$$

where we defined x as $e^{2x} \triangleq \lambda$ at the end. Note that we can recover the τ by knowing either λ or $1/\lambda$.

5.3.1.4 Distribution Conversion Formula

Let us denote the singular value distribution of the transfer matrix as $h(\lambda)$ and the transmission coefficient distribution as $f(\tau)$. Then, $f(\tau)$ obtained from $h(\lambda)$ as below,

$$f(\tau) = h(\lambda) \left| \frac{d\lambda}{d\tau} \right| = h(\lambda) \frac{(\lambda + 1)^3}{4(\lambda - 1)} \quad (5.19)$$

$$= (2h(\lambda)\mathbb{1}_{\{\lambda \geq 1\}}) \frac{(\lambda + 1)^3}{4(\lambda - 1)} = h(\lambda) \frac{(\lambda + 1)^3}{2(\lambda - 1)} \mathbb{1}_{\{\lambda \geq 1\}}, \quad (5.20)$$

where $\mathbb{1}_{\{\lambda \geq 1\}}$ is the indicator function.

5.3.2 Free Probability

Let X_n be an $n \times n$ symmetric (or Hermitian) random matrix whose ordered eigenvalues we denote by $t_1 \geq \dots \geq t_n$. Let μ_{X_n} be the empirical eigenvalue distribution, i.e., the probability measure defined as

$$\mu_{X_n}(t) = \frac{1}{n} \sum_{j=1}^n \delta(t - t_j).$$

Now suppose that A_n and B_n are two independent $n \times n$ positive-definite random matrices that are invariant, in law, by conjugation by any orthogonal (or unitary) matrix and that as $n \rightarrow \infty$, $\mu_{A_n} \rightarrow \mu_A$ and $\mu_{B_n} \rightarrow \mu_B$. Then, free probability theory states that $\mu_{A_n \cdot B_n} \rightarrow \mu_A \boxtimes \mu_B$, a probability measure which can be characterized in terms of the S -transform as

$$\psi_{\mu_A \boxtimes \mu_B}(z) = \psi_{\mu_A}(z) \psi_{\mu_B}(z), \quad (5.21)$$

and the S -transform¹, is defined as

$$\psi_{\mu}(z) := (1 + z)/(z\xi_{\mu}^{-1}(z)),$$

where

$$\xi_{\mu}(z) = \int \frac{t}{z - t} d\mu(t)$$

, and $\xi_{\mu}(z)$ is called T -transform. The S -transform is the analogue of the Fourier transform for free multiplicative convolution \boxtimes [57].

To recover the distribution, we use an inversion formula

$$\mu(z) = -\frac{1}{\pi} \lim_{\epsilon \rightarrow 0} \text{Im} g_{\mu}(z + j\epsilon) \quad (5.22)$$

where $g_{\mu}(z)$ is the G -transform and defined as

$$g_{\mu}(z) = \int \frac{1}{z - t} d\mu(t).$$

¹Denoted here by $\psi(\cdot)$ to avoid any confusion with the S (or scattering matrix).

To recover the distribution from the S -transform, we couple the G -transform and S -transform, and get a fixed point equation as below,

$$\frac{g_\mu(z)}{zg_\mu(z) - 1} = \psi_\mu(zg_\mu(z) - 1). \quad (5.23)$$

Therefore, we can retrieve the distribution by solving this fixed point equation with respect to g_μ , and use the inversion formula (5.22). The recovering procedure of the distribution from the S -transform can be written in an algorithm format as below,

Algorithm 4 Distribution computation algorithm from S -transform

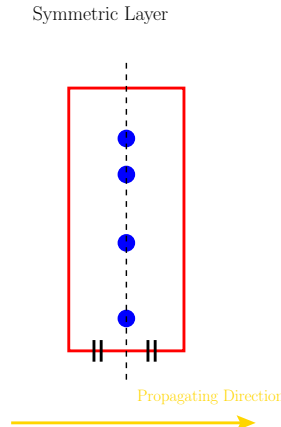
- 1: Set discretization size, N_p
 - 2: Set t_1, \dots, t_{N_p}
 - 3: **for** $i = 1$ **to** N_p **do**
 - 4: Set $z = t_i + j\epsilon$
 - 5: Obtain $g_\mu(z)$ by solving the fixed point equation, eq (5.23)
 - 6: Set $\mu(t_i) = -\frac{1}{\pi}\text{Im}(g_\mu(z))$
 - 7: **end for**
-

5.4 Proposed Random Matrix Model : Random Point-Symmetric Matrix

In this section we propose a simple matrix that is an approximation of a transfer matrix which represents a single layer in the defined scattering system as in (Fig. 5.1), i.e., a layer with a single point scatterer in the middle horizontally and at random location vertically. Then, we construct a random media by cascading these approximated matrices.

Before we begin this section, let us define the followings

- **Symmetric Layer** : A layer where the scatterers are all lined up on the line which bisects the layer and is perpendicular to the propagating direction



- Point Layer : A layer where only one point scatterer exists at a random location
- Point Symmetric Layer : A point and symmetric layer

A crude justification for defining a symmetric layer is based on the fact that if the media is large enough the probability of splitting the media into slices which contain only a single scatterer is high enough, and we can always adjust the size of the slice so that the scatterer is located in the middle by making a slice that contains no scatterer. The artificial random transfer matrix that we are going to construct approximates the transfer matrix of a point-symmetric layer, and we define it as random point-symmetric matrix.

5.4.1 Observations

Here, we are going to state the observations and facts we found about a symmetric layer and a point layer.

For a symmetric layer, we have the following facts

$$S_{11} = S_{22} \tag{5.24}$$

$$S_{21} = S_{12}. \tag{5.25}$$

The first two equations are a direct result of the geometrical symmetry of the scattering system, and one can prove it using the formulas derived in Eq. (2.6).

Now, let us discuss about the observations from a point layer.

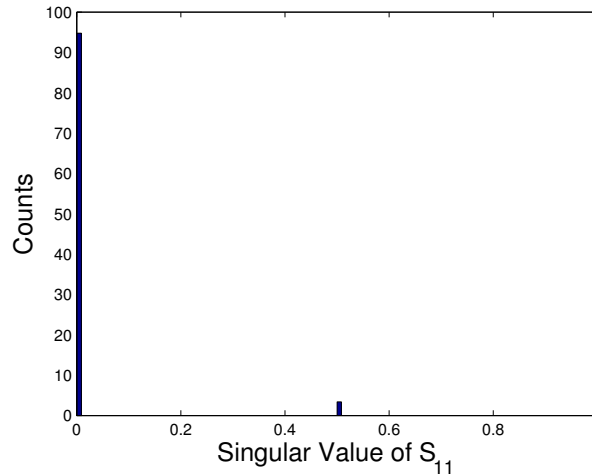


Figure 5.2: Histogram of the singular values of S_{11} of a scattering system with a single dielectric scatterer of $r = 0.001$, $n = 1.7$ and the $\lambda = 0.97$.

Fig. (5.2) plots the histogram of the singular values of S_{11} of a point layer. This suggests that the rank of the reflection matrix of a point layer will be nearly one. Fig.

(5.3) plots the response of a point layer, when the input corresponding to the largest singular value of S_{11} was excited.

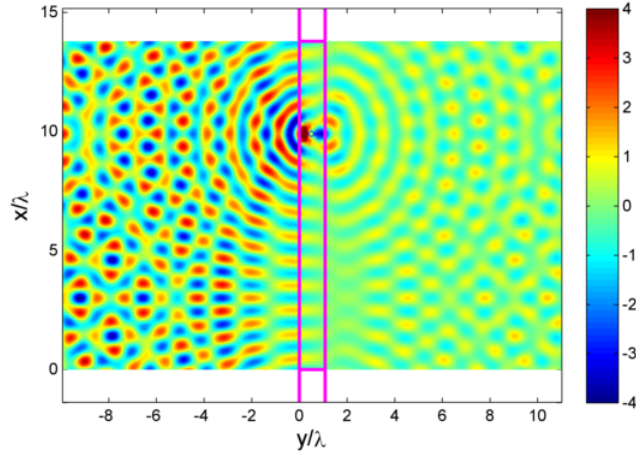


Figure 5.3: Field plot when the input corresponding to the maximum singular value of S_{11} is excited. The input corresponds to a cylinder wave centered at the center of the scatterer, and produces a outgoing cylinder wave resulting in a standing wave on the entire reflection side.

This suggests that the significant reflection is obtained by forming a cylinder wave centered at the location of the scatterer. So, if the size of the scatterer is sufficiently small compared to the wavelength so that it can be considered as a point scatterer, we can approximate the reflection matrix of a point layer to be

$$S_{11} \simeq \alpha \underline{u} \cdot \underline{v}^H \quad (5.26)$$

where α denotes the scattering strength of the scatterer, and \underline{u} and \underline{v} represent the incoming cylinder wave and the outgoing cylinder wave response from the scatterer, respectively.

Fig. (5.4) shows the relationship between the largest singular value of S_{11} and the index of refraction of the scatterer.

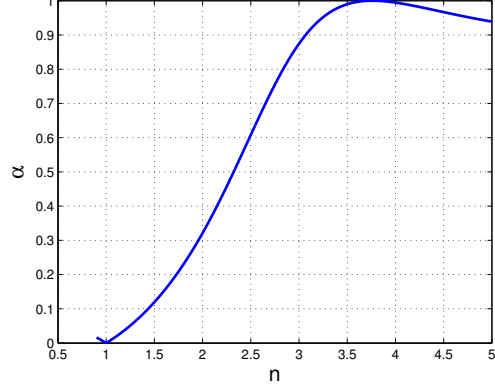


Figure 5.4: α , the largest singular value of the reflection matrix of a point layer, is plotted versus the index of refraction.

This suggests that α will be a value between $[0,1)$, depending on the index of refraction of the scatterer.

5.4.2 Construction of Random Point-Symmetric Matrix

We propose a matrix that approximates the scattering matrix of a point-symmetric layer. This matrix follows the conditions below,

- Unitary and Reciprocity conditions with the phase ambiguity set to $e^{j\phi_n} = 1$ for simplicity
- Symmetric Layer results : $S_{11} = S_{22}$ and $S_{21} = S_{12}$
- Point Layer result : Rank one reflection matrix

Let us denote the reflection matrix to be like below,

$$S_{11} = S_{22} = \alpha(F \cdot \underline{v}^*) \cdot \underline{v}^H. \quad (5.27)$$

And we can construct a transmission matrix as below,

$$S_{21} = S_{12} = \begin{bmatrix} F \cdot (\underline{v}^\perp)^* & F \cdot \underline{v}^* \end{bmatrix} \cdot \begin{bmatrix} 1 & & & & \\ & 1 & & & \\ & & \ddots & & \\ & & & 1 & \\ & & & & j\sqrt{1-\alpha^2} \end{bmatrix} \cdot \begin{bmatrix} \underline{v}^\perp \\ \underline{v} \end{bmatrix}^H$$

$$= F \cdot V^* \cdot \Sigma \cdot V^H \quad (5.28)$$

where \underline{v}^\perp is an orthogonal matrix which ranges the space orthogonal to \underline{v} ,

$$V = \begin{bmatrix} \underline{v}^\perp & \underline{v} \end{bmatrix} \text{ and } \Sigma = \begin{bmatrix} \mathbf{I} & \underline{0} \\ \underline{0}^T & j\sqrt{1-\alpha^2} \end{bmatrix}. \text{ Note that these choices will satisfy}$$

the conditions we mentioned above. Thus, we can generate a random matrix that approximates the point-symmetric scattering matrix by picking a scattering strength α between $[0, 1)$ and a random orthogonal matrix V , and we call this approximated random matrix *the random point-symmetric scattering matrix*.

Furthermore, we can write the random point-symmetric scattering matrix in a cleaner form as below,

$$\begin{aligned}
S &= \begin{bmatrix} \alpha F \cdot \underline{v}^* \cdot \underline{v}^H & F \cdot V^* \cdot \begin{pmatrix} \text{diag}(\underline{1}) & 0 \\ 0 & j\sqrt{1-\alpha^2} \end{pmatrix} \cdot V^H \\ F \cdot V^* \cdot \begin{pmatrix} \text{diag}(\underline{1}) & 0 \\ 0 & j\sqrt{1-\alpha^2} \end{pmatrix} \cdot V^H & \alpha F \cdot \underline{v}^* \cdot \underline{v}^H \end{bmatrix} \\
&= \begin{bmatrix} F \cdot V^* & 0 \\ 0 & F \cdot V^* \end{bmatrix} \cdot \begin{bmatrix} \begin{pmatrix} \text{diag}(\underline{0}) & 0 \\ 0 & \alpha \end{pmatrix} & \begin{pmatrix} \text{diag}(\underline{1}) & 0 \\ 0 & j\sqrt{1-\alpha^2} \end{pmatrix} \\ \begin{pmatrix} \text{diag}(\underline{1}) & 0 \\ 0 & j\sqrt{1-\alpha^2} \end{pmatrix} & \begin{pmatrix} \text{diag}(\underline{0}) & 0 \\ 0 & \alpha \end{pmatrix} \end{bmatrix} \cdot \begin{bmatrix} V & 0 \\ 0 & V \end{bmatrix}^H.
\end{aligned}$$

Using the scattering matrix and transfer matrix conversion formula from appendix VI, we get an expression for the random point-symmetric transfer matrix,

$$\begin{aligned}
T &= \begin{bmatrix} F \cdot V^* \cdot \begin{pmatrix} \text{diag}(\underline{1}) & 0 \\ 0 & \frac{j}{\sqrt{1-\alpha^2}} \end{pmatrix} \cdot V^H & -\frac{j\alpha}{\sqrt{1-\alpha^2}} F \cdot \underline{v}^* \cdot (F \cdot \underline{v}^*)^H \\ \frac{j\alpha}{\sqrt{1-\alpha^2}} \underline{v} \cdot \underline{v}^H & V \cdot \begin{pmatrix} \text{diag}(\underline{1}) & 0 \\ 0 & -\frac{j}{\sqrt{1-\alpha^2}} \end{pmatrix} \cdot (F \cdot V^*)^H \end{bmatrix} \\
&= \begin{bmatrix} F \cdot V^* & 0 \\ 0 & V \end{bmatrix} \cdot \begin{bmatrix} \begin{pmatrix} \text{diag}(\underline{1}) & 0 \\ 0 & \frac{j}{\sqrt{1-\alpha^2}} \end{pmatrix} & \begin{pmatrix} \text{diag}(\underline{0}) & 0 \\ 0 & -\frac{j\alpha}{\sqrt{1-\alpha^2}} \end{pmatrix} \\ \begin{pmatrix} \text{diag}(\underline{0}) & 0 \\ 0 & \frac{j\alpha}{\sqrt{1-\alpha^2}} \end{pmatrix} & \begin{pmatrix} \text{diag}(\underline{1}) & 0 \\ 0 & -\frac{j}{\sqrt{1-\alpha^2}} \end{pmatrix} \end{bmatrix} \cdot \begin{bmatrix} V & 0 \\ 0 & F \cdot V^* \end{bmatrix}^H.
\end{aligned}$$

5.4.3 Singular Values of the Random Point-Symmetric Transfer Matrix

To compute the singular value of the random point-symmetric transfer matrix, let us look at the unitary decomposition of $T^H \cdot T$,

$$T^H \cdot T = \begin{bmatrix} V & 0 \\ 0 & F \cdot V^* \end{bmatrix} \cdot \left[\begin{array}{cc} \begin{pmatrix} \text{diag}(\mathbf{1}) & 0 \\ 0 & \frac{1+\alpha^2}{1-\alpha^2} \end{pmatrix} & \begin{pmatrix} \text{diag}(\mathbf{0}) & 0 \\ 0 & -\frac{2\alpha}{1-\alpha^2} \end{pmatrix} \\ \begin{pmatrix} \text{diag}(\mathbf{0}) & 0 \\ 0 & -\frac{2\alpha}{1-\alpha^2} \end{pmatrix} & \begin{pmatrix} \text{diag}(\mathbf{1}) & 0 \\ 0 & \frac{1+\alpha^2}{1-\alpha^2} \end{pmatrix} \end{array} \right] \cdot \begin{bmatrix} V & 0 \\ 0 & F \cdot V^* \end{bmatrix}^H. \quad (5.29)$$

Using the formula (5.13), from the first $M - 1$ entries of the diagonal matrices, we get

$$\frac{1 + 1 \pm \sqrt{2^2 - 4(1 - 0)}}{2} = 1.$$

From the last entry of the diagonal matrices, we get

$$\frac{1 + \alpha}{1 - \alpha} \text{ and } \frac{1 - \alpha}{1 + \alpha}.$$

Therefore, the singular values of the random point-symmetric transfer matrix are $(2M - 2)$ ones, $\sqrt{\frac{1 + \alpha}{1 - \alpha}}$ and $\sqrt{\frac{1 - \alpha}{1 + \alpha}}$. Consequently, the empirical singular value squared distribution of the point-symmetric matrix can be written as

$$h(\lambda) = \left(1 - \frac{2}{2M}\right)\delta(\lambda - 1) + \frac{1}{M}\delta\left(\lambda - \frac{1 + \alpha}{1 - \alpha}\right) + \frac{1}{M}\delta\left(\lambda - \frac{1 - \alpha}{1 + \alpha}\right). \quad (5.30)$$

5.4.4 S -Transform of the Distribution

Let us define a K -point-symmetric layer to be a layer which has K point scatterers and is symmetric. Here, we consider a random media which is a cascade of K -point-symmetric layers. Let us denote the transfer matrix of the n th K -point-symmetric layer as T_n , then the transfer matrix of the entire random media, T , can be written as

$$T = \prod_{n=1}^{N_{\text{lay}}} T_n. \quad (5.31)$$

The empirical eigenvalue distribution of $T_n^H \cdot T_n$ is

$$h_n(\lambda) = \left(1 - \frac{2k}{2M}\right)\delta(\lambda - 1) + \frac{k}{2M} \sum_{i=1}^k \delta(\lambda - \theta_i) + \frac{k}{2M} \sum_{i=1}^k \delta(\lambda - 1/\theta_i),$$

where we denoted θ_i as the i th non-unit singular value squared of T_n .

Assuming that each layer is statistically identical and independent, i.e. T_n s are i.i.d., the S -transform of the empirical eigenvalue distribution of $T^H \cdot T$, $\psi_{h_M^{N_{\text{lay}}}}(z)$, can be written as below using Eq. (5.21)

$$\psi_{h_M^{N_{\text{lay}}}}(z) = \psi_{\mu(T^H \cdot T)}(z) = \prod_{n=1}^{N_{\text{lay}}} \psi_{\mu(T_n^H \cdot T_n)}(z) = (\psi_{h_1}(z))^{N_{\text{lay}}} = \left(\left(1 + \frac{1}{z}\right) \frac{1}{\xi_{h_1}^{-1}(z)} \right)^{N_{\text{lay}}} \quad (5.32)$$

The T -transform of $h_1(\lambda)$, $\xi_{h_1}(z)$, can be expanded with respect to $\frac{k}{2M}$, and it is

$$\xi_{h_1}(z) = \xi_0(z) + \frac{k}{2M} \xi_1(z)$$

where $\xi_0(z) = \frac{1}{z-1}$ and $\xi_1(z) = z \left(\sum_{i=1}^{N_{\text{lay}}} \left\{ \frac{1}{z-\theta_i} + \frac{1}{z-\frac{1}{\theta_i}} \right\} - \frac{2}{z-1} \right)$. Also the term $\left(1 + \frac{1}{z}\right) \frac{1}{\xi_{h_1}^{-1}(z)}$ can be expanded with respect to $\frac{k}{2M}$ by perturbation theory [58] and we simplify Eq. (5.32),

$$\psi_{h_M^{N_{\text{lay}}}}(z) = \left(1 - \frac{k}{2M} \frac{\xi_1(1 + \frac{1}{z})}{z(z+1)} + O\left(\left(\frac{k}{2M}\right)^2\right) \right)^{N_{\text{lay}}}.$$

As $M, N_{\text{lay}} \rightarrow \infty$ with $N_{\text{lay}}/M \rightarrow c$ we have:

$$\psi_h(z) = \lim_{\substack{M, N_{\text{lay}} \rightarrow \infty \\ N_{\text{lay}}/M \rightarrow c}} \psi_{h_M^{N_{\text{lay}}}}(z) = \lim_{\substack{M, N_{\text{lay}} \rightarrow \infty \\ N_{\text{lay}}/M \rightarrow c}} \left(1 - \frac{k}{2M} \frac{\xi_1(1 + \frac{1}{z})}{z(z+1)} + O\left(\left(\frac{k}{2M}\right)^2\right) \right)^{cM} \quad (5.33)$$

$$= \exp\left(-\frac{ck}{2} \frac{\xi_1(1 + \frac{1}{z})}{z(z+1)}\right) \quad (5.34)$$

Let us consider the case where the index of refraction of the scatterer has a distribution $\eta(n)$, and the corresponding distribution for the largest singular value squared of the point-symmetric matrix is $\Theta(\theta)$. Then, everything remains the same except

$$\xi_1(z) = z \left(\int \left(\Theta(\theta) + \Theta\left(\frac{1}{\theta}\right) \frac{1}{\theta^2} \right) \frac{d\theta}{z-\theta} - \frac{2}{z-1} \right). \quad (5.35)$$

Now, we know the S -transform of the distribution of $h(\lambda)$ in Eq. (5.34). Given the S -transform, we can compute the distribution by solving the fixed point equation in Eq. (5.23), and it is equivalent to solve,

$$\log(zg_h) - \log(zg_h - 1) - \log(\psi_h(zg_h - 1)) = 0 \quad (5.36)$$

Let us define $F(z, g_h) = \log(zg_h) - \log(zg_h - 1) - \log(\psi_h(zg_h - 1))$, then the algorithm for computing the transmission coefficient distribution can be written in a Matlab form as below,

Algorithm 5 Transmission Coefficient Distribution Computation Algorithm

```

1: Set discretization size,  $N_p$ 
2: Set  $\lambda_1, \dots, \lambda_{N_p} \in [0, 1)$ 
3: %  $h(\lambda)$  computation
4: for  $i = 1$  to  $N_p$  do
5:   Set  $z = \lambda_i + j\epsilon$ 
6:   Set  $G_0$  with a random initial guess
7:    $\tilde{F} = @(g_1, g_2) [\text{Im}(F(z, g_1 + jg_2)); \text{Re}(F(z, g_1 + jg_2))]$ 
8:    $[\text{Gsol}, \text{fval}, \text{exitflag}] = \text{fsolve}(\tilde{F}, G_0)$ 
9:   Set  $h(\lambda_i) = -\frac{1}{\pi} \text{Im}(\text{Gsol})$ 
10: end for
11: % Jacobian Computation
12: for  $i = 1$  to  $N_p$  do
13:   Set  $J_i = \frac{4(\lambda_i + 1)^3}{\lambda_i - 1}$ 
14: end for
15: %  $f(\tau)$  computation
16: for  $i = 1$  to  $N_p$  do
17:   Set  $\tau_i = \frac{4}{\lambda_i + \lambda_i^{-1} + 2}$ 
18:   Set  $f(\tau_i) = 2h(\lambda_i)J_i$ 
19: end for

```

Note that the formula used in step 17 comes from Eq. (5.17).

5.5 Results

5.5.1 Distribution Comparison

Here, we compare the physical distribution we obtain from the scattering simulator to the distribution obtained from Algorithm 5. We considered three cases where the index of refraction of the point scatterers is fixed or atomic distributed or uniformly distributed.

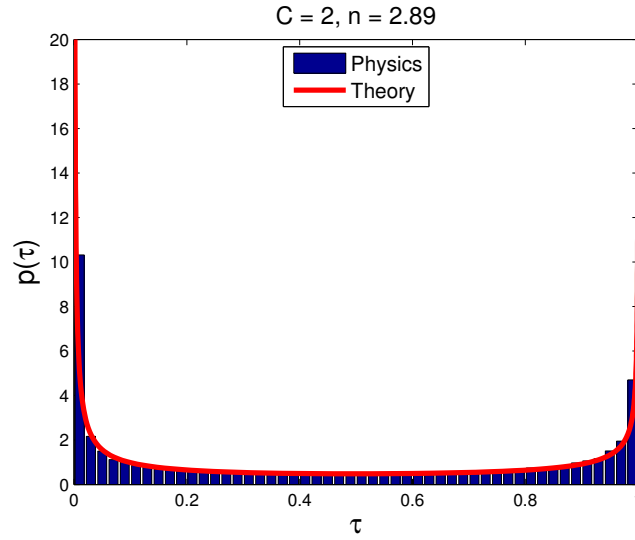


Figure 5.5: Here, the scatterer's index of refraction is fixed to be $n = 2.89$, or equivalently $\alpha = 0.82$. The settings were $K = 1, M = 101, C = 2$ for 200 trials.

Fig. 5.5 plots the transmission coefficient distribution when the largest singular value of the point-symmetric transfer matrix was fixed, $\Theta(\theta) = \delta(\theta - \theta_1)$, where $\theta_1 = 0.1$. The $\xi_1(z)$ for this case is,

$$\xi_1(z) = z \left(\frac{1}{z - \theta_1} + \frac{1}{z - \theta_1^{-1}} - \frac{2}{z - 1} \right). \quad (5.37)$$

The theoretical prediction and the histogram from the numerical simulator match very well.

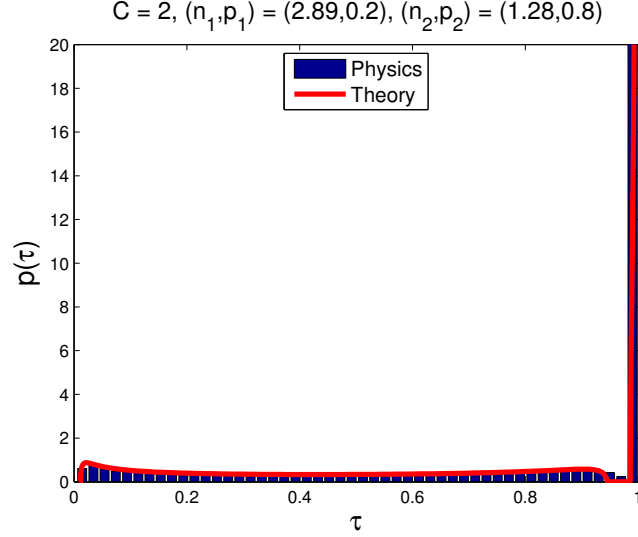


Figure 5.6: Here, the scatterer's index of refraction distribution was atomic distributed, $P(n = 2.89) = 0.2$ and $P(n = 1.28) = 0.8$, or equivalently $P(\alpha = 0.82) = 0.2$ and $P(\alpha = 0.1) = 0.8$. The settings were $K = 1, M = 101, C = 2$ for 200 trials.

Fig. 5.6 plots the transmission coefficient distribution when the largest singular value of the point-symmetric transfer matrix was atomic distributed, $\Theta(\theta) = p_1\delta(\theta - \theta_1) + p_2\delta(\theta - \theta_2)$, where $p_1 = 0.2, \theta_1 = 0.1, p_2 = 0.8$ and $\theta_2 = 0.9$. The $\xi_1(z)$ for this case is,

$$\xi_1(z) = z \left(\frac{p_1}{z - \theta_1} + \frac{p_1}{z - \theta_1^{-1}} + \frac{p_2}{z - \theta_2} + \frac{p_2}{z - \theta_2^{-1}} - \frac{2}{z - 1} \right). \quad (5.38)$$

In this case, interestingly, the histogram had a very unusual shape, but yet our theory predicted very well.

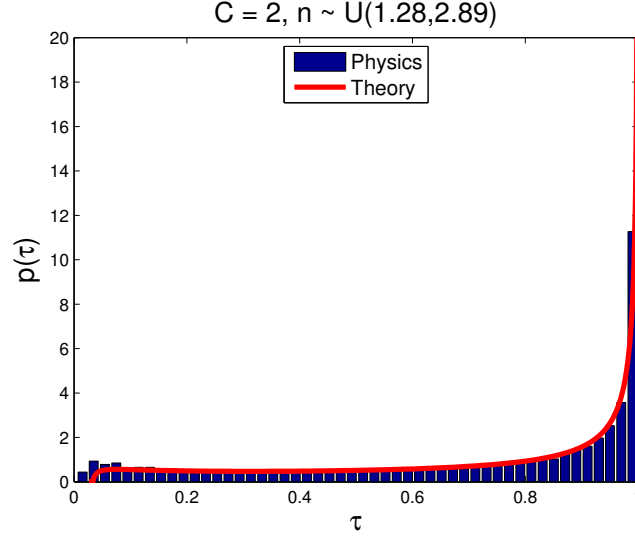


Figure 5.7: Here, the largest singular value of the point-symmetric transfer matrix was uniformly distributed between 0.1 and 0.9, where 0.1 corresponds to $\alpha = 0.82$ or $n = 2.89$ and 0.9 corresponds to $\alpha = 0.05$ or 1.28. The settings were $K = 1, M = 101, C = 2$ for 200 trials.

Fig. 5.7 plots the transmission coefficient distribution when the largest singular value of the point-symmetric transfer matrix was uniformly distributed, $\Theta(\theta) = \frac{\mathbb{1}_{\theta_1 \leq \theta \leq \theta_2}}{\theta_2 - \theta_1}$, where $\theta_1 = 0.1$ and $\theta_2 = 0.9$. The $\xi_1(z)$ for this case is,

$$\xi_1(z) = \frac{z}{\theta_2 - \theta_1} \left(\log \left(\frac{z - \theta_1}{z - \theta_2} \right) + \frac{\theta_2 - \theta_1}{z} + \frac{1}{z^2} \log \left(\frac{\theta_2 z - 1}{\theta_1 z - 1} \right) - \frac{2}{z - 1} \right). \quad (5.39)$$

The theoretical prediction and the histogram from the numerical simulator match very well.

5.5.2 Moments

5.5.2.1 First Moment

Since we have derived the closed form for the transmission coefficient distribution, we can also derive the moments of the distribution. The first moment can be

derived as follows,

$$\begin{aligned}
\langle \tau \rangle &= \int \tau f(\tau) d\tau \\
&= \int \frac{4\lambda}{\lambda + \lambda^{-1} + 2} h(\lambda) d\lambda \\
&= -4 \underbrace{\left. \frac{d\xi(z)}{dz} \right|_{z=-1}}_{:=\xi'} = \frac{-4}{\left. \frac{d\xi^{-1}(z)}{dz} \right|_{z=-0.5}} = \frac{-4}{\left. \frac{d(1+z)/(z\psi_h(z))}{dz} \right|_{z=-0.5}} \\
&= \frac{1}{1 + 2c \int \left(\frac{\theta - 1}{\theta + 1} \right)^2 \Theta(\theta) d\theta} \\
&= \frac{1}{1 + 2c E_\theta \left[\left(\frac{\theta - 1}{\theta + 1} \right)^2 \right]} = \frac{1}{1 + 2c E_\alpha [\alpha^2]}.
\end{aligned}$$

5.5.2.2 Second Moment

Similar to the derivation of the first moment, the second moment can be derived as follows,

$$\begin{aligned}
\langle \tau^2 \rangle &= \int \tau^2 f(\tau) d\tau \\
&= \int \left(\frac{4\lambda}{\lambda + \lambda^{-1} + 2} \right)^2 h(\lambda) d\lambda \\
&= 16 \left\{ \int \frac{h(\lambda) d\lambda}{(\lambda + 1)^2} - 2 \int \frac{h(\lambda) \lambda d\lambda}{(\lambda + 1)^4} - \int \frac{h(\lambda) d\lambda}{(\lambda + 1)^4} \right\} \\
&= 16 \left\{ \underbrace{\left. \frac{1}{6} \frac{d^3 \xi(z)}{dz^3} \right|_{z=-1}}_{:=\xi'''} - \underbrace{\left. \frac{1}{2} \frac{d^2 \xi(z)}{dz^2} \right|_{z=-1}}_{:=\xi''} \right\}.
\end{aligned}$$

For further evaluation, use the following formulas,

$$\begin{aligned}
\frac{d^2 \xi(z)}{dz^2} &= - \frac{\frac{d^2 \xi^{-1}(z)}{dz^2}}{\left(\frac{d\xi^{-1}(z)}{dz} \right)^3}. \\
\frac{d^3 \xi(z)}{dz^3} &= \frac{3 \left(\frac{d^2 \xi^{-1}(z)}{dz^2} \right)^2 - \frac{d\xi^{-1}(z)}{dz} \frac{d^3 \xi^{-1}(z)}{dz^3}}{\left(\frac{d\xi^{-1}(z)}{dz} \right)^5}.
\end{aligned}$$

5.5.2.3 Ratio of Moments

$$\begin{aligned}
\frac{\langle \tau^2 \rangle}{\langle \tau \rangle} &= \frac{16 \left\{ \frac{1}{6} \xi''' - \frac{1}{2} \xi'' \right\}}{-4\xi'} \\
&= \frac{2 \xi^{-1'} \xi^{-1'''} - 3(\xi^{-1''})^2 - 3(\xi^{-1'})^2 \xi^{-1''}}{3 (\xi^{-1'})^4} \\
&= \frac{2^{12} \left(\int \left(\frac{\theta - 1}{\theta + 1} \right)^2 \Theta(\theta) d\theta \right)^8 c^4 \left(1 + O\left(\frac{1}{c}\right) \right)}{3^{12} \left(\int \left(\frac{\theta - 1}{\theta + 1} \right)^2 \Theta(\theta) d\theta \right)^8 c^4 \left(1 + O\left(\frac{1}{c}\right) \right)}.
\end{aligned}$$

Therefore,

$$\lim_{c \rightarrow \infty} \frac{\langle \tau^2 \rangle}{\langle \tau \rangle} = \frac{2}{3}. \tag{5.40}$$

Note that in the limit of $c \rightarrow \infty$, the ratio's dependency on $\Theta(\theta)$, the material property of the scatterers, vanishes. In other words, the transmission coefficient distribution of random media will have a universal shape regardless of the properties of the scatterer when the media is large enough. This universal behavior has been already discussed in the literature [1], and the $\frac{2}{3}$ result we obtained agrees with the existing result.

CHAPTER VI

Conclusion

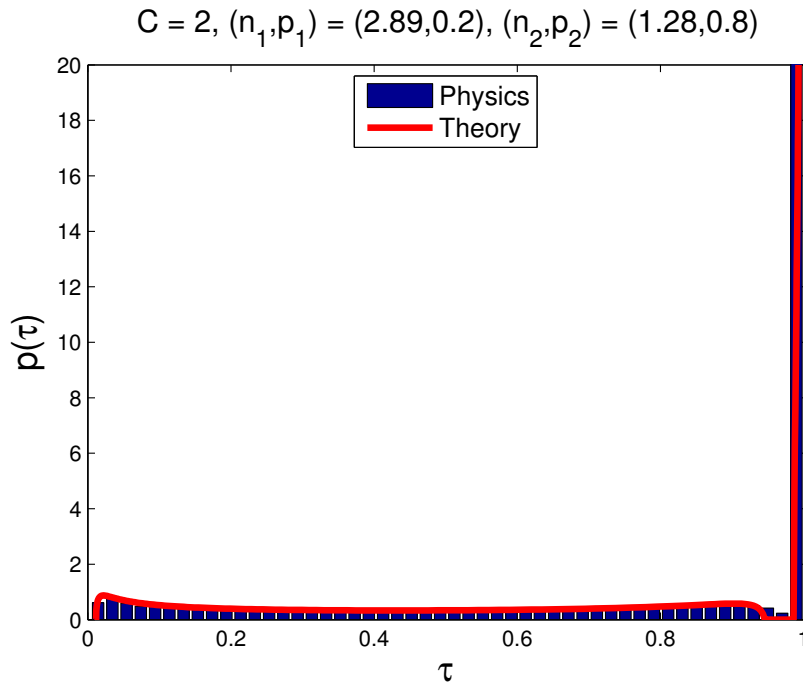


Figure 6.1: Here, the scatterer's index of refraction distribution was atomic distributed, $P(n = 2.89) = 0.2$ and $P(n = 1.28) = 0.8$. The settings were $K = 1, M = 101, C = 2$ for 200 trials.

We have developed a highly-accurate scattering solver that solves Maxwell's equations for a two-dimensional periodic scattering setting, and used it to generate accurate scattering matrices. We used many numerical techniques to guarantee accuracy and reasonable computation speed, and the errors were all controllable. Using the accurate scattering solver, we have numerically verified the existence of eigen-wavefronts with transmission coefficients approaching one in highly scattering systems for the first time. Also, we were the first to observe the physical shape of these perfectly transmitting wavefronts, which suggests that the wavefronts are formed in a way that it can effectively avoid where the scatterers are. Along with

the numerical development, we have identified three important theoretical properties of the scattering matrix, which come from power conservation, time-reversible symmetry and reciprocity. These properties have given us measures to check the accuracy of the solver and most importantly many intuitions to solve our challenging problems.

We developed physically realizable algorithms for finding these highly transmitting eigen-wavefronts using backscatter analysis. We also developed a physically realizable algorithm for forming a focused input using the highly transmitting eigen-wavefronts identified by the previous algorithm. Via numerical simulations it was shown that the algorithms converged to a near-optimal wavefront in just a few iterations.

Also, we have shown theoretically and using numerically rigorous simulation that non-iterative, phase-only modulated techniques for transmission maximization using backscatter analysis can expect to achieve about $25 \pi\% \approx 78.5\%$ transmission in highly backscattering random media in the DMPK regime where amplitude and phase modulated can yield 100% transmission. We have developed two new, iterative and physically realizable algorithms for constructing highly transmitting phase-only modulated wavefronts using backscatter analysis. We showed using numerical simulations that the steepest descent variant outperforms the gradient descent variant and that the wavefront produced by the steepest descent algorithm achieves about 71% transmission while converging within 15 – 20 measurements. The development of iterative phase-only modulated algorithms that bridge the 10% transmission gap between the steepest descent algorithm presented here and the non-iterative SVD and SDP algorithms remains an important open problem.

The proposed algorithms are quite general and may be applied to scattering problems beyond the 2-D setup described in the simulations. We are currently investigating extensions to imaging and sensing applications. A detailed study, guided by the insights in [18], of the impact of periodic boundary conditions on the results obtained is also underway.

Finally, we were able to derive the transmission coefficient distribution exactly using random matrix theory, and we accomplished the task of bridging scattering theory and random matrix theory. We have compared the theoretical results to the numerical results, and they have shown a very close agreement. Also, it agrees with the existing universal transmission theory, which tells that all types of media will behave the same when the media gets very long or deep enough, no matter how they are composed or structured.

APPENDICES

APPENDIX A

Orthogonality of the periodic modes

The n -th periodic mode is defined as below in our two dimensional periodic setting,

$$\varphi_n(\underline{\rho}) = e^{-j(k_{x_n}x + k_{y_n}y)}. \quad (\text{A.1})$$

where periodicity is induced in the x direction with period L , $k_{x_n} = \frac{2\pi}{L}n$, and $k_{y_n} = \pm\sqrt{|\frac{2\pi}{\lambda}|^2 - k_{x_n}^2}$. Any periodic waves can be expressed by a modal expansion with these modes as below,

$$\varphi(\underline{\rho}) = \sum_{n=-N}^N a_n e^{-j(k_{x_n}x + k_{y_n}y)}. \quad (\text{A.2})$$

The periodic modes are orthogonal in the sense that the power flowing in the forward direction ($+y$ direction) by φ can be calculated by the summation of individual power carried by each mode, i.e. $\sum_{n=-N}^N \cos(\theta_n)|a_n|^2$, where the angle of the n -th mode θ_n is defined as $\theta_n = \arcsin(\frac{k_{x_n}}{\|k_n\|_2})$.

The *complex poynting theorem* tells us that the time-averaged power is

$$\frac{1}{2}\text{Re}(E(\underline{\rho}) \times H^*(\underline{\rho})) \quad (\text{A.3})$$

So the spatial-averaged and time-averaged power flowing into the system can be calculated below,

$$\frac{1}{2L} \int_L \text{Re}(E(\underline{\rho}) \times H^*(\underline{\rho})) \cdot (\hat{y}dx) \quad (\text{A.4})$$

Suppose the waves are TM modes, whose electric field oscillates along with the z axis. Then, the wave going into the left side of the system and wave coming out from the left side of the system are like below,

$$\text{Electric Field going in} = E_a(\underline{\rho}) = \sum_{m=-N}^N \hat{z} a_m e^{-j(\frac{2\pi m}{L}x + k_{y_m}y)} \quad (\text{A.5})$$

$$\text{Electric Field coming out} = E_b(\underline{\rho}) = \sum_{m=-N}^N \hat{z} b_m e^{-j(\frac{2\pi m}{L}x - k_{y_m}y)}. \quad (\text{A.6})$$

From this point, we will fix k_{y_n} to be $k_{y_n} = \sqrt{|\frac{2\pi}{\lambda}|^2 - k_{x_n}^2}$ and pull out the sign explicitly in the equations.

The corresponding magnetic fields are like below,

$$\text{Magnetic Field going in} = H_a(\underline{\rho}) = \frac{j}{\omega\mu} \nabla \times E_a = \sum_{m=-N}^N (\hat{k}_m \times \hat{z}) \frac{a_m}{\eta} e^{-j(\frac{2\pi m}{L}x + k_{ym}y)} \quad (\text{A.7})$$

$$\text{Magnetic Field coming out} = H_b(\underline{\rho}) = \frac{j}{\omega\mu} \nabla \times E_b = \sum_{m=-N}^N (-\hat{k}_{-m} \times \hat{z}) \frac{b_m}{\eta} e^{-j(\frac{2\pi m}{L}x - k_{ym}y)}. \quad (\text{A.8})$$

where η is the *intrinsic impedance* of the media.

Plugging Equations (A.5) to (A.8) into Eq. (A.4) we get,

$$\frac{1}{2L} \int_L \text{Re}(E(\underline{\rho}) \times H^*(\underline{\rho})) \cdot (\hat{y}dx) \quad (\text{A.9})$$

$$= \frac{1}{2L} \text{Re} \left(\int_L E(\underline{\rho}) \times H^*(\underline{\rho}) \cdot (\hat{y}dx) \right) \quad (\text{A.10})$$

$$= \frac{1}{2L} \text{Re} \left(\int_L \left(\sum_{m=-N}^N \hat{z} a_m e^{-j(\frac{2\pi m}{L}x + k_{ym}y)} + \sum_{m=-N}^N \hat{z} b_m e^{-j(\frac{2\pi m}{L}x - k_{ym}y)} \right) \times \left(\sum_{m=-N}^N (\hat{k}_m \times \hat{z}) \frac{a_m^*}{\eta^*} e^{j(\frac{2\pi m}{L}x + k_{ym}y)} + \sum_{m=-N}^N (-\hat{k}_{-m} \times \hat{z}) \frac{b_m^*}{\eta^*} e^{j(\frac{2\pi m}{L}x - k_{ym}y)} \right) \cdot (\hat{y}dx) \right) \quad (\text{A.11})$$

$$= \frac{1}{2L} \text{Re} \left(L \sum_{m=-N}^N \frac{|a_m|^2}{\eta^*} \cos(\theta_m) - L \sum_{m=-N}^N \frac{|b_m|^2}{\eta^*} \cos(\theta_m) - L \sum_{m=-N}^N \frac{a_m b_m^*}{\eta^*} e^{-j2k_{ym}y} \cos(\theta_m) + L \sum_{m=-N}^N \frac{b_m a_m^*}{\eta^*} e^{j2k_{ym}y} \cos(\theta_m) \right) \quad (\text{A.12})$$

where we used the fact that $\hat{z} \times (\hat{k}_m \times \hat{z}) = \hat{k}_m$ and $\theta_m = \arccos\left(\frac{k_{ym}}{k}\right)$.

Assuming that the media is lossless, i.e. $\eta^* = \eta$, the two terms in Eq. (A.12) can be expressed as

$$-L \sum_{m=-N}^N \frac{a_m b_m^*}{\eta^*} e^{-j2k_{ym}y} \cos(\theta_m) + L \sum_{m=-N}^N \frac{b_m a_m^*}{\eta^*} e^{j2k_{ym}y} \cos(\theta_m) \quad (\text{A.13})$$

$$= -L \sum_{m=-N}^N \left(\frac{a_m b_m^*}{\eta^*} e^{-j2k_{ym}y} \cos(\theta_m) - \left(\frac{a_m b_m^*}{\eta^*} e^{-j2k_{ym}y} \cos(\theta_m) \right)^* \right). \quad (\text{A.14})$$

The sum of these two terms is purely imaginary. So Eq. (A.12) is simplified like below,

$$\frac{1}{2L} \int_L \operatorname{Re}(E(\underline{\rho}) \times H^*(\underline{\rho})) \cdot (\hat{y} dx) \quad (\text{A.15})$$

$$= \frac{1}{2L} \operatorname{Re} \left(L \sum_{m=-N}^N \frac{|a_m|^2}{\eta^*} \cos(\theta_m) - L \sum_{m=-N}^N \frac{|b_m|^2}{\eta^*} \cos(\theta_m) \right) \quad (\text{A.16})$$

$$= \frac{1}{2\eta} \sum_{m=-N}^N |a_m|^2 \cos(\theta_m) - \frac{1}{2\eta} \sum_{m=-N}^N |b_m|^2 \cos(\theta_m) \quad (\text{A.17})$$

We can see that the power going into the system can be calculated by adding up the power carried by individual modes with proper normalization $\cos(\theta_n)$, i.e. modes are uncorrelated when considering power.

Summarizing this section, if the wave is going into the system, the spatially-averaged and time-averaged power going into the system is

$$\sum_{m=-N}^N |a_m|^2 \cos(\theta_m) \quad (\text{A.18})$$

If the wave is coming out from the system, the spatially-averaged and time-averaged power going into the system is

$$- \sum_{m=-N}^N |a_m|^2 \cos(\theta_m) \quad (\text{A.19})$$

Note that we omitted $\frac{1}{2\eta}$ for notational convenience and the results will be similar for TE modes as well.

APPENDIX B

Additional Theorem

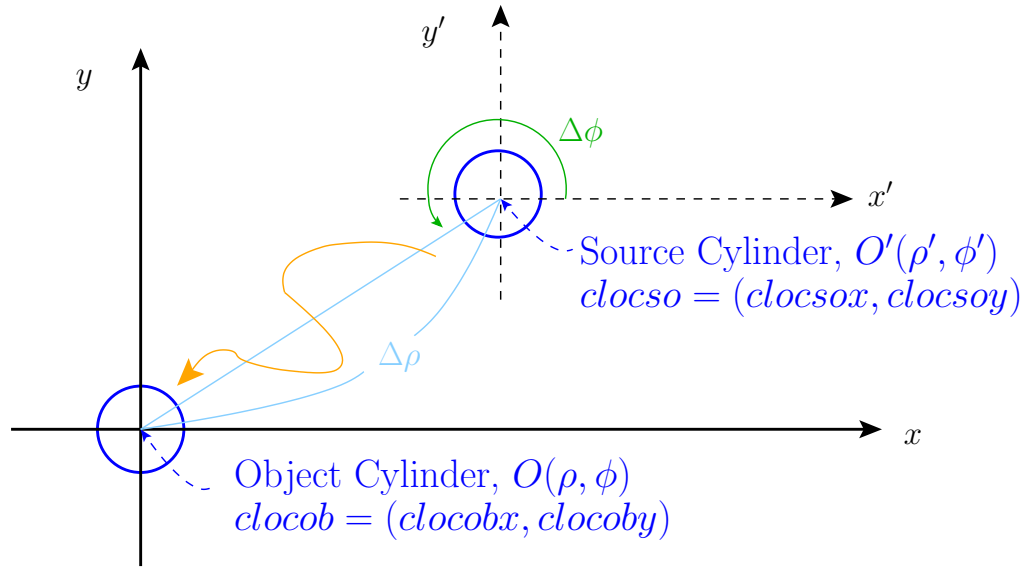


Figure B.1: T Matrix transforms the cylinder wave coming from the source cylinder into a cylinder wave going into the object cylinder. This involves a coordinate transformation from the source cylinder's coordinate system O' to the object cylinder's coordinate system O .

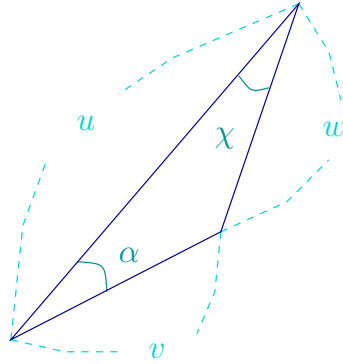
The role of T matrix is to convert the cylinder wave coming from the source cylinder into cylinder waves going into the object cylinder. In other words, we have to describe the cylinder wave coming from the source cylinder of coordinate system $O'(\rho', \phi')$ in terms of cylinder modes of the coordinate system $O(\rho, \phi)$. There are two things to keep in mind. The first is the wave generated from the source cylinder is an outgoing traveling wave, $H_n^{(2)}(k\rho)e^{jn\phi}$. The second is that the approximated cylinder waves at the object cylinder should be in terms of $J_n(k\rho)e^{jn\phi}$ since the input to the scattering coefficient matrix is supposed to be the cylinder vector in terms of Bessel function of the first kind. So our problem boils down to

find the coefficient $b_{cmob,cmso}$ such that

$$H_{cmso}^{(2)}(k\rho')e^{jcmso\phi'} = \sum_{cmob=-\infty}^{\infty} b_{cmob,cmso} J_{cmob}(k\rho)e^{jcmob\phi} \quad (\text{B.1})$$

where $cmob$ is the order of the mode of the object cylinder and $cmso$ is the order of the mode of the source cylinder.

To get $b_{cmob,cmso}$ we need to use two properties of bessel function. The first is Graf's Addition Theorem [28],



$$w = \sqrt{u^2 + v^2 + 2u \cdot v \cdot \cos(\alpha)}$$

$$u - v \cos(\alpha) = w \cos(\chi)$$

$$v \sin(\alpha) = w \sin(\chi)$$

Figure B.2: Geometric figure for Graf's additional theorem.

$$H_n^{(2)}(w)e^{jn\chi} = \sum_{m=-\infty}^{\infty} H_{n+m}^{(2)}(u)J_m(v)e^{jm\alpha}, \quad \text{for } |v| < |u| \quad (\text{B.2})$$

The second is the following equation [28].

$$J_{-n}(z) = (-1)^n J_n(z) \quad (\text{B.3})$$

Now we are ready to derive the formula for $b_{cmob,cmso}$. The detailed geometrical situation related to Graf's additional theorem looks like below.

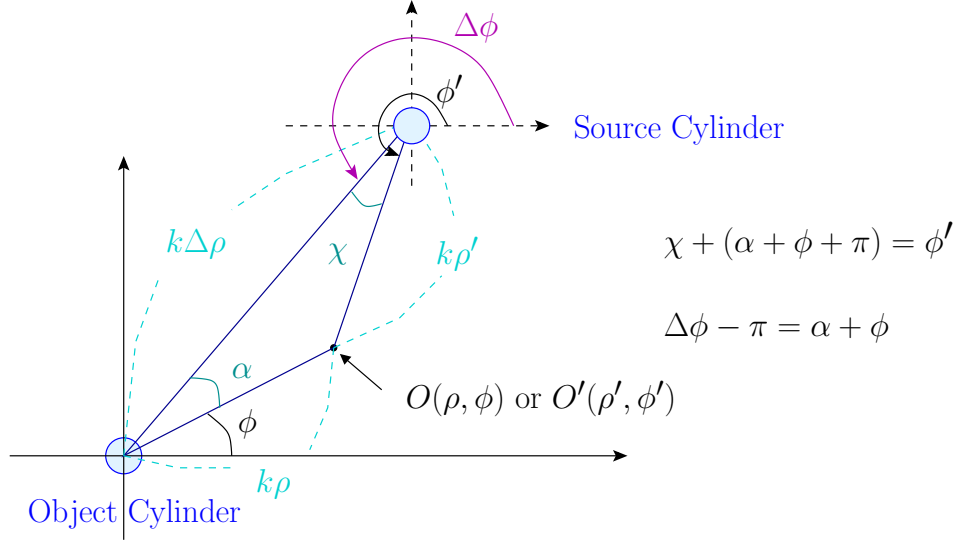


Figure B.3: Detailed geometric figure for Graf's additional theorem combined to our situation.

From this picture we can see two important angle relationships as follows.

$$\chi + (\alpha + \phi + \pi) = \phi' \tag{B.4}$$

$$\Delta\phi - \phi = \pi + \alpha \tag{B.5}$$

Let us begin with the Graf's additional theorem eq. (B.2) with multiplying

$e^{jcmso(\alpha+\phi+\pi)}$ on both sides and using Eq. (B.4),

$$H_{cmso}^{(2)}(k\rho')e^{jcmso\phi'} = \sum_{m=-\infty}^{\infty} H_{cmso+m}^{(2)}(k\Delta\phi)J_m(k\rho)e^{jm\alpha}e^{jcmso(\alpha+\phi+\pi)} \quad (\text{B.6})$$

$$= \sum_{m=-\infty}^{\infty} H_{cmso-m}^{(2)}(k\Delta\phi)J_{-m}(k\rho)e^{-jm\alpha}e^{jcmso(\alpha+\phi+\pi)}, \quad (\because m \leftarrow -m) \quad (\text{B.7})$$

$$= \sum_{m=-\infty}^{\infty} H_{cmso-m}^{(2)}(k\Delta\phi)e^{-jm\pi}J_m(k\rho)e^{-jm\alpha}e^{jcmso(\alpha+\phi+\pi)}, \quad (\because \text{eq. (B.3)}) \quad (\text{B.8})$$

$$= \sum_{m=-\infty}^{\infty} H_{cmso-m}^{(2)}(k\Delta\phi)J_m(k\rho)e^{-jm(\alpha+\pi)}e^{jcmso(\alpha+\phi+\pi)} \quad (\text{B.9})$$

$$= \sum_{m=-\infty}^{\infty} H_{cmso-m}^{(2)}(k\Delta\phi)J_m(k\rho)e^{j(cmso-m)(\alpha+\pi)}e^{jcmso\phi} \quad (\text{B.10})$$

$$= \sum_{m=-\infty}^{\infty} H_{cmso-m}^{(2)}(k\Delta\phi)J_m(k\rho)e^{j(cmso-m)(\Delta\phi-\phi)}e^{jcmso\phi}, \quad (\because \text{eq. (B.5)}) \quad (\text{B.11})$$

$$= \sum_{m=-\infty}^{\infty} H_{cmso-m}^{(2)}(k\Delta\phi)e^{j(cmso-m)\Delta\phi}J_m(k\rho)e^{jm\phi} \quad (\text{B.12})$$

Changing m to $cmob$ and comparing it to Eq. (B.1), we get

$$b_{cmob,cmso} = H_{cmso-cmob}^{(2)}(k\Delta\rho)e^{j(cmso-cmob)\Delta\phi} \quad (\text{B.13})$$

APPENDIX C

Planewave and Cylinder wave conversion formula

C.1 Planewave to Cylinder wave conversion

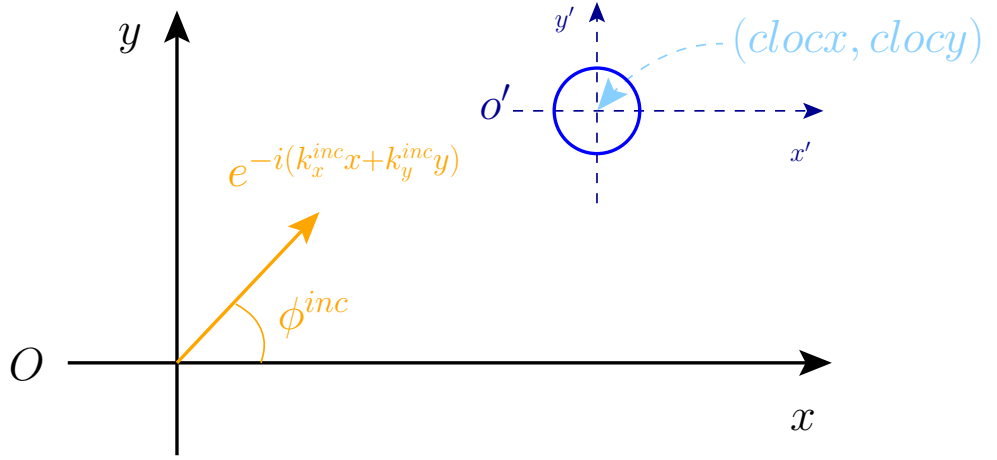


Figure C.1: Planewave with incident angle ϕ^{inc} is shined on a cylinder positioned at $(clocx, clocy)$. We have to convert planewave, whose coordinate system is O into cylinder waves, whose coordinate systems is the cylinder coordinate o' .

Since the incident wave is a planewave, which is finite all over the space, we use the bessel function of the first kind, $J_n(k\rho)e^{jm\phi}$, to express the incident wave as follows,

$$e^{-j(k_x^{inc}x + k_y^{inc}y)} = \sum_{m=-\infty}^{\infty} a_m J_m(k\rho') e^{jm\phi'} \quad (C.1)$$

where $k_x^{inc} = k \cos(\phi^{inc})$, $k_y^{inc} = k \sin(\phi^{inc})$, $x' = \rho' \cos(\phi')$, $y' = \rho' \sin(\phi')$.

Because $x - clox = x'$, $y - cloy = y'$

$$e^{-j(k_x^{inc}(x'+clox)+k_y^{inc}(y'+cloy))} = \sum_{m=-\infty}^{\infty} a_m J_m(k\rho') e^{jm\phi'} \quad (C.2)$$

$$e^{-j(k_x^{inc} clox+k_y^{inc} cloy)} \cdot e^{-j(k_x^{inc} x'+k_y^{inc} y')} = \sum_{m=-\infty}^{\infty} a_m J_m(k\rho') e^{jm\phi'} \quad (C.3)$$

Now we multiply $e^{-jn\phi}$ on both sides and integrate the equation with respect to ϕ over $[0, \pi]$.

$$e^{-j(k_x^{inc} clox+k_y^{inc} cloy)} \cdot \int_0^{2\pi} e^{-j(k_x^{inc} x'+k_y^{inc} y')} \cdot e^{-jn\phi'} d\phi' = a_n J_n(k\rho') \cdot 2\pi \quad (C.4)$$

$$e^{-j(k_x^{inc} clox+k_y^{inc} cloy)} \cdot \int_0^{2\pi} e^{-jk\rho \cos(\phi'-\phi^{inc})} \cdot e^{-jn\phi'} d\phi' = a_n J_n(k\rho') \cdot 2\pi \quad (C.5)$$

By changing variables $\phi_{new} = \phi' - \phi^{inc}$ and using the fact that the functions inside the integral are periodic with 2π

$$e^{-j(k_x^{inc} clox+k_y^{inc} cloy)} \cdot \int_{-\phi_{new}}^{2\pi-\phi_{new}} e^{-jk\rho' \cos(\phi_{new})} \cdot e^{-jn(\phi_{new}+\phi^{inc})} d\phi_{new} = a_n J_n(k\rho') \cdot 2\pi \quad (C.6)$$

$$e^{-j(k_x^{inc} clox+k_y^{inc} cloy)} \cdot e^{-jn\phi^{inc}} \cdot \int_0^{2\pi} e^{-jk\rho' \cos(\phi_{new})} \cdot e^{-jn\phi_{new}} d\phi_{new} = a_n J_n(k\rho') \cdot 2\pi \quad (C.7)$$

Arranging Eq. (C.7), we get

$$J_n(k\rho') = \frac{1}{2\pi} \cdot \int_0^{2\pi} \left(\frac{e^{-j(k_x^{inc} clox+k_y^{inc} cloy)} \cdot e^{-jn\phi^{inc}}}{a_n} \right) \cdot e^{-jk\rho' \cos(\phi)} \cdot e^{-jn\phi'} d\phi' \quad (C.8)$$

Comparing this to the well-known integral representation of bessel function [28],

$$J_n(k\rho) = \frac{1}{2\pi} \cdot \int_0^{2\pi} e^{j\frac{n\pi}{2}} \cdot e^{-jk\rho \cos(\phi)} \cdot e^{-jn\phi} d\phi \quad (C.9)$$

then we get the following conversion formula,

$$a_n = e^{-j(k_x^{inc} clox+k_y^{inc} cloy)} \cdot e^{-jn\phi^{inc}} \cdot e^{-j\frac{n\pi}{2}} \quad (C.10)$$

C.2 Cylinderwave to Plane wave conversion

The wave at (x, y) coming from the cm^{th} mode of a fixed cylinder and its repeated counterparts can be expressed like below when the incident angle is ϕ_{inc} ,

$$\sum_{n=-\infty}^{\infty} H_{cm}^{(2)}(k\|(x, y) - n \cdot (L, 0)\|) e^{j(cm) \arctan((x,y)-n \cdot (L,0))} \cdot e^{-jk_x^{inc} n \cdot L} \quad (C.11)$$

This can be expressed in a different way using convolution with respect to x like below,

$$\begin{aligned} & \sum_{n=-\infty}^{\infty} H_{cm}^{(2)}(k\|(x, y) - n \cdot (L, 0)\|) e^{jcm \cdot \arctan((x,y)-n \cdot (L,0))} \cdot e^{-jk_x^{inc} nL} \\ &= H_{cm}^{(2)}(k\|(x, y)\|) e^{jcm \cdot \arctan((x,y))} * \sum_{n=-\infty}^{\infty} \delta(x - nL) e^{-jk_x^{inc} nL} \end{aligned} \quad (C.12)$$

To express this in terms of planewaves, we use planewave decomposition of Hankel function. This can be done by following the same procedure done in [59] except setting the integration contour from $(\epsilon - j\infty)$ to $(-\epsilon + j\infty)$ (reverse direction of the contour done in the reference). Then the planewave decomposition of the cylinder wave will be like below,

$$\begin{aligned} & H_{cm}^{(2)}(k\|(x, y)\|) e^{jcm \cdot \arctan((x,y))} \\ &= \int_{-\infty}^{\infty} \frac{(\text{sign}(y))^{cm} (-1)^{cm}}{\pi k_y(\beta)} \cdot e^{-jcm \cdot \text{sign}(y) \arcsin(\frac{\beta}{k})} \cdot e^{-j\beta x} \cdot e^{-jk_y(\beta)|y|} d\beta \end{aligned} \quad (C.13)$$

$$, \text{ where } k_y(\beta) = \begin{cases} \sqrt{k^2 - \beta^2}, & |\beta| \leq k \\ -j\sqrt{\beta^2 - k^2}, & |\beta| > k \end{cases}$$

Plugging eq. (C.13) into Eq. (C.12), Eq. (C.11) becomes

$$\int_{-\infty}^{\infty} \frac{(\text{sign}(y))^{cm} (-1)^{cm}}{\pi k_y(\beta)} \cdot e^{-jcm \cdot \text{sign}(y) \arcsin(\frac{\beta}{k})} \cdot \left(\sum_{n=-\infty}^{\infty} e^{-jnLk_x^{inc}} \cdot e^{-j\beta(x-nL)} \right) \cdot e^{-jk_y(\beta)|y|} d\beta \quad (C.14)$$

$$= \int_{-\infty}^{\infty} \frac{(\text{sign}(y))^{cm} (-1)^{cm}}{\pi k_y(\beta)} \cdot e^{-jcm \cdot \text{sign}(y) \arcsin(\frac{\beta}{k})} \cdot \left(\sum_{n=-\infty}^{\infty} e^{j(\beta - k_x^{inc})nL} \right) \cdot e^{-j\beta x} \cdot e^{-jk_y(\beta)|y|} d\beta \quad (C.15)$$

Let us use the identity below from fourier analysis,

$$\sum_{n=-\infty}^{\infty} e^{jwnL} = \frac{2\pi}{L} \sum_{n=-\infty}^{\infty} \delta(\omega - \frac{2\pi}{L}n) \quad (C.16)$$

then Eq. (C.15) becomes,

$$= \int_{-\infty}^{\infty} \frac{(\text{sign}(y))^{cm} (-1)^{cm}}{\pi k_y(\beta)} \cdot e^{-jcm \cdot \text{sign}(y) \arcsin(\frac{\beta}{k})} \cdot \left(\sum_{n=-\infty}^{\infty} \frac{2\pi}{L} \delta(\beta - k_x^{inc} - \frac{2\pi}{L}n) \right) \cdot e^{-j\beta x} \cdot e^{-jk_y(\beta)|y|} d\beta \quad (\text{C.17})$$

$$= \sum_{n=-\infty}^{\infty} \frac{2(\text{sign}(y))^{cm} (-1)^{cm}}{L k_y(k_x^{inc} + \frac{2\pi}{L}n)} \cdot e^{-jcm \cdot \text{sign}(y) \arcsin(\frac{k_x^{inc} + \frac{2\pi}{L}n}{k})} \cdot e^{-j(k_x^{inc} + \frac{2\pi}{L}n)x} \cdot e^{-jk_y(k_x^{inc} + \frac{2\pi}{L}n)|y|} \quad (\text{C.18})$$

$$= \sum_{n=-\infty}^{\infty} \text{sign}(y)^{cm} \cdot e^{-jk_{x_n}x} \cdot e^{-jk_{y_n}|y|} \cdot e^{-jcm(\text{sign}(y) \cdot \arcsin(\frac{k_{x_n}}{k}) - \pi)} \cdot \frac{2}{k_{y_n} \cdot L} \quad (\text{C.19})$$

where $k_{x_n} = k_x^{inc} + \frac{2\pi}{L}n$ and $k_{y_n} = k_y(k_{x_n})$.

APPENDIX D

Boundary Value Problem

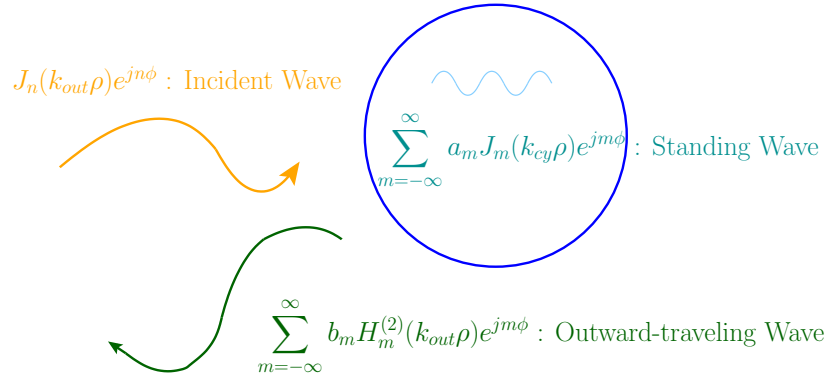


Figure D.1: $J_n(k_{out}\rho)e^{jn\phi}$ is incident on the scatterer, and scattered waves are produced inside and outside of the scatterer. We find the scattering coefficients, a_n s and b_n s, by matching the boundary conditions.

Scattering Coefficients are the coefficients of the scattered cylinder wave when unit cylinder wave is incident to a scatterer. We excite a cylinder's wave $J_n(k_{out}\rho)e^{jn\phi}$ and this will produce scattered waves inside and outside of the scatterer. Scattering coefficients are obtained by expressing the scattered waves with proper type of Bessel functions and using boundary conditions.

We write the scattered wave outside as $\sum_{m=-\infty}^{\infty} b_m H_m^{(2)}(k_{out}\rho)e^{jm\phi}$ since the scattered waves outside should be an outgoing-traveling wave, and we write the scattered wave inside as $\sum_{m=-\infty}^{\infty} a_m J_m(k_{cy}\rho)e^{jm\phi}$ since the internal wave should be finite at the origin of the scatterer.

There are four boundary conditions in electromagnetic problems which are derived

from Maxwell's equations.

$$E_{t1} = E_{t2} \quad (\text{D.1})$$

$$\mathbf{N} \times (\mathbf{H}_1 - \mathbf{H}_2) = \mathbf{J}_s \quad (\text{D.2})$$

$$B_{n1} = B_{n2} \quad (\text{D.3})$$

$$\mathbf{N} \cdot (\mathbf{D}_1 - \mathbf{D}_2) = \rho \quad (\text{D.4})$$

where E_{t1}, E_{t2} are tangential components of the electric field in medium1 and medium2 respectively, $\mathbf{H}_1, \mathbf{H}_2$ are the magnetic field vector in medium1 and medium2 respectively, B_{n1}, B_{n2} are normal components of the magnetic flux density in medium1 and medium2 respectively, $\mathbf{D}_1, \mathbf{D}_2$ are the electric flux density vector in medium1 and medium2 respectively, \mathbf{J}_s is the surface current density, \mathbf{N} is the unit normal vector from medium2.

Note that \mathbf{J}_s is the density of a sheet current which has the unit of ampere per meter (A/m). This is different from the volume current density \mathbf{J} , whose unit is ampere per area (A/m^2). This surface current does not exist for finite volume currents in the media except for the perfect electric conductor case. So tangential magnetic field is continuous for almost all physical media except for perfect electric conductor due to Eq. (D.2). Similarly since there is no electric field inside a perfect electric conductor, the tangential electric field must be 0 because of Eq. (D.1). The continuity of tangential magnetic field and tangential electric field will be used to match the conditions at the boundary in the following sections.

In the following two sections, we will derive scattering coefficients for cylinder-shaped scatterers, and in the last section we will briefly mention how to deal with arbitrary-shaped scatterers.

D.1 TM Solution

TM wave is the wave whose electric field oscillates only in z direction which implies that it only has tangential components at the boundary of cylinders.

D.1.1 TM - PEC Case

Due to Gauss's law we know that the electric field inside a perfect electric conductor must be zero anywhere. This tells us that $a_m = 0$ for all m , and also the electric field on the surface of the conductor must be zero due to Eq. (D.1). We can write this as below.

$$\left(J_n(k_{out}\rho)e^{jn\phi} + \sum_{m=-\infty}^{\infty} b_m H_m^{(2)}(k_{out}\rho)e^{jm\phi} \right)_{\rho=r_0} = 0 \quad (\text{D.5})$$

$$J_n(k_{out}r_0)e^{jn\phi} + \sum_{m=-\infty}^{\infty} b_m H_m^{(2)}(k_{out}r_0)e^{jm\phi} = 0 \quad (\text{D.6})$$

$$J_n(k_{out}r_0)e^{jn\phi} + b_n H_n^{(2)}(k_{out}r_0)e^{jn\phi} + \sum_{m \neq n} b_m H_m^{(2)}(k_{out}r_0)e^{jm\phi} = 0 \quad (\text{D.7})$$

Since this condition should hold for any ϕ ,

$$b_m = 0, \quad \forall m \neq n \quad (\text{D.8})$$

$$J_n(k_{out}r_0)e^{jn\phi} + b_n H_n^{(2)}(k_{out}r_0)e^{jn\phi} = 0 \quad (\text{D.9})$$

From Eq. (D.9) we get,

$$b_n = -\frac{J_n(k_{out}r_0)}{H_n^{(2)}(k_{out}r_0)} \quad (\text{D.10})$$

D.1.2 TM - Dielectric Case

For dielectric cylinder we have internal waves and outgoing waves both. So we will have unknowns a_n s and b_n s. We will use Eq. (D.1) and Eq. (D.2) which tell us that the tangential component of the electric field and magnetic field must be continuous. From Eq. (D.1) we get

$$\left(J_n(k_{out}\rho)e^{jn\phi} + \sum_{m=-\infty}^{\infty} b_m H_m^{(2)}(k_{out}\rho)e^{jm\phi} \right)_{\rho=r_0} = \left(\sum_{m=-\infty}^{\infty} a_m J_m(k_{cy}\rho)e^{jm\phi} \right)_{\rho=r_0} \quad (\text{D.11})$$

To make this satisfied for all ϕ ,

$$a_m = 0, \quad b_m = 0, \quad \forall m \neq n \quad (\text{D.12})$$

$$a_n J_n(k_{cy}r_0) = J_n(k_{out}r_0) + b_n H_n^{(2)}(k_{out}r_0) \quad (\text{D.13})$$

To simplify the boundary condition Eq. (D.2), we have to use Faraday's law to get the magnetic field.

$$\nabla \times E = -j\omega\mu H \longrightarrow H = \frac{j}{\omega\mu} \nabla \times E \quad (\text{D.14})$$

Since the Eq. (D.2) states the continuity of the tangential component of the magnetic field, we only have to match the ϕ component which can be derived by below,

$$H_\phi = \frac{j}{\omega\mu} (\nabla \times E)_\phi \quad (\text{D.15})$$

$$= \frac{j}{\omega\mu} \left(\frac{1}{\rho} \begin{vmatrix} \hat{\rho} & \rho\hat{\phi} & \hat{z} \\ \frac{\partial}{\partial\rho} & \frac{\partial}{\partial\phi} & \frac{\partial}{\partial z} \\ 0 & 0 & E_z \end{vmatrix} \right)_\phi \quad (\text{D.16})$$

$$= -\frac{j}{\omega\mu} \frac{\partial E_z}{\partial\rho} \quad (\text{D.17})$$

With the similar argument as before, we know that

$$a_m = 0, \quad b_m = 0, \quad \forall m \neq n \quad (\text{D.18})$$

Using Eq. (D.17), Eq. (D.2) reduces to

$$-\frac{j}{\omega\mu_{out}}(k_{out}J'_n(k_{out}r_0) + b_n k_{out}H_n^{(2)'}(k_{out}r_0)) = -\frac{j}{\omega\mu_{cy}}a_n k_{cy}J'_n(k_{cy}r_0) \quad (D.19)$$

$$k_{out}\mu_{cy}J'_n(k_{out}r_0) + b_n k_{out}\mu_{cy}H_n^{(2)'}(k_{out}r_0) = a_n k_{cy}\mu_{out}J'_n(k_{cy}r_0) \quad (D.20)$$

Combining Eq. (D.13) and Eq. (D.20) we get

$$b_n = \frac{-k_{out}\mu_{cy}J_n(k_{cy}a)J'_n(k_{out}a) + k_{cy}\mu_{out}J_n(k_{out}a)J'_n(k_{cy}a)}{k_{out}\mu_{cy}J_n(k_{cy}a)H_n^{(2)'}(k_{out}a) - k_{cy}\mu_{out}J'_n(k_{cy}a)H_n^{(2)}(k_{out}a)} \quad (D.21)$$

To simplify this solution, we use the *dispersion relation*.

$$k^2 = \omega^2 \mu \epsilon \quad (D.22)$$

$$k = \omega \sqrt{\mu \epsilon} = \omega \sqrt{\mu_0 \mu_r \epsilon_0 \epsilon_r} = \omega \sqrt{\mu_0 \epsilon_0} \sqrt{\mu_r \epsilon_r} \quad (D.23)$$

$$= \omega \frac{1}{c} \sqrt{\mu_r \epsilon_r}, \quad c \text{ is speed of light in vacuum} \quad (D.24)$$

$$= \frac{2\pi}{T} \frac{T}{\lambda_0} \sqrt{\mu_r \epsilon_r}, \quad T \text{ is time-period of light} \quad (D.25)$$

$$= \frac{2\pi}{\lambda_0} \sqrt{\mu_r \epsilon_r} \quad (D.26)$$

where ϵ_0 and μ_0 are permittivity and permeability in vacuum respectively, and ϵ_r and μ_r are relative permittivity and relative permeability respectively. Using the relation above, we will have the following facts,

$$k_{out} = \frac{2\pi}{\lambda_0} \sqrt{\tilde{\epsilon}_{out} \tilde{\mu}_{out}} \quad (D.27)$$

$$k_{cy} = \frac{2\pi}{\lambda_0} \sqrt{\tilde{\epsilon}_{cy} \tilde{\mu}_{cy}} \quad (D.28)$$

$$\epsilon_{out} = \epsilon_0 \tilde{\epsilon}_{out}, \quad \mu_{out} = \mu_0 \tilde{\mu}_{out} \quad (D.29)$$

$$\epsilon_{cy} = \epsilon_0 \tilde{\epsilon}_{cy}, \quad \mu_{cy} = \mu_0 \tilde{\mu}_{cy} \quad (D.30)$$

Substituting these to Eq. (D.21), we have

$$b_n = \frac{-\sqrt{\tilde{\epsilon}_{out} \tilde{\mu}_{cy}} J_n(k_{cy}a) J'_n(k_{out}a) + \sqrt{\tilde{\epsilon}_{cy} \tilde{\mu}_{out}} J_n(k_{out}a) J'_n(k_{cy}a)}{\sqrt{\tilde{\epsilon}_{out} \tilde{\mu}_{cy}} J_n(k_{cy}a) H_n^{(2)'}(k_{out}a) - \sqrt{\tilde{\epsilon}_{cy} \tilde{\mu}_{out}} J'_n(k_{cy}a) H_n^{(2)}(k_{out}a)} \quad (D.31)$$

D.2 TE Solution

TE wave is the wave whose magnetic field oscillates only in z direction which implies that it only has tangential components at the boundary of cylinders.

D.2.1 TE - PEC Case

Due to Gauss's law we know that the magnetic and electric field inside a perfect electric conductor must be zero anywhere, thus $a_m = 0$ for all m , and also the

electric field on the surface of the conductor must be zero due to Eq. (D.1) but not the magnetic field due to the surface current. So we will obtain the solution by setting the tangential electric field to zero. To do so, we have to calculate the tangential electric field from the magnetic field. The electric field can be obtained from Ampere's Law

$$\nabla \times H = J + j\omega\epsilon E \longrightarrow E = -\frac{j}{\omega\epsilon} \nabla \times H \quad (\text{D.32})$$

The tangential component of the electric field is the ϕ component. To extract this from the formula above,

$$E_\phi = -\frac{j}{\omega\epsilon} (\nabla \times H)_\phi \quad (\text{D.33})$$

$$= -\frac{j}{\omega\epsilon} \left(\frac{1}{\rho} \begin{vmatrix} \hat{\rho} & \rho\hat{\phi} & \hat{z} \\ \frac{\partial}{\partial\rho} & \frac{\partial}{\partial\phi} & \frac{\partial}{\partial z} \\ 0 & 0 & H_z \end{vmatrix} \right)_\phi \quad (\text{D.34})$$

$$= \frac{j}{\omega\epsilon} \frac{\partial H_z}{\partial\rho} \quad (\text{D.35})$$

Applying this result to Eq. (D.1) and using the geometric symmetry,

$$b_m = 0, \quad \forall m \neq n \quad (\text{D.36})$$

$$J'_n(k_{out}r_0) + b_n H'_n{}^{(2)}(k_{out}r_0) = 0 \quad (\text{D.37})$$

Therefore,

$$b_n = -\frac{J'_n(k_{out}r_0)}{H'_n{}^{(2)}(k_{out}r_0)} \quad (\text{D.38})$$

D.2.2 TE - Dielectric Case

For dielectric cylinder we have internal waves and outgoing waves both. So we will have unknowns a_n s and b_n s. We will use Eq. (D.1) and Eq. (D.2) which tells us that the tangential component of the electric field and magnetic field must be continuous. From Eq. (D.2) we get

$$\left(J_n(k_{out}\rho)e^{jn\phi} + \sum_{m=-\infty}^{\infty} b_m H_m^{(2)}(k_{out}\rho)e^{jm\phi} \right)_{\rho=r_0} = \left(\sum_{m=-\infty}^{\infty} a_m J_m(k_{cy}\rho)e^{jm\phi} \right)_{\rho=r_0} \quad (\text{D.39})$$

To make this satisfied for all ϕ ,

$$a_m = 0, \quad b_m = 0, \quad \forall m \neq n \quad (\text{D.40})$$

$$a_n J_n(k_{cy}r_0) = J_n(k_{out}r_0) + b_n H_n^{(2)}(k_{out}r_0) \quad (\text{D.41})$$

To use the boundary condition Eq. (D.1) we need to use Eq. (D.35) to get the tangential electric field. Then we will have

$$\frac{j}{\omega\epsilon_{out}}(k_{out}J'_n(k_{out}r_0) + b_n k_{out}H_n^{(2)}(k_{out}r_0)) = \frac{j}{\omega\epsilon_{cy}}a_n k_{cy}J'_n(k_{cy}r_0) \quad (D.42)$$

$$k_{out}\epsilon_{cy}J'_n(k_{out}r_0) + b_n k_{out}\epsilon_{cy}H_n^{(2)}(k_{out}r_0) = a_n k_{cy}\epsilon_{out}J'_n(k_{cy}r_0) \quad (D.43)$$

Combining Eq. (D.41) and Eq. (D.43) we get

$$b_n = \frac{-k_{out}\epsilon_{cy}J_n(k_{cy}a)J'_n(k_{out}a) + k_{cy}\epsilon_{out}J_n(k_{out}a)J'_n(k_{cy}a)}{k_{out}\epsilon_{cy}J_n(k_{cy}a)H_n^{(2)}(k_{out}a) - k_{cy}\epsilon_{out}J'_n(k_{cy}a)H_n^{(2)}(k_{out}a)} \quad (D.44)$$

Using Equations (D.27) to (D.30), Eq. (D.44) becomes

$$b_n = \frac{-\sqrt{\tilde{\epsilon}_{cy}\tilde{\mu}_{out}}J_n(k_{out}a)J'_n(k_{cy}a) + \sqrt{\tilde{\epsilon}_{out}\tilde{\mu}_{cy}}J_n(k_{cy}a)J'_n(k_{out}a)}{\sqrt{\tilde{\epsilon}_{cy}\tilde{\mu}_{out}}J_n(k_{out}a)H_n^{(2)}(k_{cy}a) - \sqrt{\tilde{\epsilon}_{out}\tilde{\mu}_{cy}}J'_n(k_{out}a)H_n^{(2)}(k_{cy}a)} \quad (D.45)$$

D.3 Arbitrary shaped cylinder

In the previous two section, we dealt with cylinder-shaped scatterer, which has a symmetric property that made n^{th} mode input only produce n^{th} mode output. Thus making the scattering coefficient matrix Z diagonal.

The natural next question is to ask is what happens if we have an arbitrary shaped scatterer. Quick answer is that the n^{th} mode input will produce different order of modes so that the scattering coefficient matrix will no longer be diagonal.

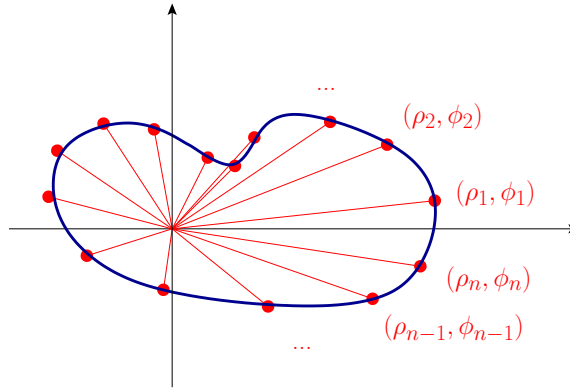


Figure D.2: For arbitrary-shaped homogeneous scatterer we have to choose finite n points at the boundary, and obtain n equations with finite amount of unknown scattering coefficients.

To deal with this we have to use *Finite Element Method*. We have to choose two parameters. One is the number of grid points to use at the boundary. From these grid points we get the boundary conditions thus the number of grid points is the same as number of equations we will get. The second parameter is the number of modes we want to use for approximation, thus this will give us the number of unknowns. Based on these equations and unknowns, we formulate a matrix vector equation to obtain the unknowns which will be our scattering coefficients.

APPENDIX E

Cascading Formula

For cascading two scattering matrices, the situation can be described as below. Using the block structure of $S^{(1)}$ and $S^{(2)}$ given as below,

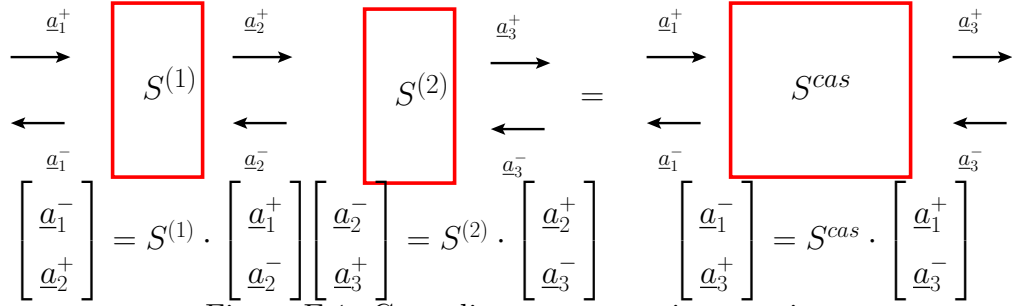


Figure E.1: Cascading two scattering matrices

$$\text{Let } S^{(1)} = \begin{bmatrix} S_{11}^{(1)} & S_{12}^{(1)} \\ S_{21}^{(1)} & S_{22}^{(1)} \end{bmatrix} \text{ and } S^{(2)} = \begin{bmatrix} S_{11}^{(2)} & S_{12}^{(2)} \\ S_{21}^{(2)} & S_{22}^{(2)} \end{bmatrix} \quad (\text{E.1})$$

we will get four equations.

Two from $S^{(1)}$

$$\underline{a}_1^- = S_{11}^{(1)} \cdot \underline{a}_1^+ + S_{12}^{(1)} \cdot \underline{a}_2^- \quad (\text{E.2})$$

$$\underline{a}_2^+ = S_{21}^{(1)} \cdot \underline{a}_1^+ + S_{22}^{(1)} \cdot \underline{a}_2^- \quad (\text{E.3})$$

The rest of the two from $S^{(2)}$

$$\underline{a}_2^- = S_{11}^{(2)} \cdot \underline{a}_2^+ + S_{12}^{(2)} \cdot \underline{a}_3^- \quad (\text{E.4})$$

$$\underline{a}_3^+ = S_{21}^{(2)} \cdot \underline{a}_2^+ + S_{22}^{(2)} \cdot \underline{a}_3^- \quad (\text{E.5})$$

Our goal is to express $(\underline{a}_1^-, \underline{a}_3^+)$ in terms of $(\underline{a}_1^+, \underline{a}_3^-)$. Let us first focus on \underline{a}_1^- . From Eq. (E.2), we can see that we need to express \underline{a}_2^- in terms of $(\underline{a}_1^+, \underline{a}_3^-)$. We can

accomplish this by plugging Eq. (E.3) into Eq. (E.4),

$$\underline{a}_2^- = S_{11}^{(2)} \cdot \underline{a}_2^+ + S_{12}^{(2)} \cdot \underline{a}_3^- \quad (\text{E.6})$$

$$= S_{11}^{(2)} \cdot (S_{21}^{(1)} \cdot \underline{a}_1^+ + S_{22}^{(1)} \cdot \underline{a}_2^-) + S_{12}^{(2)} \cdot \underline{a}_3^- \quad (\text{E.7})$$

$$(I - S_{11}^{(2)} \cdot S_{22}^{(1)}) \cdot \underline{a}_2^- = S_{11}^{(2)} \cdot S_{21}^{(1)} \cdot \underline{a}_1^+ + S_{12}^{(2)} \cdot \underline{a}_3^- \quad (\text{E.8})$$

$$\underline{a}_2^- = (I - S_{11}^{(2)} \cdot S_{22}^{(1)})^{-1} \cdot (S_{11}^{(2)} \cdot S_{21}^{(1)} \cdot \underline{a}_1^+ + S_{12}^{(2)} \cdot \underline{a}_3^-) \quad (\text{E.9})$$

Plugging Eq. (E.9) into Eq. (E.2),

$$\underline{a}_1^- = S_{11}^{(1)} \cdot \underline{a}_1^+ + S_{12}^{(1)} \cdot \underline{a}_2^- \quad (\text{E.10})$$

$$= S_{11}^{(1)} \cdot \underline{a}_1^+ + S_{12}^{(1)} \cdot (I - S_{11}^{(2)} \cdot S_{22}^{(1)})^{-1} \cdot (S_{11}^{(2)} \cdot S_{21}^{(1)} \cdot \underline{a}_1^+ + S_{12}^{(2)} \cdot \underline{a}_3^-) \quad (\text{E.11})$$

$$= (S_{11}^{(1)} + S_{12}^{(1)} \cdot (I - S_{11}^{(2)} \cdot S_{22}^{(1)})^{-1} \cdot S_{11}^{(2)} \cdot S_{21}^{(1)}) \cdot \underline{a}_1^+ + S_{12}^{(1)} \cdot (I - S_{11}^{(2)} \cdot S_{22}^{(1)})^{-1} \cdot S_{12}^{(2)} \cdot \underline{a}_3^- \quad (\text{E.12})$$

Now let us seek for \underline{a}_3^+ . From Eq. (E.5), we can see that we need to express \underline{a}_2^+ in terms of $(\underline{a}_1^+, \underline{a}_3^-)$. We can accomplish this by plugging Eq. (E.4) into Eq. (E.3),

$$\underline{a}_2^+ = S_{21}^{(1)} \cdot \underline{a}_1^+ + S_{22}^{(1)} \cdot \underline{a}_2^- \quad (\text{E.13})$$

$$= S_{21}^{(1)} \cdot \underline{a}_1^+ + S_{22}^{(1)} \cdot (S_{11}^{(2)} \cdot \underline{a}_2^+ + S_{12}^{(2)} \cdot \underline{a}_3^-) \quad (\text{E.14})$$

$$(I - S_{22}^{(1)} \cdot S_{11}^{(2)}) \underline{a}_2^+ = S_{21}^{(1)} \cdot \underline{a}_1^+ + S_{22}^{(1)} \cdot S_{12}^{(2)} \cdot \underline{a}_3^- \quad (\text{E.15})$$

$$\underline{a}_2^+ = (I - S_{22}^{(1)} \cdot S_{11}^{(2)})^{-1} \cdot (S_{21}^{(1)} \cdot \underline{a}_1^+ + S_{22}^{(1)} \cdot S_{12}^{(2)} \cdot \underline{a}_3^-) \quad (\text{E.16})$$

Plugging this into Eq. (E.5),

$$\underline{a}_3^+ = S_{21}^{(2)} \cdot \underline{a}_2^+ + S_{22}^{(2)} \cdot \underline{a}_3^- \quad (\text{E.17})$$

$$= S_{21}^{(2)} \cdot (I - S_{22}^{(1)} \cdot S_{11}^{(2)})^{-1} \cdot (S_{21}^{(1)} \cdot \underline{a}_1^+ + S_{22}^{(1)} \cdot S_{12}^{(2)} \cdot \underline{a}_3^-) + S_{22}^{(2)} \cdot \underline{a}_3^- \quad (\text{E.18})$$

$$= S_{21}^{(2)} \cdot (I - S_{22}^{(1)} \cdot S_{11}^{(2)})^{-1} \cdot S_{21}^{(1)} \cdot \underline{a}_1^+ + (S_{22}^{(2)} + S_{21}^{(2)} \cdot (I - S_{22}^{(1)} \cdot S_{11}^{(2)})^{-1} \cdot S_{22}^{(1)} \cdot S_{12}^{(2)}) \cdot \underline{a}_3^- \quad (\text{E.19})$$

Combining Eq. (E.12) and Eq. (E.19) we get,

$$\begin{bmatrix} E_i^- \\ E_j^+ \end{bmatrix} = \begin{bmatrix} S_{11}^{(1)} + S_{12}^{(1)} \cdot (I - S_{11}^{(2)} \cdot S_{22}^{(1)})^{-1} \cdot S_{11}^{(2)} \cdot S_{21}^{(1)} & S_{12}^{(1)} \cdot (I - S_{11}^{(2)} \cdot S_{22}^{(1)})^{-1} \cdot S_{12}^{(2)} \\ S_{21}^{(2)} \cdot (I - S_{22}^{(1)} \cdot S_{11}^{(2)})^{-1} \cdot S_{21}^{(1)} & S_{22}^{(2)} + S_{21}^{(2)} \cdot (I - S_{22}^{(1)} \cdot S_{11}^{(2)})^{-1} \cdot S_{22}^{(1)} \cdot S_{12}^{(2)} \end{bmatrix} \quad (\text{E.20})$$

Therefore

$$S_{cas} = \begin{bmatrix} S_{11}^{(1)} + S_{12}^{(1)} \cdot (I - S_{11}^{(2)} \cdot S_{22}^{(1)})^{-1} \cdot S_{11}^{(2)} \cdot S_{21}^{(1)} & S_{12}^{(1)} \cdot (I - S_{11}^{(2)} \cdot S_{22}^{(1)})^{-1} \cdot S_{12}^{(2)} \\ S_{21}^{(2)} \cdot (I - S_{22}^{(1)} \cdot S_{11}^{(2)})^{-1} \cdot S_{21}^{(1)} & S_{22}^{(2)} + S_{21}^{(2)} \cdot (I - S_{22}^{(1)} \cdot S_{11}^{(2)})^{-1} \cdot S_{22}^{(1)} \cdot S_{12}^{(2)} \end{bmatrix} \quad (\text{E.21})$$

APPENDIX F

Scattering Matrix and Transfer Matrix conversion formula



Transfer matrix and Scattering matrix are matrices that relate the waves \underline{a}_1^+ , \underline{a}_1^- , \underline{a}_2^+ , \underline{a}_2^- in the following way,

$$\begin{bmatrix} \underline{a}_2^+ \\ \underline{a}_2^- \end{bmatrix} = T \begin{bmatrix} \underline{a}_1^+ \\ \underline{a}_1^- \end{bmatrix}, \quad \text{where } T : \text{Transfer Matrix} \quad (\text{F.1})$$

$$\begin{bmatrix} \underline{a}_1^- \\ \underline{a}_2^+ \end{bmatrix} = S \begin{bmatrix} \underline{a}_1^+ \\ \underline{a}_2^- \end{bmatrix}, \quad \text{where } S : \text{Scattering Matrix} \quad (\text{F.2})$$

To get the conversion formula from Transfer matrix to Scattering matrix and vice versa, we have to use the block structure they have,

$$T = \begin{bmatrix} T_{11} & T_{12} \\ T_{21} & T_{22} \end{bmatrix} \quad (\text{F.3})$$

$$S = \begin{bmatrix} S_{11} & S_{12} \\ S_{21} & S_{22} \end{bmatrix} \quad (\text{F.4})$$

F.1 Scattering Matrix to Transfer Matrix

From Eq. (F.2) and Eq. (F.4) we get two equations,

$$\underline{a}_1^- = S_{11} \cdot \underline{a}_1^+ + S_{12} \cdot \underline{a}_2^- \quad (\text{F.5})$$

$$\underline{a}_2^+ = S_{21} \cdot \underline{a}_1^+ + S_{22} \cdot \underline{a}_2^- \quad (\text{F.6})$$

To formulate a transfer matrix, we need to express $(\underline{a}_2^+$ and $\underline{a}_2^-)$ in terms of $(\underline{a}_1^+$ and $\underline{a}_1^-)$. If S_{12} is invertible; i.e. if the scattering system does not have closed channels; from Eq. (F.5) we get,

$$\underline{a}_2^- = -S_{12}^{-1} \cdot S_{11} \cdot \underline{a}_1^+ + S_{12}^{-1} \cdot \underline{a}_1^- \quad (\text{F.7})$$

Plugging this result into Eq. (F.6),

$$\underline{a}_2^+ = S_{21} \cdot \underline{a}_1^+ + S_{22} \cdot \underline{a}_2^- \quad (\text{F.8})$$

$$= S_{21} \cdot \underline{a}_1^+ + S_{22} \cdot (-S_{12}^{-1} \cdot S_{11} \cdot \underline{a}_1^+ + S_{12}^{-1} \cdot \underline{a}_1^-) \quad (\text{F.9})$$

$$= (S_{21} - S_{22} \cdot S_{12}^{-1} \cdot S_{11}) \cdot \underline{a}_1^+ + S_{22} \cdot S_{12}^{-1} \cdot \underline{a}_1^- \quad (\text{F.10})$$

Combining Eq. (F.7) and Eq. (F.10),

$$\begin{bmatrix} \underline{a}_2^+ \\ \underline{a}_2^- \end{bmatrix} = \begin{bmatrix} S_{21} - S_{22} \cdot S_{12}^{-1} \cdot S_{11} & S_{22} \cdot S_{12}^{-1} \\ -S_{12}^{-1} \cdot S_{11} & S_{12}^{-1} \end{bmatrix} \begin{bmatrix} \underline{a}_1^+ \\ \underline{a}_1^- \end{bmatrix}. \quad (\text{F.11})$$

Therefore

$$T = \begin{bmatrix} S_{21} - S_{22} \cdot S_{12}^{-1} \cdot S_{11} & S_{22} \cdot S_{12}^{-1} \\ -S_{12}^{-1} \cdot S_{11} & S_{12}^{-1} \end{bmatrix}. \quad (\text{F.12})$$

Furthermore, if S_{22} is invertible, this can be rewritten as,

$$T = \begin{bmatrix} S_{22} & 0 \\ 0 & S_{12}^{-1} \end{bmatrix} \cdot \begin{bmatrix} S_{22}^{-1} \cdot S_{21} \cdot S_{11}^{-1} - S_{12}^{-1} & I \\ -I & S_{12} \end{bmatrix} \cdot \begin{bmatrix} S_{11} & 0 \\ 0 & S_{12}^{-1} \end{bmatrix}.$$

Then, we can evaluate the determinant of the T matrix,

$$\begin{aligned} \det(T) &= \det \begin{bmatrix} S_{22} & 0 \\ 0 & S_{12}^{-1} \end{bmatrix} \cdot \underbrace{\det \begin{bmatrix} S_{22}^{-1} \cdot S_{21} \cdot S_{11}^{-1} - S_{12}^{-1} & I \\ -I & S_{12} \end{bmatrix}}_{=\det(S_{22}^{-1} \cdot S_{21} \cdot S_{11}^{-1} \cdot S_{12})} \cdot \det \begin{bmatrix} S_{11} & 0 \\ 0 & S_{12}^{-1} \end{bmatrix} \\ &= \frac{\det(S_{22})}{\det(S_{12})} \cdot \frac{\det(S_{21}) \det(S_{12})}{\det(S_{22}) \det(S_{11})} \cdot \frac{\det(S_{11})}{\det(S_{12})} \\ &= \frac{\det(S_{21})}{\det(S_{12})} \\ &= 1. \quad (\because S_{21} = F \cdot S_{12}^T \cdot F) \end{aligned}$$

F.2 Transfer Matrix to Scattering Matrix

From Eq. (F.1) and Eq. (F.3) we get two equations,

$$\underline{a}_2^+ = T_{11} \cdot \underline{a}_1^+ + T_{12} \cdot \underline{a}_1^- \quad (\text{F.13})$$

$$\underline{a}_2^- = T_{21} \cdot \underline{a}_1^+ + T_{22} \cdot \underline{a}_1^- \quad (\text{F.14})$$

To formulate a scattering matrix, we need to express $(\underline{a}_1^-$ and $\underline{a}_2^+)$ in terms of $(\underline{a}_1^+$ and $\underline{a}_2^-)$. From Eq. (F.14) we get,

$$\underline{a}_1^- = -T_{22}^{-1} \cdot T_{21} \cdot \underline{a}_1^+ + T_{22}^{-1} \cdot \underline{a}_2^- \quad (\text{F.15})$$

Plugging this result into Eq. (F.13),

$$\underline{a}_2^+ = T_{11} \cdot \underline{a}_1^+ + T_{12} \cdot \underline{a}_1^- \quad (\text{F.16})$$

$$= T_{11} \cdot \underline{a}_1^+ + T_{12} \cdot (-T_{22}^{-1} \cdot T_{21} \cdot \underline{a}_1^+ + T_{22}^{-1} \cdot \underline{a}_2^-) \quad (\text{F.17})$$

$$= (T_{11} - T_{12} \cdot T_{22}^{-1} \cdot T_{21}) \cdot \underline{a}_1^+ + T_{12} \cdot T_{22}^{-1} \cdot \underline{a}_2^- \quad (\text{F.18})$$

Combining Eq. (F.15) and Eq. (F.18),

$$\begin{bmatrix} \underline{a}_1^- \\ \underline{a}_2^+ \end{bmatrix} = \begin{bmatrix} -T_{22}^{-1} \cdot T_{21} & T_{22}^{-1} \\ T_{11} - T_{12} \cdot T_{22}^{-1} \cdot T_{21} & T_{12} \cdot T_{22}^{-1} \end{bmatrix} \begin{bmatrix} \underline{a}_1^+ \\ \underline{a}_2^- \end{bmatrix} \quad (\text{F.19})$$

Therefore

$$S = \begin{bmatrix} -T_{22}^{-1} \cdot T_{21} & T_{22}^{-1} \\ T_{11} - T_{12} \cdot T_{22}^{-1} \cdot T_{21} & T_{12} \cdot T_{22}^{-1} \end{bmatrix}. \quad (\text{F.20})$$

Furthermore, if T_{12} and T_{21} are invertible, this can be rewritten as below,

$$S = \begin{bmatrix} T_{22}^{-1} & 0 \\ 0 & T_{12} \end{bmatrix} \cdot \begin{bmatrix} -I & T_{22} \\ T_{12}^{-1} \cdot T_{11} \cdot T_{21}^{-1} - T_{22}^{-1} & I \end{bmatrix} \cdot \begin{bmatrix} T_{21} & 0 \\ 0 & T_{22}^{-1} \end{bmatrix}.$$

APPENDIX G

Derivation of Eq. (4.45)

Here, we derive Eq. (4.45). For notational brevity, we replace S_{11} with B , and denote B 's m th row and n th column element as B_{mn} . We will show that

$$\frac{\partial \|B \cdot \underline{p}(\underline{\theta})\|_2^2}{\partial \underline{\theta}} = 2 \operatorname{Im} [\operatorname{diag}\{\underline{p}(-\underline{\theta})\} \cdot B^H \cdot B \cdot \underline{p}(\underline{\theta})]. \quad (\text{G.1})$$

To this end, note that the cost function can be expanded as

$$\begin{aligned} \|B \cdot \underline{p}(\underline{\theta})\|_2^2 &= \sum_{n=1}^M |B_{nm} e^{j\theta_n}|^2 \\ &= \sum_{n=1}^M \sum_{m=1}^M |B_{nm}|^2 + 2 \sum_{n=1}^M \sum_{p>q} \operatorname{Re} (B_{np} B_{nq}^* e^{j(\theta_p - \theta_q)}) \\ &= \sum_{n=1}^M \sum_{m=1}^M |B_{nm}|^2 + 2 \sum_{n=1}^M \sum_{p>q} |B_{np}| |B_{nq}| \cos(\theta_p - \theta_q + \angle B_{np} - \angle B_{nq}), \end{aligned} \quad (\text{G.2})$$

where $\operatorname{Re}(\cdot)$ denotes the operator that returns the real part of the argument. Consequently, the derivative of the cost function with respect to the k th phase θ_k can be expressed as

$$\frac{\partial \|B \cdot \underline{p}(\underline{\theta})\|_2^2}{\partial \theta_k} = -2 \sum_{n=1}^M \sum_{q \neq k} \operatorname{Im} [B_{nk} B_{nq}^* e^{j(\theta_k - \theta_q)}] \quad (\text{G.3})$$

$$= -2 \operatorname{Im} \left[e^{j\theta_k} \sum_{n=1}^M B_{nk} \sum_{q \neq k} B_{nq}^* e^{-j\theta_q} \right], \quad (\text{G.4})$$

where $\operatorname{Im}(\cdot)$ denotes the operator that returns the imaginary part of the argument. Let \underline{e}_k be the k -th elementary vector. We may rewrite Eq. (G.4) as

$$\frac{\partial \|B \cdot \underline{p}(\underline{\theta})\|_2^2}{\partial \theta_k} = -2 \operatorname{Im} \left[e^{j\theta_k} \begin{bmatrix} B_{1k} & \cdots & B_{Mk} \end{bmatrix} \cdot B^* \cdot \{I - \underline{e}_k \cdot \underline{e}_k^H\} \cdot \underline{p}(\underline{\theta})^* \right], \quad (\text{G.5})$$

or, equivalently, as

$$\frac{\partial \|B \cdot \underline{p}(\underline{\theta})\|_2^2}{\partial \theta_k} = -2\text{Im} \left[e^{j\theta_k} \begin{bmatrix} B_{1k} & \cdots & B_{Mk} \end{bmatrix} \cdot B^* \cdot \underline{p}(\underline{\theta})^* \right] - 2\text{Im} \left[\begin{bmatrix} B_{1k} & \cdots & B_{Mk} \end{bmatrix} \cdot B^* \cdot \underline{e}_k \right] \quad (\text{G.6})$$

$$= -2\text{Im} \left[e^{j\theta_k} \begin{bmatrix} B_{1k} & \cdots & B_{Mk} \end{bmatrix} \cdot B^* \cdot \underline{p}(\underline{\theta})^* \right]. \quad (\text{G.7})$$

Stacking the elements into a vector yields the relation

$$\frac{\partial \|B \cdot \underline{p}(\underline{\theta})\|_2^2}{\partial \underline{\theta}} = -2 \text{Im} \left[\text{diag}\{\underline{p}(\underline{\theta})\} \cdot B^T \cdot B^* \cdot \underline{p}(\underline{\theta})^* \right], \quad (\text{G.8})$$

or, equivalently, Eq. (G.1).

Index

G -transform, 116
 S -transform, 116
 T -transform, 116

conjugate gradients method, 72

fixed point equation, 117
free multiplicative convolution, 116
free probability theory, 116

modal expansion, 9

phase-conjugate mirroring, 67
Point Layer, 118
Point Symmetric Layer, 118
power conservation, 15

Random Point-Symmetric Matrix, 120
random point-symmetric scattering
matrix, 121
random point-symmetric transfer matrix,
121
reciprocity, 19

scattering matrix, 10
steepest descent method, 68
Symmetric Layer, 117

time-reversal symmetry, 16
transfer matrix, 10
transmission coefficient distribution, 13,
112

BIBLIOGRAPHY

BIBLIOGRAPHY

- [1] I. M. Vellekoop and A. P. Mosk. Universal optimal transmission of light through disordered materials. *Physical review letters*, 101(12):120601, 2008.
- [2] A. Ishimaru. *Wave propagation and scattering in random media*, volume 12. Wiley-IEEE Press, 1999.
- [3] O. N. Dorokhov. Transmission coefficient and the localization length of an electron in n bound disordered chains. *JETP Lett*, 36(7), 1982.
- [4] A. MacKinnon J. B. Pendry and A. B. Pretre. Maximal fluctuations—a new phenomenon in disordered systems. *Physica A: Statistical Mechanics and its Applications*, 168(1):400–407, 1990.
- [5] C. Barnes and J.B. Pendry. Multiple scattering of waves in random media: a transfer matrix approach. *Proceedings of the Royal Society of London. Series A: Mathematical and Physical Sciences*, 435(1893):185, 1991.
- [6] P. A. Mello, P. Pereyra, and N. Kumar. Macroscopic approach to multichannel disordered conductors. *Annals of Physics*, 181(2):290–317, 1988.
- [7] C. W. J. Beenakker. Applications of random matrix theory to condensed matter and optical physics. *Arxiv preprint arXiv:0904.1432*, 2009.
- [8] I. M. Vellekoop and A. P. Mosk. Phase control algorithms for focusing light through turbid media. *Optics Communications*, 281(11):3071–3080, 2008.
- [9] S. M. Popoff, G. Lerosey, R. Carminati, M. Fink, A. C. Boccarda, and S. Gigan. Measuring the transmission matrix in optics: an approach to the study and control of light propagation in disordered media. *Physical review letters*, 104(10):100601, 2010.
- [10] T. W. Kohlgraf-Owens and A. Dogariu. Transmission matrices of random media: Means for spectral polarimetric measurements. *Optics letters*, 35(13):2236–2238, 2010.
- [11] Z. Shi, J. Wang, and A. Z. Genack. Measuring transmission eigenchannels of wave propagation through random media. In *Frontiers in Optics*. Optical Society of America, 2010.

- [12] M. Kim, Y. Choi, C. Yoon, W. Choi, J. Kim, Q.-Han. Park, and W. Choi. Maximal energy transport through disordered media with the implementation of transmission eigenchannels. *Nature Photonics*, 6(9):583–587, 2012.
- [13] E. G. van Putten, A. Lagendijk, and A. P. Mosk. Optimal concentration of light in turbid materials. *JOSA B*, 28(5):1200–1203, 2011.
- [14] J. Aulbach, B. Gjonaj, P.M. Johnson, A.P. Mosk, and A. Lagendijk. Control of light transmission through opaque scattering media in space and time. *Physical review letters*, 106(10):103901, 2011.
- [15] M. Cui. A high speed wavefront determination method based on spatial frequency modulations for focusing light through random scattering media. *Optics Express*, 19(4):2989–2995, 2011.
- [16] M. Cui. Parallel wavefront optimization method for focusing light through random scattering media. *Optics letters*, 36(6):870–872, 2011.
- [17] C. Stockbridge, Y. Lu, J. Moore, S. Hoffman, R. Paxman, K. Toussaint, and T. Bifano. Focusing through dynamic scattering media. *Optics Express*, 20(14):15086–15092, 2012.
- [18] W. Choi, A. P. Mosk, Q.-H. Park, and W. Choi. Transmission eigenchannels in a disordered medium. *Physical Review B*, 83(13):134207, 2011.
- [19] C. Jin, R. R. Nadakuditi, E. Michielssen, and S. Rand. An iterative, backscatter-analysis based algorithm for increasing transmission through a highly-backscattering random medium. In *Statistical Signal Processing Workshop (SSP), 2012 IEEE*, pages 97–100. IEEE, 2012.
- [20] E. G. van Putten, I. M. Vellekoop, and A. P. Mosk. Spatial amplitude and phase modulation using commercial twisted nematic lcds. *Applied optics*, 47(12):2076–2081, 2008.
- [21] C. Jin, R. R. Nadakuditi, E. Michielssen, and S. Rand. Iterative, backscatter-analysis algorithms for increasing transmission and focusing light through highly scattering random media. *JOSA A*, 30(8):1592–1602, 2013.
- [22] O. N. Dorokhov. On the coexistence of localized and extended electronic states in the metallic phase. *Solid state communications*, 51(6):381–384, 1984.
- [23] J. B. Pendry. A transfer matrix approach to localisation in 3d. *Journal of Physics C: Solid State Physics*, 17:5317, 1984.
- [24] C. W. J. Beenakker. Random-matrix theory of quantum transport. *Reviews of modern physics*, 69(3):731, 1997.
- [25] D. Y. K. Ko and J. C. Inkson. Matrix method for tunneling in heterostructures: Resonant tunneling in multilayer systems. *Physical Review B*, 38(14):9945, 1988.

- [26] H. A. Haus. *Waves and fields in optoelectronics*, volume 1. Prentice-Hall New Jersey, 1984.
- [27] A. E. Siegman. *Lasers*. mill valley, 1986.
- [28] M. Abramowitz and I. A. Stegun. *Handbook of mathematical functions with formulas, graphs, and mathematical tables*. Dover publications, 1964.
- [29] A. Sidi. *Practical extrapolation methods: theory and applications*, volume 10. Cambridge Univ Pr, 2003.
- [30] M. N. Senhadji. On condition numbers of the shanks transformation. *Journal of computational and applied mathematics*, 135(1):41–61, 2001.
- [31] R. A. Horn and C. R. Johnson. *Matrix analysis*. Cambridge university press, 1990.
- [32] M. Fink. Time-reversal mirrors. *Journal of Physics D: Applied Physics*, 26(9):1333, 1999.
- [33] M. Cui and C. Yang. Implementation of a digital optical phase conjugation system and its application to study the robustness of turbidity suppression by phase conjugation. *Optics Express*, 18(4):3444–3455, 2010.
- [34] M. Cui, E. J. McDowell, and C. Yang. An in vivo study of turbidity suppression by optical phase conjugation (tsopc) on rabbit ear. *Optics Express*, 18(1):25–30, 2010.
- [35] I. M. Vellekoop, A. Lagendijk, and A. P. Mosk. Exploiting disorder for perfect focusing. *Nature Photonics*, 4(5):320–322, 2010.
- [36] H. A. Van der Vorst. *Iterative Krylov methods for large linear systems*, volume 13. Cambridge University Press, 2003.
- [37] L. N. Trefethen and D. Bau. *Numerical linear algebra*. Number 50. Society for Industrial Mathematics, 1997.
- [38] S. Grilli, P. Ferraro, S. De Nicola, A. Finizio, G. Pierattini, and R. Meucci. Whole optical wavefields reconstruction by digital holography. *Optics Express*, 9(6):294–302, 2001.
- [39] J. A. Kong. *Electromagnetic wave theory*. Wiley New York et al. , 1986.
- [40] R. Carminati, J. J. Saenz, J.-J. Greffet, and M. Nieto-Vesperinas. Reciprocity, unitarity, and time-reversal symmetry of the s matrix of fields containing evanescent components. *Physical review A*, 62(1):012712, 2000.
- [41] R. J. Potton. Reciprocity in optics. *Reports on Progress in Physics*, 67(5):717, 2004.

- [42] M. Nieto-Vesperinas. *Scattering and diffraction in physical optics*. Wiley New York, 1991.
- [43] C. Prada and M. Fink. Eigenmodes of the time reversal operator: A solution to selective focusing in multiple-target media. *Wave motion*, 20(2):151–163, 1994.
- [44] M. Fink, C. Prada, F. Wu, and D. Cassereau. Self focusing in inhomogeneous media with time reversal acoustic mirrors. In *Ultrasonics Symposium, 1989. Proceedings., IEEE 1989*, pages 681–686. IEEE, 1989.
- [45] M. F. Yanik and S. Fan. Time reversal of light with linear optics and modulators. *Physical review letters*, 93(17):173903, 2004.
- [46] W. H. Press, S. A. Teukolsky, W. T. Vetterling, and B. P. Flannery. *Numerical recipes 3rd edition: The art of scientific computing*. Cambridge University Press, 2007.
- [47] R. C. McPhedran, L. C. Botten, A. A. Asatryan, N. A. Nicorovici, P. A. Robinson, and C. M. De Sterke. Calculation of electromagnetic properties of regular and random arrays of metallic and dielectric cylinders. *Physical Review E*, 60(6):7614, 1999.
- [48] S. Singh and R. Singh. On the use of shank’s transform to accelerate the summation of slowly converging series. *Microwave Theory and Techniques, IEEE Transactions on*, 39(3):608–610, 1991.
- [49] Z.-Q. Luo, W.-K. Ma, A. M.-C. So, Y. Ye, and S. Zhang. Semidefinite relaxation of quadratic optimization problems. *Signal Processing Magazine, IEEE*, 27(3):20–34, 2010.
- [50] L. Vandenberghe and S. Boyd. Semidefinite programming. *SIAM review*, 38(1):49–95, 1996.
- [51] CVX Research Inc. CVX: Matlab software for disciplined convex programming, version 2.0. <http://cvxr.com/cvx>, August 2012.
- [52] M. Grant and S. Boyd. Graph implementations for nonsmooth convex programs. In V. Blondel, S. Boyd, and H. Kimura, editors, *Recent Advances in Learning and Control*, Lecture Notes in Control and Information Sciences, pages 95–110. Springer-Verlag Limited, 2008. http://stanford.edu/~boyd/graph_dcp.html.
- [53] K. H. Toh, M. J. Todd, and R. H. Tutuncu. SDPT3 version 4.0 – a MATLAB software for semidefinite-quadratic-linear programming.
- [54] G. H. Golub and C. F. Van Loan. *Matrix computations*, volume 3. JHU Press, 2012.

- [55] C. R. Rao. *Linear statistical inference and its applications*, volume 22. Wiley.com, 2009.
- [56] S. T. Smith. Optimum phase-only adaptive nulling. *Signal Processing, IEEE Transactions on*, 47(7):1835–1843, 1999.
- [57] S. Olver and R. R. Nadakuditi. Numerical computation of convolutions in free probability theory. *arXiv preprint arXiv:1203.1958*, 2012.
- [58] C. Schwartz. A classical perturbation theory. *Journal of Mathematical Physics*, 18:110, 1977.
- [59] G. Cincotti, F. Gori, M. Santarsiero, F. Frezza, F. Furno, and G. Schettini. Plane wave expansion of cylindrical functions. *Optics communications*, 95(4-6):192–198, 1993.